

SEMICONDUCTOR STRUCTURES, INTERFACES, AND SURFACES

Charge Carrier Transport through the Contact of Metal with a Superconducting Semiconductor

G. V. Kuznetsov

Shevchenko National University, Vladimirskaya ul. 64, Kiev, 01033 Ukraine

Submitted January 14, 2002; accepted for publication February 14, 2002

Abstract—Mechanisms controlling the charge carrier transport through the contact of a metal with a superconducting semiconductor were studied. The current–voltage characteristics of the contact was calculated for the thermionic, thermal–field, and tunnel emission currents. The dependences of the current transport conditions on the contact parameters and applied voltage were determined. The transition of the semiconductor to the superconducting state was shown to cause a decrease in the current through the contact in the voltage range controlled by the potential–barrier height and the energy band parameters of the superconductor. © 2002 MAIK “Nauka/Interperiodica”.

1. INTRODUCTION

The dominant mechanism of carrier transport through a conventional metal–superconductor contact is tunneling under the conditions of low temperatures and a rather thin potential barrier [1]. The role of the above-barrier passage of carriers under such conditions is insignificant and therefore remains almost obscure. The conditions of current flow in contact structures based on superconducting materials with a rather low carrier concentration (degenerate semiconductors and oxide high-temperature superconductors) can significantly differ [2–6]. The wide and low potential barrier at the contact interface offers the possibility of a significant increase in the thermionic current component. The above-barrier current can become dominant in such contact structures when there is a further decrease of the carrier concentration and an increase of the critical temperature T_c of the transition to the superconducting state. The possibility of controlling the potential barrier properties and, hence, the conditions of carrier passage simply by varying the semiconductor doping level is of additional interest. The metal–semiconductor contact is a well-studied system [7]; nevertheless, the mechanisms of current flow in the contacts with superconducting semiconductors call for additional detailed analysis.

This study is aimed at the consideration of the influence of the transition of a semiconductor to the superconducting state under the conditions of carrier passage in the metal–semiconductor contact structure. Calculations were carried out and formulas were suggested for the determination of the passing current in relation to the contact parameters and the applied voltage.

2. RESULTS AND DISCUSSION

2.1. Model of the Metal–Superconducting Semiconductor Contact

We restrict ourselves to the consideration of a simple model of the metal–semiconductor contact, where the current passage in the contact is controlled only by the potential barrier of the semiconductor space-charge region, and the influence of the intermediate layer at the interface is insignificant. Figure 1 displays the energy band diagram of an idealized contact between a metal and an n -type superconducting semiconductor, where ϕ_b is the potential barrier height, eV_b is the diffusion potential, eV_n is the Fermi level energy (positive for a degenerate semiconductor) with respect to the bottom of the semiconductor conduction band, Δ is the parameter of the superconductor energy band, and V is the

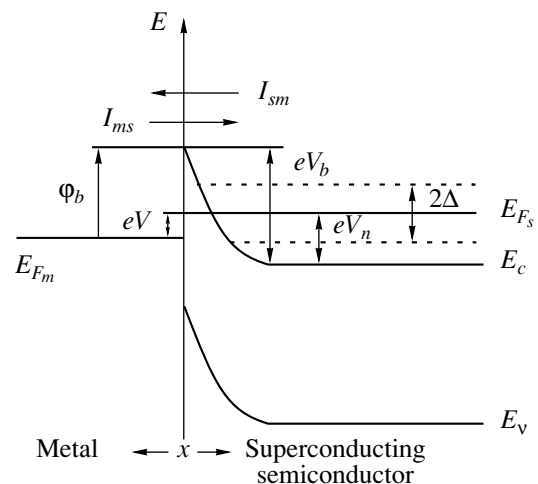


Fig. 1. Energy band diagram of the metal–(superconducting semiconductor) contact.

voltage applied to the contact. In comparison with an ordinary metal–semiconductor contact, a modification of this model consists in the use of the density of states of the superconductor in the bulk of the semiconductor material at a temperature $T < T_c$. Free carriers are absent in the region of the semiconductor space charge.

We will analyze the transport of majority carriers in the approximations of the diode theory. If the potential barrier height $\phi_b \gg kT$ and current flow do not disturb the thermodynamic equilibrium in the emission region, the total current I_n through the contact is controlled by the difference between the semiconductor-to-metal current J_{sm} and the opposite metal-to-semiconductor current J_{ms} [7]. The number of electrons that pass from the semiconductor to the metal in the energy range from E to $E + dE$ is proportional to the number of semiconductor occupied states $N_s(E)f(E)dE$, the number of metal unoccupied states $N_m(E - eV)[1 - f(E - eV)]dE$, and the probability $P_{sm}(E)$ of overcoming the potential barrier,

$$J_{sm} \propto P_{sm}(E)N_s(E)N_m(E - eV) \times f(E)[1 - f(E - eV)]dE. \quad (1)$$

A similar relation can be written for the metal–semiconductor electron flux,

$$J_{ms} \propto P_{ms}(E)N_s(E)N_m(E - eV) \times f(E - eV)[1 - f(E)]dE. \quad (2)$$

In (1) and (2), the following notation was introduced:

$$N_s(E) = N_n(E)n_s(E), \quad N_n(E) = \frac{4\pi(2m^*)^{3/2}(E - E_c)^{1/2}}{h^3}$$

is the density of states in the conduction band of the semiconductor in the nonsuperconducting state, $n_s(E) =$

$$\frac{|E - E_{Fs}|}{[(E - E_{Fs})^2 - \Delta^2]^{1/2}}$$

is the superconducting structure of the density of states, $N_m(E - eV)$ is the density of states

$$\text{in the metal, and } f(E) = \left[1 + \exp\left(\frac{E - eV_s}{kT}\right)\right]^{-1} \text{ and}$$

$$f(E - eV) = \left[1 + \exp\left(\frac{E - eV_n + eV}{kT}\right)\right]^{-1}$$

are the Fermi distribution functions in the semiconductor and metal, respectively. The energy is measured from the bottom $E_c = 0$ of the semiconductor conduction band. Further, it is conventionally assumed that the probability of carrier transport is independent of the direction of motion, $P_{sm}(E) = P_{ms}(E) = P(E)$, while the density of states in a metal and nonsuperconducting semiconductor are slow-varying functions and are equal to their values at the Fermi surface: $N_n(E) = N_n(0)$ and $N_m(E - eV) = N_m(E) = N_m(0)$. Introducing the notation $G_n = eAN_n(0)N_m(0)$ (G_n is the contact conductance in the nonsuperconducting state) and integrating over all the

probable energies, the total current density I_n in a general form can be written as

$$I_n = \frac{G_n}{e} \left\{ \int_{eV_n + \Delta}^{\infty} n_s(E)P(E)[f(E) - f(E - eV)]dE + \int_0^{eV_n - \Delta} n_s(E)P(E)[f(E) - f(E - eV)]dE \right\}. \quad (3)$$

Expression (3) defines the total number of electrons capable of passing through the interface in the metal–(superconducting semiconductor) contact at temperatures $T < T_c$.

2.2. Thermionic Emission

The problem of determining the thermionic current component I_{th} in the metal–(superconducting semiconductor) contact is reduced to determining the number of electrons passing above the potential barrier: $eV_b = \phi_b + eV_n - eV$. Using the accepted assumptions for above-barrier electrons of energy $E > eV_b$, we may set $P(E) = 1$. Let us analyze an explicit form of the current–voltage characteristic of the metal–(superconducting semiconductor) contact in relation to the range of the applied external voltage V .

Voltage range $eV < \phi_b - \Delta$. In this range, above-barrier electrons are characterized by the minimum energy $eV > eV_n + \Delta$ and the current through the contact is controlled only by the first term in (3). At $\Delta \gg kT$, the conditions

$$\exp\left(\frac{E - eV_n}{kT}\right) \gg 1 \text{ and } \exp\left(\frac{E - eV_n + eV}{kT}\right) \gg 1$$

are met in the entire range of probable energies $E \geq eV_b$. Then, the difference of the Fermi distribution functions is written as $f(E) - f(E - eV) =$

$$\left[1 - \exp\left(-\frac{eV}{kT}\right)\right] \exp\left(-\frac{E - eV_n}{kT}\right).$$

We take into account the influence of the superconducting state on the dependence of the current on the applied voltage, restricting ourselves to the first term of the expansion into the series near the potential barrier maximum $eV_b = \phi_b +$

$$eV_n - eV, \text{ i.e., } n_s(E) \approx \left[1 - \left(\frac{\Delta}{\phi_b - eV}\right)\right]^{-1/2}.$$

After substitution of the obtained values into (3) and integration within the limits from eV_b to ∞ , the density of the thermionic current in the voltage range $eV < \phi_b - \Delta$ is written as

$$I_{th} = \frac{A^*T^2}{\sqrt{1 - \left(\frac{\Delta}{\phi_b - eV}\right)^2}} \exp\left(-\frac{\phi_b}{kT}\right) \left[\exp\left(\frac{eV}{kT}\right) - 1 \right]. \quad (4)$$

Here, the notation $\frac{kT}{e} G_n = A^* T^2$ is used, which follows from the transformation of (4) at $\Delta \rightarrow 0$ into the known expression for the thermionic current density in the ordinary metal–semiconductor contact [7],

$$\begin{aligned} I_{\text{th}} &= I_s \left[\exp\left(\frac{eV}{kT}\right) - 1 \right] \\ &= A^* T^2 \exp\left(-\frac{\Phi_b}{kT}\right) \left[\exp\left(\frac{eV}{kT}\right) - 1 \right], \end{aligned} \quad (5)$$

where $A^* = \frac{4\pi e m^* k^2}{h^3}$ is the Richardson constant for thermionic emission.

Voltage range $\Phi_b - \Delta \leq eV \leq \Phi_b + \Delta$. When calculating in this voltage range, one should take into account the contribution of both parts of (3) to the total current. After substitutions $x = E - eV_n - \Delta$ and $x = -E - eV_n - \Delta$ in the first and second terms, respectively, expression (3) takes the form

$$\begin{aligned} I_{\text{th}} &= \frac{G_n}{e} \left\{ \exp\left(-\frac{\Delta}{kT}\right) \left[1 - \exp\left(-\frac{eV}{kT}\right) \right] \right. \\ &\quad \left. + \exp\left(-\frac{\Phi_b + \Delta}{kT}\right) \left[\exp\left(\frac{eV}{kT}\right) - 1 \right] \right\} \\ &\quad \times \int_0^{\infty} \frac{x + \Delta}{\sqrt{x(x + 2\Delta)}} \exp\left(-\frac{x}{kT}\right) dx. \end{aligned} \quad (6)$$

We set the upper limit of integration in the second term of (3) as $x_m = eV_n - \Delta \rightarrow \infty$, which is valid owing to the rapidly decreasing Fermi function in the degenerate semiconductor at $E < eV_n$. The integral in (6) may be found in the tabulated Laplace transforms (see [8]),

$$\int_0^{\infty} \frac{(x + \Delta) \exp\left(-\frac{x}{kT}\right)}{\sqrt{x\left(x + 2\frac{\Delta}{kT}\right)}} dx = \Delta \exp\left(\frac{\Delta}{kT}\right) K_1\left(\frac{\Delta}{kT}\right),$$

where $K_1\left(\frac{\Delta}{kT}\right)$ is a first-order modified Bessel function of the second kind. At $\Delta \gg kT$, the asymptotic expression $K_1\left(\frac{\Delta}{kT}\right) \approx \left(\frac{\pi kT}{2\Delta}\right)^{1/2} \exp\left(-\frac{\Delta}{kT}\right)$ can be used for the Bessel function. Then, after a corresponding substitution, we arrive at the current density in the voltage range $\Phi_b - \Delta \leq eV \leq \Phi_b + \Delta$

$$\begin{aligned} I_{\text{th}} &= A^* T^2 \left(\frac{\pi\Delta}{2kT}\right)^{1/2} \exp\left(-\frac{\Delta}{kT}\right) \left[1 + \exp\left(-\frac{\Phi_b - eV}{eT}\right) \right. \\ &\quad \left. - \exp\left(\frac{eV}{kT}\right) - \exp\left(-\frac{\Phi_b}{kT}\right) \right]. \end{aligned} \quad (7)$$

The minimum ratio of the thermionic current $I_{\text{th}}(S)$ in the superconducting state to the current $I_{\text{th}}(N)$ in the nonsuperconducting state is attained at the voltage $eV = \Phi_b$. Comparing (5) and (7), one finds that the ratio $I_{\text{th}}(S)/I_{\text{th}}(N)$ is defined by the value of Δ/kT and is independent of the potential barrier height Φ_b ,

$$\left[\frac{I_{\text{th}}(S)}{I_{\text{th}}(N)} \right]_{\min} = \left(\frac{2\pi\Delta}{kT}\right)^{1/2} \exp\left(-\frac{\Delta}{kT}\right). \quad (8)$$

Voltage range $eV > \Phi_b + \Delta$. In this range, the potential barrier maximum $eV_b = \Phi_b + eV_n - eV$ is below the Fermi level eV_n in the semiconductor. The major contribution to the above-barrier current is made by carriers in the energy range of $0 \leq E \leq eV_n - \Delta$; therefore, we restrict ourselves to the calculation of the second term in (3). At $\Delta \gg kT$ in this energy range, the relations

$$\exp\left(\frac{E - eV_n}{kT}\right) \ll 1, \quad \exp\left(\frac{E - eV_n + eV}{kT}\right) \gg 1, \quad \text{and}$$

$$f(E) - f(E - eV) = \left[1 - \exp\left(-\frac{eV}{kT}\right) \right]$$

are valid. After integration within the limits from $eV_b = \Phi_b + eV_n - eV$ to $eV_n - \Delta$ in the voltage range $eV < \Phi_b + \Delta$, we arrive at a close-to-linear dependence of the current on the applied voltage

$$I_{\text{th}} = A^* T^2 \left[1 - \exp\left(-\frac{eV}{kT}\right) \right] \sqrt{\left(\frac{eV - \Phi_b}{kT}\right)^2 - \left(\frac{\Delta}{kT}\right)^2}. \quad (9)$$

Voltage range $eV < 0$. The found relations (4), (7), and (9) are independent of the applied voltage sign and can be used to describe the reverse portion of the current–voltage (I – V) characteristic of the contact. The transition of the semiconductor into the superconducting state has an effect on the dependence of the thermionic current on the reverse applied voltage provided that $\Delta > \Phi_b$.

Figure 2a displays the thermionic emission current I_{th} in the metal–(superconducting semiconductor) contact, which was calculated for the potential barrier height $\Phi_b = 0.2$ eV and various parameters Δ of the semiconductor energy band. Figure 2b shows the temperature variations in the I – V characteristic of the metal–superconducting semiconductor contact at $\Phi_b = 0.2$ eV and $\Delta = 0.05$ eV.

The transition of the semiconductor into the superconducting state gives rise to a special feature in the I – V characteristic, which is caused by the energy gap 2Δ in the density of states of the semiconductor. The changes in the I – V characteristic are observed in the voltage range close to the potential barrier height and,

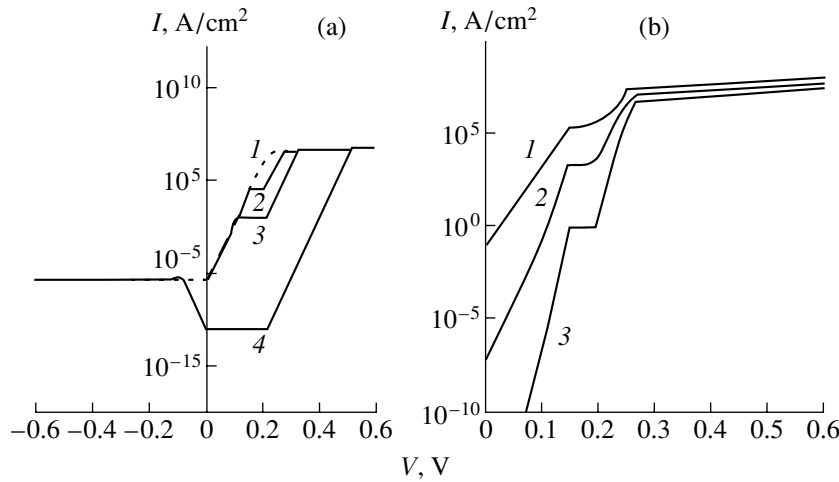


Fig. 2. Thermionic current in the metal-superconducting semiconductor contact at $\phi_b = 0.2$ eV: (a) $T = 77$ K, $\Delta/\phi_b = (1)$ 0, (2) 0.25, (3) 0.5, and (4) 1.5; (b) $\Delta = 0.5$ eV, $T = (1)$ 150, (2) 77, and (3) 30 K.

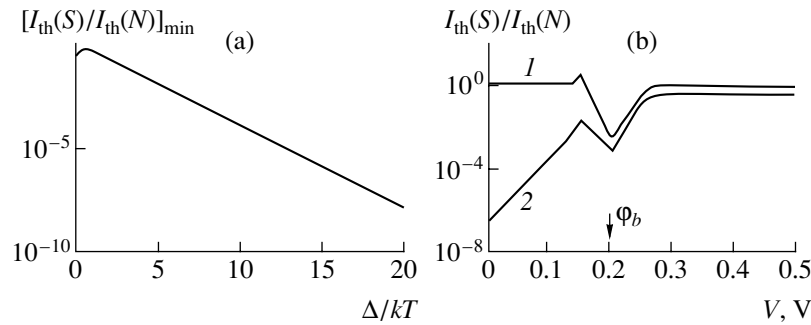


Fig. 3. (a) Dependence of the ratio $[I_{th}(S)/I_{th}(N)]_{min}$ of the thermionic currents in the superconducting and nonsuperconducting states at $eV = \phi_b$ on Δ/kT . (b) Dependences of the ratio $I_{th}(S)/I_{th}(N)$ on the applied voltage (I) for $I_{th}(S)$ and $I_{th}(N)$ at 77 K and (2) for $I_{th}(S)$ at 77 K and $I_{th}(N)$ at 150 K.

when $\Delta < \phi_b$, are observed only in the forward portion of the I - V characteristic. When $\Delta > \phi_b$, changes are observed both in the forward and reverse portions of the I - V characteristic. In this case, the effect of reverse rectification becomes probable (in the range $eV < \phi_b$, the forward current becomes smaller than the reverse one) (see Fig. 2, curve 4). The characteristic current increase at the voltage $\phi_b - \Delta$ is caused by a singularity in the dependence of the density of states $n_s(E)$ near the energy band edge of the superconductor.

Figure 3a shows the dependences of the ratio $[I_{th}(S)/I_{th}(N)]_{min}$ of the thermionic component of the current through the contact in the superconducting and nonsuperconducting states of the semiconductor on Δ/kT at $eV = \phi_b$, which were calculated according to (8). The current changes become more significant as the energy gap parameter Δ of the superconductor increases and the temperature T decreases. Figure 3b displays the influence of the measurement temperature on the dependence of the ratio $I_{th}(S)/I_{th}(N)$ of the currents on the applied voltage. The ratio minimum is observed at a voltage corresponding to the height of the potential barrier $eV = \phi_b$. The position of the minimum

of the ratio $[I_{th}(S)/I_{th}(N)]_{min}$ allows the determination of the potential barrier height ϕ_b at the metal-(superconducting semiconductor) interface from the applied voltage [9].

2.3. Tunneling

When determining the tunneling component I_t of the current through the metal-(superconducting semiconductor) contact, one should take into account in (3) the energy dependence of the probability $P(E)$ that the carriers can overcome the potential barrier. If the semiconductor space-charge region is a Schottky layer with a uniform distribution of impurities, one can use the expression for $P(E)$ found in the Wentzel-Kramers-Brillouin (WKB) approximation (see [4]),

$$P(E) = P_0 \exp \left\{ -\frac{eV_b}{E_{00}} \left[\sqrt{1 - \frac{E}{eV_b}} - \frac{E}{eV_b} \ln \left(\sqrt{\frac{eV_b}{eV_n}} + \sqrt{\frac{eV_b - E}{eV_n}} \right) \right] \right\}, \quad (10)$$

where $E_{00} = \frac{eh}{4\pi\sqrt{\epsilon_0\epsilon_2 m^*}} \sqrt{\frac{n_0}{m^*}}$ and P_0 is a numerical coefficient close to unity.

For heavily doped semiconductors at sufficiently low temperatures $E_{00} \gg kT$, the current through the contact is controlled by the tunneling of electrons with energies close to the Fermi level (field emission). If the Fermi energy is low in comparison with the effective barrier height, i.e., $eV_b \gg eV_n$, expression (10) when $E \approx eV_n$ may be written as

$$P(eV_n) = P_0 \exp\left(-\frac{\Phi_b + eV_n - eV}{E_{00}}\right).$$

Voltage range $-\Delta \leq eV \leq \Delta$. Factoring of the penetration coefficient in (3) outside to the integral sign allows easy determination of the contact I - V characteristic in the voltage range $-\Delta \leq eV \leq \Delta$, where the influence of the superconducting state on the tunneling current is most significant. As in the case of thermionic current, the integrals in (3) are calculated by introducing the variables $x = E - eV_n - \Delta$ and $x = -E - eV_n - \Delta$ in the first and second terms, respectively, and by integrating within the limits from 0 to ∞ . After substitution and corresponding calculations, we arrive at the final expression for the tunnel current density

$$I_t = A^* T^2 P_0 \left(\frac{\pi\Delta}{2kT}\right)^{1/2} \exp\left(-\frac{\Delta}{kT}\right) \exp\left(-\frac{\Phi_b + eV_n - eV}{E_{00}}\right) \times \left[\exp\left(\frac{eV}{kT}\right) - \exp\left(-\frac{eV}{kT}\right) \right]. \quad (11)$$

Voltage range $eV > \Delta$. In this range, the major contribution to the tunneling current is made by carriers with the energy $0 < E < eV_n - \Delta$ and the tunneling current is defined by the second term in (3). When $\Delta \gg kT$, we may assume that $\exp\left(\frac{E - eV_n}{kT}\right) \ll 1$, $\exp\left(\frac{E - eV_n + eV}{kT}\right) \gg 1$, and $f(E) - f(E - eV) = \left[1 - \exp\left(-\frac{eV}{kT}\right)\right]$. After integration within the limits from $eV_n - eV$ to $eV_n - \Delta$, the tunneling current in the voltage range $eV > \Delta$ is written as

$$I_t = A^* T^2 P_0 \exp\left(-\frac{\Phi_b + eV_n - eV}{E_{00}}\right) \times \left[1 - \exp\left(-\frac{eV}{kT}\right)\right] \sqrt{\left(\frac{eV}{kT}\right)^2 - \left(\frac{\Delta}{kT}\right)^2}. \quad (12)$$

When $\Delta \rightarrow 0$, dependence (12) is transformed (to within the preexponential factor) into the known

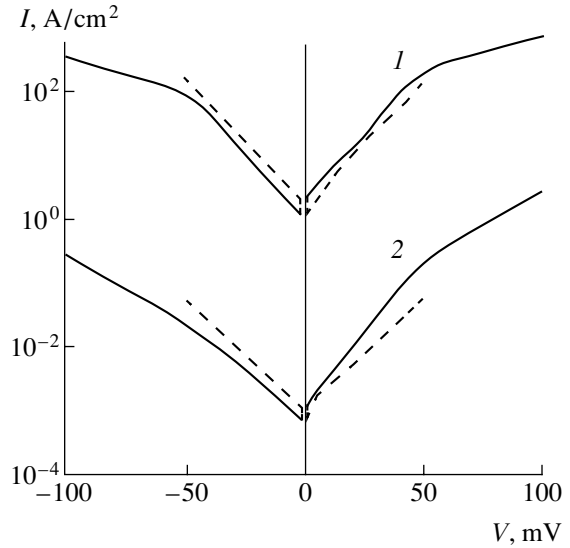


Fig. 4. Tunneling current in the metal-(superconducting semiconductor) contact (dashed lines correspond to the dependence for the rectangular barrier), $E_{00}/kT = (1)$ 10 and (2) 3.

expression for tunneling current in an ordinary metal-semiconductor contact (see [7])

$$I_t = I_{st} \exp\left(\frac{eV}{E_{00}}\right) \left[1 - \exp\left(-\frac{eV}{kT}\right)\right]. \quad (13)$$

The dependence of the potential-barrier penetrability factor on the applied voltage causes asymmetry of the current-voltage characteristic of the metal-(superconducting semiconductor) contact. Figure 4 displays the dependences of the tunneling current on the applied voltage for the Schottky barrier (the solid line) and a symmetric rectangular barrier (dashed line), whose penetrability is independent of the applied voltage. A decrease in the ratio E_{00}/kT causes a decrease in the tunneling current and an increase in the asymmetry of the I - V characteristic of the metal-(superconducting semiconductor) contact.

2.4. Thermal-Field Emission

In the range of intermediate temperatures and barrier thicknesses $E_{00} \approx kT$, the dominant mechanism is tunneling of thermally excited carriers (thermal-field emission). The probability of tunneling of thermally excited electrons increases with energy more rapidly than does a decrease in their number. The energy at which the flux of electrons tunneling through the barrier is largest is located above the Fermi level and is defined as

$$E_m = (\Phi_b + eV_n) \cosh^{-2}\left(\frac{E_{00}}{kT}\right).$$

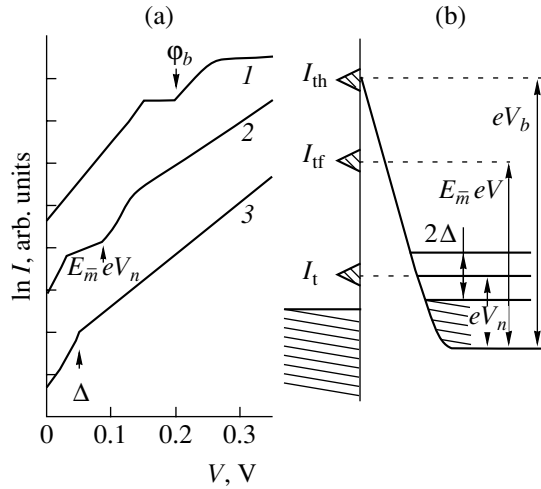


Fig. 5. (a) Current-voltage characteristics and (b) the energy distribution in the metal-(superconducting semiconductor) contact for the (1) thermionic (I_{th}), (2) thermal-field (I_{tf}), and (3) field (I_t) emission.

Expression (10) for the penetrability factor $P(E)$ at the energy E_{00} is written as $P(E_m) = P_0 \exp\left(-\frac{eV_b}{E_0}\right)$, where

$E_0 = E_{00} \coth \frac{E_{00}}{kT}$. If the contribution of electrons with $E < E_m$ to the current is ignored, the dependences of the thermal-field emission current I_{tf} on the applied voltage are determined in a similar way as the dependences considered above for the thermionic emission current I_{th} . In this case, when calculating the current for any range of the applied voltage, one should substitute the diffusion potential eV_b with the energy $E_m - eV$ of the maximum flux of tunneling electrons.

Voltage range $eV < E_m - eV_n - \Delta$. In this range, an expression for the thermal-field current density I_{tf} is found using the penetrability factor $P(E_m)$ and restricting ourselves to the first term in the expansion into the series near the energy E_m of the function $n_s(E) \approx$

$$\left[1 - \left(\frac{\Delta}{E_m - eV_n - eV}\right)\right]^{-1/2} \text{ maximum,}$$

$$I_{tf} = \frac{A^* T^2 P_0}{\sqrt{1 - \left(\frac{\Delta}{E_m - eV_n - eV}\right)^2}} \exp\left(-\frac{\Phi_b + eV_n - eV}{E_0}\right) \times \exp\left(-\frac{E_m - eV_n}{kT}\right) \left[\exp\left(\frac{eV}{kT}\right) - 1\right]. \quad (14)$$

Voltage range $E_m - eV_n - \Delta \leq eV \leq E_m - eV_n + \Delta$. In this range, the current is calculated taking into account the values of both parts of (3). As in the case of thermionic current, the substitution $x = E - eV_n - \Delta$ is

made in the first term. In the second term of (3), the variable $x = -E - eV_n - \Delta$ is introduced and the upper integration limit is taken as $x_m = eV_n - \Delta \rightarrow \infty$. After the calculation of an integral similar to (6), we find that the current density of thermal-field emission in this voltage range is

$$I_{tf} = A^* T^2 P_0 \left(\frac{\pi \Delta}{2kT}\right)^{1/2} \exp\left(-\frac{\Delta}{kT}\right) \times \exp\left(-\frac{\Phi_b + eV_n - eV}{E_0}\right) \left\{1 - \exp\left(-\frac{eV}{kT}\right)\right\} + \exp\left(-\frac{E_m - eV_n}{kT}\right) \left[\exp\left(\frac{eV}{kT}\right) - 1\right]. \quad (15)$$

Voltage range $eV > E_m - eV_n + \Delta$. In this range, the contribution of carriers with the energy $0 < E < eV_n - \Delta$ to the carrier current is prevalent. Integrating the second term of (3) within the limits from E_m to $eV_n - \Delta$, we arrive at the current density

$$I_{tf} = A^* T^2 P_0 \exp\left(-\frac{\Phi_b + eV_n - eV}{E_0}\right) \times \left[1 - \exp\left(-\frac{eV}{kT}\right)\right] \sqrt{\left(\frac{E_m - eV_n}{kT}\right)^2 - \left(\frac{\Delta}{kT}\right)^2}. \quad (16)$$

At $E_{00} \ll kT$ and $P(E) = 1$, dependences (14), (15), and (16) are transformed into (4), (7), and (9), respectively.

Figure 5 displays the I - V characteristics for the basic mechanisms of current flow in the metal-(superconducting semiconductor) contact (Fig. 5a) and the distribution of energies in the contact in the mode of direct bias (Fig. 5b) in the case of thermionic ($E_{00} \ll kT$), thermal-field ($E_{00} \approx kT$), and field ($E_{00} \gg kT$) emission.

CONCLUSION

The transition of the semiconductor bulk to the superconducting state causes significant changes in the I - V characteristic of the metal-semiconductor contact. These changes depend on the potential-barrier height and the parameter of the superconductor energy gap. For the basic mechanisms of carrier transport, calculations were carried out and formulas were suggested for determining the flowing current in relation to the contact parameters and applied voltage. The thermionic mechanism of carrier transport may be used to develop superconducting semiconductor heterostructures with rectification properties and zero resistance of the base region.

REFERENCES

1. E. L. Wolf, *Principles of Electron Tunneling Spectroscopy* (Clarendon, New York, 1985; Naukova Dumka, Kiev, 1990).
2. J. Lesueur, L. H. Greene, W. L. Fieldmann, and A. Inam, *Physica C* (Amsterdam) **191**, 325 (1991).
3. B. J. van Wees, P. de Vries, P. Magnee, and T. M. Klapwijk, *Phys. Rev. Lett.* **69**, 510 (1992).
4. R. Kummel, H. Plehn, and U. Schussler, in *Proceedings of the 23rd International Conference on Physics of Semiconductors, Berlin, 1996*, V11.E2, p. 3387.
5. M. Belogolovskii, M. Grajcar, P. Kus, *et al.*, *Phys. Rev. B* **59**, 9617 (1999).
6. F. V. Komissinskiĭ, G. A. Ovsyannikov, and Z. G. Ivanov, *Fiz. Tverd. Tela* (St. Petersburg) **43**, 769 (2001) [*Phys. Solid State* **43**, 801 (2001)].
7. S. Sze, *Physics of Semiconductor Devices* (Wiley, New York, 1981; Mir, Moscow, 1984).
8. *Tables of Integral Transforms (Bateman Manuscript Project)*, Ed. by A. Erdelyi (McGraw-Hill, New York, 1954; Nauka, Moscow, 1969), Vol. 1.
9. G. V. Kuznetsov, *Pis'ma Zh. Éksp. Teor. Fiz.* **74**, 556 (2001) [*JETP Lett.* **74**, 495 (2001)].

Translated by A. Kazantsev

SEMICONDUCTOR STRUCTURES,
INTERFACES, AND SURFACES

Adsorption and Transformation of C₆₀ Molecules at the (100) Si Surface

N. R. Gall*, E. V. Rut'kov, and A. Ya. Tontegode

*Ioffe Physicotechnical Institute, Russian Academy of Sciences,
Politekhnicheskaya ul. 26, St. Petersburg, 194021 Russia*

*e-mail: gall@ms.ioffe.rssi.ru

Submitted February 26, 2002; accepted for publication February 28, 2002

Abstract—The adsorption of C₆₀ molecules, the initial stages of the growth of the films composed of these molecules, and the transformation of C₆₀ films at the (100) Si surface in the temperature range of 300–1400 K were studied under ultrahigh-vacuum conditions. It is shown that the C₆₀ molecules retain their structure in the adsorbed state at temperatures as high as 700 K and these molecules decompose gradually at higher temperatures. The carbon atoms released at ~1300 K “forget” completely about their origin and form silicon carbide, which grows and threads into the bulk of the sample. At room temperature, the fullerite film grows according to a mechanism similar to that suggested by Stranski and Krastanov and is accompanied by the formation of crystallites over the monolayer coating. The crystallites occupy 50–60% of the surface area, which depends only slightly on the deposition time. © 2002 MAIK “Nauka/Interperiodica”.

1. INTRODUCTION

Fullerenes represent a new and relatively recently discovered allotropic form of carbon. It is necessary to understand (both for practical and scientific purposes) how the fullerene molecules interact with a material and, in particular, with solid surfaces. The fundamental study of the adsorption of C₆₀ molecules at solid surfaces represents a complicated challenge, mainly due to the complex structure of the object under investigation. Nevertheless, there are now several dozen publications concerned with such studies, which were performed using various experimental and theoretical methods. Silicon [1–5], noble metals [6–8], or refractive metals [9] were typically used as substrates.

We have previously studied the adsorption of C₆₀ molecules on the surface of a number of metals (Ir, Re, Mo, and W) [10–13]. We determined the contact and thermal stability of C₆₀ molecules at metal surfaces and studied the transformation of the adsorbed C₆₀ layer as a result of heating the substrate. It was found that the adsorbed C₆₀ molecules retain their fullerene structure when deposited on the Ir, Re, and Mo substrates up to a certain (dependent on the substrate) temperature (~800 K for the Re substrate and ~1000 K for the Ir substrate). At higher temperatures, the molecules decompose and carbon released in the adsorbed layer is dissolved in the substrate bulk (on the Re or Mo substrates) or is graphitized (on the Ir substrates). The C₆₀ molecules on the tungsten substrates decompose even at room temperature.

It is well known that C₆₀ molecules adsorbed on silicon at room temperature retain their molecular structure. At the same time, the mechanisms of the fullerite-

layer growth and the details of the transformation of the adsorbed layer as a result of heat treatment are still not clear. In this paper, we report the results of studying the desorption and thermal transformation of fullerenes at the Si(100) surface.

2. EXPERIMENTAL

The experiments were performed using a high-resolution Auger spectrometer (see [14]) in an ultrahigh-vacuum chamber with a residual pressure $p \sim 10^{-10}$ Torr. It was possible to record the Auger peaks directly from the heated samples. The latter were directly heated silicon ribbons with a size of $0.3 \times 1.5 \times 50$ mm and a face (100) at the surface; the samples were cleaned using high-temperature (~1500 K) heating for several hours. Only the silicon Auger peaks were detected from the cleaned surface.

Fullerenes were deposited onto the entire surface of the ribbon using a Knudsen cell with the flux incident at 65° to the surface normal. A C₆₀ charge of 99.5% purity (~0.05 g) was loaded into the cell. After pre-burning, the cell produced a stable and easily controlled flux of fullerene molecules with a density $\nu_{C_{60}} = 10^{10}–10^{13}$ molecule/(cm² s).

In order to determine the absolute concentration of fullerene molecules at the surface and the absolute density of their flux, we developed and implemented a method based on the high-temperature deposition of C₆₀ molecules onto an auxiliary iridium ribbon up to a certain submonolayer concentration using the same C₆₀ flux. The deposition was then stopped, and the auxiliary ribbon located at the manipulator near the operating

ribbon was heated to 1800 K; this temperature was high enough to decompose all the C₆₀ molecules into atoms but was too low for C atoms to be desorbed from the iridium surface. At this temperature, carbon atoms form a two-dimensional graphite film on both sides of the ribbon and the carbon surface concentration *N* can be measured precisely using Auger spectroscopy. The flux density of fullerene molecules (in molecule/(cm² s)) can then be easily calculated using the formula

$$v_{C_{60}} = N/60t, \quad (1)$$

where *t* is the deposition duration (it is assumed that the attachment coefficient is equal to unity at room temperature [11]).

3. AUGER SPECTROSCOPY OF ADSORBED FULLERENE

The method of Auger spectroscopy has been well developed for determining the surface concentrations of atomic adsorbates. If such complex objects as fullerene molecules reside at the surface, it is difficult to relate the observed intensities of the Auger signals to the number of carbon atoms. Fortunately, a C₆₀ molecule is spherically symmetric, which allowed us to use the approximation we referred to as quasi-atomic. This approximation implies that we ignore the internal structure of a molecule, determine experimentally the Auger signal intensity that is yielded by the surface covered by a known number of molecules, and attribute a specific sensitivity coefficient to each molecule. Similarly, we also determine the screening capacity of a molecule for the Auger electrons of the substrate. In the setup we used, the Auger electrons were collected by an analyzer within a narrow solid angle of ~1° about an angle of 4° to the normal of the surface. Therefore, the molecules that adsorbed within a monolayer did not screen the Auger signals from each other; in contrast, such a screening certainly occurred when the multilayer fullerite films were formed. The aforementioned approximation is applicable as long as the adsorbed molecule retains its shape and internal structure, i.e., so long as this molecule remains intact.

The above-described method for absolute calibration makes it possible to estimate the elemental-sensitivity coefficient, which relates the fullerene surface concentration in the first monolayer to the intensity of the Auger signal. As we found out, the sensitivity coefficient for a single C₆₀ molecule was about 30 times larger than that for a carbon atom in the graphite film; i.e., the sensitivity of a single carbon atom incorporated into a fullerene molecule is, on average, two times lower than in graphite.

It was previously found [15, 16] that the C_{KVV} Auger peak in C₆₀ molecules has an energy of 269 eV, which is about 3 eV lower than the corresponding energy in, for example, graphite, metal carbides, or adsorbed carbon clusters. Such an energy of the Auger peak is

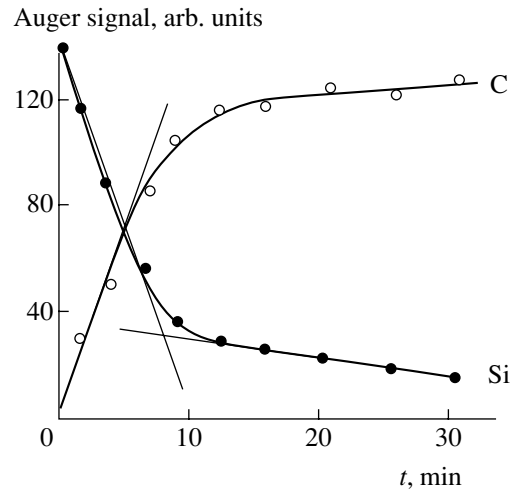


Fig. 1. Intensities of the silicon and carbon Auger signals in the course of adsorption of C₆₀ molecules on the (100) face of silicon single crystal at *T* = 300 K. The flux density of C₆₀ molecules was equal to $v_{C_{60}} \approx 3.5 \times 10^{11}$ molecule/(cm² s).

observed both for thick (5–10 monolayers) films formed of adsorbed C₆₀ molecules and for submonolayer coatings. It has been suggested that this phenomenon be used to differentiate between a fullerene adsorbed at the surface and other possible carbon states and to assess the chemical state of adsorbed C₆₀ molecules.

4. ADSORPTION AT ROOM TEMPERATURE

In Fig. 1, we show the variation in the intensities of the carbon and silicon Auger signals in the course of adsorption of the C₆₀ molecules at the Si(100) surface at room temperature. As can be seen, the silicon Auger signal decreases steadily; this signal decreases rapidly (by a factor of 4.3) in the course of the first 10 min of deposition, whereas it decreases much slower (merely by a factor of 2) during the next 20 min. The carbon Auger signal increases almost linearly up to the deposition duration of ~250 s, then increases more slowly, and levels off abruptly after ~800 s of deposition. This means that, starting with *t* = 250 s, the newly incoming C₆₀ molecules screen the Auger signal not only from the substrate but also from the carbon of previously adsorbed molecules. Thus, we may state that the adsorption of molecules into the second and subsequent layers sets in at *t* = 250 s.

The question arises as to what kind of coating grows on (100) Si during the deposition time of 250 s. It is noteworthy that this coating only insignificantly screens (by a factor of 1.9) the substrate Auger signal compared to, for example, screening by a fullerene monolayer on the Mo(100) layer; this monolayer attenuates the substrate Auger signal by ~2.9 times. Since the concentration of C₆₀ molecules in a monolayer on the Mo substrate is equal to $\sim 1.6 \times 10^{14}$ cm⁻² [12], this

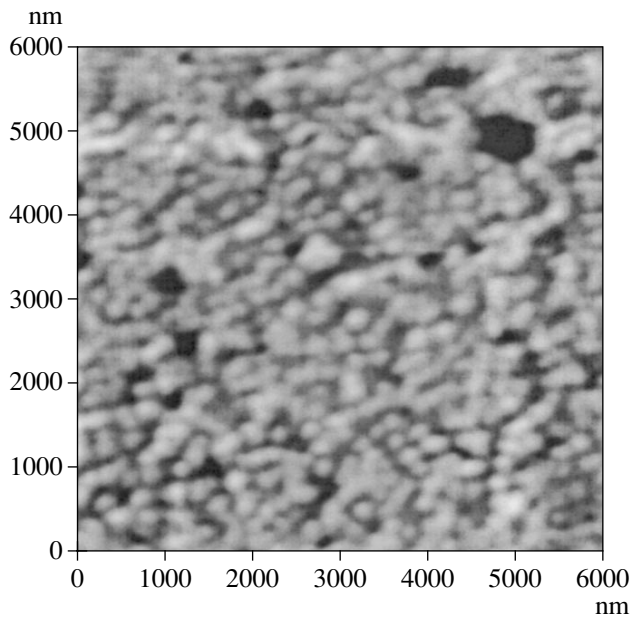


Fig. 2. An image of the (100) Si surface after deposition of C_{60} molecules at room temperature for ~ 2000 s with the C_{60} flux density being $v_{C_{60}} \approx 3.5 \times 10^{11}$ molecule/(cm^2 s). The image was obtained using atomic-force microscopy.

concentration should be much lower in the case under consideration and, by estimation, should not exceed $(7-8) \times 10^{13} cm^{-2}$.

Based on the aforementioned absolute calibration of the flux, we may state that $\sim 8.8 \times 10^{13} cm^{-2}$ of C_{60} molecules are incident on the surface after 250 s, which is in good agreement with the above-mentioned estimate. The C_{60} molecule diameter, which corresponds to the distance between the centers of the constituent atoms, is equal to 7.1 Å, and the structural-chemical diameter required for estimations is larger by the value of the covalent diameter of a C atom (by 1.4 Å) and is equal to 8.5 Å [17]. The concentration of spheres with such a diameter at the surface when packing is densest is equal to $N_{cl-packed} = 1.64 \times 10^{14}$ molecule/ cm^2 ; thus, the coating under consideration amounts to about one half of the densely packed monolayer composed of C_{60} molecules.

During the subsequent 250 s, the same number of molecules are incident on the surface; however, the Auger signal intensity increases only by a factor of ~ 1.6 . This means that a large portion of molecules is adsorbed on top of the molecules adsorbed previously. When the deposition duration is longer than 600 s, each subsequent dose of deposition results in a very weak additional screening of the Auger signal from the substrate. Previously [12], a similar dependence of the Auger signals was attributed to the growth of tower-shaped crystallites over the monolayer coating, with the surface area occupied by crystallites increasing much slower than the crystallite height. It is reasonable to assume that we are encountering a similar situation

here. For the deposition time of ~ 20 min, the Auger signal of the substrate is attenuated by a factor of ~ 6 , and for a 30-min deposition, this signal is attenuated by a factor of ~ 8 . Assuming that a fullerene monolayer attenuates the substrate signal by about three times, whereas the crystallites suppress completely the Auger signal that comes from the surface area where the crystallites are located, we can write the following expression for the intensity of the Auger signal which comes from the substrate:

$$I(t) = (1 - s)I_0/3. \quad (2)$$

Here, $I(t)$ is the measured Auger signal from the substrate for the deposition time t , I_0 is the Auger signal from the clean substrate, and s is the fraction of the area occupied by crystallites. The value of s can then be estimated using the following formula:

$$s = 1 - 3I(t)/I_0. \quad (3)$$

Substituting experimental data into (3), we obtain $s = 0.5-0.6$; i.e., the crystallites occupy only little over half of the area of the surface under investigation.

In Fig. 2, we show a microimage of the Si(100) surface after C_{60} molecules were deposited onto it. This microimage was obtained using an atomic-force microscope, with a spatial resolution close to the atomic one, under atmospheric conditions after the sample was removed from the vacuum chamber. The surface topography is represented using the gray scale, with the bright coloring corresponding to crystallites and the dark coloring corresponding to the silicon surface. It is clearly seen that the surface is covered with crystallites with flat tops and an average size of $\sim 100-200$ nm. The fraction of the area occupied by crystallites is about 50%, which is in good agreement with the aforementioned estimate.

5. ANNEALING OF FULLERITE FILM ON (100) Si

In Fig. 3, we show the variation in the carbon and silicon Auger signals as a result of annealing a thick fullerite film. The average surface concentration of fullerene molecules in the film is estimated at about $6 \times 10^{14} cm^{-2}$. It can be seen that the Auger signals corresponding to the adsorbate and substrate remain unchanged up to 700 K. The energy of the carbon Auger peak is equal to 269 eV; this means that it is the C_{60} molecules that reside at the surface. In the range of 700–770 K, the film is rapidly destroyed; i.e., the amplitude of the carbon Auger signal decreases by 20%, whereas the amplitude of the substrate Auger signal increases appreciably (by almost a factor of 3). At the aforementioned temperatures, even separate carbon atoms have not yet dissolved in the silicon bulk. The C_{60} molecules are deposited uniformly over the ribbon surface; therefore, the escape of particles due to migration is unlikely. Consequently, the single plausible cause of the escape of the C_{60} molecules from the surface is related to thermal desorption. The desorption of

fullerene molecules in a similar temperature range was also observed for other substrates (Mo [12], Re [10], and W [13]).

At higher temperatures (in the range of 800–1150 K), there is a clearly defined plateau, where the amplitudes of both Auger signals remain unchanged. In order to gain insight into the nature of the adsorption layer in this temperature range, a detailed analysis of the shape of the C_{KVV} Auger line, which carries information about the chemical structure of adsorbed carbon, was carried out. In Fig. 4, we illustrate the transformation of the shape of the C_{KVV} Auger line as a result of heat treatment. At room temperature and up to 700 K, the lineshape is typical of fullerene, with a characteristic Auger peak energy of 269 eV. Heat treatment brings about a transformation of the Auger peak; at $T > 800$ K, the lineshape is much closer to that characteristic of silicon carbide (the peak at 251 eV is distinct). In addition, the energy of the main peak shifted to 269.5 eV. Apparently, in this temperature range, the fullerene molecules, which are located in the first monolayer and cannot desorb, gradually decompose. Judging from the lineshape, the composition of the surface layer does not yet correspond to silicon carbide; rather, this layer consists of an ensemble of carbon clusters, which are the products of the partial decomposition of fullerene molecules.

Finally, heat treatment at 1150 K brings about a sharp increase in the Auger signal of the substrate and a decrease in that of carbon. The lineshape corresponds to that typical of silicon carbide with the energy of the negative peak equal to 270 eV. Apparently, at this temperature, the final destruction of adsorbed carbon clusters occurs; the released carbon atoms “forget” that they originated from C₆₀ molecules, become partially incorporated into carbide (as was observed in [18]), and become partially dissolved in the substrate bulk.

6. DISCUSSION

Let us compare our results with the data obtained previously for carbon films grown on other substrates, i.e., Ir [15, 16], Re [10], Mo [12], and W [13]. In the case of Mo and W substrates, another, i.e., layer-by-layer, mechanism of growth of the fullerite film at room temperature was observed; for the W substrate, this process was complicated by the partial decomposition of fullerene molecules that formed the first monolayer. At the same time, the growth of crystallites observed on the molybdenum substrate at higher temperatures was very similar to the growth described in this study. Apparently, the growth of crystallites can also account for the observed trends in the adsorption of fullerene on rhenium [10].

The thermally induced transformation of adsorbed fullerene on silicon proceeds, in general, in the same way as on the metals studied previously. The following stages are distinct:

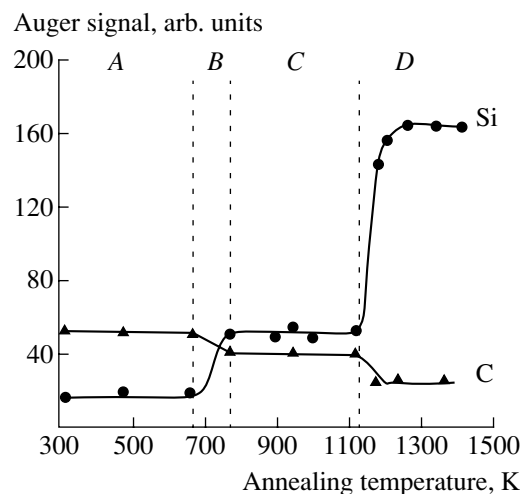


Fig. 3. Variations in the intensities of the silicon and carbon Auger signals as a result of heat treatment of a fullerite film that had the thickness of ~ 3 monolayers and was deposited on (100) Si at 300 K. *A* indicates the stability range of the fullerite film; *B* indicates the temperature region of desorption of C₆₀ molecules from the first and succeeding layers; *C* corresponds to the temperature interval of gradual decomposition of C₆₀ molecules in the first monolayer; and *D* corresponds to the temperature region of formation of the bulk silicon carbide layer.

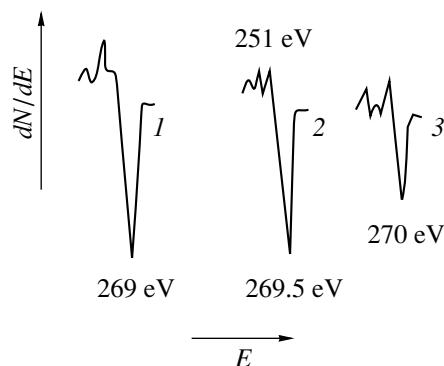


Fig. 4. The C_{KVV} Auger spectra of carbon for (1) a fullerite film that had a thickness of ~ 3 monolayers and was deposited on (100) Si at 300 K, (2) an adsorbed layer after heat treatment of this film at 900 K, and (3) an adsorbed layer after heat treatment of the same film at 1200 K.

- (i) The stage of thermal stability of the fullerene film in the temperature range of 300–700 K.
- (ii) The stage of thermal desorption of fullerene molecules. For the silicon substrate, this stage occurs in the temperature range of 700–750 K, i.e., at slightly lower temperatures than in the case of the Mo (750–800 K [12]) or Ir (~ 900 K [15]) substrates. It is noteworthy that only the fullerenes from the second and subsequent monolayers are thermally desorbed, because the molecules from the first monolayer cannot desorb and are subjected to transformation at higher temperatures.
- (iii) The stage of gradual decomposition of fullerene molecules in the first monolayer. For fullerenes on the

silicon substrate, this stage corresponds to the temperature range of 750–1150 K, which is much wider than that for fullerenes on metallic substrates. Apparently, this is related to the appreciably lower catalytic activity of the semiconductor surface compared to that of the transition-metal surfaces.

(iv) The stage of the bulk-carbide growth at $T > 1150$ K. In this stage, the products of the chemical decomposition of the fullerene completely decompose; the released C atoms “forget” their origin and react with the substrate according to the chemical properties of the latter. Thus, these atoms can form graphite films on the iridium substrate, dissolve in the rhenium and molybdenum bulk, form nonequilibrium bulk carbide at the tungsten surface, and, as we have shown, form silicon carbide on the (100) Si substrate. A very narrow temperature range for the reaction was found to be specific for the (100) Si substrate: it took a temperature step of less than 50 K for the transition from nonequilibrium carbon clusters to the stable SiC film.

7. CONCLUSION

Thus, we studied the mechanisms of adsorption of C_{60} molecules on the (100) Si surface and transformations of fullerite film as a result of heat treatment. As we found out, adsorption at room temperature proceeds according to a mechanism close to that of Stranski–Krastanov; i.e., crystallites grow over the fullerene monolayer. The specificity of the growth mechanism consists in the fact that the growth of crystallites sets in even before the formation of the first monolayer is completed. In the course of the thermally stimulated transformation of the adsorbed layer, distinct temperature intervals are observed. These intervals correspond to the following processes: (I) stability of the fullerite film (300–700 K), (II) thermodesorption of C_{60} molecules from the second and succeeding layers (700–750 K), (III) gradual decomposition of molecules in the first layer (750–1150 K), and (IV) silicon carbide formation (>1150 K). Apparently, similar stages (except for, perhaps, stage IV) might be expected for fullerene on other semiconductor substrates.

ACKNOWLEDGMENTS

We thank I.Yu. Makarenko and A.N. Titkov for the measurements performed using atomic-force microscopy.

This study was supported by the program “Low-Dimensional Quantum Structures” of the Presidium of the Russian Academy of Sciences (project no. 4G19) and, in part, by the program “Controllable Synthesis of Fullerenes” of the Ministry of Science and Technology of the Russian Federation.

REFERENCES

1. Hang Xu, D. M. Chen, and W. N. Creager, *Phys. Rev. Lett.* **70**, 1850 (1993).
2. Y. Z. Li, M. Chander, J. C. Partin, and J. H. Weaver, *Phys. Rev. B* **45**, 13837 (1992).
3. T. Sato, T. Sueyoshi, and M. Iwatsuku, *Surf. Sci. Lett.* **321**, L137 (1994).
4. D. Chen and D. Sarid, *Surf. Sci.* **319**, 74 (1994).
5. P. H. Beton, A. W. Dunn, and P. Moriarty, *Surf. Sci.* **361/362**, 878 (1996).
6. T. Hashizume, K. Motai, X. D. Wang, *et al.*, *J. Vac. Sci. Technol. A* **12**, 2097 (1994).
7. T. Chen, S. Howelles, M. Gallager, *et al.*, *J. Vac. Sci. Technol. B* **9**, 2461 (1991).
8. D. K. Kin, Y. D. Suh, K. H. Park, *et al.*, *J. Vac. Sci. Technol. A* **11**, 1675 (1993).
9. G. K. Wertheim, *Solid State Commun.* **88**, 97 (1993).
10. N. R. Gall, E. V. Rut'kov, A. Ya. Tontegode, and M. M. Usufov, *Mol. Mater.* **7**, 187 (1996).
11. N. R. Gall, E. V. Rut'kov, A. Ya. Tontegode, and M. M. Usufov, *Pis'ma Zh. Tekh. Fiz.* **23** (23), 26 (1997) [*Tech. Phys. Lett.* **23**, 911 (1997)].
12. N. R. Gall, E. V. Rut'kov, A. Ya. Tontegode, and M. M. Usufov, *Zh. Tekh. Fiz.* **69** (11), 117 (1999) [*Tech. Phys.* **44**, 1371 (1999)].
13. N. R. Gall, E. V. Rut'kov, and A. Ya. Tontegode, *Fullerene Sci. Technol.* **9** (2), 111 (2001).
14. N. R. Gall, S. N. Mikhailov, E. V. Rut'kov, and A. Ya. Tontegode, *Surf. Sci.* **191**, 185 (1987).
15. E. V. Rut'kov, A. Ya. Tontegode, and Yu. S. Grushko, *Pis'ma Zh. Éksp. Teor. Fiz.* **57**, 712 (1993) [*JETP Lett.* **57**, 724 (1993)].
16. E. V. Rut'kov, A. Ya. Tontegode, and M. M. Usufov, *Phys. Rev. Lett.* **74**, 758 (1995).
17. C. Gripon, L. Legrand, I. Rosenman, and F. Boue, *Fullerene Sci. Technol.* **4** (6), 1195 (1996).
18. V. M. Mikoushkin and Yu. S. Gordeev, in *Abstracts of the International Workshop on Fullerenes and Atomic Clusters (IWFACT'2001)*, St. Petersburg, 2001, p. 86.

Translated by A. Spitsyn

Stark Effect in Vertically Coupled Quantum Dots in InAs–GaAs Heterostructures

M. M. Sobolev, V. M. Ustinov, A. E. Zhukov,
Yu. G. Musikhin, and N. N. Ledentsov

*Ioffe Physicotechnical Institute, Russian Academy of Sciences,
Politekhnicheskaya ul. 26, St. Petersburg, 194021 Russia*

Submitted February 12, 2002; accepted for publication February 13, 2002

Abstract—The results of studies of hole energy states in vertically coupled quantum dots in InAs–GaAs p – n heterostructures by deep-level transient spectroscopy are reported. Spectra were recorded at different reverse-bias voltages. Levels related to bonding and antibonding s and p states of vertically coupled quantum dots were revealed. The energies of these states significantly depend on an external electric field applied to a heterostructure. This dependence was attributed to the quantum-dimensional Stark effect for the hole states of vertically coupled quantum dots. In addition to this, it was found that the energy of thermal activation of carriers from vertically coupled quantum dots depends on the conditions of isochronous annealing that was carried out both with the reverse bias switched-on and switched-off and both in the presence and absence of illumination. These changes, as in the case of isolated quantum dots, are typical of a bistable electrostatic dipole formed by carriers, localized in a coupled quantum dot, and ionized lattice point defects. The built-in electric field of this dipole reduces the energy barrier for the carriers in the coupled quantum dot. The investigated structures with vertically coupled quantum dots were grown using molecular-beam epitaxy taking account of self-assembling effects. © 2002 MAIK “Nauka/Interperiodica”.

1. INTRODUCTION

More and more interest, both from the pure and applied point of view, is being shown in the effects of an electric field on the electronic properties of zero-dimensional semiconductor systems [1–10]. In accordance with the results reported in [1–10], such systems with quantum dots (QDs) formed by the self-organized growth of strained heteroepitaxial layers have a high degree of freedom in controlling the band structure and electrooptical properties by both external and built-in internal electric fields. We observed in our previous studies [1–4] the effect of a built-in electric field of a bistable dipole formed by carriers localized in a QD and by ionized point defects located in the immediate vicinity of this QD; moreover, we were the first to point to the possibility of controlling the band structure of systems with QDs. Defects were generated during formation of QDs of In(GaAs) and the growth of epitaxial GaAs layers. The formation of the dipole was governed by the conditions of isochronous thermal annealing with the reverse bias switched-on or switched-off and by the conditions of irradiation by white light.

We used deep-level transient spectroscopy (DLTS) to study the InAs–GaAs structures containing both vertically coupled quantum dots (VCQDs) and single QDs. After annealing under one of the above-mentioned conditions, changes in the locations of peaks, related to the emission of carriers from the quantum states of QDs, were observed in the DLTS spectra. In addition to this, for InAs–GaAs structures with

VCQDs, we found that a DLTS peak, controlled by the emission of carriers from a quantum state of VCQD, shifted to the high-temperature region of the spectrum with an increase in the electric field [1, 2].

In several recent studies ([5–7]), the effect of an electric field on the shape of photoluminescence spectra and photocurrent from self-assembled QDs in InGaAs–GaAs structures, which were grown on substrates with a high Miller index, was investigated. The authors of these studies observed a red shift of the energy of optical transitions, which was induced by the built-in electric field. The phenomenon responsible for this shift was called the quantum-dimensional Stark effect. It was attributed to the presence of a piezoelectric field and a permanent dipole moment in a QD [5, 6]. The investigation of coupling between an exciton and longitudinal optical phonon in a QD in a InAs–GaAs structure, carried out in [7], revealed a series of new emission lines in the photoluminescence spectrum of a QD. The generation of these lines was attributed to perturbation caused by defects located in the vicinity of a QD. The authors of the theoretical study [8] investigated how the quantum-dimensional Stark effect manifests itself in the electronic properties of InAs–GaAs VCQDs in the presence of an electric field directed along the growth axis. It was demonstrated that the Stark effect, as well as the effects related to interband transitions in such systems, is much more profound in these systems than in the case of isolated QDs. In addition to this, it was shown that, for a system consisting

of two coupled QDs, bonding and antibonding states (similar to those that are formed in molecules) should be formed.

The technique of formation of arrays of electron-coupled QDs, as well as the results of studies of their electric and optical properties, were first reported in [11]. It was shown that efficient tunneling of carriers between QDs in neighboring rows, which does not occur in the case of isolated QDs, is typical of these objects. The Stark effect in VCQDs is a new physical phenomenon that could potentially be used in devices operating on an interband transition controlled by an external electric field. Therefore, it is of interest to use the DLTS to experimentally investigate this effect for VCQDs in InAs–GaAs heterostructures.

Here, we report the results of studying hole emission from the quantum states of VCQDs in InAs–GaAs heterostructures by measuring the C – V characteristics and recording the DLTS spectra at different reverse-bias voltages U_r . Four peaks were detected in the DLTS spectra, whose locations shifted to the high-temperature spectral region when an external electric field was applied. In addition to this, we found that the energy of thermal activation of carriers from VCQDs depends on the conditions of isochronous annealing: switched-on or switched-off reverse-bias voltage and the presence or absence of illumination. The obtained dependences are typical of a bistable electrostatic dipole formed by carriers, localized in a QD, and by ionized lattice point defects. These observations made it possible to attribute the four above-mentioned DLTS peaks to bonding and antibonding s and p states of VCQDs. The strong dependence of the energies of these states on the external electric field can be attributed to the Stark effect for the VCQD states. The investigated InAs–GaAs heterostructures with VCQDs were grown using self-organizing molecular-beam epitaxy (MBE).

2. EXPERIMENTAL

InAs–GaAs heterostructures with VCQDs were grown using MBE on n^+ -GaAs (100) substrates. Arrays of QDs were formed by the sixfold repeated deposition of two InAs monolayers, which were separated by a

4-nm-thick GaAs layer. It was shown in [12] that such an array of QDs is a system of VCQDs. The VCQDs were located at the center of a 0.90- μm -thick p^0 -GaAs layer doped with Be to $2 \times 10^{16} \text{ cm}^{-3}$. The p^0 -GaAs layer was coated with a 0.2- μm -thick layer of p^+ -GaAs doped with Be up to $2 \times 10^{17} \text{ cm}^{-3}$. DLTS studies of deep traps in heterostructures were carried out with the use of a DL4600 (BIO-RAD) spectrometer operating in the two-strobe integration mode. A Boonton-72B bridge operating at 1 MHz was used to measure the capacitance C . This measuring system had a sensitivity of $\Delta C/C_0 \approx 10^{-4}$. In order to carry out DLTS measurements for the structure, nonrectifying contacts were deposited on the n^+ -GaAs substrate and p^+ -GaAs layer. Before each measurement, the sample was isochronously annealed for 1 min at a fixed temperature and under one of the following conditions: the reverse bias voltage was either switched on ($U_{ra} < 0$) or switched off ($U_{ra} = 0$). Before the annealing, the sample was heated to 450 K and kept at this temperature for 1 min at $U_{ra} = 0$ if the following annealing was to be carried out at $U_{ra} < 0$. Then, the sample was cooled to the annealing temperature. If the annealing was carried out at $U_{ra} = 0$, the samples were kept for 1 min at 450 K and $U_{ra} < 0$ before the annealing. The annealing temperature ranged from 80 to 450 K. After the annealing, the sample was cooled to 80 K under one of the following conditions: $U_{ra} < 0$ or $U_{ra} = 0$. Then, DLTS measurements were carried out in the dark (unless otherwise specified) or under exposure to white light. In order to determine the carrier-distribution profile in the heterostructure, capacitance-voltage (C – V) measurements were carried out. The thermal-activation energy, E_a , and capture cross section of carriers, σ_p , were determined from the Arrhenius dependence using the “rate-window” method in conventional DLTS measurements.

3. RESULTS

Figure 1 shows a microphotograph of an InAs sample with six layers of QDs; this microphotograph was obtained using transmission electron microscopy (TEM). The mechanism of formation of VCQDs in

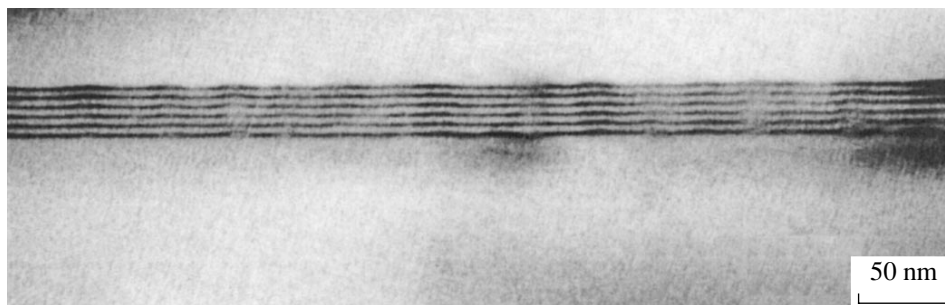


Fig. 1. TEM microphotograph of a sample with six layers of InAs QDs.

InAs–GaAs was investigated in detail in [11]. It was shown that VCQDs are formed due to the self-organizing effect, which includes transfer of In (Ga, As) from the lower to upper QDs and its replacement by GaAs [11]. It can be seen from Fig. 1 that the lateral size of the lower VCQD island does not exceed 16 nm. The lateral size of islands in each subsequent row gradually increases to 26 nm for the upper island. Each VCQD consists of six InAs islands separated by thin GaAs layers each approximately 4 nm thick (Fig. 1).

Figure 2a shows the C – V characteristic of the sample at 82 K. When the reverse-bias voltage ranges from -7.5 to -1.8 V, the behavior of the capacitance change is typical of spatially localized states [13]. There are three plateaus on the C – V characteristic, which can be attributed to depletion of the quantum states of QDs [4]. The distribution of the concentration of free holes $p^*(U_r)$ (here, U_r is the magnitude of the reverse-bias voltage), shown in Fig. 2b, was calculated on the basis of the C – V data. At low temperatures, we observed one high sharp peak at $U_r \approx 3.0$ V and two lower, broader peaks at $U_r \approx 5.0$ and ≈ 6.8 V, which were attributed to the escape of carriers from the quantum states of dots (depletion of the quantum states). Depletion regions were also observed at both sides of the first peak. The hole-concentration distributions $p^*(U_r)$ were obtained for two modes of the preliminary isochronous annealing: at $U_{ra} < 0$ and $U_{ra} = 0$ (Fig. 2b).

We carried out C – V measurements in order to determine the range of reverse-bias voltages at which signals, caused by the emission of carriers from the quantum states of VCQDs and deep levels related to defects, should be observed in the DLTS spectra. In order to determine the spatial localization of DLTS signals, we simultaneously changed the magnitudes of the filling and reverse-bias pulses (U_f and U_r , respectively), with the difference between them being maintained constant: $\Delta U = U_r - U_f = 0.5$ V (Fig. 3). When U_r was varied in the range of 2.8–3.7 V (which corresponds to the first peak in the $p^*(U_r)$ curve, related to the depletion of holes that accumulated at one of the quantum states of the QDs), a sharply defined $HD1$ peak with a high-temperature shoulder was observed in the DLTS spectra. An increase in U_r resulted in a shift of this peak and its shoulder to higher temperatures. As U_r increased, the amplitudes of the DLTS signals increased as well. The thermal-activation energy of carriers occupying this level, which is related to the $HD1$ peak, E_a , was determined from the Arrhenius dependence. As U_r increased, E_a varied from 110 to 154 meV and the capture cross section σ_p varied from 9.4×10^{-19} to 3.8×10^{-17} cm² (see table).

With a further increase in U_r in the range of 4.2–5.1 V, the first peak in the DLTS spectrum (Fig. 3, curve 4), now denoted as $HD2$, and the second peak, $HD3$, which arose to the right of it, shifted to higher temperatures. The amplitude of the $HD2$ peak remained virtually

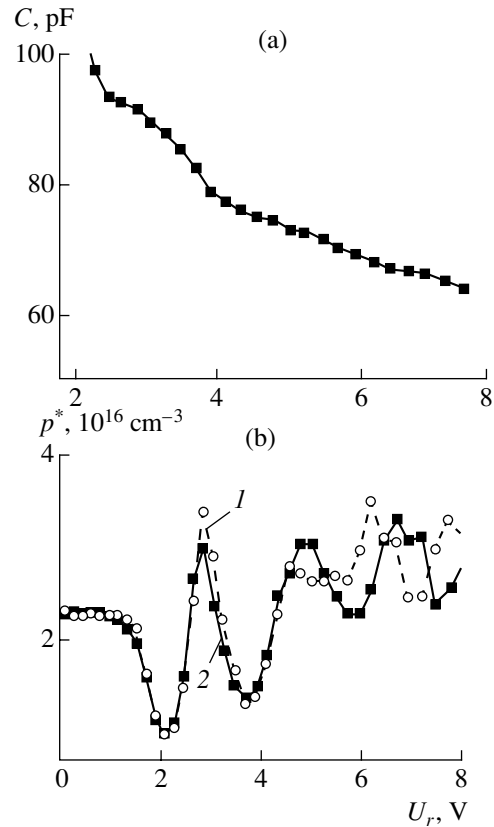


Fig. 2. (a) C – V characteristic of a p – n heterostructure with six layers of InAs QDs in a GaAs host measured at 82 K after isochronous annealing at $T_a = 400$ K and $U_{ra} < 0$; (b) distributions of concentrations of holes $p^*(U_r)$ derived from C – V characteristics measured at 82 K after isochronous annealing at (1) $U_{ra} = 0$ and (2) $U_{ra} < 0$.

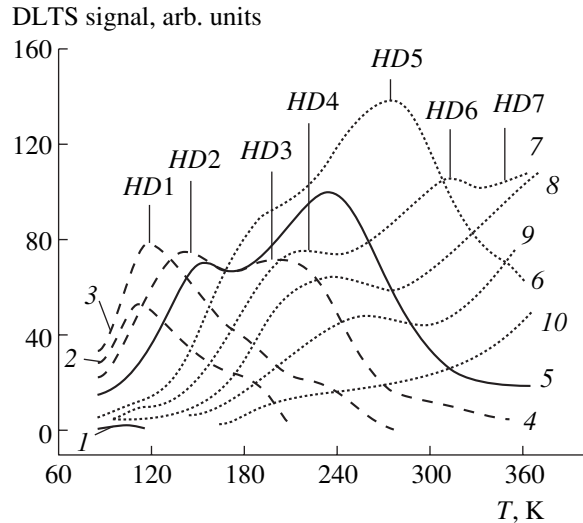


Fig. 3. DLTS spectra of a p – n heterostructure with six layers of InAs QDs in a GaAs host recorded at different magnitudes of the reverse-bias pulse $U_r = (1) 2.7, (2) 3.2, (3) 3.7, (4) 4.2, (5) 4.7, (6) 5.3, (7) 5.8, (8) 6.3, (9) 6.8, (10) 7.2$ V; the magnitude of the filling pulse, U_f , was varied in order to keep constant the difference $\Delta U = U_r - U_f = 0.5$ V. All spectra were recorded at an emission-rate window of 200 s⁻¹ and filling-pulse duration of 25 μ s.

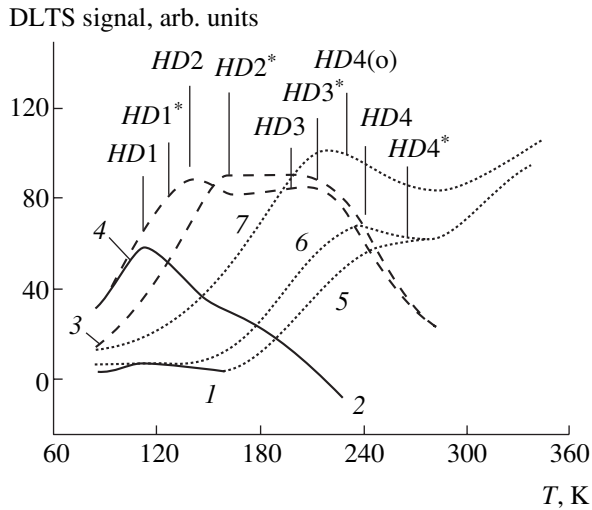


Fig. 4. The same as for Fig. 3, but after isochronous annealing at $T_a = 400$ K and preliminary cooling at $U_{ra} = 0$ (curves 1, 3, 5) and $U_{ra} < 0$ (curves 2, 4, 6, 7). $U_r = (1, 2)$ 3.3, (3, 4) 4.2, and (5–7) 6.3 V. In contrast to spectrum (6), spectrum (7) was recorded under irradiation with white light.

unchanged as U_r increased to 4.7 V. At $U_r = 5.1$ V, the height of this peak significantly decreased, while the amplitude of the second peak ($HD3$) increased. A decrease in the amplitude of the first peak, related to the depletion of one of the quantum states of the QD (caused by the escape of holes from it), and an increase in the amplitude of the second peak, related, apparently, to the depletion of some other quantum state of the QD, correspond to this range of U_r in the $p^*(U_r)$ dependence. The parameters of the level related to the $HD2$ peak changed with increasing U_r in this range as follows: $E_a = 222$ – 241 meV and $\sigma_p = 4.2 \times 10^{-16}$ – 2.5×10^{-16} cm². Significant broadening and spreading of the $HD3$ peak was observed, due to which the parameters of the level related to this peak could be reliably determined only for $U_r = 4.7$ V: $E_a = 368$ meV and $\sigma_p = 1.5 \times 10^{-16}$ cm².

Parameters of deep levels of defects, impurities, and quantum states of QDs

Designation of level	Activation energy E_a , meV	Capture cross-section σ_p , cm ²	Identification of levels
$HD1$	110	9.4×10^{-19}	
$HD2$	222	4.2×10^{-16}	
$HD3$	368	1.5×10^{-16}	
$HD4$	287	1.2×10^{-15}	
$HD5$	726	8.2×10^{-13}	$HL9$ [15]
$HD6$	526	2.0×10^{-16}	$HL8$ [15]
$HD7$	590	1.1×10^{-16}	$HS2$ [16]

An increase in U_r in the range of 5.3–7.2 V gave rise to another peak (designated as $HD4$) in the DLTS spectrum, which shifted to the high-temperature region and decreased in amplitude with increasing U_r . In this range of U_r , one more (third) peak, apparently related to the depletion of the third state of the QD, was observed in the $p^*(U_r)$ dependence. The parameters of the level related to the $HD4$ peak were reliably determined only for $U_r = 5.3$ and 5.8 V: $E_a = 287$ and 300 meV and $\sigma_p = 1.2 \times 10^{-15}$ and 1.3×10^{-17} cm², respectively. As for the DLTS spectra, three more peaks were observed in this range of U_r : $HD5$, $HD6$, and $HD7$, which were reliably attributed to known defects and impurities typical of GaAs (see table).

We carried out DLTS measurements in order to assess the dependence of DLTS spectra on the conditions of the preliminary isochronous annealing ($U_{ra} < 0$ or $U_{ra} = 0$) at three different values of U_r . We chose those values of U_r at which characteristic (the above-mentioned) changes in the behavior of DLTS spectra were observed. Figure 4 shows spectra measured after preliminary isochronous annealing at $T_a = 400$ K with the reverse bias switched-on ($U_{ra} < 0$) and switched-off ($U_{ra} = 0$) at different values of U_r (the magnitude of the reverse-bias pulse). These measurements show that the annealing at $U_{ra} = 0$ brought about a shift of $HD1$ – $HD4$ peaks to higher temperatures. The shifted peaks are designated as $HD1^*$, $HD2^*$, $HD3^*$, and $HD4^*$ in Fig. 4. A decrease in the height of the $HD1^*$ peak was also observed. The transformation of the $HD1^*$, $HD2^*$, $HD3^*$, and $HD4^*$ peaks into the $HD1$, $HD2$, $HD3$, and $HD4$ peaks was reversible. Illumination also caused a shift of these DLTS peaks, but to lower temperatures. These changes were accompanied by a significant increase in the heights of the $HD1$, $HD2$, $HD3$, and $HD4$ peaks. As an example, the optical transformation of only one peak $HD4$ to $HD4(o)$ is shown in Fig. 4. Similar changes under isochronous annealing were observed for all three peaks, related to depletion of the quantum states in QDs, in the $p^*(U_r)$ dependence (Fig. 2).

4. DISCUSSION

The TEM data shown in Fig. 1 demonstrate the presence of six InAs islands separated by thin GaAs layers ($d_{\text{GaAs}} \approx 40$ Å). It was shown in [11, 12] that, arranged in this way, QDs are multilayer systems; i.e., they are QDs electron-coupled in the vertical direction. The wave functions of the upper and lower islands overlap, and the electronic properties of VCQDs can be considered as those of a single object. As was shown in [8], such systems should have bonding and antibonding, ground and excited quantum states, which are identified in the absence of an electric field as $1s^+$, $1s^-$, $2p^+$, $2p^-$, $3d^+$, etc. Here superscripts + and – stand for bonding and antibonding states, respectively. It was shown in [8] that an electric field should cause a red energy shift of the ground state (split bonding $1s$ state) of such

a VCQD system. This phenomenon was called the quantum-dimensional Stark effect. Other VCQD states should manifest similar behavior in the presence of an electric field. In addition to this, it was found in [8] that the peak in the energy spectrum of the ground state of such a system should be shifted to its location when the field is switched-off if the lateral size of islands gradually increases from row to row. All excited states should be crossing or anticrossing with other states, which should result in the reordering of the states in a strong electric field.

The C - V characteristics, measured at 82 K, show three plateaus (Fig. 2a). These plateaus were attributed to the escape of carriers that accumulated in the quantum states of VCQDs. The distributions of the concentrations of free holes $p^*(U_r)$ contain, respectively, one high sharp peak at $U_r \approx 3.0$ V and two lower, broader peaks at $U_r \approx 5.0$ and ≈ 6.8 V (Fig. 2b). As the results of our studies showed, there is a relation between the three peaks in the $p^*(U_r)$ profile and four deep levels: $HD1$ and $HD2$ are related to the first peak, $HD3$ is related to the second peak, and $HD4$ is related to the third peak. Now let us try to determine the origin of these levels.

We have already reported in our previous publications [1–4, 9, 10] that one of the distinctive and characteristic features that can be used to attribute DLTS peaks to the quantum states of dots is the change in the peak position along the temperature axis after isochronous annealing with subsequent cooling under one of the following conditions: $U_{ra} < 0$ or $U_{ra} = 0$. The changes in the DLTS spectra are governed in these cases by an electrostatic dipole formed by carriers, localized in QDs, and ionized deep-level defects. Under isochronous annealing at 400 K with subsequent cooling to 80 K at $U_{ra} < 0$, the application of a filling pulse gives rise to a dipole, whose electric field has the same direction as the field of the p - n junction. The energy of thermal activation of holes from the quantum states decreases due to the field effect, and the DLTS peak shifts to lower temperatures. Under isochronous annealing at $U_{ra} = 0$, no dipoles are formed and the DLTS peak does not shift. Similar changes can also occur under isochronous annealing (either at $U_{ra} < 0$ or at $U_{ra} = 0$) in the DLTS spectra of structures containing VCQDs, in the immediate vicinity of which deep-level defects are located [1, 2]. Similar changes under annealing were observed for all four DLTS peaks. Taking into account their relation to the three peaks in the $p^*(U_r)$ dependence, we attributed $HD1$, $HD2$, $HD3$, and $HD4$ peaks to the quantum states of VCQDs. As was mentioned above, we observed significant shape broadening and spreading for all four peaks. This may be due to a number of causes, including the following: (1) the tunneling escape of holes to the valence band via the excited states of VCQDs and (2) fluctuations of QD sizes. The contribution of the tunneling effect can be rather significant when measuring DLTS at lower temperatures. In this case, DLTS spectra should show a plateau (provided that the emission rate of carriers is con-

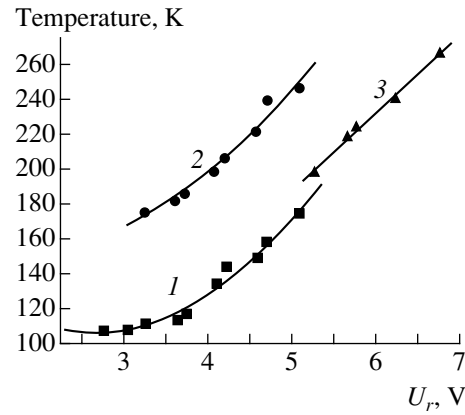


Fig. 5. Dependences of positions of DLTS peaks (1) $HD1$ and $HD2$, (2) $HD3$, and (3) $HD4$ on the magnitude of the reverse-bias pulse U_r .

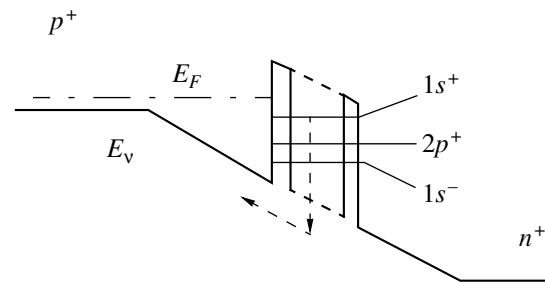


Fig. 6. The diagram of the valence band of a reverse-biased p - n structure for the case of hole emission from the $1s^+$ state of a VCQD.

stant and does not depend on temperature [17]), rather than a peak, related to the thermal emission of carriers. At higher temperatures of DLTS measurements, the emission is governed by the thermal excitation of carriers from the QD states [17, 18]. Our measurements were carried out precisely in these conditions. The thermal emission of carriers from the ground state can occur either directly to the corresponding band or via excited states with participation of the states in the wetting layer. The carriers can escape from the excited states to the valence band either via thermal emission or by tunneling through the triangular potential barrier [19]. The participation of the states of wetting layers are excluded in our measurements, since we used n^+ -GaAs as a substrate. The wetting layers are located closer to the n -GaAs layer, while the holes escape towards the p -GaAs layer. In addition to this, it was shown in [20] that the probability of a two-step process via the states of the wetting layer is low and, thus, this process can be disregarded. The authors of [21] came to the same conclusion studying hole emission from the QD states. We may also assume that, in the investigated VCQD structure containing GaAs layers with a thickness $d_{\text{GaAs}} \approx 40$ Å, the coupling of QDs into a single system is not complete and the application of an electric field can cause tunneling of carriers between the QD states.

There may be another cause of peak broadening in DLTS spectra: the alternating thin GaAs layers and InAs QDs form a superlattice in which quantum states hybridize to form minibands. In any case, the broadening of DLTS peaks in our measurements suggests that, although tunneling makes some contribution to the escape of carriers from VCQDs, this contribution is not major and decisive. For *HD1*, *HD2*, *HD3*, and *HD4* peaks, we plotted the dependences of the positions of their maxima on a temperature scale on the magnitude of the reverse-bias pulse U_r (see Fig. 5). It turned out that the curve for the *HD2* peak (Fig. 5, curve 1) continues the relevant curve for the *HD1* peak. Hence, we assumed that these two DLTS peaks are related to the same VCQD quantum state, which exhibits a strong field dependence. The energy of thermal activation of holes from this quantum state changed from 110 to 240 meV in the investigated range of U_r . The evaluations of the electric field of the p - n junction showed that it changes from 54 to 98 kV/cm in the entire range of U_r . For the *HD3* and *HD4* DLTS peaks (curves 2 and 3, respectively), we also observed the effect of the electric field. Curves 2 (*HD3* peak) and 1 (*HD1* and *HD2* peaks), shown in Fig. 5, run parallel to each other. When the influence of an electric field on the emission of carriers from the quantum states of VCQDs is studied, the following effects, related to changes in the carrier-emission rate, can be observed: (1) a decrease in the barrier height for thermal emission [22], (2) an increase in the probability of the tunneling of carriers through the triangular barrier [23], and (3) a manifestation of the quantum-dimensional Stark effect [8, 18]. The authors of [22, 23] reported results of studying the influence of the first two effects on the energy of thermal emission of carriers from a QD and quantum well, respectively. The shift of DLTS peaks, which is controlled by the emission of carriers from the quantum states, to lower temperatures is typical of both these effects. This shift is related to an increase in the emission rate and a decrease in the thermal-activation energy. In our opinion, it is more probable that we observed a manifestation of the quantum-dimensional Stark effect, which results in a shift of the levels related to the quantum states to higher energies [8]. Apparently, in accordance with the theoretical results reported in [8], curves 1 and 2 (Fig. 5) represent dependences of quantities which are functions of the energies of the bonding $2p^+$ and $1s^+$ states of VCQDs, respectively, on the electric field. Curve 3 (*HD3* peak) crosses curve 1 at $U_r \approx 5.25$ V. Apparently, curve 1 (also in accordance with the data reported in [8]) represents the dependence of a quantity which is a function of the energy of the antibonding $1s^-$ state of a VCQD on the electric field.

Figure 6 shows the diagram of the valence band of a reverse-biased p - n structure. The value of the reverse bias corresponds to the following situation: holes start to be emitted from the $1s^+$ state of the VCQD, while $2p^+$ and $1s^-$ states have already been depleted. The experi-

mental dependences shown in Fig. 5 verify that there should be splitting of the ground $1s^-$ and excited $2p$ states of the VCQD and that a red energy shift, caused by an electric field, should be observed for these states. These dependences also confirm that we experimentally observed the quantum-dimensional Stark effect in VCQDs (its manifestation does not require that the structures be grown on substrates with a high Miller index [5–7]). It is worth noting that we first observed a field dependence of the energy of thermal activation of carriers from the ground VCQD state in DLTS measurements of laser InAs–GaAs structures with VCQDs [1, 2]. The effect we observed was not referred to then as the quantum-size Stark effect. This effect, as well as Coulomb interaction between electronic states in QDs and defects, opens up new possibilities of controlling the band structure and electrooptical properties of semiconductor heterostructures with VCQDs by using an external electric field and isochronous annealing.

5. CONCLUSION

We carried out detailed DLTS studies of the emission of holes from the quantum states of VCQDs in reverse-biased InAs–GaAs heterostructures at different values of the reverse bias. We also studied the effect of the electrostatic interaction between carriers localized at quantum states in VCQDs and at ionized lattice defects on hole emission. The investigated structures with VCQDs were obtained by the sixfold repeated MBE deposition of two InAs monolayers, separated by a 4-nm-thick GaAs layer, on n^+ -GaAs (100) substrates. The DLTS spectra of such a structure contain four peaks, whose positions depend on the conditions of the initial isochronous annealing and illumination. We explained the obtained data in terms of the Coulomb interaction between carriers localized at the VCQD states and in terms of ionized point defects located in the immediate vicinity of VCQDs. This made it possible to attribute the DLTS peaks to the VCQD states. In our opinion, the shift of DLTS peaks to the high-temperature spectral region, caused by an increase in the reverse-bias, is a manifestation of the quantum-dimensional Stark effect for VCQD states. The form of the dependences of the peak locations on the reverse bias suggests that the observed DLTS peaks can be attributed to bonding and antibonding, ground and excited VCQD states, which were designated as $1s^+$, $1s^-$, and $2p^+$, respectively.

ACKNOWLEDGMENTS

This study was supported by the Russian Foundation for Basic Research (project no. 00-02-16848) and by Scientific Cooperation between Eastern Europe and Switzerland (SCOPES) 2000–2003 (project no. 7SUPJ 062392).

REFERENCES

1. M. M. Sobolev, F. R. Kovsh, V. M. Ustinov, *et al.*, Fiz. Tekh. Poluprovodn. (St. Petersburg) **31**, 1249 (1997) [Semiconductors **31**, 1074 (1997)].
2. M. M. Sobolev, A. R. Kovsh, V. M. Ustinov, *et al.*, in *Proceedings of the 19th International Conference on Defects in Semiconductors, Aveiro, Portugal, 1997*, Mater. Sci. Forum **258–263** (3), 1619 (1997).
3. M. M. Sobolev, I. V. Kochnev, V. M. Lantratov, *et al.*, Physica B (Amsterdam) **273–274**, 959 (1999).
4. M. M. Sobolev, I. V. Kochnev, V. M. Lantratov, *et al.*, Fiz. Tekh. Poluprovodn. (St. Petersburg) **34**, 200 (2000) [Semiconductors **34**, 195 (2000)].
5. A. Patanè, A. Levin, A. Polimeny, *et al.*, Appl. Phys. Lett. **77**, 2979 (2000).
6. M. Gurioli, S. Sanguinetti, and M. Henini, Appl. Phys. Lett. **78**, 931 (2001).
7. A. Lemaitre, A. D. Ashmore, J. J. Finley, *et al.*, Phys. Rev. B **63**, 161309 (2001).
8. W. Sheng and J.-P. Leburton, Appl. Phys. Lett. **78**, 1258 (2001).
9. M. M. Sobolev, I. V. Kochnev, V. M. Lantratov, and N. N. Ledentsov, Fiz. Tekh. Poluprovodn. (St. Petersburg) **35**, 1228 (2001) [Semiconductors **35**, 1175 (2001)].
10. M. M. Sobolev and V. M. Lantratov, Physica B (Amsterdam) **308–310**, 1113 (2002).
11. N. N. Ledentsov, V. A. Shchukin, M. Grundmann, *et al.*, Phys. Rev. B **54**, 8743 (1996).
12. M. V. Maksimov, Yu. M. Shernyakov, S. V. Zaitsev, *et al.*, Fiz. Tekh. Poluprovodn. (St. Petersburg) **31**, 670 (1997) [Semiconductors **31**, 571 (1997)].
13. R. A. Suris, in *Proceedings of the 7th Winter School on Physics of Semiconductors, Leningrad, 1975*, p. 245.
14. R. Wetzler, C. M. A. Kapteyn, R. Heitz, *et al.*, Phys. Status Solidi B **224**, 79 (2001).
15. A. Mtonneau, G. M. Martin, and A. Mircea, Electron. Lett. **13**, 666 (1977).
16. H. Hasagawa and A. Majerfeld, Electron. Lett. **11**, 286 (1975).
17. X. Letartre, D. Stiévenard, and M. Lanno, J. Appl. Phys. **69**, 7336 (1991).
18. P. W. Fry, I. E. Itskevich, D. J. Mowbray, *et al.*, Phys. Rev. Lett. **84**, 733 (2000).
19. H. Pettersson, C. Pryor, L. Landin, *et al.*, Phys. Rev. B **61**, 4795 (2000).
20. S. Ghosh, B. Kochman, J. Singh, and P. Bhattacharaya, Appl. Phys. Lett. **76**, 2571 (2000).
21. C. M. A. Kapteyn, M. Lion, R. Heitz, *et al.*, Phys. Status Solidi B **224**, 57 (2001).
22. S. Anand, N. Carlsson, M.-E. Pistol, *et al.*, J. Appl. Phys. **84**, 3747 (1998).
23. K. Schmalz, I. N. Yassievich, F. Collart, and D. J. Gravest-eijn, Phys. Rev. B **54**, 16799 (1996).

Translated by Yu. Sin'kov

LOW-DIMENSIONAL
SYSTEMS

The Influence of Heat Treatment Conditions on the Evaporation of Defect Regions in Structures with InGaAs Quantum Dots in the GaAs Matrix

D. S. Sizov*, M. V. Maksimov*, A. F. Tsatsul'nikov*, N. A. Cherkashin*,
N. V. Kryzhanovskaya*, A. B. Zhukov*, N. A. Maleev*, S. S. Mikhrin*,
A. P. Vasil'ev*, R. Selin**, V. M. Ustinov*, N. N. Ledentsov*,
D. Bimberg**, and Zh. I. Alferov*

* *Ioffe Physicotechnical Institute, Russian Academy of Sciences,
Politekhnicheskaya ul. 26, St. Petersburg, 194021 Russia*

** *Institut für Festkörperphysik Technische Universität Berlin, D-10623 Berlin, Germany*

Submitted March 11, 2002; accepted for publication March 13, 2002

Abstract—Structures with In(Ga)As quantum dots in the GaAs matrix obtained using molecular-beam epitaxy are investigated using photoluminescence (PL) measurements and transmission electron microscopy. The structures were subjected *in situ* to the procedure of the selective thermal elimination of defect regions. Based on the results of the analysis of luminescence properties, a method for evaluating the crystalline quality of structures using the measurements of PL intensity for the GaAs matrix at high temperatures (as high as 400 K) is suggested. Procedures for the elimination of defects are investigated, namely, the single-stage selective elimination of InAs defect islands at 600°C and a two-stage procedure. The latter procedure additionally includes selective overgrowth with a thin AlAs layer and high-temperature (650–700°C) heat treatment. The optimal conditions of the process, which permit the obtaining of structures with a relatively low defect density without a considerable decrease in the density of coherent quantum dots, are found. © 2002 MAIK “Nauka/Interperiodica”.

1. INTRODUCTION

One of the most important directions in the development of optoelectronics is the improvement of optical amplifiers, photodetectors, and emitters, which operate in the wavelength range of 1.25–1.7 μm . Lasers and optical amplifiers for this range are key components in rapidly developing fiber-optics communications. The range at 1.3 μm corresponds to zero dispersion of a standard optical fiber, which dominates in modern fiber-optics communications and provides the highest speed with a fixed communication-link length. Recently, good results have been attained in the design of semiconductor injection lasers on GaAs substrates with quantum dots (QDs) in the active region, which emit at a wavelength of 1.3 μm [1–3]. The lasers with QDs in the active region (QD lasers), which are grown on GaAs substrates, are especially promising for applications in fiber-optics communications. They can replace the lasers based on InP substrates, which are used at present. This is caused by a number of reasons. First, GaAs substrates have a high strength and heat conduction. In addition, they are low-cost. Second, lasers with quantum wells (QWs) which are based on InGaAsP and InGaAlAs solid solutions lattice-matched to InP substrates rank below AlGaAs lasers in the thermal stability of the threshold current density due to distinctions between the band structures of these compounds [4–6].

The use of GaAs substrates also makes it possible to fabricate surface-emitting lasers using GaAs–AlAs or GaAs–Al(Ga)O multilayer mirrors. These mirrors, with a relatively small number of periods (20–25 and 5–6, respectively), have a high peak reflectivity (>99.5%) and an extended plateau in the reflection spectrum, which is substantially more complicated to attain for the compounds lattice-matched to the InP substrate. In addition, for a QD laser, the localization of charge carriers over all three spatial directions can suppress their diffusion to defect regions, prolong the service life, and increase the optical power density, which catastrophically impairs the mirrors [7, 8]. The possibility of developing microlasers also emerges. The QD structures also demonstrate improved dynamic characteristics compared with the QW lasers [9]. At the same time, the In(Ga)As/GaAs QDs make it possible to attain a high intensity of photoluminescence (PL) at room temperature in the wavelength range of 1.3–1.4 μm [10–12]. In contrast with this, using In(Ga)As/GaAs QWs, it is difficult to ensure lasing at a wavelength longer than 1.1 μm . Thus, the use of the In(Ga)As/GaAs QDs is very promising for injection lasers emitting at a wavelength longer than 1.25 μm . At the present time, QD stripe lasers on GaAs substrates for the long-wavelength range, which have unprecedentedly low threshold current densities, are being fabricated [13]. For stripe

lasers, a high output power and high differential efficiency are demonstrated [14, 15]. Surface-emitting lasers operating at a wavelength of 1.3 μm in the continuous operation mode are also being fabricated [16, 17].

Notably, despite the above advances, the temperature stability of the threshold current for the QD lasers above room temperature is still below that characteristic of QW lasers grown on GaAs substrates for the region of 1 μm . This effect is caused by the limited density of electron states in the active region of the InGaAs QDs [18]. The presence of defects associated with the spontaneous formation of dislocations, dislocation loops, defect dipoles, etc., can also adversely affect the device characteristics. These defects are formed at a higher probability in the structures with relatively large QDs, which are used for attaining long-wavelength emission in lasers. If the defect density is relatively high, the nonradiative recombination at the defects is comparable with the radiative recombination at the levels in the QDs, which leads to a noticeable decrease in the injection efficiency. Due to this, the threshold current can increase, the differential efficiency can decrease, and the peak output power can decrease. It is noteworthy that the laser characteristics of long-wavelength QD lasers are impaired at elevated temperatures only (close to room temperature and above), whereas the parameters of QD lasers below room temperature are almost ideal [19].

In connection with the above, the problem of obtaining defect-free In(Ga)As/GaAs QD structures emitting in the long-wavelength ($>1.25 \mu\text{m}$) region is of great importance. A series of publications is devoted to the development of the epitaxial growth of layers with In(Ga)As/GaAs QDs in order to obtain structures with a low defect density and the required emission wavelength [10, 12, 20, 21]. Specifically, the method of *in situ* heat treatment (at 600°C) of a layer with QDs overgrown by a thin GaAs layer (2 nm) was suggested [21]. Due to this procedure, a substantial decrease in the defect density and improvement of laser characteristics are achieved.

In studies [1, 22], a method for the elimination of defects in structures with partially relaxed QWs was suggested. The InGaAs strained layers, whose thickness is above the critical one for the formation of misfit defects, were grown on an AlGaAs surface. Further, an AlAs thin layer was deposited and high-temperature heat treatment was carried out at 700°C. Dislocations were eliminated by this procedure, which was accompanied by an increase in the photoluminescence intensity by more than 2 orders of magnitude. The idea behind the method is as follows. A thin AlGaAs cap layer is deposited on defect-free regions of coherent growth of the InGaAs layer. The relaxed defect-containing regions have another lattice constant compared with InGaAs and remain intact. The reason is that the deposition of AlGaAs, GaAs, or AlAs layers on these regions is energetically less favorable. Heat treatment

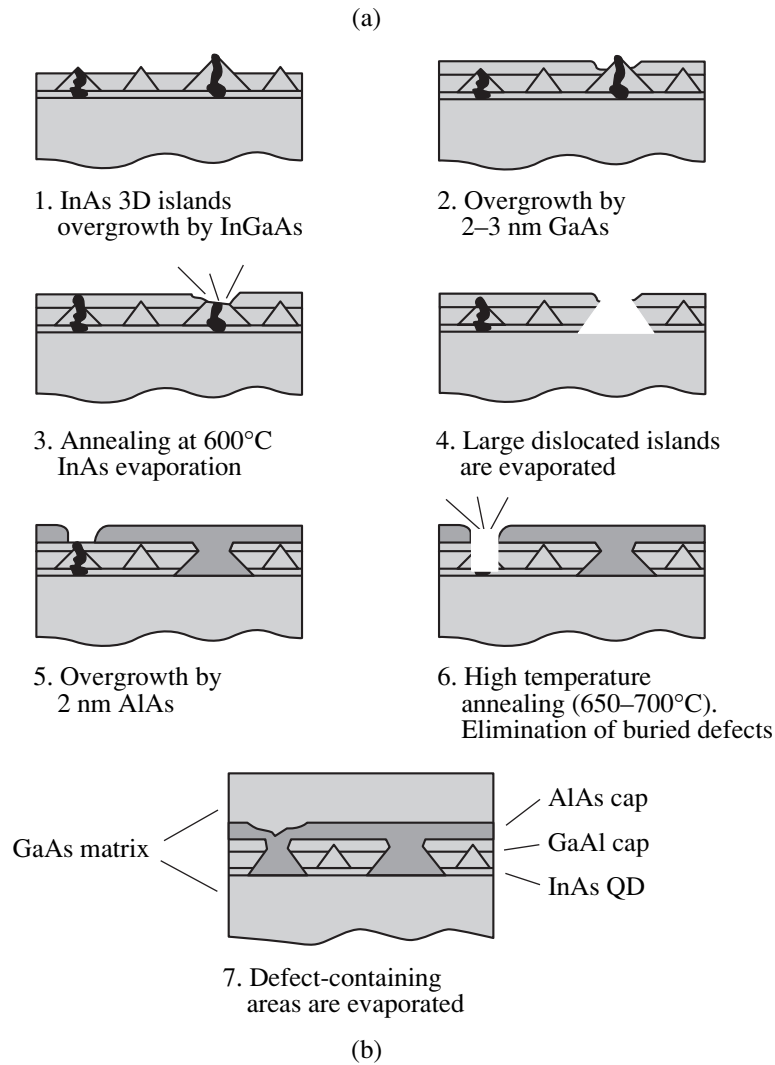
leads to the evaporation of such uncoated defect-containing regions. In addition, the structures were overgrown with a GaAs layer.

In this study, a method for the two-stage elimination of defects in QD structures is suggested. After the overgrowth of the QD layer with a thin GaAs layer and the *in situ* elimination of defects at 600°C, a thin AlAs layer was deposited. Then, high-temperature thermal treatment was carried out at 650–700°C. The structures were investigated using transmission electron microscopy (TEM) and high-temperature PL measurements at 290–470°C. At high temperatures, the thermal energy kT , where k is the Boltzmann constant, and T is the temperature, becomes comparable with the energy of localization of charge carriers in QDs. Consequently, the thermal ejection and retrapping of carriers at the defects become quite significant. The major test for the quality of the structure is the intensity of PL of the GaAs matrix. The reason is that the defects, which capture free nonequilibrium carriers from the matrix, reduce the population of the states of the matrix. Thermal ejection from the QDs at elevated temperatures enhances this process. This means that the PL sensitivity to defects in the structure increases.

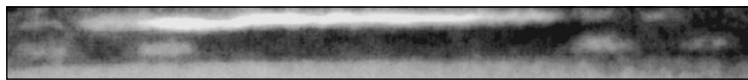
2. EXPERIMENTAL

The structures under investigation were grown on semi-insulating GaAs(100) substrates by molecular-beam epitaxy (MBE) using a Riber-32P system. The formation of QDs was monitored from the pattern of reflection high-energy electron diffraction (RHEED) using a system for recording the RHEED patterns. After deposition of the GaAs buffer layer at 600°C, a $\text{Al}_{0.3}\text{Ga}_{0.7}\text{As}/\text{GaAs}$ superlattice was grown (five pairs 3 nm/3 nm) to prevent carrier leakage from the active region into the substrate and buffer layer. In addition, a GaAs layer 0.16 μm thick was grown at the same temperature. Then, the temperature was decreased to 485°C and a QD layer was deposited.

The QD layer was grown by depositing a InAs layer with an effective thickness of 2.5 monolayers for the formation of initial nanoislands, which was overgrown with the $\text{In}_{0.15}\text{Ga}_{0.85}\text{As}$ layer with the purpose of obtaining QDs emitting in the long-wavelength region (1.3 μm) [10]. Further, a procedure for the elimination of defects, which is schematically illustrated in Fig. 1a, was used. A thin GaAs layer (2 nm) was deposited at the same temperature as the QD layer (485°C). In this case, GaAs was not deposited on large clusters with a dislocation structure due to a significant difference in lattice parameters. The temperature was then increased to 600°C, and the first stage of the elimination of defects was carried out at this temperature for 1 min. During this process, uncoated regions in the vicinity of dislocations and islands evaporated, whereas coated regions of coherent growth did not evaporate. The reason is that 600°C is above the temperature at which InGaAs begins to evaporate, but below the evaporation temper-

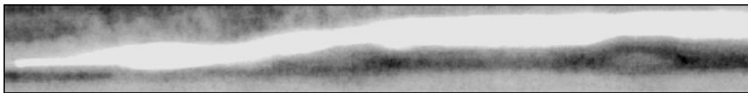


InAs/InGaAs + 2 nm GaAs + 600°C + 2 nm AlAs + GaAs



DF (002) along [010]

InAs/InGaAs + 2 nm GaAs + 600°C + 2 nm AlAs + 700°C + GaAs



DF (002) along [010]

100 nm

Fig. 1. (a) Schematic drawing illustrating the procedure for eliminating defects: (1) InAs islands are grown and overgrown with the InGaAs layer (QDs for the wavelength of 1.3 μm); (2) quantum dots are overgrown with the GaAs thin layer; (3, 4) heat treatment (600°C), evaporation of uncoated defects; (5) overgrown with the AlAs thin layer; (6) high-temperature heat treatment, evaporation of shallow defects; and (7) overgrowth with the matrix material, obtaining the defect-free QDs. (b) Top images of the samples obtained using a transmission electron microscope: after one stage of heat treatment (upper image), and after two stages of heat treatment (bottom image).

ature of GaAs in the growth chamber. Next, a thin AlAs layer 2 nm thick was deposited on the surface of the samples at 600°C, the temperature was increased to 650–700°C, and the second stage of heat treatment was

carried out. The thickness of the cap layer was smaller in the regions which contained dislocations and small clusters with a dislocation structure. The second stage of heat treatment leads to the redistribution of the mate-

rial and to the opening of the defect regions. The temperature of 700°C is below the temperature of AlAs evaporation, and only dislocation-containing regions evaporated during the second stage of heat treatment. Further, the temperature was lowered to 650°C and a GaAs layer 40 nm thick was grown. In addition, a $\text{Al}_{0.3}\text{Ga}_{0.7}\text{As}/\text{GaAs}$ confining superlattice (five pairs 3 nm/3 nm) was grown to prevent the leakage and non-radiative surface recombination of the carriers. The superlattice was overgrown with 10-nm-thick GaAs layer. Samples were also grown in which the QDs were overgrown with GaAs rather than with AlAs after the first stage of heat treatment. These samples were grown in order to check experimentally the necessity of overgrowth of the AlAs layer before the high-temperature heat treatment at 700°C. In these samples, the QDs were grown in the $\text{Al}_{0.15}\text{Ga}_{0.85}\text{As}$ matrix in order to prevent the possible evaporation of the material of the matrix at 700°C. A QD-containing reference sample coated with two InAs monolayers with a PL peak at 1.07 μm was also grown. It is known that such MBE-grown QDs are defect-free, since the amount of InAs is less than the critical amount for defect formation. This sample was used for a quantitative comparison of the PL intensity with the samples under investigation.

The PL was excited using an Ar^+ laser ($\lambda = 514.5 \text{ nm}$, the excitation density $P_{\text{ex}} = 5000 \text{ W/cm}^2$) and detected using a Ge-based cooled photodiode. The transmission electron microscopy (TEM) investigations were carried out using a PHILIPS-EM-420 microscope with an accelerating voltage of 100 kV.

3. RESULTS AND DISCUSSION

The TEM top images for the samples fabricated using one-stage and two-stage heat treatments are shown in Fig. 1b. The upper image shows a sample with AlAs-overgrown QDs after the first stage of defect elimination. It is clearly seen that AlAs coats the QD layer incompletely. In this case, the regions containing no QDs (wetting layer) and certain QDs which correspond to the coherent lattice-matched growth are overgrown with AlAs. Large dislocation-containing QDs are not overgrown by the AlAs layer. It can be seen from the lower image that the QDs uncoated with the AlAs layer are partially substituted by AlAs due to the second stage of heat treatment. In the course of heat treatment, the partial interdiffusion between InAs and GaAs, as well as the partial evaporation of the largest dots in the QD array, can proceed. Despite the existence of a cap layer, if this GaAs/AlAs layer is not sufficiently thick, not only dislocation-containing regions but also large QDs can open during high-temperature heat treatment (700°C). The reason is that it is known that the material on the top of the QD is also partially relaxed [23]. Due to this, the thickness of the cap layer above large QDs is insufficient to prevent the evaporation of the dots. Thus, the second stage of heat treatment at 700°C can lead to the partial evaporation of QDs

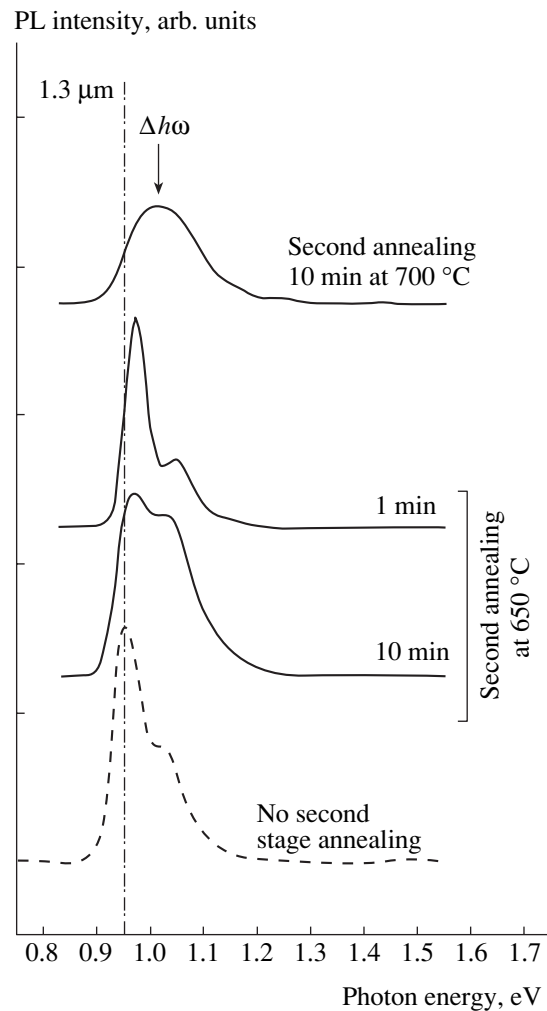


Fig. 2. Photoluminescence spectra of quantum dots in the samples grown using the procedure of elimination of defects. Various conditions for the second stage of elimination of defects were used: treatments for 10 min at 700°C, for 10 min at 650°C, and for 1 min at 650°C.

despite the existence of the cap layer. A decrease in the QD density can lead to a decrease in the intensity of QD PL. However, improvement of the crystal structure during the elimination of defects should increase the intensity of the QD PL. These two competitive processes need not be resolved in the course of the PL investigation of electron transitions in QDs.

The PL spectra for the QD-containing samples which were grown using various modes for the elimination of defects are shown in Fig. 2 on the same scale. It can be seen that the intensities of the observed PL peaks differ only slightly. The exception is the sample that underwent the second stage of heat treatment for 10 min at 700°C. The intensity of the QD PL for this sample is lower by a factor of 2 when compared with other samples. In addition, this peak is shifted to shorter wavelengths. We relate this peak to an increase in the density and average QD size. Furthermore, with noncongruent

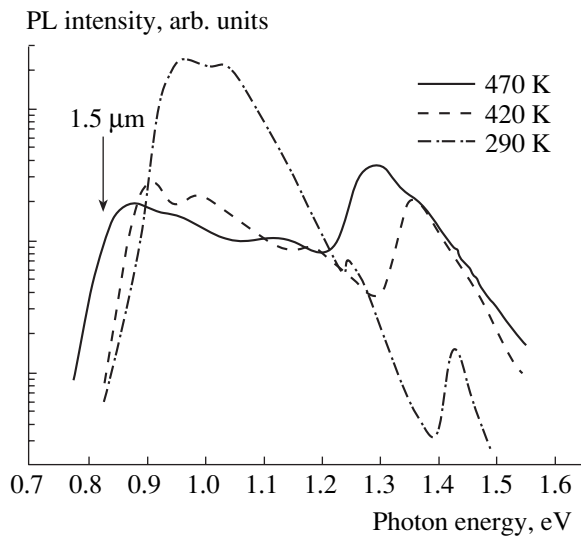


Fig. 3. Photoluminescence spectra of quantum dots for the samples grown using the procedure of the two-stage elimination of defects. The measurement temperatures are 290, 420, and 470 K.

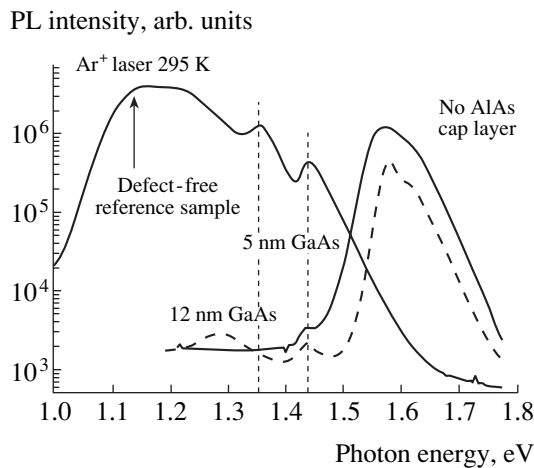


Fig. 4. Photoluminescence spectra of the samples grown without overgrowth with the AlAs layer.

evaporation, the formation of point defects and threading defects is possible. This also reduces the PL intensity.

In this case, the degree of imperfection of the structures under investigation could not be determined from the intensity of QD PL peaks. The PL investigation of electron transitions in the GaAs host allows one to make such evaluations in greater detail. It is easy to find that, even at room temperature, the number of holes in the host is comparable with that of carriers in QDs due to thermal ejection of the latter from QDs. A further increase in temperature leads to an increase in the thermal ejection of carriers from QDs and, consequently, to an increase in the population of the host.

The PL spectra of the sample which was grown using the two-stage elimination of defects with a sec-

ond stage of heat treatment at 650°C were measured at 290, 420, and 470 K. The results of the measurements are shown in Fig. 3. It can be seen from the spectra that an increase in temperature leads to an appreciable intensification of the PL peak from the host due to an increase in the population of electron and hole levels in the host. At 420 K, this peak becomes comparable with the intensity of the QD PL peak, and, at 470 K, the PL peak of the matrix dominates over the QD PL peak. However, the integrated intensity decreases by an order of magnitude upon heating, which can be explained by retrapping of the released carriers by defects.

Since the PL intensity is directly proportional to the population of a semiconductor by electrons and holes, we may state that the population of carriers injected into the host is higher for the samples with a lower defect density. The defects, which are centers of nonradiative recombination, trap the carriers, thus decreasing the population of the host. The QD-localized carriers can not be trapped by defects until they are delocalized in the host. For this reason, note once more that the estimation of the defect density from the intensity of the QD PL peak is significantly rougher. If the population of the host is larger than or comparable with the population of QDs, the degree of structural imperfection can be evaluated from the PL peak of the matrix irrespective of the luminescence properties of the QDs.

Structures were investigated in which the QD layer was overgrown with GaAs rather than AlAs after the first stage of heat treatment. The second stage of heat treatment was carried out for 30 s and 2 min at 700°C. The PL spectra for these structures in comparison with the defect-free reference sample are shown in Fig. 4. The QD PL peak for the sample heat-treated for 30 s (dashed curve) is 3 orders of magnitude weaker compared with the peak for the reference sample. No QD PL peak at all is observed for the second sample, which differs from the first one by a longer heat treatment (2 min). This phenomenon is explained by the fact that GaAs is evaporated at 700°C. For this reason, it cannot prevent the evaporation of the QD layer during heat treatment. However, the PL peak of the matrix for these samples is comparable in intensity with the peak of the defect-free reference sample, which indicates that the defect density for these samples is low. The heat treatment mode, which was used for these samples, destroys the QDs completely or almost completely. However, the crystalline quality of the matrix is restored in this case.

The PL spectra of the GaAs host in the structures investigated are shown in Fig. 5; the spectra were measured at 420 K. It can be seen from Fig. 5 that the intensity of the PL peak for the host of the sample grown using the two-stage elimination of defects is substantially higher than that for the sample grown using the one-stage elimination of defects (dashed curve). The samples subjected to the second stage of heat treatment at 650°C for 10 min demonstrate the highest PL inten-

sity. The intensity of the PL peak for the host of such samples is higher by a factor of 4 compared with the sample with the one-stage elimination of defects. For the second stage of heat treatment at 650°C for 1 min, the PL intensity of the matrix is substantially lower. It is possible that this duration of heat treatment is insufficient for the process of reevaporation of the defect region. If the second stage of heat treatment is carried out at 700°C for 10 min, the PL intensity for the matrix also differs insignificantly from the PL for the sample annealed according to the one-stage treatment. Thus, it is clear that two-stage heat treatment after overgrowth with thin GaAs and AlAs layers can substantially enhance the efficiency of radiative recombination of carriers populating the host. This indicates that the effect of nonradiative recombination caused by defects of the crystal lattice becomes less pronounced.

As was demonstrated among the samples investigated, the second stage of heat treatment at 650°C for 10 min is the most efficient. At the same time, a decrease in the integrated PL intensity for this sample upon heating points to the existence of a substantial number of defects. However, a series of experimental investigations demonstrated superior parameters of lasing for structures with a QD-containing active region which were grown in the same mode [12, 16, 24] as the samples investigated in this study. Specifically, these devices demonstrated a high temperature stability of the threshold current density. Further improvement of the crystalline quality of the structure permits one to expect the improvement of such laser characteristics as the internal differential efficiency, temperature stability of the threshold current density, and the service life of the device.

It is also of interest that a noticeable PL at the wavelength of 1.5 μm is observed in the PL spectrum of the sample with the two-stage elimination of defects at the measurement temperature of 470 K (Fig. 3). This effect is caused by temperature variation in the band gap. The existence of luminescence at the wavelength of 1.5 μm allows us to advance the idea of developing QD injection lasers that emit at a wavelength close to 1.5 μm . Such lasers are used widely for fiber-optics communications. Since such devices must operate at high temperatures (above 150°C), the attainment of defect-free growth is necessary in the development of such devices.

Thus, it is demonstrated that the high-temperature thermal treatment of structures with QDs overgrown with a thin GaAs/AlAs layer improves the crystalline quality of the structure. At the same time, the material of the QD can be evaporated during heat treatment. Thus, it is necessary to find a compromise variant for the elimination of defects, by which the largest number of defects is annihilated but no evaporation of QDs occurs at all. Among the samples investigated, the sample with a 2-nm-thick GaAs cap layer, for which the second-stage thermal treatment temperature was

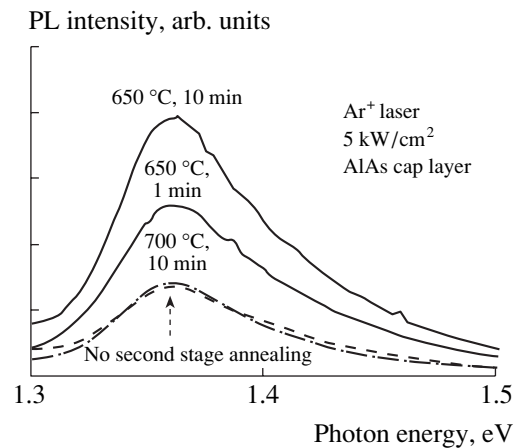


Fig. 5. Photoluminescence spectra of the GaAs matrix for the samples grown using the procedure of elimination of defects. The measurement temperature is 420 K. The temperature and duration of the second stage of heat treatment after overgrowth with an AlAs layer are indicated in the figure panel.

650°C, seems to be optimal. The reason is that this sample demonstrates the most intense luminescence of the host with no degradation of QD luminescence.

4. CONCLUSION

In this study, QD-containing samples which emit at a wavelength close to 1.3 μm were investigated using transmission electron microscopy and photoluminescence measurements. The samples were grown using the two-stage elimination of defects, which ensured a substantial decrease in the density of crystal lattice defects that emerged during strain-involving growth. The two-stage elimination of defects is based on the overgrowth of the QD layer with a thin GaAs cap layer, heat treatment *in situ* at 600°C, further overgrowth with a thin GaAs/AlAs layer, and a second heat treatment *in situ* at 650–700°C.

It is demonstrated that the PL measurement above room temperature makes possible the effective investigation of the degree of imperfection of the QD-containing structures. The PL measurements at high temperatures (300–420 K) demonstrated that the PL intensity of the host of the QD-containing structure increases by almost an order of magnitude, which indicates that the elimination of defects is successful. The necessity of overgrowing the structure with an AlAs layer before the second heat treatment at 700°C to prevent the evaporation of the coherent material is demonstrated. For the samples investigated, the optimal parameters of the two-stage elimination of defects are determined. These are the overgrowth of the QD layer with a 2-nm-thick GaAs layer, heat treatment for 1 min at 600°C, subsequent overgrowth with a 2-nm-thick GaAs layer, and a second heat treatment at 650°C.

The improvement of the crystalline quality of a structure is an important stage in refining the characteristics of laser devices with a QD-containing active region.

REFERENCES

1. N. N. Ledentsov, in *Proceedings of the IX National Conference on Crystal Growth, Moscow, 2000*.
2. P. Gyoungwon, O. B. Shchekin, D. L. Huffaker, and D. G. Deppe, *IEEE Photonics Technol. Lett.* **12** (3), 230 (2000).
3. R. L. Sellin, Ch. Ribbat, M. Grundmann, *et al.*, *Appl. Phys. Lett.* **78**, 1207 (2001).
4. S. Seki, H. Oohasi, H. Sugiura, *et al.*, *J. Appl. Phys.* **79**, 2192 (1996).
5. B. B. Elenkrig, S. Smetona, J. G. Simmons, *et al.*, *J. Appl. Phys.* **85**, 2367 (1999).
6. O. B. Shchekin, G. Park, D. L. Huffaker, *et al.*, *Appl. Phys. Lett.* **77**, 466 (2000).
7. J. K. Kim, R. L. Naone, and L. A. Coldren, *IEEE J. Sel. Top. Quantum Electron.* **6** (3), 504 (2000).
8. N. N. Ledentsov, D. Bimberg, V. M. Ustinov, *et al.*, *Semicond. Sci. Technol.* **14**, 99 (1999).
9. P. Borri, S. Schneider, W. Langbein, *et al.*, *Appl. Phys. Lett.* **79**, 2633 (2001).
10. F. Ferdos, M. Sadeghi, Q. X. Zhao, *et al.*, *J. Cryst. Growth* **227**, 1140 (2001).
11. A. Passaseo, G. Maruccio, M. De Vittorio, *et al.*, *Appl. Phys. Lett.* **78**, 1382 (2001).
12. M. V. Maximov, A. F. Tsatsul'nikov, B. V. Volovik, *et al.*, *Phys. Rev. B* **62**, 16671 (2000).
13. G. T. Liu, A. Stintz, H. Li, *et al.*, *Electron. Lett.* **35**, 1163 (1999).
14. A. E. Zhukov, A. R. Kovsh, N. A. Maleev, *et al.*, *Appl. Phys. Lett.* **75**, 1926 (1999).
15. M. Grundmann, F. Heinrichsdorff, N. N. Ledentsov, *et al.*, *Jpn. J. Appl. Phys.* **39** (4B), 2341 (2000).
16. J. A. Lott, N. N. Ledentsov, V. M. Ustinov, *et al.*, in *Abstract Book of LEOS 2000: Proceedings of the Lasers and Electro-Optics Society Annual Meeting, Rio Grande, Puerto Rico, 2000*, p. 304.
17. A. V. Sakharov, I. L. Krestnikov, N. A. Maleev, *et al.*, *Fiz. Tekh. Poluprovodn. (St. Petersburg)* **35**, 889 (2001) [*Semiconductors* **35**, 854 (2001)].
18. P. Gyoungwon, O. B. Shchekin, S. Csutak, *et al.*, *Appl. Phys. Lett.* **75**, 3267 (1999).
19. N. N. Ledentsov, V. M. Ustinov, V. A. Shchukin, *et al.*, *Fiz. Tekh. Poluprovodn. (St. Petersburg)* **32**, 385 (1998) [*Semiconductors* **32**, 343 (1998)].
20. A. Passaseo, G. Maruccio, M. De Vittorio, *et al.*, *Appl. Phys. Lett.* **78**, 1382 (2001).
21. N. N. Ledentsov, M. V. Maximov, D. Bimberg, *et al.*, *Semicond. Sci. Technol.* **15**, 604 (2000).
22. I. L. Krestnikov, N. A. Cherkashin, D. S. Sizov, *et al.*, *Pis'ma Zh. Tekh. Fiz.* **27** (6), 34 (2001) [*Tech. Phys. Lett.* **27**, 233 (2001)].
23. O. Stier, M. Grundmann, and D. Bimberg, *Phys. Rev. B* **59**, 5688 (1999).
24. G. T. Liu, A. Stintz, H. Li, *et al.*, *IEEE J. Quantum Electron.* **36**, 1272 (2000).

Translated by N. Korovin

AMORPHOUS, VITREOUS, AND POROUS SEMICONDUCTORS

Photoluminescent and Electronic Properties of Nanocrystalline Silicon Doped with Gold

É. B. Kaganovich*, I. M. Kizyak, S. I. Kirillova, É. G. Manoïlov,
V. E. Primachenko, S. V. Svechnikov, and E. F. Venger

*Institute of Semiconductor Physics, National Academy of Sciences of Ukraine,
pr. Nauki 45, Kiev, 03028 Ukraine*

* e-mail: dept_5@isp.kiev.ua

Submitted January 30, 2002; accepted for publication January 31, 2002

Abstract—Doping nanocrystalline silicon (*nc*-Si) films grown by laser ablation with gold leads to a considerable suppression of the nonradiative recombination of the charge carriers and excitons, an increase in the intensity and stability of the visible photoluminescence, and enhancement of the low-energy (1.5–1.6 eV) photoluminescence band. In Au-doped samples, the magnitude of the photovoltage and the rate of electron capture by traps in the film are reduced, and the density of boundary electron states and the concentration of deep electron traps at the single-crystal silicon (*c*-Si) substrate are decreased as well. The observed effect of doping on the photoluminescent and electronic properties of *nc*-Si films and *nc*-Si/*c*-Si structures is caused by the passivation of dangling Si bonds with Au and by the further oxidation of silicon at the surface of nanocrystals, which results in the formation of high-barrier SiO₂ layers. © 2002 MAIK “Nauka/Interperiodica”.

1. INTRODUCTION

Significant advances have been made over the last ten years in the investigation of efficient room-temperature photoluminescence (PL) in the visible spectral range of low-dimensional systems based on nanocrystalline silicon (*nc*-Si) [1–5]. It was found that the origin of the visible PL is related to quantum-confinement and dielectric effects and that kinetically coupled systems of electron–hole pairs and excitons are involved in the radiative recombination. It was established that the PL intensity largely depends on the degree of suppression of the nonradiative recombination.

In porous silicon (*por*-Si), which is obtained through electrochemical etching, the conditions for the passivation of dangling Si bonds by ions of hydrogen, oxygen, hydroxyl groups, etc., exist during the growth process itself. To enhance the PL intensity and stability, subsequent treatments are carried out with the aim of replacing weaker Si–H and Si–OH bonds with stronger Si–O and Si=O bonds. The most complete passivation is attained upon adding HCl to the electrolyte [6]. This beneficial effect is related to the formation of a thin SiO₂ layer (instead of SiO_x with 0 < *x* < 2) at the surface of nanocrystals.

Nanocrystalline Si films, grown using ion implantation, chemical vapor deposition, magnetron sputtering, spark discharge, laser ablation, and other techniques, are exceeded by *por*-Si in PL efficiency. However, *nc*-Si films have a number of advantages over *por*-Si: they possess higher mechanical strength, their fabrication is more technologically effective, they can be

grown in clean vacuum or gas environment conditions, other substrates than single-crystal silicon (*c*-Si) can be used, etc. At the same time, in contrast to the case of *por*-Si, special measures have to be taken during the growth of *nc*-Si films in order to suppress nonradiative recombination. There is little information in the literature about progress along this line.

In this study, we found that nonradiative recombination of electron–hole pairs in *nc*-Si films obtained by laser ablation is suppressed considerably when the films are doped with gold during their growth. Such doping is also found to bring about a notable decrease in the density of boundary electron states (BES) in *c*-Si substrate and a reduction in the electron capture by traps. We believe that these results are explained by efficient processes of passivation of dangling Si bonds with gold and further oxidation of silicon at the nanocrystal surface, which leads to the formation of SiO₂ barrier layers in place of SiO_x with 0 < *x* < 2.

2. EXPERIMENTAL

2.1. On the Choice of Gold as the Dopant

Ions of Au, Ag, Cu, Hg, Pd, and other electropositive metals that appear to the right of Si in the series of elements ordered by their normal potentials are reduced at the silicon surface when capturing electrons from Si atoms. Electrons from Si atoms with dangling bonds will be captured by metal ions most readily, the latter being discharged via this process; thus, the dangling bonds become passivated due to the formation of Si–M bonds (where M denotes the metal) [7]. This should

lead to a decrease in the rate of nonradiative recombination related to dangling bonds and, consequently, to an increase in the PL intensity. Furthermore, the presence of strong Si–M bonds will favor an enhancement in the PL stability.

Capturing of valence electrons from silicon by deposited metal ions is equivalent to the breaking of Si–Si bonds, which facilitates the binding of oxygen with surface silicon atoms. The catalytic activation of the oxidation process by metals will lead to the formation of a SiO₂ layer, instead of the usually formed SiO_x layer with $0 < x < 2$, at the surface of silicon. This should also contribute to the enhancement of the PL intensity due to the following factors: (1) improved confinement of electron–hole pairs by a higher potential barrier, (2) increased importance of excitons in the PL process due to the dielectric effect (the permittivity of SiO₂ is lower than that of SiO_x), and (3) involvement of a larger number of Si nanocrystals in the emission process due to a decrease in their sizes upon oxidation.

In the series of electropositive metals, gold has both the largest electron affinity (2.31 eV) and first ionization energy (9.26 eV). This means that gold should offer the largest dangling-bond passivation effect and the most efficient oxidation of the surface of Si nanocrystals in comparison with other electropositive metals.

Efficient passivation of dangling Si bonds by Au ions was confirmed experimentally by one of the authors in a study of electron spin resonance in *c*-Si powders [8]. Thus, we suggested that the presence of Au ions in the erosion plume that forms under laser ablation of a silicon target with an admixture of gold will lead to favorable consequences, outlined above, for the photoluminescent properties of *nc*-Si films.

2.2. Samples and Experimental Procedures

Photoluminescent *nc*-Si films were obtained by laser ablation [9]. The beam of a Q-switched Nd³⁺:YAG laser operating at the wavelength $\lambda = 1.06 \mu\text{m}$ was scanned over the target, which was either a bare wafer of KDB-10 crystalline silicon (*p*-Si:B with a resistivity of $10 \Omega \text{ cm}$) or such a wafer covered with a nearly 80-nm-thick film of gold. The laser parameters were as follows: pulse energy density, $\sim 20 \text{ J/cm}^2$; pulse duration, 10 ns; and pulse repetition rate, 25 Hz. The target and the substrate, mounted in the same plane, were placed in a vacuum chamber in an atmosphere of argon under a pressure of $\sim 13 \text{ Pa}$. The interaction of the Ar atoms with the particles of the erosion plume resulted in the deposition of a film from their backward flux onto the substrate. The deposition rate was about 15–20 nm/min; the film thickness and porosity were $\sim 500 \text{ nm}$ and $\sim 40\%$, respectively.

For the grown structures (*nc*-Si film on a *c*-Si substrate), we measured the time-resolved PL spectra [10] and the temperature dependences of the photovoltage

that appeared upon irradiation of a structure with light pulses of high intensity [11]. The PL was excited by the radiation of a nitrogen laser ($\lambda = 337 \text{ nm}$) with a pulse duration of $\tau_p = 8 \text{ ns}$. The gated detection of the signal was carried out in the photon counting mode. The photon counts were accumulated over a time interval determined by a gate pulse with a minimum duration 250 ns. To obtain the spectra of the fast PL component, whose time constant $\tau < 250 \text{ ns}$, the leading edge of the gate pulse was set to coincide with that of the laser pulse. PL relaxation times shorter than 50 ns were estimated by oscilloscope traces. As a rule, sequences of time-resolved spectra were taken with the gate-pulse delay (with respect to the laser pulse) being varied in multiples of the gate-pulse duration. In the measurements of the longest relaxation times (tens of microseconds), the gate-pulse width and delay were increased arbitrarily. To estimate the PL stability, we kept records of the variations in the PL intensity with time under laser irradiation or upon prolonged exposure of the samples to air.

To measure the photovoltage, a measurement capacitor formed by a semitransparent conductive layer of SnO₂:Sb on mica pressed to the (*c*-Si substrate)/(*nc*-Si film) structure under study was mounted in a vacuum cryostat. The photovoltage induced in the substrate was measured upon illumination of the capacitor with red-light pulses, and the overall photovoltage induced in the film and in the substrate was measured using white-light pulses. The photovoltage in the sample illuminated by red light V_{ph} is equal in magnitude (but opposite in sign) to the surface potential ϕ_s of the *c*-Si substrate. The photovoltage was recorded using a storage oscilloscope. An ISSh-100 flash lamp was used as the light source, with the duration and intensity of the pulses being $10 \mu\text{s}$ and $10^{21} \text{ photon/(cm}^2 \text{ s)}$, respectively. The measurement procedure of photovoltage is described in more detail elsewhere [11].

3. RESULTS AND DISCUSSION

It was demonstrated in preliminary experiments that the largest increase in the PL intensity upon doping of *nc*-Si films with electropositive metals (Au, Ag, Cu) is attained in the case of Au, while electronegative impurities (In, Al) have no effect. It was established that the optimum thickness of the gold film covering the silicon target is $\sim 80 \text{ nm}$. In all likelihood, with a lesser amount of gold, passivation of most of the dangling Si bonds would not be achieved, while adding a greater amount of gold would lead to a situation where the generated electron–hole pairs would leave the Si nanocrystals.

In Fig. 1, we present time-resolved PL spectra of the films grown without (curve 1) and with (curves 2, 3) the addition of Au in the erosion plume. The PL of the films grown without Au has a fast component only (PL relaxation time $\tau < 50 \text{ ns}$); its spectrum spans the wavelength range from 400 to 700 nm (the photon energy $h\nu =$

1.8–3.1 eV) and is peaked at ~ 500 nm (curve 1). The PL of the films doped with Au has a slow component as well, the relaxation times being as large as 10–20 μ s (Fig. 1, curve 3). Its spectrum covers a wider wavelength range (400–900 nm); there are two emission bands with peaks at $\lambda \approx 500$ nm and $\lambda \approx 700$ –800 nm. The intensity of the long-wavelength band is 3–4 times higher than that of the short-wavelength band. The spectrum of the fast component of the PL in doped films (Fig. 1, curve 2) also has a long-wavelength band (absent in the case of undoped films), but the relative intensity of the short-wavelength band is much lower.

Since the PL quantum yield of all of the films under study is in the range of several percent, the measured PL relaxation times are determined by nonradiative recombination. As is shown by the data of Fig. 1, the nonradiative-recombination time in Au-doped films is nearly three orders of magnitude longer than that in undoped films. Thus, doping with Au causes a considerable suppression of the fast nonradiative recombination, which leads to a rise in the PL intensity. Nanocrystals with larger sizes are passivated more efficiently, and this results in a stronger enhancement of the long-wavelength PL band. This band is also enhanced as a result of a higher excitonic radiative-recombination rate. The exciton binding energy increases with an increase in the depth of the potential well, which occurs due to the formation of an SiO_2 layer in place of SiO_x with $0 < x < 2$. This layer grows on the surface of Si nanocrystals due to the presence of residual oxygen in the vacuum chamber and the catalytic action of gold.

Data characterizing the PL stability are shown in Fig. 2, which represents the variation in the PL intensity with time. Under the continuous laser irradiation of undoped films, the PL intensity decreases by 40–45% in the first 20 min (curve 1). In contrast, the films doped with Au exhibit much higher stability, with the PL intensity decreasing by no more than 5% (curve 2). The Au-doped films are also more stable than undoped ones when exposed to air for a long period of time (curves 3, 4). For instance, one can see from Fig. 2 that the PL intensity of undoped films increases by $\sim 30\%$ after being kept in air for half a year; this takes place due to the gradual process of further oxidation of SiO_x layers. Meanwhile, the PL intensity of Au-doped films varies with time by 5–10% at most, since in this case there is substantial initial coverage of Si nanocrystals with SiO_2 .

The temperature dependences of the photovoltage V_{ph} of $nc\text{-Si}/c\text{-Si}$ structures are shown in Fig. 3 (a negative photovoltage corresponds to the negative polarity at the $\text{SnO}_2\text{:Sb}$ electrode). Curves 1, 1', 2, and 2' correspond to an undoped $nc\text{-Si}$ film; curves 3, 3', 4, and 4' correspond to a Au-doped film. Curves 1–4 represent the photovoltage induced by the first light pulse in a train; curves 1 and 3 were recorded under red-light illumination and curves 2 and 4, under white-light illumina-

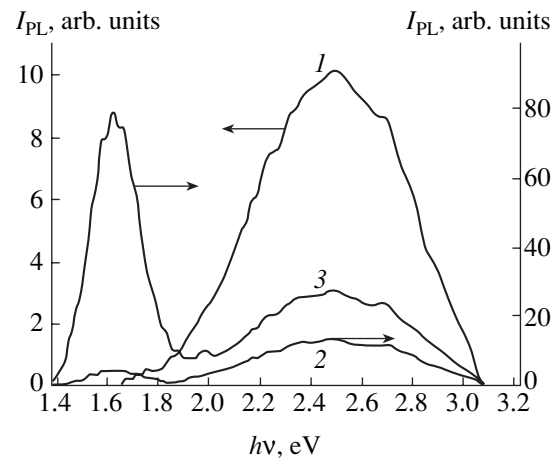


Fig. 1. Time-resolved photoluminescence spectra of (1) undoped and (2, 3) Au-doped nanocrystalline $nc\text{-Si}$ films. Curves 1 and 2 represent fast photoluminescence components ($\tau < 50$ ns and $\tau < 250$ ns, respectively) and curve 3 represents integrated photoluminescence ($250 < \tau < 10 \mu$ s).

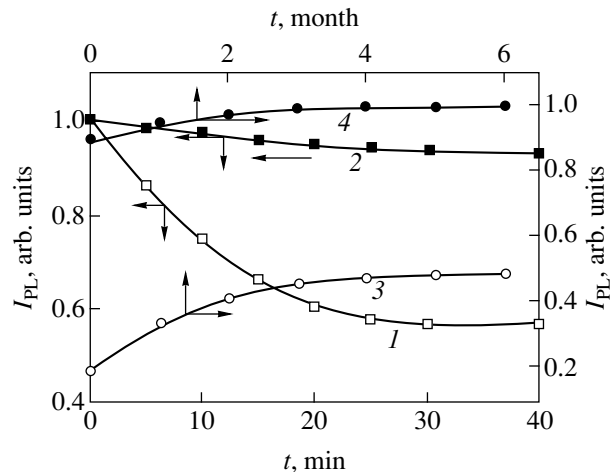


Fig. 2. Variation of the photoluminescence intensity with time (1, 2) under irradiation of the samples by pulses from an N_2 laser and (3, 4) upon exposure to air; curves 1 and 3 correspond to undoped $nc\text{-Si}$ films, curves 2 and 4 correspond to Au-doped ones.

tion. At temperatures $T < 220$ K, the values of V_{ph} measured at the second (as well as any other subsequent) light pulse in a train had a reduced magnitude (see curves 1'–4'). This means that, at lowered temperatures, photomemory phenomena are present [7]. These are related to the capture of electrons by traps. Under red-light illumination, the traps located at the boundary between the substrate and the film are important; under white-light illumination, the effect of those traps located in the film itself is added. In the presence of photomemory, the measurements were carried out as described in [11].

One can see from Fig. 3 that, at $T > 200$ K, the values of V_{ph} measured under red- and white-light illumination

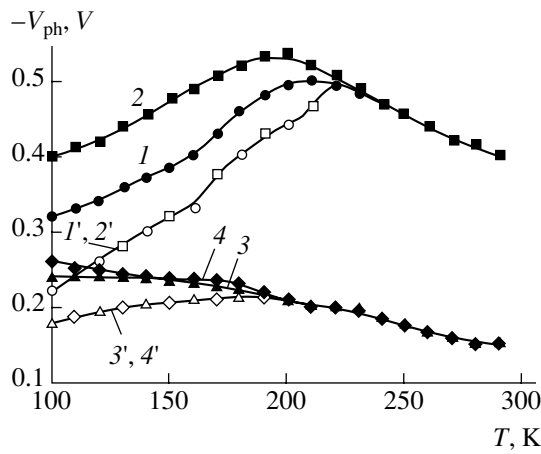


Fig. 3. Temperature dependences of the photovoltage V_{ph} induced in the structures (*nc*-Si film)/(*c*-Si substrate). Curves 1, 1', 3, and 3' were recorded under red-light illumination and curves 2, 2', 4, and 4' were recorded under white-light illumination. Curves (1–4) represent the measurements taken at the first light pulse in a train and curves (1'–4'), at the second.

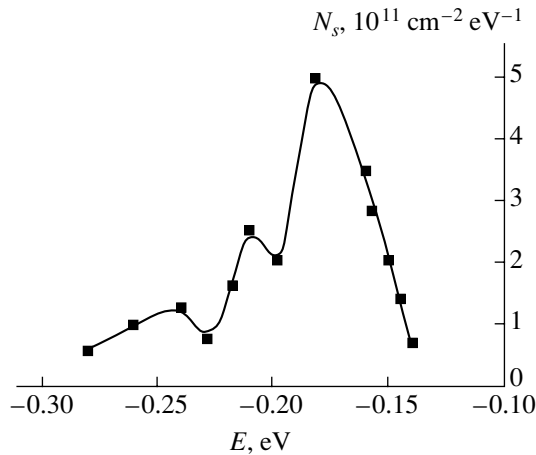


Fig. 4. Distribution of the boundary-electron-state density below the midgap E_i in *c*-Si covered by a Au-doped *nc*-Si film.

coincide. This means that photovoltage is not induced in the *nc*-Si film at these temperatures. The increase in $|V_{ph}|$ upon lowering the temperature in this region is related to the charging of the BES in *c*-Si substrate by holes, which takes place upon the shift of the Fermi level in *c*-Si towards the valence band. Calculations carried out by the method described in [12] indicate that, in the case of an undoped film, the Fermi level at the boundary between the film and the substrate virtually remains pinned as the temperature is varied; this is caused by the high density of BES (in excess of $1 \times 10^{12} \text{ cm}^{-2} \text{ eV}^{-1}$) at 0.1 eV above the midgap energy E_i .

At $T < 200 \text{ K}$, the magnitude of the photovoltage $|V_{ph}|$ in the structures with an undoped film decreases with decreasing temperature (see Fig. 3, curves 1, 2);

this is a consequence of a rearrangement of the BES due to reversible changes at the boundary between the film and the substrate [13]. Such a rearrangement of the BES system is not observed at the boundary between the Au-doped film and the substrate (see curves 3, 4 in Fig. 3). This makes it possible to calculate the distribution of the BES density $N_s(E)$ in the band gap in the energy range $E_i - (0.1-0.3) \text{ eV}$ at the *c*-Si surface covered by a Au-doped film (Fig. 4). One can see that $N_s(E)$ has peaks at the energies of 0.18, 0.21, and 0.24 eV below the midgap E_i . The highest BES density $N_s = 5 \times 10^{11} \text{ cm}^{-2} \text{ eV}^{-1}$ is attained at $E_i - 0.18 \text{ eV}$.

Thus, the density of the BES is reduced substantially upon the introduction of Au into the film. Previously, it was usually observed that doping of the Si surface with Au from solutions of Au salts in water or in various etchants had the opposite effect: the density of the BES increased [7]. The reduction of the BES density in the case under study can be explained by the structural transition at the *c*-Si surface taking place under the influence of the particles from the erosion plume (note that, prior to film deposition, the *c*-Si surface had a primarily hydride coating) [7]. This is corroborated by the observation of a decrease in the BES density at the silicon surface in the case of the laser sputtering of a target consisting of pure gold. It should be noted that the peaks in $N_s(E)$ appear in the range where two P_b centers are revealed at the Si–SiO₂ interface [14]; their origin remains unclear.

One can see from Fig. 3 that a difference between the values of V_{ph} (measured during the first pulse in a train) under white- and red-light illumination appears at temperatures $T < 230 \text{ K}$ and $T < 190 \text{ K}$ for structures with undoped and doped films, respectively. This means that, at lowered temperatures, a photovoltage V_{ph}^{nc-Si} in *nc*-Si films arises. It has a negative sign, similarly to the photovoltage in the *c*-Si substrate. Figure 5a shows the temperature dependences of (V_{ph}^{nc-Si}) determined from the difference in the photomemory effect under white- and red-light illumination; curves 1 and 2 correspond to an undoped and a Au-doped film, respectively. In both cases, the magnitude of the photovoltage in the film increases upon lowering the temperature, although in different ways. The very fact of the appearance of photovoltage in the films at lowered temperatures, as well as its variation with T , suggests that it is related to structural stresses in the film, which develop when the temperature is lowered. These stresses cause the formation of a positive built-in charge in the region of the film most distant from the *nc*-Si/*c*-Si boundary, and this is responsible for the arising photovoltage. A smaller photovoltage is observed in Au-doped films in comparison with undoped ones, which implies that these stresses are smaller in the former case. This conclusion agrees with the fact that, in structures with doped *nc*-Si films, there is no rearrangement of the BES

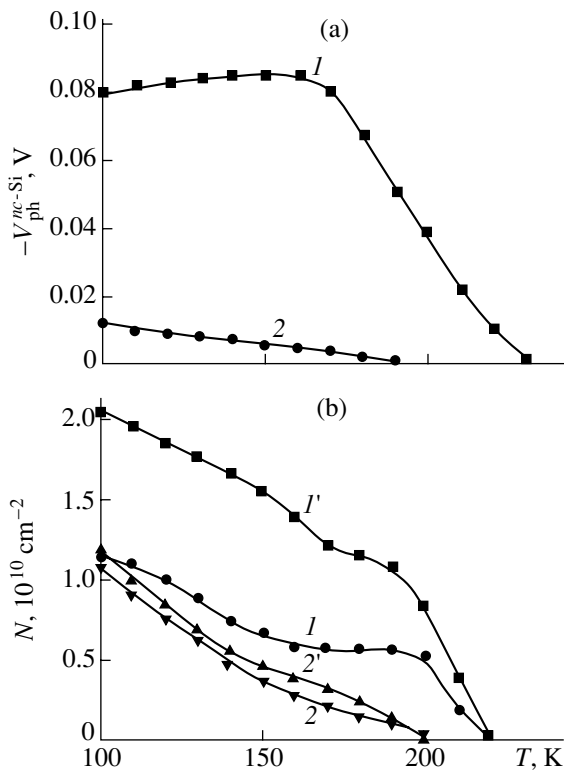


Fig. 5. (a) Temperature dependences of the photovoltage induced in (1) an undoped and (2) a Au-doped *nc*-Si film. (b) Temperature dependences of the density of electrons captured by traps in (1, 1') an undoped and (2, 2') a Au-doped film. Curves 1 and 2 correspond to electron capture at the film/substrate boundary and curves (1', 2') correspond to net electron capture at the boundary and within the film.

spectrum upon lowering the temperature, while considerable rearrangement takes place in the structures with undoped films (cf. Fig. 3).

The differences in the $V_{ph}(T)$ dependences represented by curves 1, 2 and 1', 2' and curves 3, 4 and 3', 4' in Fig. 3 can be used to calculate the density of trapped electrons. In Fig. 5b, we plot the temperature dependences of the density of nonequilibrium electrons captured by traps at the boundary between the *c*-Si substrate and the *nc*-Si film (curves 1, 2) and of the net density of electrons captured both at the film/substrate boundary and in the film itself (curves 1', 2'); curves 1 and 1' correspond to undoped films and curves 2 and 2', to Au-doped films. Note that, when calculating curves 1' and 2', we determine the lower limit for the number of electrons captured by traps in the film, because the trapped electrons are responsible for the potential drop not only in the substrate, but in the bulk of the film as well.

Since the traps become saturated with electrons even after the first light pulse in a train, the $N(T)$ curves in Fig. 5b also represent the temperature dependences of the density of traps capable of capturing the electrons. An increase in the number of traps upon lowering

the temperature is explained by the involvement of shallower traps in electron capturing. Figure 5b indicates that doping of *nc*-Si films with Au leads to a reduction in the number of deep traps at the substrate/film boundary (cf. curves 1 and 2). The doping also results in a considerable decrease in the trap density in the film itself, which is shown by the substantially smaller difference between curves 2 and 2' in comparison with curves 1 and 1'. These results demonstrate that doping *nc*-Si films with gold leads to a significant reduction in the number of traps capturing electrons at lowered temperatures. These traps are related to dangling bonds at the interface between the Si nanocrystals and the SiO_x matrix and to the defects in the matrix itself. Thus, there is agreement between the results of investigating the effect of Au doping on the PL and on the surface photovoltage in *nc*-Si films.

4. CONCLUSIONS

(1) Doping *nc*-Si films grown by laser ablation (the film is deposited from the backward flux of the erosion-plume particles onto the substrate) with Au leads to a substantial suppression of the nonradiative recombination of the charge carriers and excitons and to an increase in the intensity and stability of the film PL.

(2) Doping *nc*-Si films with Au during their deposition leads to a considerable decrease in the density of electron states at the *c*-Si/*nc*-Si boundary and in the density of deep-electron traps at the *c*-Si substrate. Moreover, another consequence of doping is the considerable reduction in the photovoltage induced in *nc*-Si films themselves and in the rate of electron capture by traps in the films at lowered temperatures.

(3) The results of the PL and the photovoltage measurements agree with each other and provide evidence that the following two processes contribute to the mechanism for the enhancement of PL intensity and stability upon Au doping of the *nc*-Si films: the passivation of dangling bonds by Au at the surface of Si nanocrystals and the formation of high-barrier, structurally more perfect SiO_2 layers in place of SiO_x with $0 < x < 2$.

REFERENCES

1. A. G. Cullis, L. T. Canham, and P. D. Calcott, *Appl. Phys. Rev.* **82**, 909 (1997).
2. Y. Kanemitsu, *Phys. Rep.* **263**, 1 (1995).
3. D. Kovalev, H. Heckler, G. Polisski, and F. Koch, *Phys. Status Solidi B* **215**, 871 (1999).
4. O. Bisi, O. Ossicini, and L. Pavesi, *Surf. Sci. Rep.* **38**, 1 (2000).
5. *Porous Semiconductors—Science and Technology: Extended Abstracts of II International Conference, Madrid, 2000.*

6. A. I. Belogorokhov and L. I. Belogorokhova, *Fiz. Tekh. Poluprovodn. (St. Petersburg)* **33**, 198 (1999) [*Semiconductors* **33**, 169 (1999)].
7. V. E. Primachenko and O. V. Snitko, *Physics of Metal-Doped Semiconductor Surfaces* (Naukova Dumka, Kiev, 1988).
8. V. M. Maevskii, V. E. Primachenko, O. V. Snitko, and N. G. Frolova, *Poverkhnost*, No. 1, 101 (1983).
9. É. B. Kaganovich, É. G. Manoïlov, and S. V. Svechnikov, *Ukr. Fiz. Zh.* **46**, 1196 (2001).
10. A. V. Sachenko, É. B. Kaganovich, É. G. Manoïlov, and S. V. Svechnikov, *Fiz. Tekh. Poluprovodn. (St. Petersburg)* **35** (12), 1445 (2001) [*Semiconductors* **35**, 1383 (2001)].
11. E. F. Venger, É. B. Kaganovich, S. I. Kirillova, *et al.*, *Fiz. Tekh. Poluprovodn. (St. Petersburg)* **33**, 1330 (1999) [*Semiconductors* **33**, 1202 (1999)].
12. E. F. Venger, S. I. Kirillova, V. E. Primachenko, and V. A. Chernobaï, *Ukr. Fiz. Zh.* **42**, 1333 (1997).
13. S. I. Kirillova, V. E. Primachenko, V. A. Chernobaï, and O. V. Snitko, *Poverkhnost*, No. 11, 74 (1991).
14. S. I. Kirillova, V. E. Primachenko, A. A. Serba, and V. A. Chernobaï, *Mikroélektronika* **29**, 390 (2000).

Translated by M. Skorikov

AMORPHOUS, VITREOUS, AND POROUS SEMICONDUCTORS

Strains and Crystal Lattice Defects Arising in Macroporous Silicon under Oxidation

E. V. Astrova*, V. V. Ratnikov, A. D. Remenyuk, and I. L. Shul'pina

*Ioffe Physicotechnical Institute, Russian Academy of Sciences,
Politekhnicheskaya ul. 26, St. Petersburg, 194021 Russia*

*e-mail: east@pop.ioffe.rssi.ru

Submitted February 27, 2002; accepted for publication February 28, 2002

Abstract—The deformation behavior of a macroporous silicon wafer subjected to high-temperature oxidation has been studied, and the basic parameters describing the sample bending and subsequent stress relaxation when oxide is removed are determined. X-ray diffractometry and topography were used to determine the sample bending radius and lattice parameters, and to reveal the areas of dislocation generation. The strain of a silicon lattice in oxidized macroporous Si is about 10^{-4} , and it decreases by an order of magnitude after oxide dissolution. The plastic part of the strain is accompanied by the generation of dislocations in the most strained regions of a structure, i.e., at the interfaces between the porous layer and substrate in the vertical direction and between the central porous region and the pore-free edge in the horizontal plane. The dislocation density is $\sim 10^4$ cm $^{-2}$. © 2002 MAIK “Nauka/Interperiodica”.

1. INTRODUCTION

Macroporous silicon (*ma*-Si), in differing from micro- or nanoporous, is a material with a regular system of cylindrical channels (macropores) with vertical walls; their length ranges up to hundreds of micrometers, and they have a diameter in the range of several micrometers (see, e.g., Fig. 1a). The technique of macropore formation by photoanodization of (100) *n*-Si was first proposed in [1]. The properties of *ma*-Si attract considerable interest owing to the wide spectrum of its applications, from solid-state and vacuum electronics to micromachinery. Capacitors of high specific capacitance [2], *n-n*⁺ structures [3], short pass optical filters [4], and X-ray optical components [5] have been fabricated using *ma*-Si; definite progress has been made in deriving a new generation of microchannel plates for electron-optical converters [6], X-ray image recording matrices [7], micropumps [8], etc. One of the most attractive applications of *ma*-Si is the optical processing of information. *ma*-Si represents a two-dimensional photonic crystal [9], which can be used for light modulators, low-loss waveguides, and high-quality microcavities [10], which, combined with recent progress in the area of Si light emitting diodes [11, 12], opens the way to all-silicon optoelectronics.

Commercial applications of *ma*-Si depend, to a large extent, on its compatibility with standard silicon technology. The principal process in the technology of silicon devices and integrated circuits, thermal oxidation, plays nearly the same role in the case of *ma*-Si. A SiO₂ film that coats the internal surface of channels serves as an electric insulator in microchannel plates and structures with dielectric insulation. Masking properties of the oxide film are used to control the diffusion

of dopants. In addition, SiO₂ passivates the surface during the selective etching of structures based on *ma*-Si and serves as a sacrificial layer to enlarge the channel diameter. Owing to a strong mismatch between the thermal expansion coefficients of Si and SiO₂, stresses and strains arise in the structures, which are especially strong when the relief surfaces are oxidized [13]. In the majority of cases, these processes are detrimental, because they change the device geometry, interfere with photolithography, and produce dislocations and other defects, thus deteriorating the electrical parameters of the material. Nevertheless, in some specific situations, the controllable bending of the wafer may be of practical interest, e.g., in X-ray optical components.

Earlier high-resolution X-ray diffractometric and topographic studies of a *ma*-Si structure [14, 15] showed that the Si crystal lattice remains virtually undistorted after the formation of macropores. The thermal oxidation of *ma*-Si results in disruptions of the crystal structure, such as changes in interplanar spacings and misorientation of atomic planes. The incomplete relaxation of stresses in *ma*-Si samples after removal of the oxide layer, especially under repeated oxidations, indicates the development of plastic deformation with the generation of dislocations.

The present study investigates the macrodeformation behavior of wafers containing *ma*-Si areas with different characteristics (porosity, pattern of seed pits, through and dead-end channels, etc.).

2. EXPERIMENT

ma-Si was obtained through the photoelectrochemical etching of (100) *n*-Si with 15–20 Ω cm, resistivity

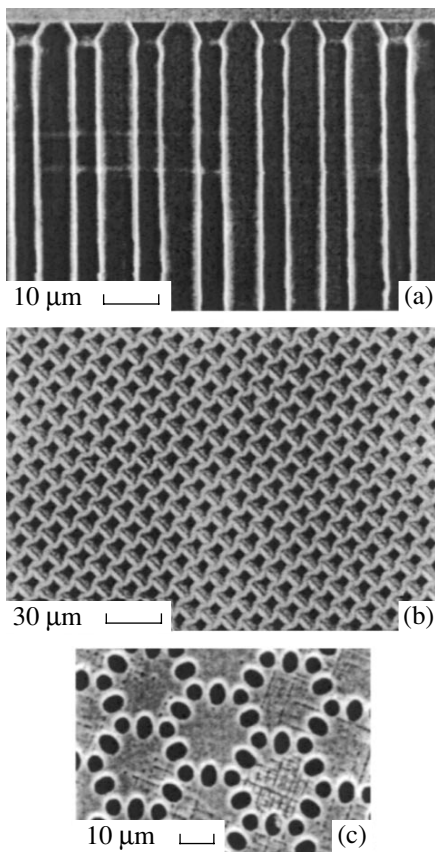


Fig. 1. SEM images of *ma*-Si samples: (a) cross-sectional view and plan views of samples with (b) triangular (AT-3) and (c) honeycomb (AT-2) pit patterns.

(for technological details, see [14]). The initial wafers were 25 mm in diameter and 300 μm thick; a porous area 20 mm in diameter was located in the central part of a wafer surrounded at the periphery with a 2.5-mm-wide pore-free edge ring. On the front face of the wafer, 5.4- μm -deep seed pits formed a regular macropore pattern: either a triangular lattice with a 12- μm period (photomask AT-3, Fig. 1b), or a honeycomb structure with pores in the apexes of a regular hexagon with 12- μm sides and an additional pore in the middle of each side (photomask AT-2, Fig. 1c). The surface density of the macropores was $N = 7.94 \times 10^5$ and $1.33 \times 10^5 \text{ cm}^{-2}$ for AT-3 and AT-2 masks, respectively, which yields a different porosity of *ma*-Si for the same channel diameter. After the formation of *ma*-Si, the seed pits were removed from some of the samples by mechanical polishing of their front faces. To obtain through channels, the pores were opened by lapping and polishing the back side of a wafer to $\sim 200 \mu\text{m}$ thickness, with subsequent washing. To study the influence of the pore-free edge and of the interface between the porous and pore-free areas, the edge was removed from several samples by mechanical cutting or etching. Table 1 presents cross sections of the obtained structures. They can be classified as homogeneous or inhomogeneous over


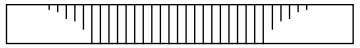
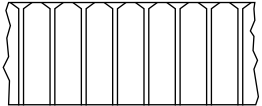
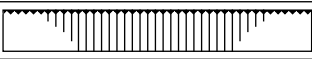
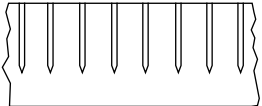

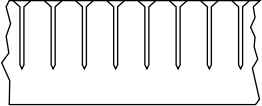

their area (without the pore-free edge and with it, respectively) and across their thickness. Only the samples with through channels and no pits (types 1 and 1K) can be regarded as homogeneous across their thickness (single-layer). The other samples are classified as two- and three-layered. Two-layer structures are types 2 and 2K (without and with edge). They can appear in two different versions: 2a, through channels with seed pits (first layer, seed pits; the second, *ma*-Si); or 2b, dead-end channels without pits (first layer, *ma*-Si; the second, Si substrate). Correspondingly, three-layer structures are samples with dead-end pores and unremoved pits (3 and 3K). Thermal oxidation in water vapor at $T = 1200^\circ\text{C}$ for 100 min resulted in covering the front, back sides of the samples and the entire internal surface of channels with an $\sim 1.2\text{-}\mu\text{m}$ -thick SiO_2 layer. Each of the additional oxidation treatments was performed after removing the oxide with hydrofluoric acid.

The radius of curvature R was measured with a double-crystal diffractometer following the method used in [16]. The idea is to measure the angular shift of the X-ray reflection peak $\delta\Theta$ from the planes parallel to the sample surface (Bragg configuration, reflection (004)) under scanning in the X-ray beam with a step δl . The dependence of the total shift of the reflection peak $\Sigma(\delta\Theta) = f(l)$ was obtained for each of the recorded points, and the radius of curvature R was defined as a cotangent of the slope angle of this dependence. The step of scanning was $(1 \pm 0.01) \text{ mm}$, the position of a diffraction peak was determined with an accuracy of $\pm(1''\text{--}10'')$ depending on the diffraction characteristics of a sample (the half-width of a rocking curve). This provided an accuracy of 5% for bending radii in the range $R \leq 5 \text{ m}$, 10% for $R = 10\text{--}100 \text{ m}$, and 20% for $R \geq 100 \text{ m}$.

The lattice parameter was measured using a triple-crystal diffractometer in the reference mode (see, e.g., [17]). The initial Si single crystal used for the fabrication of *ma*-Si served as a reference. Its lattice parameter measured by the Bond method was $a_0 = 5.4311 \pm 0.0001 \text{ \AA}$. The dispersion-free ($n, -n, n$) symmetric Bragg reflection configuration yielded values of the normal-to-surface strain ε_z and lattice parameter a_z . The lateral strain and lattice parameter ε_x and a_x were obtained from an asymmetric (224) reflection. The difference between the lattice parameters of the reference and studied samples was determined by measuring the variation of the double Bragg angle $\Delta(2\Theta)$ when the reference was replaced with a sample. The measurement accuracy was determined by the accuracy of recording the reflection peak of the sample under study and of the analyzer; it was $\leq 0.0001 \text{ \AA}$ for the lattice constant and ≤ 0.00001 for the strain.

The generation of new defects in the samples containing a *ma*-Si region was studied before and after oxidation using projection X-ray topography in the reflection ($\text{CuK}\alpha$) and transmission ($\text{MoK}\alpha$) configurations, with data recorded from both sides of a sample in sym-

Table 1. Classification of *ma*-Si samples

Number of layers	Description and the type notation	Cross section	Wafer bending after oxidation
1	Through channels without seed pits 1: without pore-free edge		Concave $R_1 < 0$
	1K: with edge		$R_{1K} < 0$
2	Through channels with seed pits 2a: without pore-free edge		Convex
	2aK: with edge		$R_2 > 0$
	Dead-end channels without seed pits 2b: without pore-free edge		$R_{2K} > 0$
	2bK: with edge		
3	Dead-end channels with seed pits 3: without pore-free edge		Convex $R_3 > 0$
	3K: with edge		$R_{3K} > 0$

metric and asymmetric reflections, and also by the section method in the (MoK_α) reflection configuration for the depth-limited (dead-end) channels [18]. A beveled cross section at an angle of 1° was prepared on the OA26 sample with dead-end channels so as to bring the interface between the *ma*-Si and substrate to the surface. It allowed us to study the distribution of dislocations across the sample thickness.

3. RESULTS

3.1. Sample Bending

Initial samples (prior to oxidation). All the initial samples with a pore-free edge were either flat or slightly concave ($|R| > 200$ m). Only the edge region was markedly bent ($R = \pm 67.8$ m in the edge region of sample 9H25). The bending of samples with a removed pore-free edge (OA 27 and 006) is considerably stronger, and their curvature depends on the method of edge removal (the bending during etching is smaller than during cutting).

Samples after oxidation. Table 2 presents the curvature radii of *ma*-Si samples at different stages of oxidation. The oxidation of samples results in their considerable bending, with its value, sign, and distribution depending on several parameters. First, the bending sign depends on the structure type. As a rule, single-layer structures (1 and 1K) become concave at the front face, $R < 0$, while multilayer structures (2, 2K, 3, and

3K) are convex, $R > 0$ (Figs. 2 and 3, respectively). For all the samples, the absolute value of the bending radius after oxidation was $|R| < 0.8\text{--}6.0$ m. As a rule, the samples with a pore-free edge are more strongly bent than those without an edge; the same effect is usually connected with an increase in the number of layers:

$$|R_1| > |R_{1K}|, \quad R_2 > R_{2K}, \quad R_3 > R_{3K};$$

$$|R_1| > R_2 > R_3 \quad \text{and} \quad |R_{1K}| > R_{2K} > R_{3K}.$$

It is noteworthy that the interface between the pore-free edge and the porous region or other local homogeneity distortions over area, such as defect regions with dead-end channels in type 1 and 2a samples, produce similar effects: oxidation results in the formation of regions with a smaller radius of curvature. This effect manifests itself as local variations of the bending sign for concave samples (Fig. 2) or stronger bending near the edge of convex wafers. Figure 3 shows sample 9N14 of the 2aK type with through channels, seed pits, and a pore-free edge, whose curvature was measured after the sixth oxidation. It is uniformly spherically bent in the region of channels, and the bending is very strong (with a convex front face, $R = +1.72$ m). In the edge and transaction regions, the curvature is even higher, $R = +0.06$ and $+0.71$ m, respectively, which gives the sample a saucer shape.

Figure 4 demonstrates the modification of the sample curvature after multiple oxidations and oxide

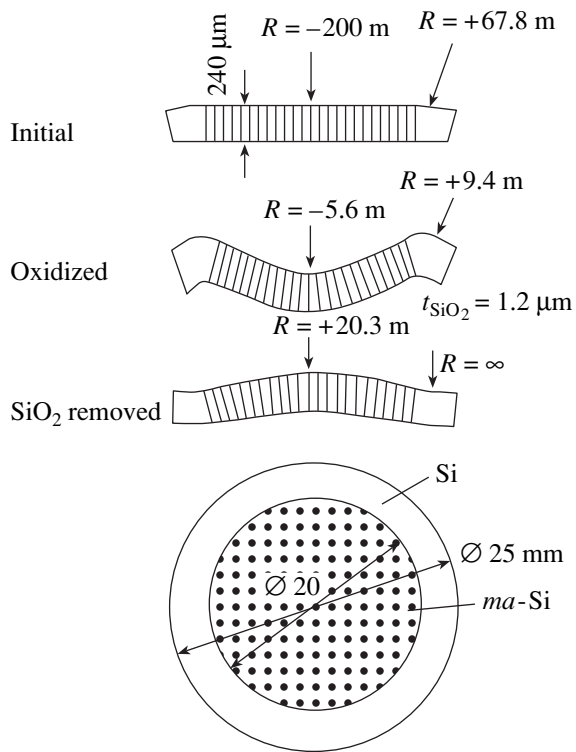


Fig. 2. Modification of the shape of sample 9H25 (through channels, no seed-pit layer) after the oxidation and oxide removal.

removal, with sample OF23 as an example. The initial curvature is restored after the first oxide removal. Even excess unbending is possible with the inversion of the bending sign (see also Fig. 2). The second oxidation bends the samples again, and for the majority of cases it is stronger than the first oxidation. The second oxide removal again unbends the samples, but to a smaller extent than the first. To reveal the relative contributions

of oxide located on the flat surfaces of a sample and on the walls of channels, we carried out a successive removal of oxide from sample OF23: from the back side of the wafer by etching in HF, from the front face by mechanical polishing, and from the channels by immersion in HF. The oxide removal from the back side resulted in only a small increase of the curvature from $R = +0.880$ to $R = +0.805$ m, and further oxide removal from the front face reduced the curvature to $R = +0.845$ m. Only the removal of oxide from the channels significantly reduced the sample curvature (to $R = +37.5$ m), though it did not restore the initial value. It was noticed that in many cases the homogeneity of the sample bending (its sphericity) was violated after twofold oxidation and oxide removal.

After the third oxidation, all samples were even more strongly bent and the oxide removal was followed by stronger residual deformation; thus, we find an oscillatory behavior of the bending radius under the repeated oxidation–(oxide removal) procedure. This trend is stronger for the samples with through channels, e.g., OA27, where the ratio of the bending radii before and after the oxide removal decreases from 7.7 in the first cycle to 1.6 in the third.

Table 3 presents vertical and lateral strains ϵ_z and ϵ_x and the corresponding absolute values of the lattice parameter. The data characterize a (6–10)- μm -thick surface layer on the front face and back side of the wafers after the third oxidation. In both samples, a strong difference is observed between the data for opposite sides, as well as substantially different behavior of deformation. On the convex front face of sample OF-23 with dead-end channels, the normal strain ϵ_z is negative, while the lateral ϵ_x is positive, so that $|\epsilon_z/\epsilon_x| = 0.83$. On the back side (the Si-substrate), the behavior of both components is inverted and $|\epsilon_z/\epsilon_x| = 0.38$. The strains are similar in magnitude (slightly over 1×10^{-4})

Table 2. Radius of curvature R of *ma*-Si wafers subjected to several cycles of oxidation and oxide removal

Sample no	Structure type	Photomask pattern	R , m						
			initial	first oxidation	removal of the first oxide	second oxidation	removal of the second oxide	third oxidation	removal of the third oxide
OA27	1	AT-3	-9.5	-2.7	-20.8	-2.7	-12.2	-1.7	-2.8
006	1	AT-3	-30.8	-1.4	-30.3	-0.72	-19.5		
OA28B	1K	AT-3	-291	-0.77	-14.3	-0.96	-10		
9N25	1K	AT-2	-200	-5.6	+20.3				
9N14	2aK	AT-2						+1.8 (sixth oxidation)	
OF23*	2b	AT-3	∞	+0.97	-330	+0.88	+37.5	+0.65	+29.7
OA26*	3K	AT-3	-240	+0.81	+71.7	+0.69	+30.3		

* Pore depth is 150 μm .

but have opposite signs. The unit cell is extended along the convex and compressed along the concave surface; the zero-strain line $\epsilon_z = \epsilon_x = 0$ lies within the crystal. For sample OA-27 with through channels, the measured strains and variations of the lattice constant are significantly higher. In this case, they have the same sign at both surfaces and, since $|\epsilon_z(\text{face})| < |\epsilon_z(\text{back})|$ and $|\epsilon_x(\text{face})| < |\epsilon_x(\text{back})|$, the zero-strain line is outside the crystal (above its front surface). For both samples, oxide removal resulted in nearly total elimination of strains on both sides and the lattice constant returned to values close to those in the initial crystal.

3.2. Dislocations

In sample OA26 with a pore-free edge, seed pits and 150- μm -deep channels, X-ray topograms recorded before the oxidation did not reveal new structure defects, as compared with the initial pore-free silicon. After the oxidation and subsequent oxide removal, the topograms showed that dislocations had been created. A beveled edge was made on the sample, and it was studied again. The generation of dislocations was especially intensive in the edge region (Fig. 5a). Some portion of the dislocations penetrated from the edge into the *ma*-Si region. In the edge region, these were mainly straight-line dislocations parallel to $\langle 110 \rangle$ direction, which were generated at the interface with the *ma*-Si region and on the bands of concentration inhomogeneities in the edge related to the crystal growth; their shape differed strongly from the mainly curvilinear and short or loop dislocations in the porous region. All the topograms obtained from the *ma*-Si region in the transmission or reflection configuration clearly demonstrate a fall in the number of dislocations near the regions where the wedge goes beyond the region of channels (Figs. 5b and 5c). However, the rising of the dislocation density with an increase in the thickness of the porous region was observed only near the edge of the wedge, which indicates that the majority of dislocations are concentrated in some surface layer. Since the place where the wedge goes beyond the region of channels is

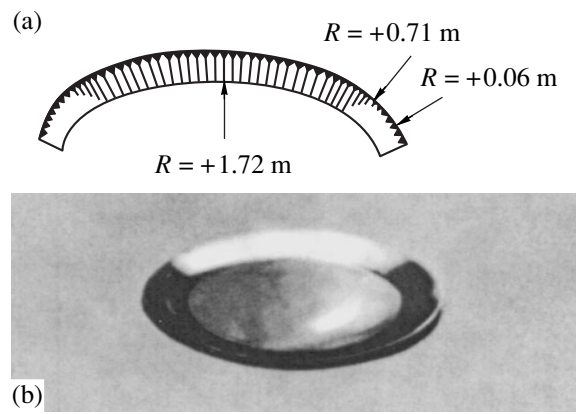


Fig. 3. Sample 9N14 (through channels, with seed-pit layer) after 6-fold oxidation: (a) schematic view; (b) photograph (front face down).

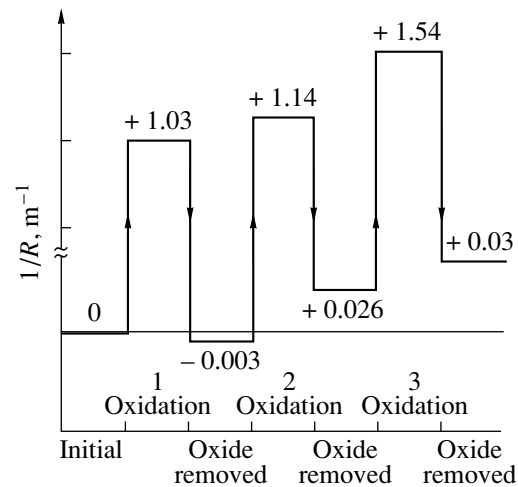


Fig. 4. Curvature of sample OF23 at different stages of 3-fold oxidation and oxide removal. The values of R^{-1} , m^{-1} , are indicated at horizontal sections.

clearly seen at the sample as the boundary between the dull (porous) and bright (pore-free) areas, the difference in widths of the pore-free region on the sample and

Table 3. Strain and lattice parameters of *ma*-Si samples after the third oxidation

			OF23		OA27	
			<i>z</i> normal	<i>x</i> lateral	<i>z</i> normal	<i>x</i> lateral
Front side	Oxidized	ϵ , 10^{-4}	-1.0	+1.2	-3.5	+1.0
		<i>a</i> (Å)	5.4305	5.4318	5.4291	5.4317
	Oxide removed	ϵ , 10^{-4}	+0.1	+0.1	-0.2	0
		<i>a</i> (Å)	5.4312	5.4312	5.4310	5.4311
Rear side	Oxidized	ϵ , 10^{-4}	+0.5	-1.3	-7.3	+14.4
		<i>a</i> (Å)	5.4314	5.4303	5.4269	5.4397
	Oxide removed	ϵ , 10^{-4}	-0.1	0	+0.1	+0.1
		<i>a</i> (Å)	5.4310	5.4311	5.4312	5.4312

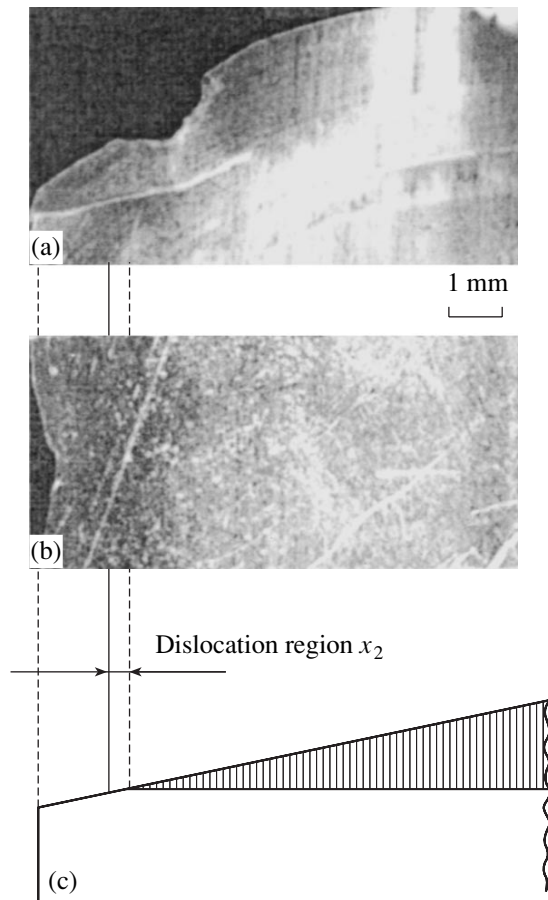


Fig. 5. Fragments of an X-ray topogram obtained by the Lang method from sample OA26 after repeated oxidation, oxide removal, and preparation of a beveled edge ($\text{MoK}\alpha$ radiation, reflection (220)): (a) edge region, (b) region of microchannels, (c) schematic of the sample.

the dislocation-free region on the topograms allowed us to estimate the depth of penetration of dislocations into the substrate. According to these estimates, the majority of dislocations penetrates only for $x_2 = 10 \mu\text{m}$ downward from the internal front of channels, though single dislo-

cations reach the back surface of the sample. This result is confirmed by sectional reflection topograms obtained from the back side of the sample. The length of dislocation penetration upwards from the front of channels, x_1 , could be estimated from sectional topograms obtained from the front face of the sample (Fig. 6). It appeared to be $\sim 60 \mu\text{m}$. The density of dislocations in the layer of thickness $t = x_1 + x_2 \approx 70 \mu\text{m}$ can be estimated as $\sim 10^4 \text{ cm}^{-2}$. As stated above, the dislocations appear in the form of loops or short curvilinear segments.

4. DISCUSSION

The specific volume per one Si atom increases by a factor of 2.27 during thermal oxidation. On a planar surface, this excess volume is accommodated by free expansion in the normal direction. The accommodation can be hindered during the oxidation of relief surfaces; strong compressive stresses arise in the growing oxide, and their relaxation occurs via the viscous flow of oxide or the deformation of silicon under the oxide. Second, and most important, the source of stresses in the Si-SiO₂ system is the strong difference between their thermal expansion coefficients: $\alpha_{\text{Si}} = 3.1 \times 10^{-6} \text{ K}^{-1}$ and $\alpha_{\text{SiO}_2} = 5 \times 10^{-7} \text{ K}^{-1}$ for silicon and oxide, respectively. This gives rise to stresses $\sim 0.3 \text{ GPa}$ in oxide of about $1 \mu\text{m}$ thickness on a flat surface [19]. Stresses in silicon substrate are significantly weaker, and they strongly depend on its thickness.

As known, micro- and nanoporous silicon is characterized by its extremely developed surface, which defines its high chemical activity. The specific surface area of 1 cm^3 of microporous Si is $S = 200\text{--}600 \text{ m}^2$ [20] with a typical porosity $p = 60\text{--}90\%$. *ma*-Si has low porosity (several percent) and a significantly smaller specific surface area S proportional to the diameter of cylindrical macropores. For *ma*-Si with an AT-2 "lattice," $S = 41.7d$ [cm^2], where d is the diameter of channels in μm ; for AT-3, $S = 249d$. For a typical pore diameter $d = 3 \mu\text{m}$ in the initial (unoxidized) *ma*-Si, this yields, respectively, $S = 125$ and 747 cm^2 . In this case,

Table 4. *ma*-Si parameters and their variation in the process of oxidation and oxide removal. Samples with the AT-2* pattern of seed pits, sample thickness $180 \mu\text{m}$

Oxidation no	Pore diameter prior to oxidation $d_0, \mu\text{m}$	Oxide thickness $t_{\text{SiO}_2}, \mu\text{m}$	Pore diameter after oxidation $d_1, \mu\text{m}$	Porosity prior to oxidation $p_0, \%$	Porosity after oxidation $p_1, \%$	Specific surface area S_0, cm^2	Wafer deflection $\Delta t, \mu\text{m}$		Radius of curvature R, m	
							sample type and no			
							1K	2K	1K	2K
							OYa2	OYa29	OYa21	OYa29
1	3.00	1.2	1.66	0.94	0.275	125	-8	+42	-9.75	+1.86
2	4.06	1.2	2.72	1.72	0.74	169	-120	+248	-0.65	+0.315
3	5.12	1.2	3.78	2.74	1.43	213	-177	+275	-0.44	+0.284
4	6.18	1.2	4.84	3.99	2.34	258	-270	-	-0.29	-

* Average specific porosity in the seed layer $S_p = 243 \text{ cm}^2$, maximal $S_{pm} = 400 \text{ cm}^2$.

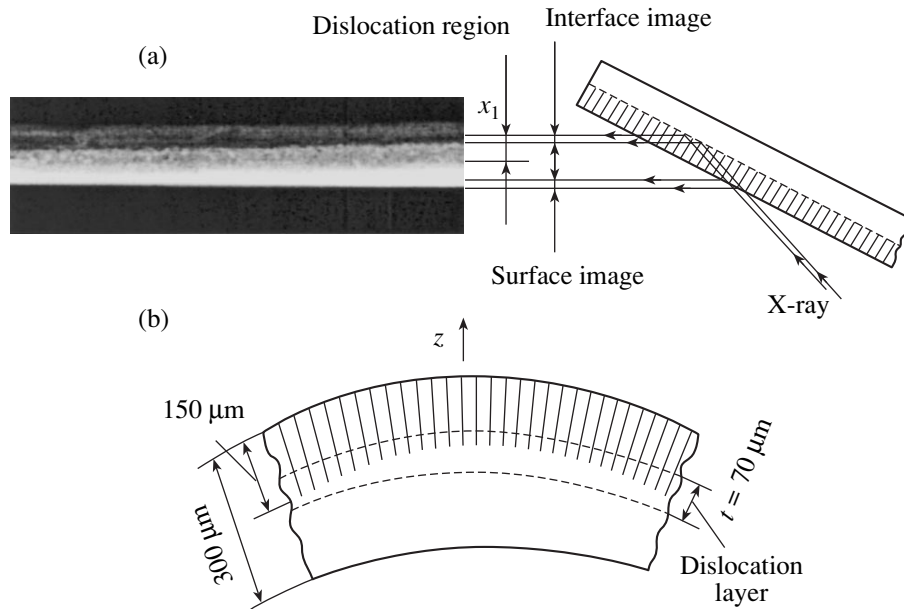


Fig. 6. Dislocations in a *ma*-Si structure with dead-end channels: (a) cross-sectional X-ray topogram of sample OA26 and the experimental configuration (Bragg configuration, $\text{MoK}\alpha$ radiation, reflection (400) from the front face of the sample); (b) localization of dislocations across the sample thickness.

the porosity is 0.94% for the AT-2 pattern and 5.6% for the AT-3.

A comparison of the curvature of similar structures fabricated with an AT-2 or AT-3 pattern shows that the samples with a higher porosity and specific surface area undergo stronger deformation under oxidation. The observed increasing of strain during subsequent oxidations is attributed to an increase of the pore diameter after the oxide is removed, with the relevant increase of p and S . It is of interest to analyze which factor, porosity or specific surface area, is the decisive one. To do this, we monitor the variation in the channel diameter, porosity, internal area of channels, and the curvature of samples with through channels; these parameters are presented in Table 4. Owing to an increase in volume at the Si to SiO_2 transition, the channel diameter decreases after oxidation; it becomes $d_1 = d_0 - 1.12t_{\text{SiO}_2}$, where t_{SiO_2} is the oxide thickness (see Fig. 7a). The dissolution of the oxide results in the channel diameter rising to $d_2 = d_0 + 0.88t_{\text{SiO}_2}$, which means an increase in the porosity and specific surface area of *ma*-Si. Here, the subscript “0” corresponds to the porosity p_0 and specific surface area S_0 prior to the next oxidation; “1” (p_1 and S_1), to oxidized *ma*-Si; and “2,” to the values after the oxide removal (p_2 and S_2). Therefore, in each new oxidation cycle we deal with material with a higher p and S . We plotted the dependence of the sample curvature R^{-1} on the channel diameter for the single-layer (type 1K) sample OYa21 and found that the experimental points fall on a straight line (Fig. 8), which indicates a linear dependence between the curvature and specific

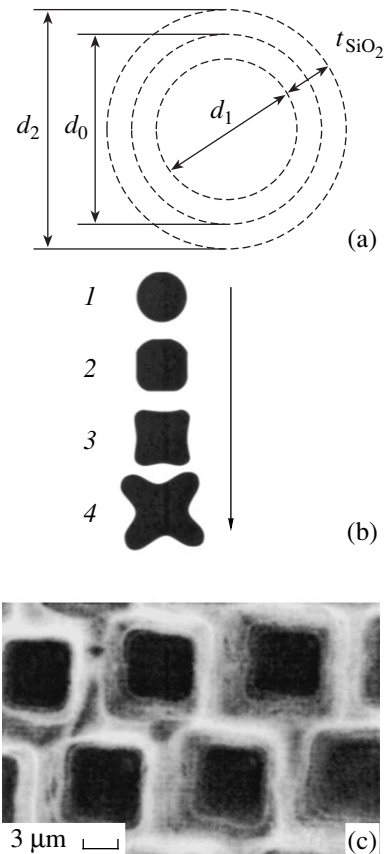


Fig. 7. Cross-section of channels in *ma*-Si: (a) channel diameter before oxidation d_0 , after oxidation d_1 , and after the oxide removal d_2 ; (b) modification of the shape of a cross section along the channel depth; (c) SEM image of through channels on the back side of the wafer.

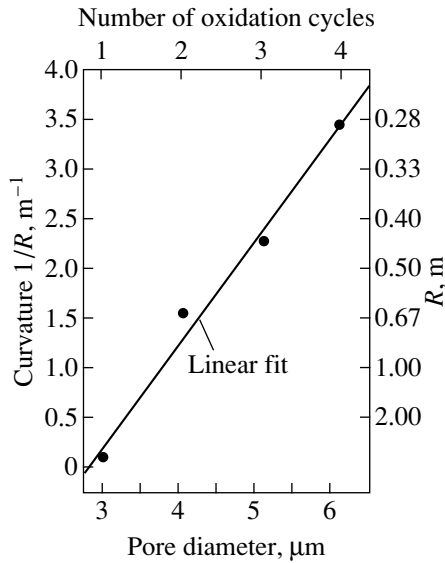


Fig. 8. Curvature of oxidized *ma*-Si vs. the diameter of channels. Sample OYa21, through pores, no seed pits. The number of oxidation cycles is given along the upper horizontal axis.

surface area of *ma*-Si, because it is precisely the latter quantity that is proportional to the pore diameter, while the porosity is proportional to its square. A comparison with the data for a similar sample, but with seed pits (OYa29, type 2aK), shows that the presence of seed pits raises the curvature and reverses the sign of bending (convex sample). Indeed, calculations show that the layer of seed pits is characterized by a significantly higher surface area than for *ma*-Si (see Table 4, note).

The oxide layer and the adjacent silicon are bound together but strained to different extents. Consequently, there arises a so-called constrained deformation [21]; as a result, there are compressive stresses in the SiO_2 layer at the flat surface and tensile stresses in Si [19]. For homogeneous layers with sharp boundaries, the problem can be resolved in terms of a biaxial stress field. In this model, the stresses vary only across the wafer thickness, $\sigma_x(z) = \sigma_y(z)$ and $\sigma_z = 0$. The distribution problem for local stress fields under the oxidation of relief Si surfaces is much more complicated. Recently, the stresses arising under oxidation of complex surfaces have been analyzed in several studies [13, 22–24]. In our case, the superposition of stress and strain microfields forms a macrofield, which is presumably quasi-homogeneous and flat and extends over the whole wafer. The interpretation of our results is based on the model that assumes that a *ma*-Si wafer consists of layers parallel to the surface, but which differ in their specific surface areas S . This model can be applied to the samples without a pore-free edge. For example, the layer of seed pits with the highest S contains a higher volume fraction of oxide; i.e., the effective value of the temperature expansion coefficient α and the elastic constants of this medium differ from those of Si. The

quantitative estimations are problematic; however, it is evident that the difference between these parameters and the parameters of Si increases as S rises. According to our interpretation, the layers with a more developed surface are stretched after the oxidation, while the attached layers with smaller S are compressed. The layers with high S are the *ma*-Si layer on the Si substrate or the layer of seed pits on *ma*-Si in the wafers with through channels. Dead-end channels with seed pits can be regarded as a three-layer system, where S in every underlying layer is lower than in the upper one. These structures behave similarly: they become convex after oxidation.

The simplest estimations of stresses can be made for two-layer systems. For type 2a samples with through channels and a relatively thin layer of seed pits, we use the Stoney relation [25] and the elastic constants of Si [13] to find the stresses in the seed pit layer:

$$\sigma_p = -(E_{\text{Si}}^* t_{ma}^2) / 6R_2 t_p = -0.13 \text{ GPa}, \quad (1)$$

where $E_{\text{Si}}^* = 200 \text{ GPa}$ is the conditional biaxial modulus of elasticity of Si, $t_{ma} = 200 \mu\text{m}$ is the thickness of the underlying layer *ma*-Si, $R_2 = 0.86 \text{ m}$ is the radius of the sample curvature, and $t_p = 5.4 \mu\text{m}$ is the thickness of the seed-pit layer. For type 2b two-layer structures (dead-end channels without seed pits), where the thickness t_{ma} of *ma*-Si is comparable to that of the silicon substrate t_{Si} , using the relation for a bicrystal [21] and assuming that the elastic constants of the layers are equal to those of silicon, we can find the difference between the strains in *ma*-Si and Si:

$$\varepsilon_{\text{Si}} - \varepsilon_{ma} = (t_{\text{Si}}^3 + t_{ma}^3) / 6R_2 t_{\text{Si}} t_{ma} = 5 \times 10^{-5}, \quad (2)$$

where the experimental values of $t_{ma} = t_{\text{Si}} = 150 \mu\text{m}$ and $R_2 = +0.97 \text{ m}$ were used. $\varepsilon_{\text{Si}} = \alpha_{\text{Si}} \Delta T = 3.72 \times 10^{-3}$. Then, the strain of the whole wafer is

$$\varepsilon_p = (t_{\text{Si}} \varepsilon_{\text{Si}} + t_{ma} \varepsilon_{ma}) / (t_{\text{Si}} + t_{ma}) = 3.7 \times 10^{-3}. \quad (3)$$

Taking into account that the strain varies linearly along the vertical axis z , the stresses at the top and bottom surfaces, with + and – signs, respectively, are

$$\sigma = \pm E_{\text{Si}}^* [\varepsilon_p + (t_{\text{Si}} + t_{ma}) / 2R_2] = \pm 0.77 \text{ GPa}. \quad (4)$$

The obtained values of σ are certain average characteristics of the layer, while the local microstresses in Si surrounding the channels can be even higher.

The suggested model does not explain why single-layer structures (through channels, no seed pits) become concave after oxidation, though the front face and back surface seem to be equipotent. The observed bending might correspond to S increasing from the front face to the back side. Scanning electron microscopy of the beveled edge shows that in many cases the

shape of cross sections of channels changes with depth (Fig. 7b). The cross section is round in the upper part, then it becomes square, and further it can be even cruciform, thus enlarging the specific area in the direction from the front face to the back side of a sample. The shape of the cross section depends on the etching mode, and in the majority of cases it is a square (Fig. 7c), but this is enough to produce asymmetry between the front face and back side.

An additional factor affecting the bending of samples that are inhomogeneous over their area (with a pore-free edge) is the density gradient arising at the border between the porous region and the pore-free edge. Its influence is observed even in the initial samples (bending in the edge region). In single-layer structures with a pore-free edge (type 1K), we deal with a membrane subjected to lateral compression after oxidation. The radial force is produced by the contraction of the pore-free edge during cooling. This position of the membrane is unstable (bifurcational), and even a small initial deviation from planarity is enough to initiate bending in one direction or another after oxidation.

The study of the lattice parameter of sample OF23 after the third oxidation and subsequent oxide removal shows higher strain in silicon near the front face than at the back side. This means that the zero-deformation line is closer to the sample backside and the strain $\epsilon_x > 0$ immediately under the front of the microchannels. This can be related to possible hydrostatic stresses which appear along with biaxial stresses in the near-bottom *ma*-Si layer, which has a more complicated microchannel-wall structure, where the viscous-flow accommodation of oxide is incomplete. Some kind of swelling of the near-bottom layer results in strong bending and deformations.

The stresses arising in the Si surrounding isolated rectangular and square trenches of various depths were studied in [26]. It was shown that the main contribution to stresses in the matrix is made by the regions adjacent to the bottom of the trenches and their outlet to the surface. The domain of strong shear stresses located in the near-bottom region is responsible for the possible generation of dislocations. This analysis offers a fair analogy with our samples; it correlates qualitatively with the observed deformation and the generation of dislocations in oxidized *ma*-Si in samples OF23 and OA26. Since the zero-deformation line in these samples lies slightly below the internal front of channels, the dislocations propagate not only to the front face of the samples, but also some distance in Si under *ma*-Si, which was observed by X-ray topography.

5. CONCLUSION

The present study confirms our earlier conclusions on the high structural perfection of unoxidized *ma*-Si samples. They are virtually flat (only the edge is bent), and their diffraction properties are close to those of a

perfect single-crystal, which means that electrochemical etching does not produce new defects in Si.

After thermal oxidation, the samples are strongly bent. In the porous region of a sample, the bending is spherical, but not always elastic, especially for repeated oxidations. The sample bending is mainly induced by the difference between the thermal expansion coefficients of Si and oxide, and it is defined by the configuration of a *ma*-Si structure (its specific surface area, the presence and width of the pore-free edge). The oxidation of the channel walls plays the decisive role in wafer bending. The sample curvature depends linearly on the specific surface area of *ma*-Si, and its sign is determined by the variation of the specific area of layers across the structure thickness. It means, in fact, that all the samples with dead-end channels and those with an unremoved layer of seed pits become convex after oxidation. Only *ma*-Si samples with through channels and without seed pits become concave. The presence of an inhomogeneity in the sample area, for example, a pore-free edge, can induce local modulations of curvature up to the inversion of its sign.

The stresses relax after the oxide layer is removed, and the samples return, partially or completely, to their initial state. Partial relaxation of stresses proceeds via plastic deformation with the generation of dislocations. Dislocations appear preferentially near the internal front of channels and near the border of the pore-free edge. They are concentrated near the bottom of pores and distributed in a layer several tens of micrometers thick. Dislocations are produced in the process of relaxation of local stresses in the near-bottom region of channels in *ma*-Si and at its border with the pore-free edge under the effect of macrostresses, which arise from sample bending during oxidation. Their further propagation is determined by the distribution of these stresses.

Under repeated operations of oxidation and oxide removal, the curvature increases in each subsequent cycle and residual deformation after oxide dissolution increases.

ACKNOWLEDGMENTS

We are grateful to A.G. Tkatchenko, L.S. Graniysyna, A.V. Nashchekin, and V.A. Tolmachev for assistance in sample preparation, electron-microscopic studies, and sample photographing.

This study was supported by the program of the Ministry of Industry, Science, and Technology "Physics of Nanostructures" (project no. 8) and by the Russian Foundation for Basic Research (project nos. 00-02-16760 and 00-15-96770).

REFERENCES

1. V. Lehmann and H. Foll, J. Electrochem. Soc. **137**, 653 (1990).

2. V. Lehmann, W. Honlein, H. Reisinger, *et al.*, *Thin Solid Films* **276**, 138 (1996).
3. E. V. Astrova, V. B. Voronkov, I. V. Grekhov, *et al.*, *Phys. Status Solidi A* **182**, 145 (2000).
4. V. Lehman, R. Stengl, H. Reisinger, *et al.*, *Appl. Phys. Lett.* **78**, 589 (2001).
5. V. V. Aristov, L. G. Shabel'nikov, V. V. Starkov, *et al.*, *Mikrosist. Tekh.*, No. 8, 39 (2001).
6. C. P. Beetz, R. Boerstler, J. Steinbeck, *et al.*, *Nucl. Instrum. Methods Phys. Res. A* **422**, 443 (2000).
7. P. Kleimann, J. Linnros, and S. Peterson, *Mater. Sci. Eng. B* **69–70**, 29 (2000).
8. F. Muller, A. Birner, J. Schilling, *et al.*, in *Proceedings of the 2nd International Conference "Porous Semiconductors – Science and Technology," Madrid, 2000*, O-56.
9. U. Gruning and V. Lehmann, *Appl. Phys. Lett.* **68**, 747 (1996).
10. A. Birner, A.-P. Li, F. Muller, *et al.*, *Mater. Sci. Semicond. Process.* **3**, 487 (2000).
11. M. A. Green, J. Zhao, A. Wang, *et al.*, *Nature* **412**, 805 (2001).
12. Wai Lek Ng, M. A. Lourenco, R. M. Gwilliam, *et al.*, *Nature* **410**, 192 (2001).
13. S. M. Hu, *J. Appl. Phys.* **70**, R53 (1991).
14. E. V. Astrova, A. D. Remenyuk, A. G. Tkachenko, and I. L. Shul'pina, *Pis'ma Zh. Tekh. Fiz.* **26** (24), 31 (2000) [*Tech. Phys. Lett.* **26**, 1087 (2000)].
15. E. V. Astrova, V. V. Ratnikov, A. D. Remenyuk, *et al.*, *Pis'ma Zh. Tekh. Fiz.* **27** (2), 1 (2001) [*Tech. Phys. Lett.* **27**, 41 (2001)].
16. G. A. Rozgonyi and C. A. Miller, *Thin Solid Films* **31**, 185 (1976).
17. R. N. Kyutt and T. S. Argunova, *Nuovo Cimento D* **19**, 267 (1997).
18. I. L. Shul'pina, *Kristallografiya* **37**, 451 (1992) [*Sov. Phys. Crystallogr.* **37**, 234 (1992)].
19. J. R. J. Jaccodine and W. A. Schlegel, *J. Appl. Phys.* **37**, 2429 (1966).
20. A. Halimaoui, in *Proceedings of the Winter School "Porous Silicon Science and Technology," Les Houches, France, 1994*, Ed. by J.-C. Vial and J. Derrien (Springer-Verlag, Berlin, 1995), p. 34.
21. N. P. Zakharov and A. V. Bagdasaryan, *Mechanical Phenomena in Integrated Structures* (Radio i Svyaz', Moscow, 1992).
22. K. Barla, A. Herino, and G. Bomshil, *J. Appl. Phys.* **59**, 439 (1986).
23. C. S. Rafferty and R. W. Dutton, *Appl. Phys. Lett.* **54**, 1815 (1989).
24. H. Hsueh and A. G. Evans, *J. Appl. Phys.* **54**, 6672 (1983).
25. G. S. Stoney, *Proc. R. Soc. London, Ser. A* **82**, 172 (1925).
26. S. M. Hu, *J. Appl. Phys.* **67**, 1092 (1990).

Translated by D. Mashovets

AMORPHOUS, VITREOUS, AND POROUS SEMICONDUCTORS

Hysteresis of the Photonic Band Gap in VO₂ Photonic Crystal in the Semiconductor–Metal Phase Transition

V. G. Golubev*, D. A. Kurdyukov*, A. B. Pevtsov*, A. V. Sel'kin*,
E. B. Shadrin*, A. V. Il'inskiĭ**, and R. Boeyink***

* *Ioffe Physicotechnical Institute, Russian Academy of Sciences, St. Petersburg, 194021 Russia*

e-mail: pevtsov@gvg.ioffe.rssi.ru

** *BUAP, Puebla, 72000 Pue, Mexico*

*** *Department of Physics and Astronomy, University of Utrecht, 3584 CC Utrecht, The Netherlands*

Submitted March 11, 2002; accepted for publication March 13, 2002

Abstract—VO₂ photonic crystals exhibiting a semiconductor–metal phase transition at 55–75°C have been synthesized by the infiltration of vanadium dioxide (VO₂) into opal crystals and the subsequent removal of SiO₂ by etching. A study of the optical reflection spectra of such crystals demonstrated that they are characterized by a wide photonic band gap (in the [111] direction of light propagation) in the visible spectral range. The energy position of this band gap changes abruptly upon a phase transition. The temperature shift and hysteresis of the position of the photonic band gap were measured. Quantitative calculations of the reflection spectra of photonic crystals of opal and VO₂ were performed in terms of the model of a layered periodic medium, and numerical values of the geometric parameters and optical constants of the studied three-dimensional periodic structures were obtained. © 2002 MAIK “Nauka/Interperiodica”.

1. INTRODUCTION

Vanadium dioxide (VO₂) is a material that possesses a wide variety of physical properties and, therefore, is of particular interest to researchers. It should be noted, in the first place, that VO₂ undergoes a semiconductor–metal phase transition of the first order at a temperature $T_c = 67^\circ\text{C}$ [1, 2]. Above T_c , this material is a metal with tetragonal lattice symmetry, and below T_c , a semiconductor with monoclinic symmetry [2]. The phase transition in VO₂ is accompanied by a significant change in its electrical and optical properties [2, 3], namely, the conductivity and optical constants. An important feature of VO₂ is that ultrashort times of the semiconductor–metal phase transition, on the order of hundreds of femtoseconds, can be achieved [4]. All this makes vanadium dioxide a promising material for solving various applied problems: creating IR optical modulators based on VO₂, light beam intensity limiters, and reversible media for recording optical information and holograms, in particular.

The present study is concerned with new specific features of the phase transition in vanadium dioxide, which manifest themselves in the optical properties of a photonic crystal synthesized on the basis of VO₂. The basic property of a photonic crystal, which is a three-dimensional (3D) periodic structure, is the existence of a photonic band gap (PBG), which contains a spectral region where the propagation of an electromagnetic wave is impossible for some (or all) wave vector directions [5, 6]. The use of VO₂ as a material for designing photonic crystals opens up the possibility of controlling

the PBG parameters by means of the semiconductor–metal phase transition [7].

2. EXPERIMENTAL

Samples of VO₂ photonic crystals were synthesized using artificial opals with a face-centered cubic lattice formed by close-packed monodisperse spheres of amorphous SiO₂ as the template. About 26% of the total volume of the opal template is accounted for by interconnected voids that are accessible to filling by other substances. The average sphere diameter was 230 ± 5 nm. The opals had a polydomain structure, the size of a single domain with a high degree of ordering of SiO₂ spheres varying within 30–100 μm . The photonic crystal was formed on the basis of VO₂ by two stages. In the first stage, voids of the opal template were preliminarily filled with a solution of vanadium pentoxide in nitric acid and then V₂O₅ was reduced to VO₂ through the high-temperature annealing of a sample in a vacuum. In the second stage, the composite was subjected [8, 9] to inversion by etching out the skeleton of SiO₂ spheres with hydrofluoric acid.

Visually, separate domains of the inverted structure stand out against the surface of a sample as bright spots of red reflected light. A strongly magnified (~10- to 20-fold) image of such a domain was projected onto the entrance slit of a spectrometer. A diaphragm served to select separate parts of the domain for measurements. Specular-reflection spectra were recorded at an incidence angle

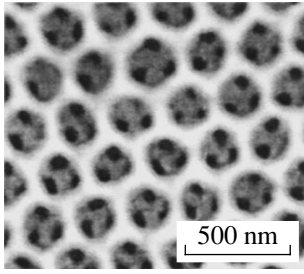


Fig. 1. SEM image of a vanadium dioxide photonic crystal with inverted opal structure.

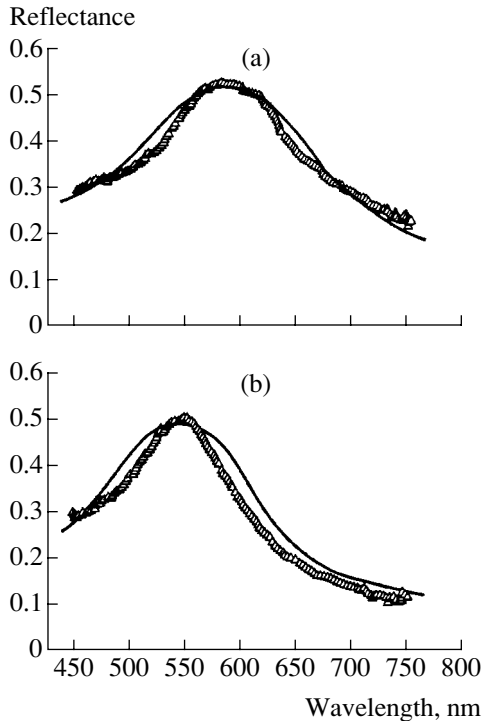


Fig. 2. Optical reflection spectra of vanadium dioxide photonic crystals with inverted opal structure at (a) 15 and (b) 87°C. Points, experiment; solid lines, theoretical calculation.

$\theta = 10^\circ$ in the lock-in mode on a computerized installation.

As shown by electron-microscopic studies, the thus-synthesized samples were entirely composed of vanadium dioxide and had the form of an inverted replica of the opal template, reproducing spatially its face-centered structure (Fig. 1). The difference between the inverted sample and the starting opal consists in that intersphere voids of the opal are filled with crystalline VO_2 and SiO_2 spheres are removed. The former places of the spheres are now occupied by air voids surrounded by a skeleton of crystalline vanadium dioxide. This skeleton has apertures at the places of contact between the SiO_2 spheres of the template, which are not filled with vanadium dioxide and serve to etch out SiO_2

in the course of inversion. The aforesaid is confirmed by an electron micrograph of the surface of a synthesized sample. The image shows a (111) section of the outer layer of spherical voids, with a lattice of white regions corresponding to the section of the VO_2 skeleton; the gray regions inside this lattice represent the whole set of lower half-spheres of the cut-off layer. Moreover, dark apertures are well seen in each half-sphere at the places of sintering between SiO_2 spheres in the opal template. These apertures connect the spherical voids.

Figure 2 shows experimental specular-reflection spectra for a domain of the VO_2 photonic crystal synthesized in this study; these spectra correspond to the semiconducting (Fig. 2a, $T = 15^\circ\text{C}$) and metallic (Fig. 2b, $T = 87^\circ\text{C}$) phases of VO_2 . The observed broad bands of strong reflection of light, which result from the Bragg diffraction of an electromagnetic wave on a spatially periodic structure, indicate that the PBG exists for photonic states in the [111] direction of light propagation. It can be seen that the reflection peak, corresponding to PBG, is shifted by 38 nm upon the semiconductor–metal phase transition to shorter wavelengths, becoming narrower and losing its intensity.

Such behavior of the reflection spectrum is in qualitative agreement with how the dielectric constant ϵ_{VO_2} of vanadium dioxide changes in the phase transition of this material from the semiconducting to the metallic state. It is known that the real part ϵ'_{VO_2} of the complex dielectric constant of VO_2 takes a smaller value, with both the averaged real dielectric constant $\langle\epsilon\rangle$ of the periodic structure under consideration and its dielectric contrast decreasing (see below). As a result, the Bragg reflection peak shifts to shorter wavelengths and the reflection band becomes narrower [7].

Spectra of this kind were also measured for an opal– VO_2 composite [7] and an inverted composite filled with glycerol (the glycerol filling the spherical voids has a refractive index $n = 1.47$, which is close to that of the opal spheres). Taking into account the fact that glycerol is a surface-active compound that strongly depresses the temperature of the phase transition in vanadium dioxide [10], we intended to use this compound as a tool for controlling the switching temperature of the photonic crystal. As expected, the filling of voids in the inverted composite returns the diffraction reflection peaks to 639 nm (VO_2 in the semiconducting state) and 598 nm (VO_2 in the metallic state), which virtually coincides with their positions [7] in the initial opal– VO_2 composite.

Figure 3 presents temperature hysteresis loops of the peak position in the reflection spectra of an opal– VO_2 photonic composite (Fig. 3a), an inverted composite (VO_2 photonic crystal, Fig. 3b), and an inverted composite whose spherical voids are filled with glycerol (Fig. 3c). Figure 4 shows temperature hysteresis

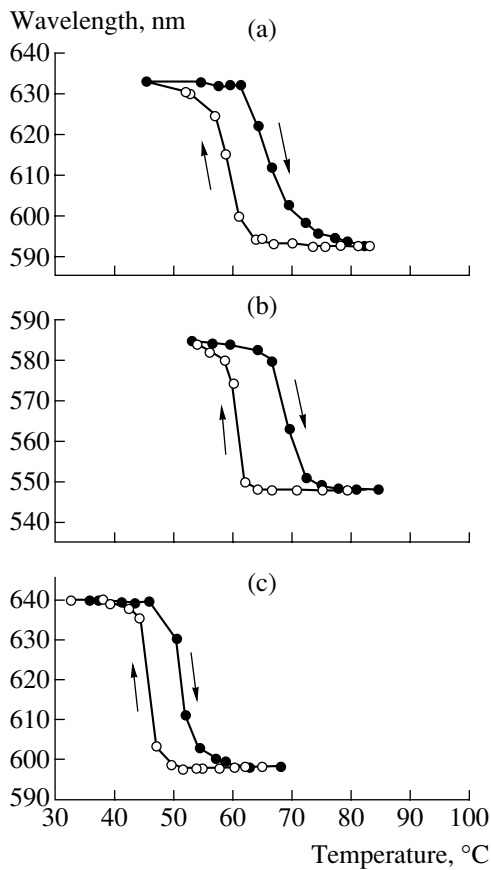


Fig. 3. Hysteresis of the temperature dependence of the peak positions in reflection spectra of photonic-crystalline structures based on vanadium dioxide: (a) opal-VO₂ composite, (b) VO₂ photonic crystal (inverted opal-VO₂ composite), and (c) VO₂ photonic crystal with spherical voids filled with glycerol. Full circles, hysteresis loop branches corresponding to sample heating; open circles, branches corresponding to cooling.

loops of the electrical conductivity of the opal-VO₂ composite (Fig. 4a) and VO₂ photonic crystal (Fig. 4b).

3. DISCUSSION

3.1. Reflection Spectra

The λ_m value can be roughly evaluated from the spectral position $\langle \epsilon \rangle$ of the peak in a reflection spectrum if we use the Bragg formula

$$\lambda_m = 2d_{111} \sqrt{\langle \epsilon \rangle - \sin^2 \theta},$$

where d_{111} is the spatial period of the structure along the [111] direction and θ is the angle of incidence of light onto the (111) plane of the outer boundary of the photonic crystal. On the other hand,

$$\langle \epsilon \rangle = (1 - f)\epsilon_a + f\epsilon_b,$$

where $f \approx 0.74$ is the spatial factor of structure filling with spheres, and ϵ_a and ϵ_b are, respectively, the dielectric constants of the intersphere space filled with VO₂

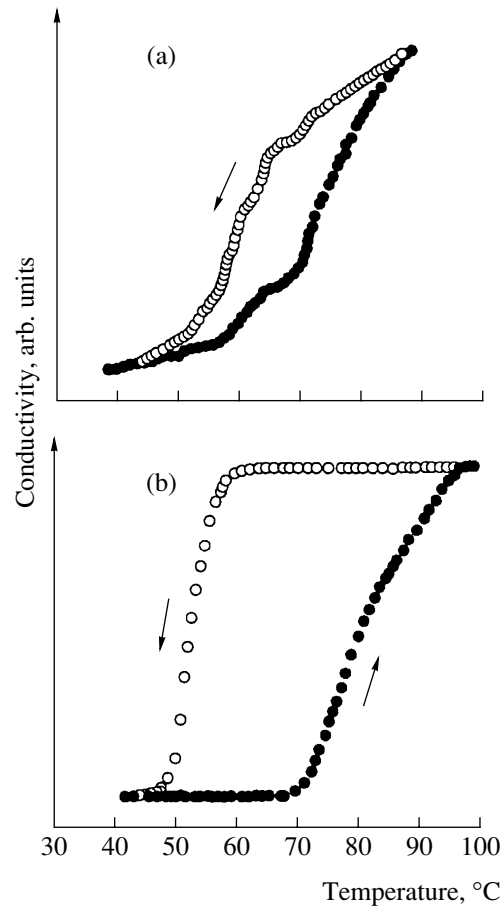


Fig. 4. Hysteresis of the temperature dependence of electrical conductivity for photonic-crystalline structures based on vanadium oxide: (a) opal-VO₂ composite and (b) VO₂ photonic crystal with inverted opal structure. Full circles, hysteresis loop branches corresponding to sample heating; open circles, branches corresponding to cooling.

and the sphere material (for the particular case of air, $\epsilon_b = 1$). Thus, having evaluated the $\langle \epsilon \rangle$ value by means of the Bragg formula, we can estimate ϵ_a and, consequently, ϵ_{VO_2} if VO₂ fills the intersphere voids with sufficient density.

Strictly speaking, estimates of this kind are sufficiently accurate only in the case of a weak dielectric contrast

$$q \equiv \left| \frac{\epsilon_a - \epsilon_b}{\epsilon_a + \epsilon_b} \right| \ll 1,$$

when the periodic component of the dielectric constant of the structure can be regarded as a minor perturbation. In the case under study, this weak-contrast condition is evidently not satisfied and some other approach to the problem of reflection of light from a photonic crystal is required, which should be based on a more complete analysis of the spectral profile of reflection.

In order to describe theoretically the spectra of specular reflection of light in the PGB range, we calculated

the spectra in terms of the model of a periodic layered medium by performing layer-by-layer averaging of the 3D-periodic dielectric constant of the medium, $\epsilon(x, y, z)$, in directions perpendicular to the z direction [111]. As a result of such averaging, the dielectric constant becomes a periodic function of only the single spatial coordinate z , i.e., $\epsilon = \epsilon(z) = \epsilon(z + d_{111})$. Quantitative calculations of the reflection spectra were carried out using the transmission matrix method by approximating $\epsilon(z)$ with a step function: within each period d_{111} , the dielectric medium was regarded as a multilayer medium comprising a system of N uniform dielectric layers of the same thickness. Calculations give a stable (virtually independent of N) result at $N > 50$. The number of periods was taken to be 100, which allowed us to regard the model system as semi-infinite along the z axis.

It should be noted that the procedure we used for the layer-by-layer averaging of $\epsilon(x, y, z)$ was actually done in terms of the scheme proposed in [11], with the only difference in that the refractive index $n(x, y, z)$ was used as the quantity being averaged, instead of $\epsilon(x, y, z)$, and the transmission spectra of opal were analyzed. Our calculation scheme also includes the effects of shrinkage (sintering of SiO₂ spheres) in the opal template, which is associated with the intersection of the spheres. Effects of this kind can be described quantitatively by introducing the shrinkage factor $\eta \equiv \Delta a/a$, where a is the lattice constant of the photonic crystal and Δa is its decrease through shrinkage. In calculating the reflection spectra, we used, as variable parameters of the theory, the sphere diameter D , the dielectric constants ϵ_a and ϵ_b , and also the shrinkage factor η . Moreover, we added an imaginary part $i\epsilon''$ to the total dielectric constant, and this effectively accounted for the effect of light scattering and absorption on the resulting spectra.

Figure 2 compares the calculated (solid lines) and experimental reflection spectra. It should be noted that the theoretical curves in Fig. 2 were constructed with actually only two parameters, ϵ_a and ϵ'' , used in the fitting. The ϵ_b value for the spherical voids was taken as unity. The numerical values of the remaining parameters, $D = 228$ nm and $\eta = 0.01$, were determined by analyzing the reflection spectra of the initial opal, which was used to obtain the inverted structure—VO₂ photonic crystal. The best agreement between theory and experiment is achieved at $\epsilon_a = \epsilon'_{\text{VO}_2} = 7.5$, $\epsilon'' = 0.48$ for the semiconducting phase (Fig. 2a) and $\epsilon_a = \epsilon'_{\text{VO}_2} = 6.1$, $\epsilon'' = 0.36$ for the metallic phase (Fig. 2b).

Indeed, according to the known patterns of the phase transition in VO₂ [2], the dielectric constant ϵ'_{VO_2} decreases in the vicinity of the point of the phase transition in VO₂ as the temperature of the synthesized photonic crystal increases. In this case, the calculated reflection band markedly shifts to shorter wavelengths and, simultaneously, becomes narrower, which is in

agreement with the experiment. As for the imaginary part of the dielectric constant, it takes a smaller value in the high-temperature phase. Such behavior of ϵ'' presumably reflects the fact that the decrease in ϵ_a leads to a smaller contribution to the extinction coefficient, associated with light scattering, in the high-temperature phase (because of the decrease in the dielectric contrast in the structure [12]). It is noteworthy that the theoretical spectra are somewhat broader when compared with the experimental spectra. It should also be noted that the reflection spectra of the VO₂ photonic crystal were analyzed, with the frequency dispersion of the optical constants ignored. However, such an approximation is not very precise for studying spectra in such a wide (the entire visible range) spectral interval. In addition, the fact that light rescattering, the statistical scatter of globule sizes, as well as irregularities in their spatial arrangement [13] were disregarded in calculation may lead to certain limitations on the interpretation of the experimental results in terms of the employed theoretical model.

3.2. Hysteresis of Optical and Electrical Properties

As already mentioned, the nature of the temperature hysteresis loops of the PGB position (Fig. 3) and electrical conductivity (Fig. 4) is determined by the hysteresis of the physical properties of vanadium dioxide in a phase transition from the semiconducting to the metallic phase (on sample heating) and back (on sample cooling). In this case, a new phase nucleates in the bulk of the old one and the nuclei can grow when the temperature deviates to a certain extent, ΔT , from the phase equilibrium temperature T_c . For a single crystal, $\Delta T \approx 2\text{--}3^\circ\text{C}$ and the narrow hysteresis loop has nearly vertical (relative to the temperature axis) “heating” and “cooling” branches.

For a polycrystalline VO₂ film, the hysteresis loop is much wider ($20\text{--}30^\circ\text{C}$) and has branches that are extended along the temperature axis [3]. This is due to the fact that the film is composed of a large number of grains (crystallites) exhibiting a wide scatter in both their size and defectiveness. This, in turn, leads to a significant scatter in both the width (because of the martensitic nature of the given phase transition) and position along the temperature axis of the hysteresis loops of each particular grain of the film (named elementary loops) [3]. The principal loop of the VO₂ film, obtained by summing up all the elementary loops, is wider, and its heating and cooling branches become more extended along the temperature axis.

Returning to the VO₂ photonic crystal, we note that the hysteresis loop obtained in this study for the PGB position in a domain (Fig. 3b) is much broader and has heating and cooling branches that are more extended along the temperature axis when compared with the narrow and virtually rectangular loop of the single crystal. At the same time, it is much narrower and its

branches are less extended along the temperature axis than those of loops obtained for polycrystalline VO₂ films. This means that, first, the dimensional effects (martensitic state) also occur in the inverted VO₂-opal composite (with the loop being wider than that in a single crystal) and, second, the synthesized vanadium dioxide photonic crystals show smaller variance in the crystallite size of vanadium dioxide as compared with polycrystalline films.

The temperature hysteresis loops of conductivity of the synthesized samples also indicate that crystalline vanadium dioxide is synthesized within the opal voids. In some of the samples studied, the loop corresponding to the noninverted opal-VO₂ composite (Fig. 4a) has step-like heating and cooling branches, which is due, in our opinion, to dimensional effects associated with the presence inside the initial opal of several kinds of voids with different, but fixed, sizes. VO₂ crystals in the voids undergo a phase transition at different, but fixed, temperatures, each related to its own type of void. The loop corresponding to the VO₂ photonic crystal (Fig. 4b) shows no steps.

A possible reason for the disappearance of steps is the high sensitivity of the well-developed surface of the VO₂ skeleton to surface-active compounds (hydrofluoric acid, oleic acid, glycerol, etc.). The action of these substances on VO₂ gives rise to donors with a wide distribution of concentrations, which causes a general depression and wider scatter in the phase equilibrium temperatures in structural units of the VO₂ skeleton. It is the occurrence of such a scatter that leads to the smearing of the step-like structure of the loop.

A clear indication of the influence exerted by the second factor is that the temperature hysteresis loop of the position of the Bragg reflection peak for the VO₂ photonic crystal (Fig. 3c) is markedly shifted (by 15°C) to lower temperatures when compared with the hysteresis loop for the VO₂-opal composite (Fig. 3a). This can be attributed (in accordance with our assumption) to the effect of the surface-active substance, namely, to the fact that glycerol, filling the spherical voids in the inverted crystal, injects hydrogen ions acting as donors into vanadium dioxide. The increase in the concentration of free electrons in the VO₂ crystal depresses the phase transition temperature [14], thus providing an additional tool for controlling the properties of the photonic crystal.

4. CONCLUSION

Thus, a photonic crystal in the form of a 3D-periodic inverted opal-like structure formed by crystalline vanadium dioxide has been synthesized and studied for the first time. The relatively high dielectric constant of VO₂ and its pronounced change in the semiconductor-metal

phase transition ensure the existence in the structure of a broad temperature-controlled photonic band gap in the visible spectral range. The possibility of the rapid phase transition under the action of external factors (according to our estimates, in times on the order of hundreds of femtoseconds) makes it possible to regard the material synthesized in this study as a basis for creating systems for the ultrafast control of light beams.

ACKNOWLEDGMENTS

We thank INTAS (grant no. 01-0642) for supporting this study, as well as the program of the Russian Academy of Sciences "Low-Dimensional Quantum Structures," and the program of the Ministry of Science "Physics of Solid-State Nanostructures."

REFERENCES

1. N. F. Mott, *Metal-Insulator Transitions* (Taylor & Francis, London, 1974; Nauka, Moscow, 1979).
2. A. A. Bugaev, B. P. Zakharchenya, and F. A. Chudnovskii, *Phase Transition Metal-Semiconductor and Its Application* (Nauka, Leningrad, 1979), p. 183.
3. E. B. Shadrin and A. V. Il'inskiĭ, *Fiz. Tverd. Tela* (St. Petersburg) **42**, 1092 (2000) [*Phys. Solid State* **42**, 1126 (2000)].
4. A. Cavalleri, Cs. Toth, C. W. Siders, *et al.*, *Phys. Rev. Lett.* **87**, 237401 (2001).
5. *Photonic Band Gap Materials*, Ed. by C. M. Soukoulis (Kluwer, Dordrecht, 1996), NATO ASI Ser., Ser. E, Vol. 315.
6. A. Birner, R. B. Wehrspohn, U. M. Gösele, and K. Busch, *Adv. Mater.* **13**, 377 (2001).
7. V. G. Golubev, V. Yu. Davydov, N. F. Kartenko, *et al.*, *Appl. Phys. Lett.* **79**, 2127 (2001).
8. Y. Xia, B. Gates, Y. Yin, and Y. Lu, *Adv. Mater.* **12**, 693 (2000).
9. V. G. Golubev, V. A. Kosobukin, D. A. Kurdyukov, *et al.*, *Fiz. Tekh. Poluprovodn.* (St. Petersburg) **35**, 710 (2001) [*Semiconductors* **35**, 680 (2001)].
10. W. Bruckner, H. Opperman, W. Reicheld, E. I. Terukov, F. A. Tschudnovskii, and E. Wolf, *Vanadium Oxide* (Akademie-Verlag, Berlin, 1983), p. 251.
11. Yu. A. Vlasov, M. A. Kaliteevskii, and V. V. Nikolaev, *Phys. Rev. B* **60**, 1555 (1999).
12. H. S. Sözüer, J. W. Haus, and R. Inguva, *Phys. Rev. B* **45**, 13962 (1992).
13. Yu. A. Vlasov, V. N. Astratov, A. V. Baryshev, *et al.*, *Phys. Rev. E* **61**, 5784 (2000).
14. E. I. Nikulin, F. A. Chudnovskii, E. B. Shadrin, and D. A. Myasnikov, *Zh. Tekh. Fiz.* **58** (12), 2411 (1988) [*Sov. Phys. Tech. Phys.* **33**, 1473 (1988)].

Translated by M. Tagirdzhanov

PHYSICS
OF SEMICONDUCTOR DEVICES

Photoelectric Phenomena in ZnO(ITO)/*a*-Si:H(*n*)/*c*-Si(*p*)/Al Solar Cells

Yu. A. Nikolaev*, V. Yu. Rud'**, Yu. V. Rud'*, E. I. Terukov*,
W. Fuhs***, and A. Froitzheim***

* *Ioffe Physicotechnical Institute, Russian Academy of Sciences,
Politekhnikeskaya ul. 26, St. Petersburg, 194021 Russia*

** *St. Petersburg State Technical University, Politekhnikeskaya ul. 29, St. Petersburg, 194021 Russia*

*** *Hahn–Meitner Institute, D-12489 Berlin, Germany*

Submitted February 18, 2002; accepted for publication February 19, 2002

Abstract—Solar cells Al/ZnO/*a*-Si:H(*n*)/*c*-Si(*p*)/Al and Al/ITO/*a*-Si:H(*n*)/*c*-Si(*p*)/Al were fabricated on single-crystal Si substrates. The photoelectric properties of these solar cells were investigated under exposure to natural and linearly polarized radiation at $T = 300$ K. The polarization photosensitivity of the solar cells, which emerges under the conditions of oblique incidence of linearly polarized radiation, was observed. The origin of the induced photopleochroism of solar cells with ZnO and ITO antireflection coatings is ascertained. The oscillations in the spectrum of the induced photopleochroism, which are associated with interference phenomena in oxide films, are observed. The results obtained point to the possibility of using the solar cells as selective photosensors. At the same time, polarization spectroscopy can ensure effective monitoring of the antireflection coatings of solar cells. © 2002 MAIK “Nauka/Interperiodica”.

1. INTRODUCTION

One of the major directions in the development of effective photoconverters for the optical spectral range is based on the investigation of structures which include a contact between various polymorphs of materials with the same atomic composition [1–5]. Such structures have already made it possible to attain a quantum efficiency of photoconversion in heterojunctions between amorphous and crystalline Si as high as 18%. Polarization photosensitivity was observed in these heterojunctions. It is obvious that, in reference to the most widespread heterojunctions between materials with various atomic compositions, there are no problems with possible interdiffusion through the interface for structures whose atomic composition is invariable over the coordinate. This study belongs to this field of research. It is devoted to the investigation of the photoelectric properties of solar cells, whose active region comprises the heterojunction between crystalline and amorphous Si.

2. EXPERIMENTAL

Solar cells investigated in this study were fabricated at the Hahn–Meitner Institute, and their design is shown in Fig. 1. In order to fabricate the solar cells, *p*-Si(111) wafers 300 μm thick with an area as large as 10 cm^2 with a resistivity $\rho = 0.5\text{--}2 \Omega \text{ cm}$ at 300 K were used. The 30-nm-thick *a*-Si:H(*n*) films were deposited on the polished surface of a wafer using radio-frequency glow discharge. Subsequently, the film of ZnO or ITO (indium–tin oxide) high-conductivity transpar-

ent oxides, 80 nm thick, was deposited on the upper surface of the film. Finally, the rear surface of the film was coated with a continuous Al layer 1–1.5 μm thick, whereas the free surface of the ZnO or ITO films was coated with an Al contact grid. The area of the solar cells was as large as 4 cm^2 .

A schematic drawing of illumination of the solar cell with the natural and linearly polarized radiation (LPR) for various angles of incidence θ is shown in Fig. 1. The side surface of the solar cell was protected with a light-tight screen in order to exclude radiation incidence. In order to vary the LPR angle of incidence, the structures were mounted on an STF-1 adjustment unit. This unit made it possible to control the angle of incidence and azimuth angle ϕ between the incidence plane (IP) of LPR and the vector of the electric field of the optical wave \mathbf{E} to within $\pm 30'$. The ratio between the areas of the photodetecting surface and the optical beam was maintained during measurements so that the photodetecting plane of the solar cell was within the cross section of the optical beam over the entire measurement range θ . The relative quantum efficiency of photoconversion η was defined as the ratio of the short-circuit photocurrent to the number of incident photons per second.

3. RESULTS AND DISCUSSION

Typical steady-state current–voltage (I – V) characteristics for each type of the solar cells fabricated, namely, Al/ZnO/*a*-Si:H(*n*)/*c*-Si(*p*)/Al and Al/ITO/*a*-Si:H(*n*)/*c*-Si(*p*)/Al, are shown in Fig. 2. Both types of solar cells

differ only in the material of the antireflection coating, whereas their energy barriers are identical and comprise the contact between crystalline and amorphous Si. It can be seen from Fig. 2 that, in accordance with the energy diagram, an identical polarity of rectification and similar I - V characteristics are observed for both types of solar cells. The forward portion of the I - V characteristics of the solar cell corresponds to the positive potential on c -Si. This is caused by the fact that the electrical properties of solar cells are determined mainly by the a -Si:H(n)/ c -Si(p) energy barrier.

For the region of forward biases $V < 0.4$ V, the steady-state I - V characteristics for the solar cells fabricated, irrespective of the type of antireflection oxide, within the limits of 5 orders of the current variation follow the relationship known for photodiodes; i.e.,

$$I = I_s [\exp(eU/kT) - 1]. \quad (1)$$

The diode coefficient n for all of the solar cells investigated was within the limits of 1.3–1.5 at $T = 300$ K. This can be associated with competition between the diffusion and recombination mechanisms of the forward current in such structures. The linear approximation of the I - V characteristics of the solar cell has the form $U = U_0 + R_0 I$. Upon increasing the forward bias voltage to $U > 0.5$ V, such an approximation yields the cutoff voltage $U_0 \cong 0.6$ V and residual resistance $R_0 \cong (2.3\text{--}7) \times 10^2 \Omega$.

All of the solar cells fabricated feature pronounced rectification. For the voltages $|U| \cong 1$ V, the forward current exceeds the reverse one by no less than a factor of 10^3 . The solar cells fabricated are of high quality. This is demonstrated by the fact that the reverse currents for the voltages as high as 5 V are no larger than 10^{-8} A at $T = 300$ K. It is noteworthy that the lowest values for the residual resistance and the diode coefficient were observed for solar cells with the ZnO antireflection coating.

Upon illumination of the solar cell, the photovoltage emerges, which is associated with the separation of photogenerated pairs by the active region a -Si:H(n)/ c -Si(p). It was characteristic of all solar cells that the substrate of these structures, c -Si, is always charged positively. This is in agreement with the rectifying direction of solar cells and their approximate band diagram. The saturation photovoltage U_{oc}^∞ for the solar cells fabricated (see table) was close to the cutoff voltage for the forward I - V characteristics of these structures. This allowed us to treat these values as the potential barrier height, which emerges with the formation of the contact between p -Si crystalline substrates and amorphous a -Si:H films.

The load I - V characteristic for a typical solar cell with an area $S = 4$ cm² is shown in Fig. 3. Load characteristics for solar cells with ZnO and ITO antireflection coatings were similar since these characteristics are determined by the energy barrier between a crystal and

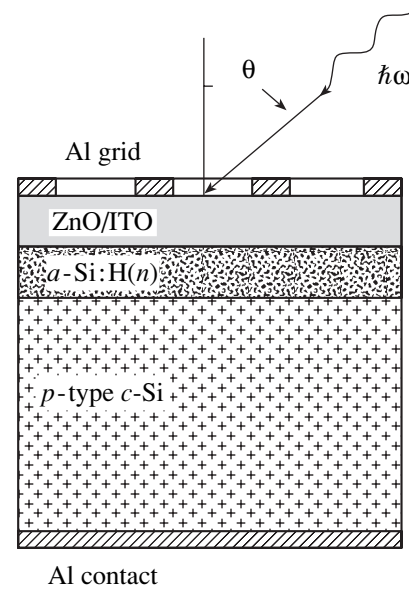


Fig. 1. Design of the Al/ZnO(ITO)/a-Si:H(n)/c-Si(p)/Al solar cell and schematic representation of photodetection.

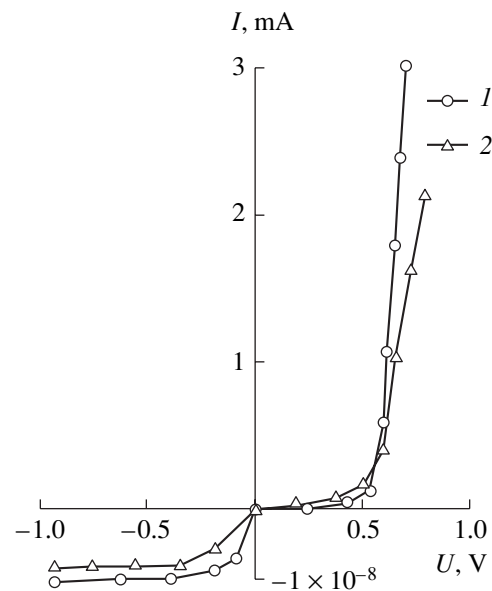


Fig. 2. Steady-state current-voltage characteristics of the Al/ZnO/a-Si:H(n)/c-Si(p)/Al (curve 1, sample 30p) and Al/ITO/a-Si:H(n)/c-Si(p)/Al (curve 2, sample 31p) solar cells at $T = 300$ K. The forward bias corresponds to the positive polarity of the external bias on c -Si.

an amorphous Si film. It can be seen that high short-circuit current densities are characteristic of the solar cells fabricated. For the best structures, this quantity is as large as $j_{sc} = 27$ mA/cm² with the filling factor of the load I - V characteristic $\beta \cong 78\%$ and efficiency $\sim 14\%$ under normal conditions. The quantities mentioned were well reproducible and exhibited no degradation during measurements.

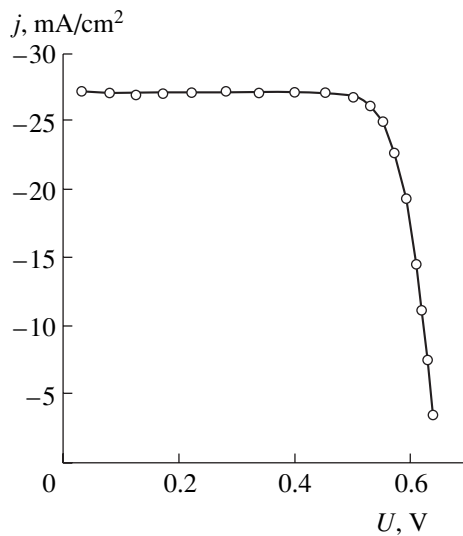


Fig. 3. Load characteristic of the Al/ZnO/a-Si:H(n)/c-Si(p)/Al solar cell at $T = 300$ K. The structure area $S = 4$ cm², the illumination power density $L = 100$ mW/cm², and the atmospheric mass is AM1.5. The polarities of U and j correspond to c -Si(p).

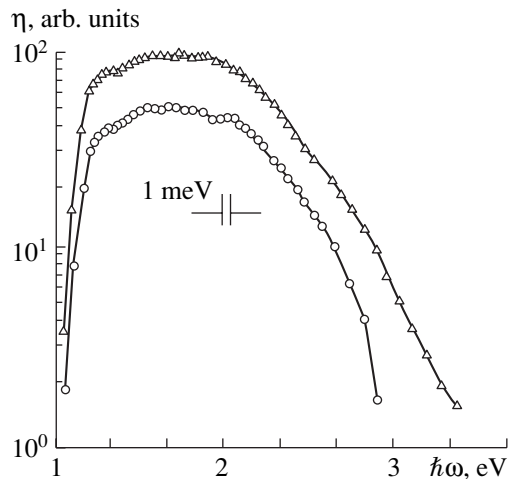


Fig. 4. Spectral dependences of the relative quantum efficiency of photoconversion of the Al/ZnO/a-Si:H(n)/c-Si(p)/Al (curve 1) and Al/ITO/a-Si:H(n)/c-Si(p)/Al (curve 2) solar cells for the unpolarized radiation at $T = 300$ K. To exclude overlaps, the spectra are shifted along the ordinate.

Spectral dependences of the relative quantum efficiency of photoconversion for typical solar cells under their exposure to polarized light are shown in Fig. 4.

Photoelectric properties of solar cells at $T = 300$ K

Solar cell type	U_0 , V	R_0 , Ω	n	U_{oc} , V	$\Delta\hbar\omega^m$, eV	$\delta_{1/2}$, eV	P_I^m , %
ITO/a-Si:H/c-Si/Al	0.56	700	~1.5	0.62	1.6–2.0	1.27	37
ZnO/a-Si:H/c-Si/Al	0.58	230	1.3–1.5	0.60	1.6–1.95	1.23	38

Solar cells have two antireflection coatings of different compositions. The width of the spectral photosensitive region upon illumination of solar cells from the side of the wide-gap films ($E_G^{\text{ITO}} \cong 3.2\text{--}3.45$ eV [6], $E_G^{\text{ZnO}} = 3.6$ eV [7] at $T = 300$ K) was determined. From this region, we determined a wide range of photon energies $\Delta\hbar\omega^m$, in which η attains its highest level (see table). The long-wavelength boundary of photosensitivity for solar cells is determined by band-to-band transitions within the narrow-gap component, specifically, crystalline Si, which is common for both types of structures.

In the coordinates $\sqrt{\eta} \hbar\omega = f(\hbar\omega)$, the long-wavelength falloff of photosensitivity for solar cells is straightened. Its extrapolation yields a cutoff for the energy of ~ 1.1 eV, which corresponds to the band gap of c -Si [7]. The full width at half-maximum $\delta_{1/2}$ of the photosensitivity spectra for the solar cells fabricated, as can be seen from the table, also demonstrates the broad-band photosensitivity of the structures. In these structures, the wide-gap component is obtained at the sacrifice of long-range order in Si. It is also noteworthy that the η spectra of solar cells contain no pronounced oscillations, which are indicative of interference from nonpolarized radiation (Fig. 4).

If we compare the η spectra for the solar cells fabricated with the data from [4], our attention is drawn to the considerable increase in the $\delta_{1/2}$ quantity from 0.7 to 1.27 eV. Such an increase was attained due to decreasing the thickness of the a -Si:H films from 100 to 30 nm. The pronounced short-wavelength falloff in the spectra of solar cells for $\hbar\omega > 2$ eV can apparently be associated with fundamental absorption in the a -Si:H films, since strong optical absorption in oxide films used in the development of solar cells emerges only for $\hbar\omega > 3$ eV [6, 7].

The investigations of the photosensitivity of solar cells under LPR demonstrated that, upon their illumination along the normal to the photodetecting plane of the oxide (ZnO and ITO), the photocurrent is independent of the spatial orientation of the \mathbf{E} vector. This is caused by isotropic photoactive absorption in the components forming this structure. Such a phenomenon leads to the photopleochroism coefficient

$$P_I = \left(\frac{i^p - i^s}{i^p + i^s} \right) \times 100\%, \quad (2)$$

where i^p and i^s are the photocurrents in the cases of $\mathbf{E} \parallel \text{IP}$ and $\mathbf{E} \perp \text{IP}$, being exactly equal to zero in the entire

range of photosensitivity of the solar cell. For this reason, there are grounds to conclude that natural photopleochroism [8] is absent in these structures. The photosensitivity of the solar cells was measured under the conditions of the oblique LPR incidence (Fig. 1). In this case, distinctions emerge between i^p and i^s for $\theta = \text{const}$ due to which the photopleochroism coefficient begins to differ from zero. This coefficient gradually increases as the angle of incidence increases according to the quadratic law $P_I \propto \theta^2$, which corresponds to the analysis in [9]. For $\theta = 0$, the polarization difference of the photocurrents is absent; i.e., $\Delta = i^p - i^s \equiv 0$. For this reason, with allowance made for [10], the polarization photosensitivity, which emerges when $\theta > 0$, should be treated as photopleochroism induced by oblique LPR incidence (induced photopleochroism).

A series of polarization investigations of solar cells based on two Si phases was performed. This complex involved the measurement of photocurrents i^p and i^s in relation to the angle of incidence and the photocurrent in relation to the azimuth angle φ between \mathbf{E} and an incidence plane i_φ for $\hbar\omega = \text{const}$. The measurements were carried out over the entire photosensitivity range of the structures.

The azimuthal dependences of the photocurrent over the entire range $0^\circ < \theta < 90^\circ$ for both types of solar cells were identical and followed the relationship

$$i_\varphi = i^p \cos^2 \varphi + i^s \sin^2 \varphi. \quad (3)$$

In this case, the relationship $|i^p| > |i^s|$ was valid over the entire photosensitivity range, whereas the angle position of the photocurrent extrema remained unchanged.

Certain dependences of photocurrents i^p and i^s on the angle of LPR incidence, which are typical of solar cells, are shown in Fig. 5. These dependences were found to be affected by the energy of incident photons. For example, for $\hbar\omega = 1.27$ eV, the dependences of i^p and i^s on θ are in agreement with those expected from the Fresnel relations for the optical wave transmission across the air-ITO (ZnO) interface [11–13]. In this case, an increase in the i^p quantity is associated with the elimination of losses for the reflection of the p wave only. At the same time, with increasing the photon energy, regions also exist in which an increase in photocurrent is observed both for the p and s waves (Fig. 5, curve 2). This may indicate that clarification emerges not only for the p wave but also for the s wave. Due to this, the θ dependences of i^p and i^s converge, and P_I correspondingly decreases relative to the previous case (Fig. 1, curve 1). According to [10], such trends in the dependences $i^p(\theta)$ and $i^s(\theta)$ may be associated with the LPR interference in such ITO and ZnO films. As follows from Fig. 5, within the photosensitivity range for the solar cells fabricated, anomalous dependences of the photocurrent on the angle θ emerge when $i^p < i^s$. Due to this, the coefficient P_I becomes negative (curve 3).

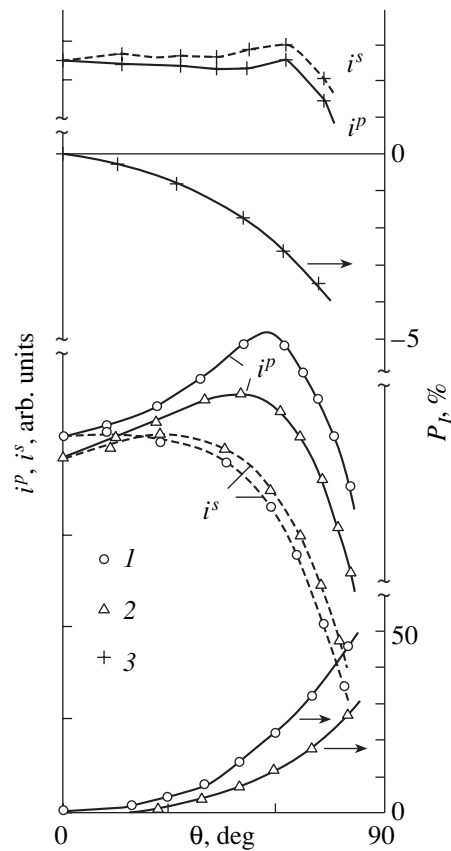


Fig. 5. Dependences of the short-circuit photocurrent and an induced photopleochroism coefficient on the angle of LPR incidence for Al/ITO/a-Si:H(n)/c-Si(p)/Al solar cells at $T = 300$ K. The illumination from the ITO side; $\hbar\omega = (1)$ 1.27, (2) 1.55, and (3) 1.94 eV.

According to theory [10], the amplitude of the coefficient of induced photopleochroism for the solar cells fabricated increases gradually throughout their entire photosensitivity range according to the law

$$P_I \propto \theta^2. \quad (4)$$

However, for the solar cells fabricated, the amplitude of the induced photopleochroism varies when there is variation in the incident photon energy for $\theta = \text{const}$ (Fig. 5). With allowance made for [10], this is indicative of the interference phenomena in ZnO and ITO films, which disagrees with the theory [9], in which interference was not taken into account at all.

Typical spectral dependences of the induced photopleochroism coefficient for both types of solar cells for $\theta = 75^\circ$ are shown in Fig. 6. In contrast to the analysis [9], the spectra P_I are clearly oscillatory. It can be seen from Fig. 6 that the experimental values of the induced photopleochroism coefficient in the maxima (curves 1, 2) are, on the one hand, close to each other ($P_I \cong 38\%$); on the other hand, they almost coincided with the calculated spectral dependence P_I (curve 3), which was obtained for the air-ITO and air-ZnO inter-

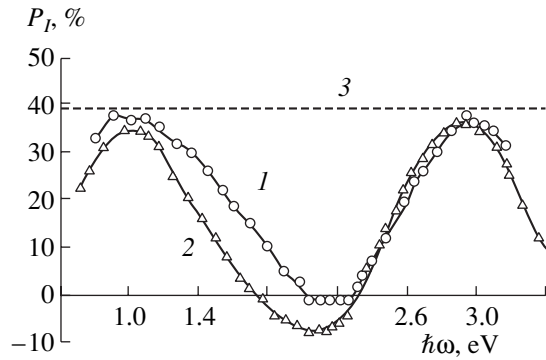


Fig. 6. Spectral dependences of P_I for the Al/ZnO/a-Si:H(n)/c-Si(p)/Al (curve 1) and Al/ITO/a-Si:H(n)/c-Si(p)/Al (curve 2) solar cells at $T = 300$ K ($\theta = 75^\circ$; curve 3 represents the calculation [9] for the air-oxide interface with $n \cong 2$).

faces based on [9]. By virtue of the fact that the refractive indices for these oxides are close to each other ($n \cong 2-2.1$ [6, 7]), this is a common dependence. Experimental spectral dependences $P_I(\hbar\omega)$ make it possible to specify the spectral regions in which the solar cells investigated can be used as selective photodetectors of linearly polarized radiation ($\hbar\omega_1 \cong 1.0$ eV and $\hbar\omega_2 \cong 3.0$ eV) or natural radiation ($\hbar\omega_3 \cong 2-2.2$ eV). It is evident that the choice of parameters of the antireflection ZnO and ITO oxides can be used to control the spectral range of the induced polarization photosensitivity for solar cells. Here, it is important to point out the new possibility of using polarization photoelectric spectroscopy to optimize the parameters of fabricated solar cells. Since the polarization condition $P_I = 0$ corresponds to complete clarification [10] and, correspondingly, to an increase in the quantum efficiency η , photoelectric spectroscopy can be used in the rapid monitoring of solar cells. Specifically, the P_I spectra shown in Fig. 6 also indicate that the antireflection coatings designed are actually inoperative in the region of the highest quantum efficiency of the solar cell. Consequently, the development of antireflection coatings for the energy range 1–1.8 eV, which is promising for solar cells, can provide a further increase in the quantum efficiency of photoconversion attained for the structures under consideration.

4. CONCLUSION

Thus, solar cells based on the heterojunction between the crystalline and amorphous Si phases with an antireflection oxide film (ITO, ZnO) can be used as selective photosensors of linearly polarized radiation. In this case, polarization photoelectric spectroscopy permits the rapid nondestructive analysis of the solar cells under consideration and, consequently, the conducting of a purposeful correction to the type and method of deposition of optically uniform antireflection coatings.

REFERENCES

1. K. O. Kuda, H. Okamoto, and Y. Hamakawa, *J. Appl. Phys.* **22**, L605 (1999).
2. R. De Rosa, M. L. Grill, G. Sasikala, and M. Tucci, *Solid State Phenom.* **67-68**, 563 (1999).
3. V. Yu. Rud' and Yu. V. Rud', *Fiz. Tekh. Poluprovodn. (St. Petersburg)* **31**, 254 (1997) [*Semiconductors* **31**, 197 (1997)].
4. Yu. A. Nikolaev, V. Yu. Rud', Yu. V. Rud', and E. I. Terukov, *Fiz. Tekh. Poluprovodn. (St. Petersburg)* **34**, 818 (2000) [*Semiconductors* **34**, 790 (2000)].
5. H. Mell, Yu. A. Nikolaev, V. Yu. Rud', *et al.*, *Fiz. Tekh. Poluprovodn. (St. Petersburg)* **35**, 1316 (2001) [*Semiconductors* **35**, 1259 (2001)].
6. S. Ashok, P. P. Sharma, and S. J. Fonash, *IEEE Trans. Electron Devices* **ED-27**, 725 (1980).
7. *Physicochemical Properties of Semiconductor Materials: A Handbook* (Nauka, Moscow, 1979).
8. F. P. Kesamanly, V. Yu. Rud', and Yu. V. Rud', *Fiz. Tekh. Poluprovodn. (St. Petersburg)* **30**, 1921 (1996) [*Semiconductors* **30**, 1001 (1996)].
9. G. A. Medvedkin and Yu. V. Rud', *Phys. Status Solidi A* **67**, 333 (1981).
10. F. P. Kesamanly, V. Yu. Rud', and Yu. V. Rud', *Fiz. Tekh. Poluprovodn. (St. Petersburg)* **33**, 513 (1999) [*Semiconductors* **33**, 483 (1999)].
11. G. S. Landsberg, *Optics* (Nauka, Moscow, 1976).
12. V. M. Botnaryuk, A. V. Koval', V. Yu. Rud', *et al.*, *Fiz. Tekh. Poluprovodn. (St. Petersburg)* **31**, 800 (1997) [*Semiconductors* **31**, 677 (1997)].
13. Yu. V. Rud', *Izv. Vyssh. Uchebn. Zaved., Fiz.* **29**, 68 (1986).

Translated by N. Korovin

PHYSICS
OF SEMICONDUCTOR DEVICES

**Analysis of High-Frequency Response
and Nonlinear Coherent Generation
of Resonance–Tunneling Diodes
within a Broad Frequency Range with Account
of Electron–Electron Interaction**

V. F. Elesin, I. Yu. Kateev, and A. I. Podlivaev

*Moscow State Institute of Engineering Physics (Technical University),
Kashirskoe sh. 31, Moscow, 115409 Russia*

Submitted January 8, 2002; accepted for publication February 25, 2002

Abstract—The response and power of the coherent generation of a resonance-tunneling diode have been calculated numerically taking into account the electron–electron interaction within a broad frequency range within the framework of a consistent quantum mechanical model. The “quantum” generation mode is shown to persist even in the presence of electron–electron interaction. Thus, a high-power generation at frequencies exceeding the resonance level width is possible. One can even expect an improvement of the generation parameters in the “classical” mode, in particular, the lowering of the generation threshold. This results from a rise in the negative differential conductance due to electron–electron interaction. © 2002 MAIK “Nauka/Interperiodica”.

1. INTRODUCTION

To date, no generally accepted theory of high-frequency response and resonance-tunneling diode (RTD) generation exists despite the intensive study and the unquestionable practical importance of this phenomenon [1]. An analytic theory of the high-frequency response and generation in RTD was developed in [2] within the framework of the theory that consistently takes into account the quantum interference of electrons and open boundary conditions (see also a review of preceding works there). This model was used in subsequent works [3, 4], where the nonlinear generation theory was developed both analytically and numerically. However, the effect of electron–electron interaction upon the high-frequency response and generation in RTD was not taken into account in these works, though one might expect high sensitivity of the high-frequency response to the electron–electron interaction. This follows from the fact that a shift of the resonance level ϵ_R , which is small in comparison with ϵ_R but comparable with the resonance width Γ , abruptly changes the resonance current.

Indeed, as it is shown within the framework of the coherent tunneling model in [5], taking the electron–electron interaction into account leads to a sharp rise of the current and to the hysteresis of the current–voltage characteristic. Therefore, electron–electron interaction must be essential for the achievement of high-power RTD generation.

The aim of this work is to study the effect of electron–electron interaction on the high-frequency

response and generation of RTD within the framework of a consistent model with open boundary conditions.

2. STATEMENT OF THE PROBLEM.
BASIC EQUATIONS

Following [2], we consider a one-dimensional (1D) quantum well (QW) with two delta-function barriers at $x = 0$ and $x = L$. A steady electron flow, proportional to q^2 and with an energy ϵ , which is approximately equal to the resonance level energy ϵ_R , is supplied to the QW from the left. An ac electric field with the potential $V_{ac}(x, t)$

$$V_{ac}(x, t) = \begin{cases} -\frac{e v x \cos(\omega t)}{L} \Theta(x), & x < L \\ -e v \cos(\omega t), & x > L \end{cases} \quad (1)$$

acts across the QW region.

The one-particle wave function $\Psi(x, t)$ of the electron satisfies the 1D time-dependent Schrödinger equation:

$$i\hbar \frac{\partial \Psi}{\partial t} = -\frac{\hbar^2}{2m^*} \frac{\partial^2 \Psi}{\partial x^2} + [\alpha \delta(x) + \alpha \delta(x - L) + V_c(x, t)] \Psi(x, t) + V_{ac}(x, t) \Psi(x, t), \quad (2)$$

where $V_c(x, t) = g|\Psi(x, t)|^2$ is the self-consistent potential of the local electron interaction in the Hartree–Fock approximation (see [5]).

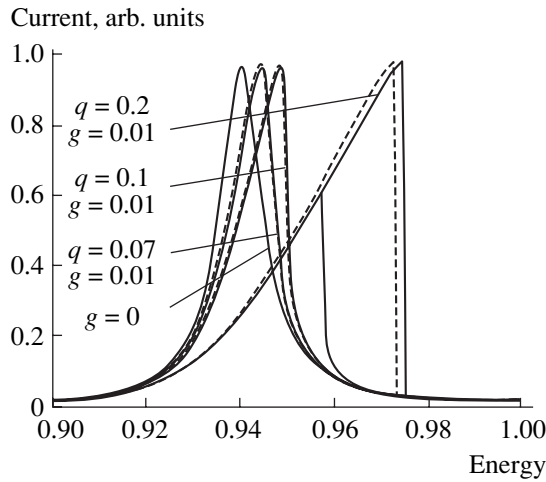


Fig. 1. Dependence of the dc current J_0 on the energy ε . Solid lines: analytic results; dashed lines: numerical results.

The ac field induces the polarization current

$$J_c(x, t) = -ie \left\{ \Psi^*(x, t) \frac{\partial \Psi(x, t)}{\partial x} - \Psi(x, t) \frac{\partial \Psi^*(x, t)}{\partial x} \right\} \quad (3)$$

$$= J_c(x) \cos \omega t + \sum_{k=2} J_k(x) \cos k \omega t.$$

The spatially averaged current is calculated as follows:

$$J_c = \frac{1}{L} \int_0^L J_c(x) dx. \quad (4)$$

The boundary conditions for the Schrödinger equation can be written similarly to [4]:

$$\begin{cases} \Psi(0, t) \left(1 - \frac{\alpha}{ik_1} \right) + \frac{1}{ik_1} \frac{\partial \Psi(0, t)}{\partial x} = 2q \exp\left(-\frac{iEt}{\hbar}\right) \\ \Psi(L, t) \left(1 - \frac{\alpha}{ik_2} \right) - \frac{1}{ik_2} \frac{\partial \Psi(L, t)}{\partial x} = 0, \end{cases} \quad (5)$$

where $k_1 = \sqrt{\frac{2m^*E}{\hbar^2}}$ and

$$k_2 = \sqrt{\frac{2m^*(E - V_c(x, t) - V_{ac}(x, t))}{\hbar^2}}$$

are, respectively, the electron wave vectors to the left and to the right of the structure, and m^* is the effective electron mass in the structure. These boundary conditions describe the electron flow incident from the left and their reflection and transfer to the region $x > L$. They are valid at $\omega \ll \varepsilon$.

The problem is solved iteratively: first, the Ψ function is calculated using (2) at some point of the time mesh, then, the interaction potential V_c is found, which is substituted into (2), and so on up to convergence. Then, the next point of the time mesh is calculated. The space and time mesh widths are, respectively, $dx = L/300$ and $dt = 2\pi/(100\omega)$.

A structure similar to [4] is chosen for calculations: $\alpha = 10$, $L = 2\pi$. The energy of the resonance level for this structure is $\varepsilon_R \approx 0.94$; its halfwidth $\Gamma \approx 5.5 \times 10^{-3}$. The coefficient g was assumed in calculations to be equal to 10^{-2} , which approximately corresponds to the value of electron–electron interaction in real structures.

3. DIRECT CURRENT THROUGH THE RESONANCE-TUNNELING DIODE WITH ALLOWANCE MADE FOR ELECTRON–ELECTRON INTERACTION

Analytic expressions for the dc resonance current J_0 through RTD and for the electron density n_0

$$n_0 = \frac{1}{L} \int_0^L |\Psi_0(x)|^2 dx$$

at $V(x, t) = 0$.

The energy ε dependence of the current J_0 for various values of $Q = k_1 q^2$ is represented in Fig. 1 by the solid line. It is seen that a symmetric dependence is observed at small q , as is the case at $g = 0$. As q grows, the curve becomes distorted; it shifts to larger values of ε , while the derivative at the descending portion of the $J_0(\varepsilon)$ curve (i.e., the absolute value of negative differential conductance (NDC)) increases. This is related to a shift of the resonance level due to electron–electron interaction. A hysteresis appears at Q and n magnitudes exceeding the critical values

$$Q_c = \frac{8L\Gamma^2}{9\sqrt{3}g} \approx 0.098, \quad n_c = \frac{4\Gamma}{3\sqrt{3}g} \approx 0.423 \quad (6)$$

(see details in [5]).

The results of solving Eq. (2) numerically are represented in Fig. 1 by the dashed line. They fit the analytic results with good accuracy; the critical values of $Q_c \approx 0.0105$ ($q_c \approx 0.104$) and of the electron density $n_c \approx 0.48$ are also in good agreement. Comparison reveals the validity of the numerical calculation of the electron–electron interaction potential V_c and of the program as a whole. Note that hysteretic phenomena are not considered in this work and that we must ensure that the electron density n does not exceed the critical value n_c .

4. HIGH-FREQUENCY RESPONSE OF THE RESONANCE-TUNNELING DIODE WITH ACCOUNT OF ELECTRON-ELECTRON INTERACTION

As was shown analytically in [2] and confirmed numerically in [4], two modes of RTD operation are possible. The first of these, called “classical,” exists if the electron energy in the maximum NDC region is chosen, i.e., $\delta < \Gamma$. Then, the amplification J_c/V_{ac} has a peak at the frequency $\omega = 0$. It is precisely this mode that has commonly been studied experimentally and theoretically [1].

In the new quantum mode occurring at $\delta > \Gamma$, the amplification has a peak at the frequency

$$\omega_{\max}^2 = \delta^2 - \Gamma^2 \quad (7)$$

and originates from quasi-resonance transitions between the states with energies ε and ε_R . Let us study the effect of electron–electron interaction on the response in these two modes.

First, we will consider the classical mode where $\omega \ll \Gamma$. We have calculated the dependence of the amplification J_c/V_{ac} on the ac field amplitude V_{ac}/Γ for $\omega/\Gamma = 10^{-2}$ and for various values of q at $\delta/\Gamma = 0.85$. Beginning from $q = 0.02$, the amplification rises at small V_{ac}/Γ and then begins to decrease at $q > 0.06$. This is related to the resonance level shift and distortion of the shape of the $J_0(\varepsilon)$ curve, which leads to a change in the NDC.

If one changes δ simultaneously with increasing q so that the NDC peak is achieved, the curves J_c/V_{ac} take the form shown in Fig. 2. The δ_{\max} value and the amplification rise with increasing q . This becomes particularly apparent at weak fields $V_{ac} \ll \Gamma$ (linear response). Such behavior results from the resonance level shift and the increase of the slope of the curve $J_0(\varepsilon)$ (see Fig. 1 and Section 3). Thus, electron–electron interaction leads to a rise in the amplification in the classical mode if the energy of electrons coming from the emitter is tuned with the rise of q .

The frequency dependence of the linear response J_c/V_{ac} for $\delta = 4\Gamma$ is presented in Fig. 3. These values of the parameters correspond to the quantum mode in the absence of electron–electron interaction. It is seen that the original (at $g = 0$) peak at the frequency $\omega_{\max} = 4\Gamma$ shifts with an increase in q to the low-frequency side and the amplification slightly rises. The frequency shift is related to the resonance level ε_R shift.

We calculated the field dependence of the nonlinear response at $\delta = \omega = 4\Gamma$. The response value falls with an increase in the driving current q , while the character of its dependence on the field V_{ac} changes rather weakly. If the level shift is compensated by the tuning of $\delta_{\max}(q)$ (see Section 4), it will be possible to substantially increase the amplification in comparison with the case

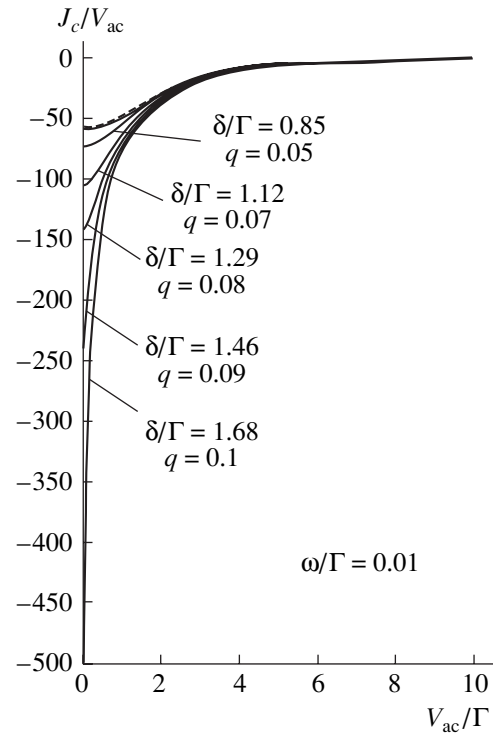


Fig. 2. Dependence of the dynamic conductance J_c/V_{ac} on the ac field amplitude V_{ac} with optimization with respect to δ . Solid lines: taking the electron–electron interaction into account ($g = 0.01$); dashed lines: without it ($g = 0$, $\delta/\Gamma = 0.58$).

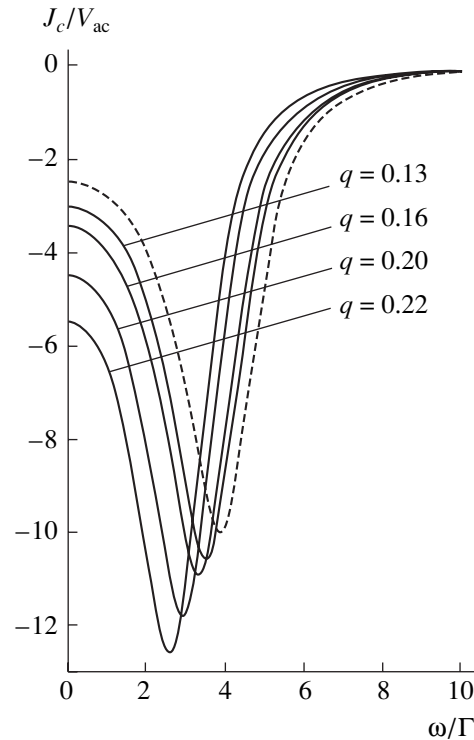


Fig. 3. Frequency dependence of the dynamic conductance J_c/V_{ac} in the quantum mode. Solid lines: with electron–electron interaction ($g = 0.01$); dashed lines: without it ($g = 0$). Parameter values for calculations: $\delta/\Gamma = 4$, $V_{ac}/\Gamma = 0.01$.

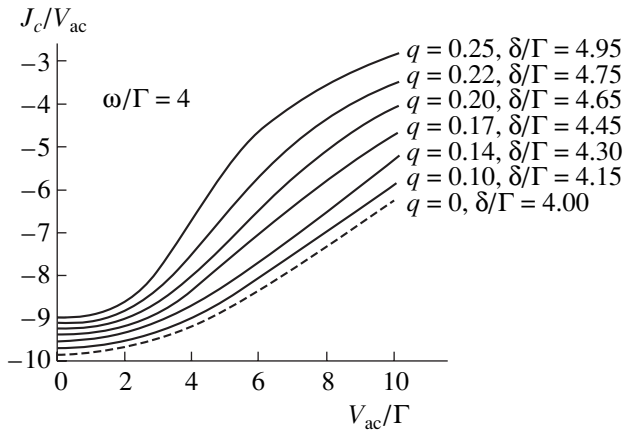


Fig. 4. Dependence of the dynamic conductance J_c/V_{ac} on the ac field amplitude V_{ac} in the quantum mode with optimization with respect to δ . Solid lines: with electron–electron interaction ($g = 0.01$); dashed line: without it ($g = 0$).

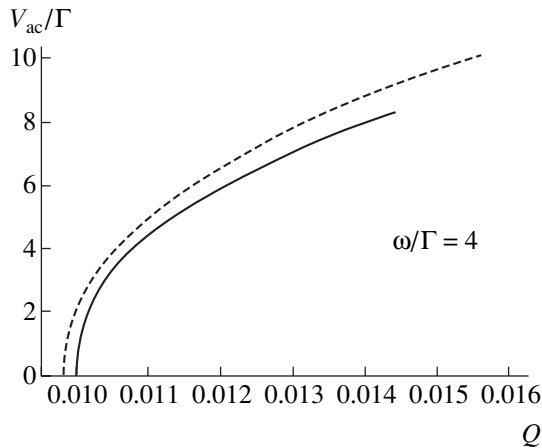


Fig. 5. Dependence of the generated field V_{ac}/Γ on the dimensionless driving current Q in the quantum mode with optimization with respect to δ . Solid line: with electron–electron interaction ($g = 0.01$); dashed line: without it ($g = 0$).

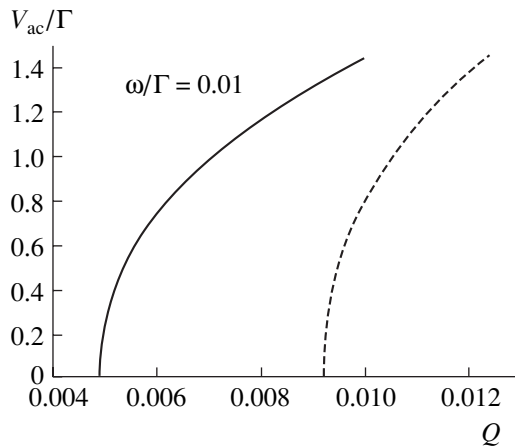


Fig. 6. Dependence of the generated field V_{ac}/Γ on the dimensionless driving current Q in the classical mode with optimization with respect to δ at $\tau \rightarrow 0$. Solid line: with electron–electron interaction ($g = 0.01$); dashed line: without it ($g = 0$).

of $\delta = 4\Gamma$. The amplification can also be increased by ω tuning. Taking into account the electron–electron interaction under a small field V_{ac} , the amplification even exceeds that accessible without consideration of the interaction.

5. GENERATION OF THE RESONANCE-TUNNELING DIODE WITH ACCOUNT OF ELECTRON–ELECTRON INTERACTION

The expression for the response (amplification) J_c/V_{ac} must be substituted into the equation [2]

$$\frac{\kappa L}{4\pi\tau_0} = \frac{J_c(Q, V_{ac})}{V_{ac}} \quad (8)$$

in order to find the field generated by RTD. Here, τ_0 is the time characterizing the energy losses in the cavity, and κ is the dielectric constant.

Depending on the cavity quality and the RTD parameters, two cases are possible. In the first case of high quality ($\tau_0 \rightarrow \infty$), the generation threshold current Q_{th} (see [2, 4]) is small in comparison with Q_c (see Section 4). The effect of electron–electron interaction is rather weak in this case; the dependence of V_{ac} on Q remains virtually unchanged in comparison with calculations at $g = 0$ [4].

In the opposite case of low quality, the effect of electron–electron interaction can be significant. The calculated dependence of the field V_{ac} on the driving current Q in the quantum mode $\delta = \omega = 4\Gamma$ show that taking electron–electron interaction into account slightly raises the threshold current Q_{th} and decreases the field generated by RTD. However, if tuning of δ is used (see Section 4), the generated power can be increased (see Fig. 5).

The classical mode is more sensitive to the interaction. Calculations show that the generated power significantly rises after tuning of the energy, but the threshold current Q_{th} changes only slightly. If the case of low quality takes place, the threshold significantly decreases due to interaction (see Fig. 6).

6. CONCLUSION

Thus, the quantum mode weakly changes due to electron–electron interaction. Therefore, high power generation is possible at frequencies exceeding the resonance level width. Some improvement of the generation parameters can be expected in the classical mode; in particular, the generation threshold can be reduced. This is caused by an increase in the magnitude of the absolute value of the negative differential conductivity due to electron–electron interaction.

ACKNOWLEDGMENTS

We thank Yu.V. Kopaev for his helpful participation in discussions.

This study was carried out with the support of the special federal program “Integratsiya” (project no. A0133), by the “Solid-State Nanostructures” program of the Ministry of Science and Technology of the Russian Federation (project no. 99-1140), and by the project “Development of a Theory of Interaction of Strong High-Frequency Electromagnetic Fields with a System of Resonance-Tunneling Diodes and Lasers.”

REFERENCES

1. H. C. Liu, Phys. Rev. B **43**, 12538 (1991).
2. V. F. Elesin, Zh. Éksp. Teor. Fiz. **116**, 704 (1999) [JETP **89**, 377 (1999)].
3. V. F. Elesin, Phys. Low-Dimens. Struct. **1/2**, 55 (2000).
4. V. F. Elesin, I. Yu. Kateev, and A. I. Podlivaev, Fiz. Tekh. Poluprovodn. (St. Petersburg) **34**, 1373 (2000) [Semiconductors **34**, 1321 (2000)].
5. V. F. Elesin, Zh. Éksp. Teor. Fiz. **119**, 816 (2001) [JETP **92**, 710 (2001)].

Translated by S. Kitorov

PHYSICS
OF SEMICONDUCTOR DEVICES

Study of the Potential Distribution in a Forward-Biased Silicon Diode Using Electrostatic Force Microscopy

A. V. Ankudinov*, A. N. Titkov*, R. Laiho**, and V. A. Kozlov*

* *Ioffe Physicotechnical Institute, Russian Academy of Sciences,
Politekhnikeskaya ul. 26, St. Petersburg, 194021 Russia*

** *Wihury Physical Laboratory, Turku, Finland*

Submitted February 26, 2002; accepted for publication February 27, 2002

Abstract—Electrostatic force microscopy was used to study the potential distribution in a forward-biased epitaxial–diffused $n^+–n–p–p^+$ silicon diode. Distributions of potential and capacitance were determined across the cleaved surface, which intersected the layers in the diode structure. Variations in the surface potential and capacitance were preliminarily measured with a submicrometer spatial resolution and were used to determine the position and width of the $n–p$ junction; the distribution of applied forward bias in the diode was also assessed. It is shown that an additional potential barrier for injected charge carriers may exist in the vicinity of the $n^+–n$ junction in the diode under consideration. For an injection-current density exceeding 100 mA/cm^2 , the voltage drop across this barrier becomes comparable with the voltage variations across the operating $n–p$ junction.
© 2002 MAIK “Nauka/Interperiodica”.

1. INTRODUCTION

For semiconductor devices, the electric-potential distribution in their bulk is an important characteristic. Recently, a new version of atomic-force microscopy (AFM), i.e., electrostatic-force microscopy (EFM), has been developed [1–4]; this new method makes it possible to study the potential distribution with a very high spatial resolution no worse than tens of nanometers. Briefly and conceptually, the EFM allows one to detect the force of electrostatic interaction between the tip and the sample surface; this force is proportional to the contact potential difference (CPD) between the tip and the surface. A variation in the CPD at the cleaved surface of device structures (in the regions where the differently doped layers crop out at the surface) makes it possible to reveal the electrical junctions in the bulk of the structures and to study the distributions of the built-in and external electric fields. It is worth noting that the EFM makes it possible to measure the potential profile in the operating devices under highly nonequilibrium conditions, for example, when large currents flow through the structure.

Recently, the EFM method was used with good results to study the distribution of potentials in light-emitting diodes and laser structures based on the III–V compounds [5–8], in thin-film solar cells [9], and in diffused and ion-implanted silicon $n–p$ diodes [2, 10]. Kikukawa *et al.* [2] were among the first who showed that it is possible to visualize a $n–p$ junction at the cleaved surface of semiconductor device structures even without applying an external voltage. Buh *et al.* [10] studied the redistribution of the surface potential in

a planar silicon diode to which a high blocking voltage was applied. An n -type region was formed in this diode through the implantation of phosphorus ions into the surface area of a lightly doped p -Si wafer. It was observed [10] that an electrical junction was pulled from the surface in the p -type region of the diode. This effect is observed upon a low level of doping of the p -type region and indicates that there are immobile, positively charged centers that attract electrons and are located in the thermal-oxide layer at the structure surface.

In this study, the EFM method was used to gain insight into the voltage distributions in the operating epitaxial–diffused $n^+–n–p–p^+$ silicon diode. By examining the cleaved surfaces, we determined the position of the $n–p$ junction and the drop of the external forward voltage across this junction. Simultaneously, we showed that, for a forward injection-current density exceeding 100 mA/cm^2 , an additional (parasitic) voltage drop developed in the region of the $n^+–n$ junction; this voltage drop was comparable with that across the main $n–p$ junction.

Measurements of the electrostatic force of interaction between the microscope tip and the structure surface were accompanied with studies of local capacitance between the tip and the local surface area under this tip. We showed that these measurements are useful for a more precise determination of the $n–p$ -junction location and for the interpretation of the observed non-monotonic variations in the surface potential in the vicinity of transition layers (interfaces) in the device.

2. EXPERIMENTAL

Let us consider the physical basics of the EFM method [1–4]. If the tip is at a potential U relative to the isolated surface under investigation, the following force of electrostatic interaction between the tip and the surface emerges:

$$F_{el} = \frac{1}{2} \frac{d(CU^2)}{dz}. \quad (1)$$

Here, C is the capacitance between the tip and the surface, and the z axis is directed perpendicularly to the sample surface. There is always a contact potential difference (CPD) V_{cd} between the tip and the surface owing to a difference in the work functions for dissimilar materials. If an external bias $U_{bias}(x)$ is applied along the x axis in the surface plane, the value of CPD is governed by the sum $V_{cd} + U_{bias}(x)$. Experimentally, dc U_{dc} and ac $U_{ac} \cos \omega t$ voltages are also applied to the tip–sample gap. Substitution of the total voltage

$$V_{cd} + U_{bias}(x) + U_{dc} + U_{ac} \cos \omega t$$

into (1) shows that the resultant force of electrostatic interaction F_{el} has three components, one of which is time-independent and the other two vary sinusoidally with the frequencies ω and 2ω . The oscillating components of the force are given by

$$F_{el}(\omega) = \frac{dC}{dz} [V_{cd} + U_{bias}(x) + U_{dc}] U_{ac} \cos \omega t, \quad (2)$$

$$F_{el}(2\omega) = \frac{1}{4} \frac{dC}{dz} U_{ac}^2 \cos 2\omega t. \quad (3)$$

An alternating electrostatic force gives rise to measurable vibrations of the tip at the frequencies ω and 2ω . The amplitudes of forced vibrations are very small (on the order of nanometers) and are linearly related to the field harmonics $F_{el}(\omega)$ and $F_{el}(2\omega)$ [1–4]. Thus, by detecting the amplitudes of the tip vibrations at the frequencies ω and 2ω , one can measure the signals $H(\omega)$ and $H(2\omega)$, which are proportional to the variation in the electrostatic forces $F_{el}(\omega)$ and $F_{el}(2\omega)$. In this case, the signal $H(2\omega)$ represents a variation in the capacitance at various points on the surface, whereas the signal $H(\omega)$ represents, in addition, a variation in CPD between the surface and the tip.

If an additional feedback loop ensuring the automatic adjustment of the value of U_{dc} is included, one can determine directly the value of V_{cd} from the value of U_{dc} that reduces the $H(\omega)$ signal (and, consequently, the force $F_{el}(\omega)$) to zero. The concept of the Kelvin mode is based on these considerations [1, 2]. In our study, we used an alternative method for determining the CPD profile; this method does not require an addi-

tional feedback loop and can be used to study semiconductor heterostructures with properties that are uniform over the plane of interfaces. In order to implement this method, the scanning direction \mathbf{x} should be chosen perpendicular to the plane of structure interfaces. When determining the $H(\omega)$ -signal topography, we successively increased the potential at the tip U_{dc} by a small fixed value after obtaining each line in the image. In the image obtained in this manner, the contrast level was adjusted within a very narrow range in the vicinity of zero so as to satisfy the condition $F_{el}(\omega, x, y) = 0$. The sequence of variations in the value of $U_{dc}(x, y)$ measured along the zero-contrast curve (the curve of the zero force $F_{el}(\omega)$) describes the behavior of CPD in the \mathbf{x} direction taking into account the aforementioned assumption concerning the uniformity of properties over the plane of interfaces.

The EFM method was used to study the distributions of potential and capacitance over the cleaved surfaces of the diode under atmospheric conditions. In the course of the measurements, the n -type contact of the diode was grounded; an external positive bias was applied to the p -type contact. We employed an Autoprobe CP Research Thermo-Microscopes atomic-force microscope, which can be used in the noncontact (resonance) mode and also in the EFM mode. We used tips made of heavily doped p -Si. The mechanical-resonance frequency of the tips was about 90 kHz. In order to excite the EFM signals, we applied an ac voltage with a frequency of 40–50 kHz and an amplitude of about 1 V to the tip; this voltage was derived from a 3325B Hewlett Packard oscillator. The EFM signals were measured simultaneously using two SRS8230 Stanford Lock-in Amplifier synchronous detectors. The detection scheme has been described in more detail elsewhere [7].

The structure of the silicon diode under investigation included the n^+ -Si(100) substrate doped with antimony to the level of $5 \times 10^{18} \text{ cm}^{-3}$. A 16- μm -thick n -type layer with an electron concentration of $2 \times 10^{15} \text{ cm}^{-3}$ was grown on the substrate using vapor-phase epitaxy; a n - p junction was then formed by the diffusion of gallium. The calculated depth of the junction was about 8 μm , with the gallium near-surface concentration being equal to $N_s \approx 1.2 \times 10^{16} \text{ cm}^{-3}$. Nonrectifying contacts to the substrate and to the boron-doped p^+ -type side (with a hole concentration of $\sim 10^{20} \text{ cm}^{-3}$) were formed by the firing-in of nickel.

3. RESULTS AND DISCUSSION

In Fig. 1a, we show the AFM image of the cleaved surface of an n^+ - n - p - p^+ structure in the region where the layers which comprise the structure crop out at the surface. The cleavage topography is rather smooth, includes hillocks with an average height of about 10 nm (see the cross section in Fig. 1a), and gives no way of

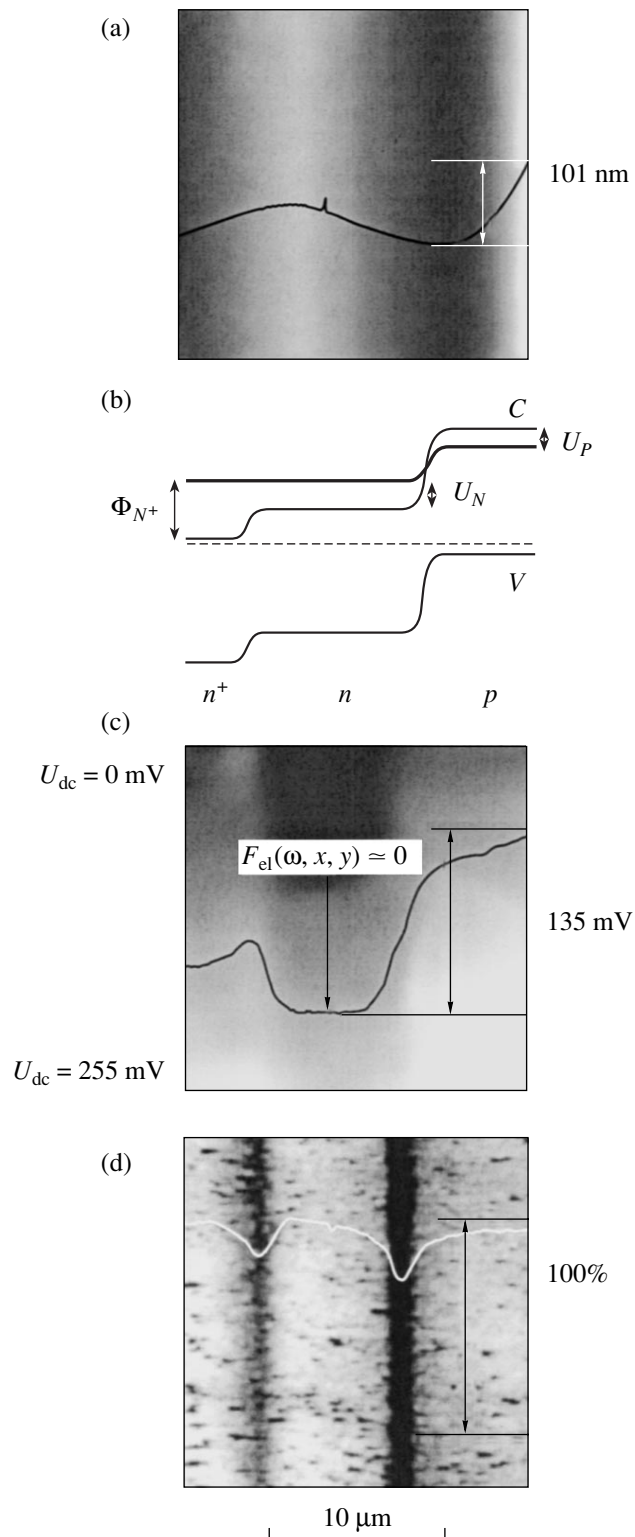


Fig. 1. The results of EFM studies of an n^+-n-p^+ diode in a state of equilibrium. (a) The topography of the cleaved-surface relief in the region where the layers, which comprise the diode, crop out at the surface; the profile of the cross section perpendicular to the interfaces is superimposed on the image. (b) The energy-band diagram of the diode in a state of equilibrium; the solid thick line illustrates schematically the behavior of the conduction-band bottom at the surface. (c) The $H(\omega)$ -signal image obtained by the successive increase of the dc voltage applied to the tip U_{dc} by 1 mV for each succeeding image line; the zero-signal contour is also shown in the image. (d) The image of the capacitance signal $H(2\omega)$ with a superimposed signal profile averaged along the direction of the structure interfaces. The images of the $H(\omega)$ and $H(2\omega)$ signals in (c) and (d) were obtained simultaneously with the data on topography in (a).

detecting the n^+-n and $n-p$ junctions in the structure whose bulk energy-band diagram in the state of equilibrium is shown schematically in Fig. 1b; the following designations are used: $U_{N(p)}$ are the energy separations of the conduction (valence) band edges in the bulk from their position at the surface, Φ_{N^+} is the distance between the position of the Fermi level and conduction-band bottom at the surface in the relevant layer of the structure, C is the valence band, and V is the valence band.

The homojunctions comprising the structure are distinctly observed in the EFM images of the same surface area; these images were obtained using the $H(\omega)$ and $H(2\omega)$ signals and are shown in Figs. 1c and 1d, respectively. In these images, vertical boundaries between different regions are represented by straight lines, which indicates that the layers in the structure are homogeneous in the plane of interfaces. The decrement in the contrast from the top down in the image using the $H(\omega)$ signal (Fig. 1c) is caused by the specificity of the suggested method for measuring the CPD across the structure interfaces. The uppermost line in the image shown in Fig. 1c and obtained using the $H(\omega)$ signal corresponds to the initial voltage $U_{dc} = 0$ mV applied to the tip; for each subsequent line, the voltage applied to the tip was increased by 1 mV, which, for 256 lines in a frame, ensured an increase in U_{dc} by 255 mV from the top down. The zero-signal profile specifying the CPD is superimposed on the image in Fig. 1c. The n^+-n and $n-p$ junctions manifest themselves as regions with appreciable variations in potential. Two dark bands (i.e., the regions of decreased capacitance) can be seen in the image shown in Fig. 1d and were obtained using the $H(2\omega)$ signal; these bands also clearly indicate electrical junctions in the structure.

Let us analyze the variations in the CPD profile in Fig. 1c. Since the magnitude of the electron affinity for the layers forming the silicon diode is the same, it is reasonable to compare the variations in the equilibrium CPD with the behavior of the position of the conduction-band energy. The CPD profile shown in Fig. 1c differs from variations in the bands in the structure bulk (see Fig. 1b). First, the largest variation in CPD is 135 mV, which is much smaller than the barrier height Φ_b at the $n-p$ junction, as follows from the energy-band diagram, and is much smaller than the silicon band gap ($E_g = 1.12$ eV). Second, the CDP at the n^+-n junction decreases (in contrast to the expected steady increase) and, in addition, passes through an additional maximum. These discrepancies are caused by the contribution of the surface. As is well known, the surface states give rise to the near-surface band bending upward by the value of U_N in the n -type layer and downward by the value of U_p in the p -type layer (see Fig. 1b). The CPD drop between the n - and p -type layers should then be governed by the difference $\Phi_b - U_p - U_N$; for a large total bending of the bands $U_p + U_N$, the value of CPD

may be small. The variation in CPD obtained by us surprisingly coincided with one of the values (130 mV) reported by Kikukawa *et al.* [2]. Perhaps, this coincidence is not accidental since, in both cases, silicon surfaces coated with a native oxide were studied. However, Kikukawa *et al.* [2] also reported a value of CPD (260 mV) twice as large for the silicon surface, but for a diode fabricated using As⁺-ion implantation into a p -type substrate. The latter discrepancy is reasonably explained by characteristics of the surface states, which govern the band bending at the surface, and by their dependence on the surface history. Apparently, this may also be the cause of a slight decrease in CPD at the n^+-n junction in the case under consideration. It is worth noting that the n^+ -type layer lies within the bulk substrate, whereas the n -type layer is epitaxially grown, so that the surface states of these two layers may differ.

It is difficult to attribute the presence of a maximum in CPD in the vicinity of the n^+-n junction to the role of the surface alone; we believe that this maximum should also be related to the structural quality of the n^+-n junction and to the specificity of the run of the potential-curve in the vicinity of this junction in the structure bulk. It is reasonable to assume that this maximum corresponds to the profile of the bulk potential which arises as a result of negative-charge screening at the interface [11]. It is noteworthy that the n^+-n junction is the growth interface with the substrate and the aforementioned negative charge may arise as a result of the presence of an imperfect layer at the epitaxial interface. It is this situation that we recently observed at the growth epitaxial interface with the substrate (n^+-n) in laser structures in a GaAs/GaAlAs system [12].

The aforementioned conclusion is also supported by data on the topography of the local-capacitance signal $H(2\omega)$; these data are shown in Fig. 1d. The level of this signal, as well as the CPD-signal amplitude, is mainly governed by interaction with the surface. Assuming that a tip-sample system consists of a metal, insulator gap, and a semiconductor, we express the capacitance of this system as

$$C = \frac{C_{TS}(C_B + C_S)}{(C_{TS} + C_B + C_S)}, \quad (4)$$

where C_{TS} is the tip-surface capacitance, C_B is the capacitance of the depletion layer in a semiconductor, and C_S is the capacitance of the surface states [11]. Introducing the derivative of (4) into (3) and assuming that only C_{TS} depends on z , we obtain

$$H(2\omega) \propto \frac{dC_{TS}}{dz} \left[\frac{C_B + C_S}{C_{TS} + C_B + C_S} \right]^2. \quad (5)$$

It can be seen that the level of the $H(2\omega)$ signal is completely governed by the derivative dC_{TS}/dz if $C_S \gg C_{TS} +$

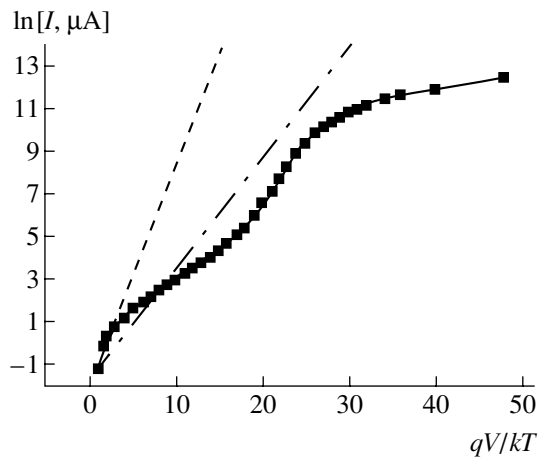


Fig. 2. The current–voltage characteristic of the diode under investigation; the dashed line corresponds to $\exp(qV/kT)$, and the dash-and-dot line corresponds to $\exp(qV/2kT)$.

C_B . By examining the profile shown in Fig. 1d, we can verify that the levels of the $H(2\omega)$ signals at the n^+ -, n -, and p -type layers away from the junctions are approximately equal to each other, although the capacitances C_B may differ by several orders of magnitude for heavily doped and undoped layers. This means that the condition $C_S \gg C_{TS} + C_B$ is undoubtedly satisfied everywhere in the structure. Let us estimate the order of magnitude of capacitances, which appear in expression (5), calculated per unit area. The depletion-layer capacitance $C_B = \epsilon_{Si}/W$, where the dielectric constant of silicon $\epsilon_{Si} = 11.9\epsilon_0$, with the dielectric constant of free space ϵ_0 being equal to $8.85 \times 10^{-12} \text{ F m}^{-1}$; the extent of the surface space-charge region varies from 3×10^{-8} to $3 \times 10^{-6} \text{ m}$ for different layers of the structure. As a result, we obtain $C_B = 3.5 \times 10^{-5} - 3.5 \times 10^{-3} \text{ F m}^{-2}$. The tip–surface capacitance $C_{TS} = \epsilon_{air}/d$, where the dielectric constant of air $\epsilon_{air} = \epsilon_0$ and the probe–surface spacing is $d = 5 \times 10^{-8} \text{ m}$; as a result, we obtain $C_{TS} = 1.77 \times 10^{-4} \text{ F m}^{-2}$. The condition $C_S \gg C_{TS} + C_B$ implies a rather high density of surface states at the interface between Si and the native SiO_2 oxide. Since $C_S = qN_{SS}$, where q is the elementary charge, this capacitance exceeds all other capacitances for the surface-state density $N_{SS} \approx 10^{16} - 10^{17} \text{ m}^{-2} \text{ V}^{-1}$ and is equal to $C_S = 1.6 \times 10^{-3} - 1.6 \times 10^{-2} \text{ F m}^{-2}$.

We now consider the possible causes of the decrease in the level of the $H(2\omega)$ signal by approximately 20% in the regions of the $n^+ - n$ and $n - p$ junctions. For the $n - p$ junction, we can mention the following factors. First, there is a drastic decrease in the capacitance C_S . Thus, there is always a locality in the $n - p$ -junction region where the band bending at the surface disappears owing to the inversion between the n - and p -type regions; this means that (i) there is no charge at the surface states and (ii) the value of C_S is small. For the same reason, a

decrease in the capacitance C_B should take place above this region. Indeed, the depletion region in the $n - p$ junction is an insulator, and the capacitance above this region should decrease. Second, there is another cause of methodological character; this consists in a possible slight decrease in C_{TS} and, consequently, in dC_{TS}/dz . As can be seen from Fig. 1d, the right-hand dark band coincides with the location of abrupt variation in the CPD profile in Fig. 1c. In the noncontact mode, the AFM negative-feedback loop adjusts the tip–surface spacing so that the amplitude of resonance vibrations of the tip remains unchanged. A large lateral gradient comes into existence in the range of CPD variations; this gradient shifts the resonance frequency, and, in order to maintain a constant vibration frequency, the negative-feedback loop draws the tip farther from the surface. As a result, the capacitance of the tip–sample system should decrease; the same is true of the amplitude of the $H(2\omega)$ signal.

However, the latter factor can hardly be important for the $n^+ - n$ junction, in which case a decrease in capacitance occurs in the vicinity of the CPD peak where the lateral gradient of electrostatic force reverses its sign. We have to assume that a dip in the capacitance signal in the $n^+ - n$ -junction region is caused by the depletion of this region, which is consistent with the aforementioned inference about a high defect concentration at the growth interface, with the latter coinciding with the $n^+ - n$ junction.

The presence of a region with a high concentration of defects in the structure under investigation was directly confirmed by studying the current–voltage ($I - V$) characteristic of the diode. This characteristic is shown in Fig. 2 and includes a gently sloped portion, which is typical of diodes and corresponds to the prevalence of the generation–recombination current; then, a steeper portion corresponding to a contribution from the diffusion current, and, finally, the $I - V$ characteristic levels off, which corresponds to an ohmic portion at a high injection level. However, both of the first two portions have a logarithmic slope which is almost two times smaller than that typical of $I - V$ characteristics for Si diodes [11] (for the sake of comparison, the lines with expected slopes of qV/kT and $qV/2kT$ are also drawn in Fig. 2). Generally, such deviations are caused by the existence of a parasitic barrier in the diode. The aforementioned data indicate that the EFM method makes it possible to determine the location of this barrier in the structure and to assess its width and height.

In Fig. 3a, we show the CPD profiles across the structure; these profiles were measured at several forward-bias voltages applied to the diode’s p contact. It can be seen that the CPD profile changes mainly in the vicinity of the $n - p$ junction for low bias voltages and currents (see curves 0–3). Simultaneously, only the right-hand dark band corresponding to the $n - p$ junction disappears in the capacitance signal in Fig. 3c (images 0–3).

This suggests that variation in the potential in the diode bulk initially occurs predominantly only at this junction. When a current with a density of about 100 mA/cm^2 flows through the diode biased at 600 mV , the CPD profile (Fig. 3a, curve 4) is straightened, thus evening the region of the $n^+ - n$ junction; simultaneously, the left-hand dark band disappears in the capacitance signal in Fig. 3c (images 4, 5)

We now attempt to assess the height of the parasitic barrier at the $n^+ - n$ junction. At a voltage up to $\sim 500 \text{ mV}$, the potential drops predominantly across the $n - p$ junction; at the same time, an appreciable potential peak in the region of the $n^+ - n$ junction is not affected at all (see curves 0–3 in Fig. 3a). As the voltage is increased to 600 mV , the peak is rapidly smoothed off; as the voltage is further increased to $\sim 700 \text{ mV}$, we observe only a shift of the entire profile downward without any deformation of the profile shape (curves 4, 5 in Fig. 3a). Using these data, we find that the parasitic-barrier height is approximately equal to 100 mV .

The EFM data also make it possible to evaluate the gradient of the impurity concentration in the $p - n$ junction. As can be inferred from an examination of the right-hand side of the CPD profile in Fig. 1c, a major variation in the signal occurs over the distance of $W \approx 2.5 \mu\text{m}$. The size of this region can also be determined from the width of the base of the corresponding dark band in Fig. 1d. Assuming that the $n - p$ junction is not abrupt, we find that the concentration gradient α (see [11]) is equal to $\alpha_{\text{exp}} = 12\varepsilon_{\text{Si}}\Phi_b/qW^3 \approx 5.7 \times 10^{18} \text{ cm}^{-4}$, where the height of the potential barrier Φ_b in the barrier is assumed to be equal to the band gap E_g in silicon. This estimate differs little from the calculated impurity-concentration profile $N_d - N_a$ in the region of the $n - p$ junction, which yields $\alpha_{\text{mod}} \approx 8.9 \times 10^{18} \text{ cm}^{-4}$.

We assume that the gallium concentration profile is described by a Gaussian function; i.e.,

$$N = N_s \exp\left(-\frac{x^2}{x_n^2}\right).$$

The $n - p$ -junction position is determined from the condition $N = N_d$; the concentration gradient is then given by

$$\alpha_{\text{mod}} = \left. \frac{dN}{dx} \right|_{N=N_d} = \frac{2N_d}{x_n} \left(\ln \frac{N_s}{N_d} \right)^{1/2}.$$

When the $n - p$ junction was formed, gallium was diffused from the surface for $t = 9 \times 10^4 \text{ s}$ at $T = 1400 \text{ K}$. Assuming that the diffusion coefficient of gallium at

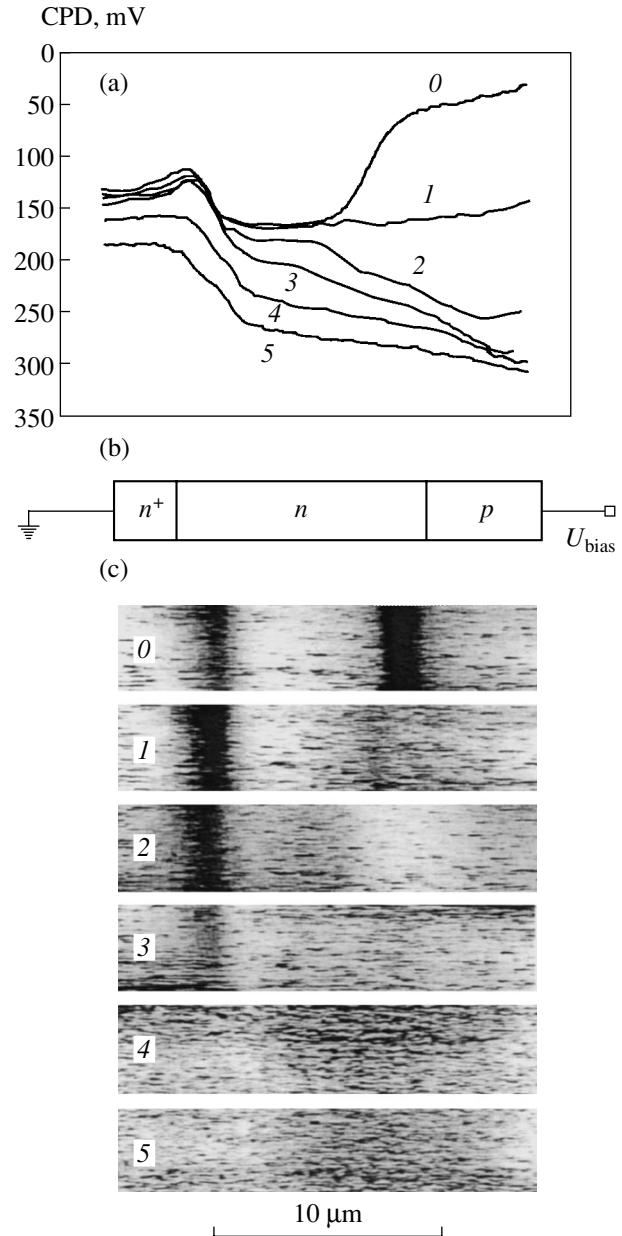


Fig. 3. The results of EFM studies of a forward-biased silicon $n^+ - n - p^+$ diode. (a) A series of CPD profiles obtained (0) in a state of equilibrium and for the bias voltages (injection currents) equal to (1) 199 mV ($2.4 \mu\text{A}$), (2) 396 mV ($30 \mu\text{A}$), (3) 508 mV (1.3 mA), (4) 598 mV (1.1 mA); $j \sim 100 \text{ mA/cm}^2$, and (5) 674 mV (35.8 mA). (b) Schematic representation of a diode with a grounded n -type region and biased p -type region. (c) A series of $H(2\omega)$ -signal images (0–5) obtained simultaneously with the CPD profiles (see (a), curves 0–5).

this temperature is equal to $D = 10^{-12} \text{ cm}^2/\text{s}$, we obtain $x_n = 2(Dt)^{1/2} = 6 \mu\text{m}$ and $\alpha_{\text{mod}} \approx 8.9 \times 10^{18} \text{ cm}^{-4}$.

4. CONCLUSION

We will now dwell briefly on the main results of this study. Using an epitaxial-diffused $n^+ - n - p^+$ silicon

diode as an example, we considered in detail the experimental potentialities of electrostatic-force microscopy (EFM) for studying the surface and bulk potential distributions in semiconductor diode structures. For the silicon diode under consideration, we studied the aforementioned distributions both under equilibrium conditions and with the application of forward bias voltages up to the point where the leveling-off of the I - V characteristics was attained. We showed that electrostatic-force microscopy is highly sensitive to the presence of parasitic barriers in a device structure and makes it possible to determine the location of these barriers and evaluate their parameters.

In order to determine the one-dimensional profiles of the contact-potential difference, we suggested a new method of EFM measurements, which does not require an additional negative-feedback loop.

ACKNOWLEDGMENTS

This study was supported by the Russian Foundation for Basic Research (project no. 00-02-16948) and by the Ministry of Industry, Science, and Technology of the Russian Federation (project 41 of the program "Microelectronics").

REFERENCES

1. M. Nonnenmacher, M. P. O'Boyle, and H. K. Wickramasinghe, *Appl. Phys. Lett.* **58**, 2921 (1991).
2. A. Kikukawa, S. Hosaka, and R. Imura, *Appl. Phys. Lett.* **66**, 3510 (1995).
3. H. O. Jacobs, P. Leuchtman, O. J. Homan, and A. Stemmer, *J. Appl. Phys.* **84** (3), 1168 (1998).
4. J. W. Hong, K. H. Noh, Sang-il Park, *et al.*, *Phys. Rev. B* **58**, 5078 (1998).
5. R. Shikler, T. Meoded, N. Fried, and Y. Rosenwaks, *Appl. Phys. Lett.* **74**, 2972 (1999).
6. G. Leveque, P. Girard, E. Skouri, and D. Yareka, *Appl. Surf. Sci.* **157**, 251 (2000).
7. A. V. Ankudinov, E. Yu. Kotel'nikov, A. A. Katsnel'son, *et al.*, *Fiz. Tekh. Poluprovodn. (St. Petersburg)* **35** (7), 874 (2001) [*Semiconductors* **35**, 840 (2001)].
8. A. Ankudinov, V. Marushchak, A. Titkov, *et al.*, *Phys. Low-Dimens. Struct.* **3/4**, 9 (2001).
9. C. Ballif, H. R. Moutinho, and M. M. Al-Jassim, *J. Appl. Phys.* **89**, 1418 (2001).
10. G. H. Buh, H. J. Chung, C. K. Kim, *et al.*, *Appl. Phys. Lett.* **77**, 106 (2000).
11. S. M. Sze, *Physics of Semiconductor Devices* (Wiley, New York, 1969; Énergiya, Moscow, 1973).
12. A. V. Ankudinov *et al.*, *Extended Abstracts of All-Russia Conference on Probing Microscopy, 2002*.

Translated by A. Spitsyn

PHYSICS
OF SEMICONDUCTOR DEVICES

MOCVD-Grown InGaAs/GaAs/AlGaAs Laser Structures with a Broad-Area Contact

P. V. Bulaev**, V. A. Kapitonov*, A. V. Lutetskii**, A. A. Marmalyuk**,
D. B. Nikitin**, D. N. Nikolaev*, A. A. Padalitsa**, N. A. Pikhtin*,
A. D. Bondarev*, I. D. Zalevskii**, and I. S. Tarasov*

* Ioffe Physicotechnical Institute, Russian Academy of Sciences,
Politekhnicheskaya ul. 26, St. Petersburg, 194021 Russia

** Sigm Plus, Moscow, 117342 Russia

Submitted March 4, 2002; accepted for publication March 11, 2002

Abstract—A metal-organic chemical vapor deposition (MOCVD) technique is developed for a diode laser heterostructure in a system of InGaAs/GaAs/AlGaAs solid solutions; the optimal sizes and the doping profile of the structure are determined to minimize the internal optical losses. Mesa-strip diode lasers with a threshold density of current $J_{th} = 150\text{--}200\text{ A/cm}^2$, internal optical loss factor $\alpha_i = 1.6\text{--}1.9\text{ cm}^{-1}$, and an internal quantum yield $\eta_i = 85\text{--}95\%$ were fabricated. In the continuous lasing mode of a diode laser with a $100\text{-}\mu\text{m}$ -wide aperture and a wavelength of $0.98\text{ }\mu\text{m}$, the optical power output was as high as 6.5 W and was limited by the catastrophic optical degradation of mirrors. The radiation divergence in the plane normal to the $p\text{--}n$ junction amounts to $\theta_{\perp} = 25^{\circ}\text{--}30^{\circ}$. The use of wide-gap waveguide layers, which deepens the potential electron well in the active region, is shown to reduce the temperature sensitivity of the InGaAs/GaAs/AlGaAs laser heterostructures in the temperature range from 0 to 70°C . © 2002 MAIK “Nauka/Interperiodica”.

1. INTRODUCTION

In our recent studies [1–3], we have thoroughly investigated laser heterostructures with separate confinement in systems of InGaAs/GaAs/InGaP and InGaAs/GaAs/AlGaAs solid solutions. In these structures, gallium arsenide epilayers were used as waveguide walls. A “strong” waveguide integrated into a laser heterostructure allows the internal optical loss in the emitters to be reduced without a considerable decrease in their doping level. As a result, the diode lasers based on such heterostructures displayed an unprecedentedly high output power in the continuous lasing mode [1, 2]. However, along with all their advantages, laser heterostructures with an arsenide gallium waveguide have a number of fundamental drawbacks. These are the considerable beam divergence in the plane perpendicular to the $n\text{--}p$ junction (θ_{\perp}) and the high-temperature sensitivity of the threshold density of current (low characteristic temperature T_0) [3]. These drawbacks are not inherent in lasers based on InGaAs/GaAs/AlGaAs heterostructures with a widened wide-gap waveguide. In this study, we consider the properties of diode lasers with a large-area mesa-strip contact based on InGaAs/GaAs/AlGaAs heterostructures obtained through metal-organic chemical vapor deposition (MOCVD).

2. EXPERIMENTAL SETUP AND LASER HETEROSTRUCTURES

We used InGaAs/GaAs/AlGaAs laser heterostructures that were grown using MOCVD in a SIGMOS-130 system with a horizontal rectangular quartz reactor. Highly homogeneous structures were obtained due to the rotation of the substrate holder by the carrier gas flow. The structures were grown at the temperature of 770°C ; the typical working pressure in the reactor chamber was 60 Torr .

As a source of Group-III elements, we applied triethylgallium, trimethylaluminum, and trimethylindium. The Group-V elements were represented by 100% arsine. A 1 : 20 silane–hydrogen mixture and diethylzinc were used as the n - and p -dopants, respectively. Before entering the gas system, arsine was subjected to a two-step purification by being blown through zeolite and a “SigmaKhIM-1.0” supercleaner. This allows one to reduce the oxygen and water content in arsine to values no larger than 0.1 ppm . As the gas carrier, we used hydrogen, which was purified by being diffused through a palladium filter heated to 450°C up to the point where its dew point was no higher than -110°C .

The structures were grown on GaAs AGNK-2S-type substrates precisely oriented in the (100) plane. The substrates were epi-ready; thus, preliminary treatment before growth initiation was unnecessary.

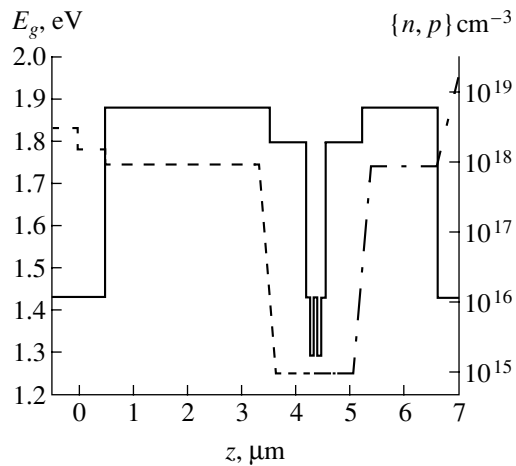


Fig. 1. Solid line shows the schematic energy diagram of the InGaAs/GaAs/AlGaAs heterostructures of separate confinement. The calculated doping profiles for the donors (Si) and acceptors (Zn) are depicted by dashed and dot-and-dash lines, respectively. z is the coordinate along the direction of growth.

Anisotype heterostructures with separate confinement were prepared for the experiments. As waveguide layers in the structures, we used $\text{Al}_x\text{Ga}_{1-x}\text{As}$ epilayers with a thickness of 0.35–0.75 μm ; the solid-solution composition corresponded to $x = 20\text{--}30\%$. 70-Å-thick intermediate layers of GaAs were grown between the waveguide and the layers of the active-region. The active region of the laser heterostructure consisted of two stressed $\text{In}_x\text{Ga}_{1-x}\text{As}$ quantum wells with $x = 15\text{--}20\%$ and a thickness of 50–80 Å. A typical energy band diagram of a heterostructure with separate confinement is shown in Fig. 1. Zinc and silicon were used as the acceptor and donor dopants, respectively. The diagram shows the doping level calculated for the wide-gap emitters and the waveguide layers.

Doping profiles, as well as the thicknesses and compositions of layers, were determined using a Polaron-4200 profilometer and a JEOL T220A scanning electron microscope.

3. THE DIODE LASER SAMPLES

Using the InGaAs/GaAs/AlGaAs heterostructures with separate confinement, we employed the conven-

tional technique for fabricating diode lasers with a wavelength of 0.98 μm and a strip width $w = 100 \mu\text{m}$ [1–3]. The diodes were mounted on a copper heat sink with their strip contact pointing down. The Fabry–Perot cavity was covered with reflective and antireflective SiO_2/Si dielectric coatings [1–3]. The I – W and I – V characteristics of the diode lasers were measured in the temperature range $T = 0\text{--}70^\circ\text{C}$ with the diodes mounted on the heat sink. The table lists the parameters of the diode lasers based on the structures with a different waveguide thickness D_w and, for the sake of comparison, with a GaAs waveguide [3].

4. RESULTS AND DISCUSSION

For all of the structures under study, the threshold density of current in the four cleaved samples ($1/L \rightarrow 0$, L is the cavity length) is about 70–80 A/cm^2 per quantum well, which, by implication of the equality for the threshold concentration of nonequilibrium carriers, confirms the high quality of the laser heterostructures. At the initial portion of the I – W characteristic of lasers with a cavity length $L = 1.5\text{--}2 \text{ mm}$, the differential quantum efficiency η_d amounts to 80–90%. Figure 2 shows a plot of the inverse differential quantum efficiency $1/\eta_d$ versus the cavity length L for the fused-on lasers with reflective and antireflective dielectric SiO_2/Si coatings on the Fabry–Perot cavity edges. The approximation of these dependences by straight lines drawn through the minimal values for each cavity length allows the determination of both the internal optical loss factor α_i and the internal quantum yield of the stimulated radiation (see table). The internal quantum yield of the diode lasers with a wide-gap waveguide approaches 100% and considerably exceeds the value attained in the diode lasers with a GaAs waveguide.

Using a wide-gap AlGaAs waveguide with a thickness $D_w = 0.75 \mu\text{m}$ leads to an increase in the internal optical loss in the S-1435 structure. This is due to the reduction of the optical confinement factor in a wide-gap waveguide. However, widening of the waveguide up to 1.5 μm in the S-1453 structure balances this change and the internal loss factor remains at the level $\alpha_i = 1.6 \text{ cm}^{-1}$, which is close to the loss in the structures with S-1450 (this study) and X-2578 [3] structures with a GaAs waveguide.

Diode Laser Parameters

Structure	Internal optical losses, α_i , cm^{-1}	Peak power of emission, W	Threshold density of current J_{th} , A/cm^2 ($L = 1.5\text{--}2.0 \text{ mm}$)	Differential quantum efficiency η_d , % ($L = 1.5\text{--}2.0 \text{ mm}$)	Internal quantum yield η_i , %
S-1435 ($D_w = 0.75 \mu\text{m}$)	1.9	5.8	230	80–83	97
S-1453 ($D_w = 1.5 \mu\text{m}$)	1.6	6.6	250	80–82	94
X-2578 [3] and S-1450 ($D_w = 0.6 \mu\text{m}$, GaAs)	1.4–1.7	5.2	120	56	60–65

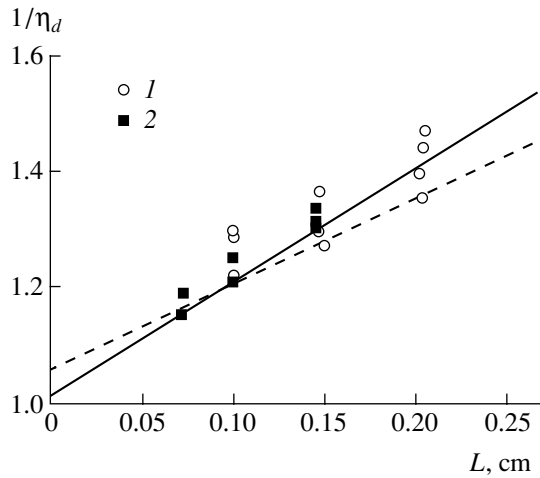


Fig. 2. The inverse differential quantum efficiency $1/\eta_d$ vs. the cavity length L for the diode lasers fabricated on the basis of (1, the solid line) S-1435 and (2, dashed line) S-1453 structures.

The beam divergence in the plane perpendicular to the epilayers is defined by the effective size of the emitting area. This area depends on the stationary configuration of the electromagnetic field, which is formed due to a discontinuity in the effective refractive index at the interfaces between the waveguide and the emitter layers. A sufficiently large discontinuity in the refractive index implies a “strong” waveguide, which decreases the emitting area but increases the beam divergence. From two waveguides of equal thickness, the wide-gap one has a lower “strength” and also a smaller divergence of radiation in the plane perpendicular to the epilayers. As a result, the beam divergence in S-1435 and S-1453 structures varies in the range 25° – 30° , while in the structure with the “strongest” GaAs waveguide it amounts to 45° – 50° . At the same time, the cutoff condition related to the possible existence of any mode except the fundamental one is defined by the waveguide “strength” (width and discontinuity of the refractive index). Consequently, in order to exclude the possibility of the generation of the second mode, the total thickness of the waveguide layers in the structure with a narrow-gap GaAs waveguide should not exceed $2\ \mu\text{m}$ (Fig. 3). It should be noted that these conditions are already suitable for the existence of the first mode in both types of structures; however, because of a negligible optical confinement factor of the first mode in the active region, the threshold lasing conditions fail and only the fundamental mode is observed.

A low divergence of radiation in heterostructures with a widened wide-gap waveguide (S-1435 and S-1453 samples) permits a more effective input of the radiation into the fiber, which has special importance in the design of optical systems. For example, for the diode lasers with a “strong” waveguide ($\theta_\perp = 45^\circ$ – 55°),

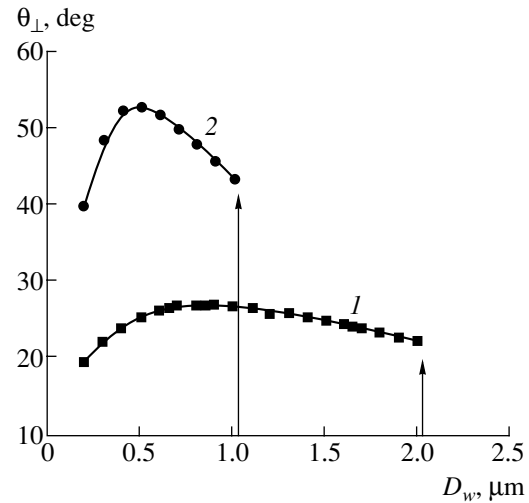


Fig. 3. Beam divergence vs. the waveguide width D_w , measured for the diode lasers with (1) a wide-gap AlGaAs waveguide S-1435 and (2) a GaAs waveguide S-1450, X-2578, according to the data from [3]. Arrows indicate the appearance of the second-order modes.

the coefficient of input into a $60\text{-}\mu\text{m}$ -diam. fiber (NA-0.22) does not exceed 60–65%, whereas for the lasers mentioned above, ($\theta_\perp = 25^\circ$ – 30°) a value as large as 85% is ensured.

We previously demonstrated [3] that the use of GaAs waveguide layers offers certain technological advantages which simplify the choice of the mode of switching between gas flows during epitaxy. However, this limits the depth of the potential quantum well for both electrons and holes. Even making the active region of the epilayer from a strained InGaAs solid solution (emitting at a wavelength of $1.03\ \mu\text{m}$) results in only a

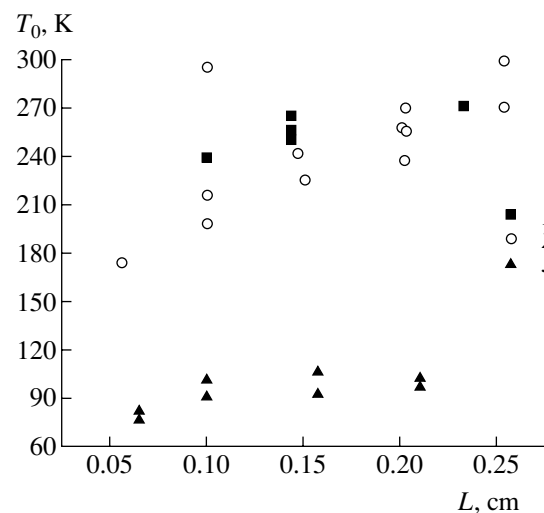


Fig. 4. Characteristic temperature T_0 vs. the cavity length L in the diode lasers with wide-gap AlGaAs waveguides (1) S-1435, (2) S-1453, and (3) with a GaAs waveguide S-1450, X-2578, according to the data from [3].

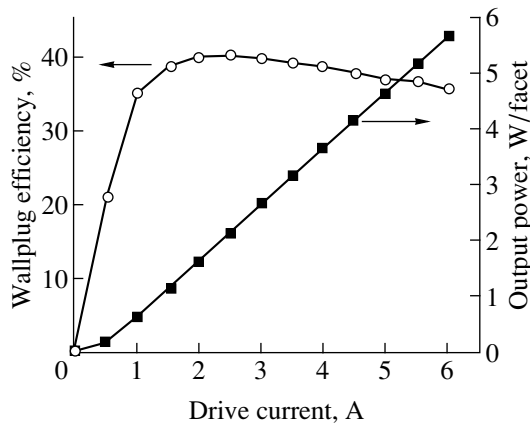


Fig. 5. W - I characteristic and the efficiency of lasing vs. the drive current for the diode laser S-1435.

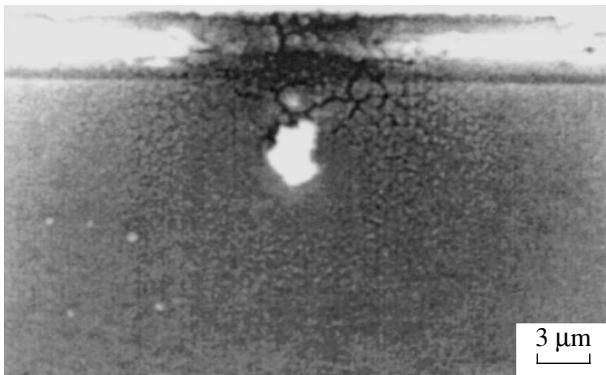


Fig. 6. The edge of a degraded diode laser S-1435 with an antireflecting SiO_2/Si coating.

slight increase in this value (~ 75 meV). As a consequence, both the threshold density of current and the differential quantum efficiency feature high temperature sensitivity [3]. This situation can be radically changed by using a wide-gap waveguide. The temperature sensitivity of the threshold density of current is conventionally characterized by the parameter T_0 , which appears in the empirical dependence of the threshold current $J_{\text{th}}(T) \propto \exp(T/T_0)$. Figure 4 shows a characteristic temperature T_0 versus the length of the diode lasers for the S-1435, S-1450, and S-1453 laser heterostructures. It can be seen that the temperature sensitivity of the threshold density of current increases with a decrease in the cavity length for all types of the laser structures except for the heterostructures with a wide-gap waveguide, where it significantly decreases. This results from the deepening of the quantum wells in the active region, which, even in short diode lasers, accounts for the suppression of additional mechanisms with increasing temperature; these mechanisms may contribute to threshold current growth due to the ejection of electrons from the active region into the waveguide layers.

Temperature dependences of the threshold density of current and the differential quantum efficiency are of great importance in the design of high-power diode lasers, since the continuous working current heats the active region of such lasers to several tens of degrees [4]. Therefore, the reduction of temperature sensitivity of the laser heterostructures in high-power diode lasers is a topical problem, which can be solved by deepening the potential well for free charge carriers.

Figure 5 shows the output power of lasing in a continuous mode and the wallplug efficiency versus the drive current. Neither the overheating of the active region nor the saturation of the I - W characteristic was noticed upon the degradation of the lasers. For all of the lasers, a threshold catastrophic degradation of mirrors was observed. A typical photograph of the Fabry-Perot cavity of a degraded diode laser is shown in Fig. 6. The mean threshold power of the catastrophic degradation of mirrors was found to be 11 MW/cm^2 , which is considerably lower than the currently known values [1, 2, 5, 6]. In our opinion, this may be attributed to the overheating of SiO_2/Si mirrors [7] deposited on the aluminum-containing layers of the heterostructure.

CONCLUSION

The metal-organic chemical vapor deposition (MOCVD) technique was elaborated for GaAs/InGaAs/AlGaAs laser heterostructures.

Mesa-strip diode lasers were fabricated, and the I - W and I - V characteristics were measured in the temperature range from 10 to 80°C . The threshold densities of current $J_{\text{th}} \approx 150 \text{ A/cm}^2$, the internal optical loss factors $\alpha_i = 1.6$ - 1.9 cm^{-1} , and the internal quantum yield $\eta_i = 85$ - 95% were attained.

In the continuous lasing mode of a diode laser with an aperture of $100 \mu\text{m}$, the obtained optical output power was as high as 6.5 W at the wavelength of $0.98 \mu\text{m}$ and was limited by the threshold of the catastrophic degradation of mirrors. Beam divergence in the plane perpendicular to the p - n junction amounted to $\theta_{\perp} = 25^\circ$ - 30° .

It is demonstrated that the use of wide-gap waveguide layers deepens the potential well in the active region of electrons and, thus, reduces the temperature sensitivity of diode lasers based on GaAs/InGaAs/AlGaAs heterostructures.

ACKNOWLEDGMENTS

We appreciate the help of T. N. Drokina, A. Yu. Leshko, and T. A. Nalet in the fabrication and preparation of the diode laser samples.

This study was supported in part by the Russian Foundation for Basic Research (project no. 01-02-17851) and

the “Physics of Solid-State Nanostructures” program (grant nos. 99-2038 and 99-2037).

REFERENCES

1. D. A. Livshits, I. V. Kochnev, V. M. Lantratov, *et al.*, Electron. Lett. **36**, 1848 (2000).
2. D. A. Livshits, A. Yu. Egorov, I. V. Kochnev, *et al.*, Fiz. Tekh. Poluprovodn. (St. Petersburg) **35** (3), 380 (2001) [Semiconductors **35**, 365 (2001)].
3. D. A. Vinokurov, V. A. Kapitonov, D. N. Nikolaev, *et al.*, Fiz. Tekh. Poluprovodn. (St. Petersburg) **35** (11), 1380 (2001) [Semiconductors **35**, 1324 (2001)].
4. E. G. Golikova, V. A. Kureshov, A. Yu. Leshko, *et al.*, Fiz. Tekh. Poluprovodn. (St. Petersburg) **34** (7), 886 (2000) [Semiconductors **34**, 853 (2000)].
5. A. Al-Muhanna, L. J. Mawst, D. Botez, *et al.*, Appl. Phys. Lett. **62**, 2402 (1993).
6. X. He, S. Srinivasan, S. Wilson, *et al.*, Electron. Lett. **34**, 2126 (1998).
7. Zh. I. Alferov, N. I. Katsavets, V. D. Petrikov, *et al.*, Fiz. Tekh. Poluprovodn. (St. Petersburg) **30** (3), 474 (1996) [Semiconductors **30**, 262 (1996)].

Translated by A. Sidorova-Biryukova

Éduard Mushegovich Kazaryan (on his 60th birthday)



Recently, Éduard Mushegovich Kazaryan celebrated his 60th birthday. He is a prominent specialist in solid-state and semiconductor physics and a full member of the Academy of Sciences of Armenia (ASA). The scientific and pedagogical activity of É.M. Kazaryan is now in its 35th year.

Kazaryan was born on January 16, 1942, into the family of a well-known Armenian journalist. In 1959, Kazaryan entered Yerevan State University (the faculty of physics); from his fourth year of studies, he was transferred to Moscow State University and graduated from there with distinction in 1965. In 1969, after the completion of postgraduate studies, Kazaryan returned to Armenia where he defended his candidate thesis in 1970 and his doctoral thesis in 1981.

In 1996, Kazaryan was elected as a full member of the ASA in the field of solid-state physics. He is a member of the Presidium of the ASA and of numerous specialized councils of experts in Armenia.

Kazaryan began his scientific activity (while still a student at Moscow State University) under the guidance of Professor V.L. Bonch-Bruevich. The main direction of Kazaryan's scientific investigations was related to theoretical studies of the energy-band structure of semiconductors; as a result of these studies, a new, plasma-related mechanism for the indirect absorption of light in a semiconductor was suggested.

The next stage of scientific activity of Kazaryan was related to studies in the field of resonance interaction of laser radiation with solids; in particular, he studied the interaction of a large-amplitude electromagnetic wave with crystal-lattice vibrations. Of special note are Kazaryan's pioneering studies in the field of optical phenomena in low-dimensional systems; he performed consistent analysis of excitonic effects on the optical-absorption coefficient in dimensionally quantized films and wires and obtained important results for the theory of optical absorption related to transitions between impurity states. Recently, Kazaryan conducted studies on the behavior of electrons and holes in cylindrical and ellipsoidal quantum dots.

A unique characteristic of Kazaryan as a scientist is the diversity of his scientific inclinations, which also helped him to prove himself as a teacher and promoter of science and education. Kazaryan began his pedagogical activity at the faculty of solid-state physics of Yerevan State University; later on, for ten years he was the head of the department of general physics at the Yerevan Polytechnical Institute. From 1987 to 1988, Kazaryan was the head of the Abovyan Armenian Pedagogical Institute. From 1993, he was back at Yerevan State University, first as a professor in the department of solid-state physics, then as the head of this department, and finally as the University's vice-head for the promotion of higher education. From 1999 to 2001, Kazaryan was the minister of education and science of Armenia.

Academician Kazaryan is the author and co-author of more than 170 scientific papers, high-school and university textbooks on solid-state and semiconductor physics, and publications devoted to the problems in teaching physics. He is the founder and the editor-in-chief of the scientific journal "Estestvoispytatel'" ("Natural Scientist") and a member of the Editorial Board of the journal "Izvestiya NAN Armenii. Fizika" ("Bulletin of the Academy of Sciences of Armenia: Physics").

Kazaryan is actively engaged in the training of scientists and teachers. The majority of his pupils and followers have become Candidates and Doctors of Science and are now successfully engaged in scientific activity in Armenia and abroad. Kazaryan was an initiator and organizer of semiconductor-theory workshops–schools for young Armenian scientists; these workshops were regularly convened in the 1970s–1980s with the participation of scientists from the Ioffe Physicotechnical Institute of the USSR Academy of Sciences and from other scientific centers of the USSR.

In recognition of the outstanding scientific achievements of Kazaryan, he was awarded the Abovyan Medal (1972) and the Prize of the Lenin's Youth Organization of Armenia (1976).

Kazaryan is celebrating his 60th birthday filled with energy and new creative ideas. We wish him good health, a long creative life, and success in every endeavor directed towards the development of science and education in Armenia.

Colleagues and friends

The Editorial Board of this journal would also like to wish Kazaryan good health and further creative achievements.

Translated by A. Spitsyn

ATOMIC STRUCTURE
AND NONELECTRONIC PROPERTIES
OF SEMICONDUCTORS

Doping of GaAs Layers with Si under Conditions of Low-Temperature Molecular Beam Epitaxy

M. D. Vilisova*, A. E. Kunitsyn**, L. G. Lavrent'eva***,
V. V. Preobrazhenskii****, M. A. Putyato****, B. R. Semyagin****,
S. E. Toropov***, and V. V. Chaldyshev**

* Siberian Physicotechnical Institute, Tomsk State University,
pr. Lenina 36, Tomsk, 634050 Russia

** Ioffe Physicotechnical Institute, Russian Academy of Sciences,
Politekhnicheskaya ul. 26, St. Petersburg, 194021 Russia

*** Tomsk State University, pr. Lenina 36, Tomsk, 634050 Russia
e-mail: lavr@ic.tsu.ru

**** Institute of Semiconductor Physics, Siberian Division, Russian Academy of Sciences,
pr. Akademika Lavrent'eva 13, Novosibirsk, 630090 Russia

Submitted January 8, 2002; accepted for publication January 16, 2002

Abstract—Using the methods of X-ray diffraction, optical absorption in the near-infrared range, and the Hall effect, the influence of growth conditions on the structure and properties of Si-doped GaAs layers grown by low-temperature molecular-beam epitaxy was investigated. The relation between the incorporation of excess As and electrical properties of the layers is analyzed. © 2002 MAIK “Nauka/Interperiodica”.

1. INTRODUCTION

It is known that GaAs grown by molecular-beam epitaxy (MBE) at low (150–250°C) temperatures (LT-GaAs) contains excess As, whose concentration is beyond the homogeneity region [1–4]. The incorporation of excess As leads to the tetragonal distortion of the LT-GaAs lattice and generation of an ensemble of point defects in it, namely, antisite defects (As_{Ga}), interstitial atoms (As_i), and vacancies (V_{Ga}). The lattice distortion and concentration of generated point defects depend on growth conditions, namely, the growth temperature, Ga and As molecular beams, and the concentration and chemical nature of dopants [5–10]. The ensemble of point defects in LT-GaAs is metastable. Heat treatment above 500°C after low-temperature growth leads to the formation of nanoscale precipitates (clusters) and a considerable decrease in the concentration of point defects [2–4].

Nominally undoped LT-GaAs usually has a resistivity of 10^2 – 10^4 Ω cm. The main mechanism of charge-carrier transport up to room temperature is hopping conduction over deep levels, which are generated by native point defects [5, 9]. After heat treatment, the defect concentration decreases, and the material becomes semi-insulating. To obtain conducting LT-GaAs layers, doping with Be (*p*-type) and Si (*n*-type) is used [8, 9].

In this study, the structure and electrical properties of undoped and Si-doped LT-GaAs layers were investigated in relation to the growth conditions. Based on these investigations, the relation between the electrical

activity of the Si donor impurity and the incorporation of excess As under conditions of low-temperature MBE is considered.

2. EXPERIMENTAL PROCEDURE

The LT-GaAs layers were grown on semi-insulating GaAs(001) substrates using a Katun' MBE system. A buffer layer 500 nm thick was initially grown on the substrate at 580°C. Then, the substrate was cooled to 150, 200, or 250°C, and an undoped or Si-doped LT-GaAs layer, 1 μ m thick, was grown. The temperature of the Si source provided a free electron density $n = 1 \times 10^{19}$ cm⁻³ for GaAs layers grown at the conventional temperature of 500°C. The As/Ga flux ratio (J_{As}/J_{Ga}) varied from 1.1 to 21. The constant growth rate of the layers was ≈ 1 μ m/h. After growth, the samples were removed from the chamber and divided into two parts. One part of each sample was investigated after growth (as-grown samples), and the other part was investigated after heat treatment in the growth chamber in an As₄ flux at 600°C for 10 min.

Structural investigations of the layers were carried out using double-crystal X-ray diffractometry (CuK_{α} radiation, (004) reflection). The electrical parameters were determined by measuring the electrical conductivity and the Hall coefficient using the van der Pauw method. To determine the concentration of antisite defects, optical absorption spectra were measured in the near-infrared (IR) range. The Si concentration in the

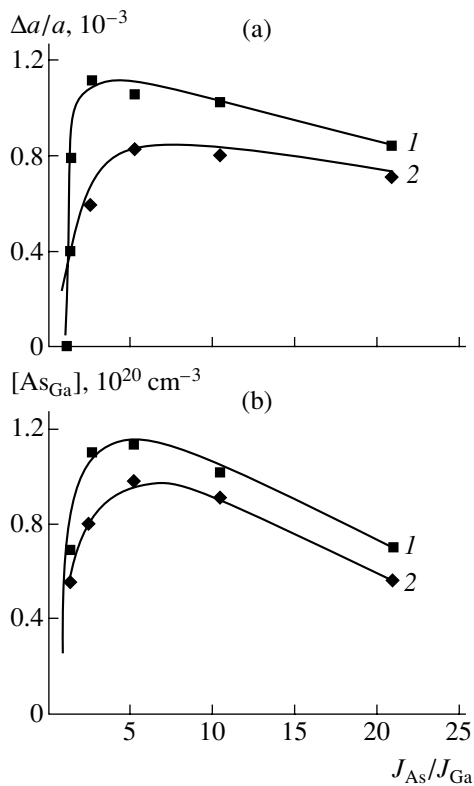


Fig. 1. Influence of the flux ratio J_{As}/J_{Ga} on the variation of (a) lattice parameter and (b) concentration of As_{Ga} defects for GaAs layers: (1) undoped and (2) Si-doped. The growth temperature is 150°C.

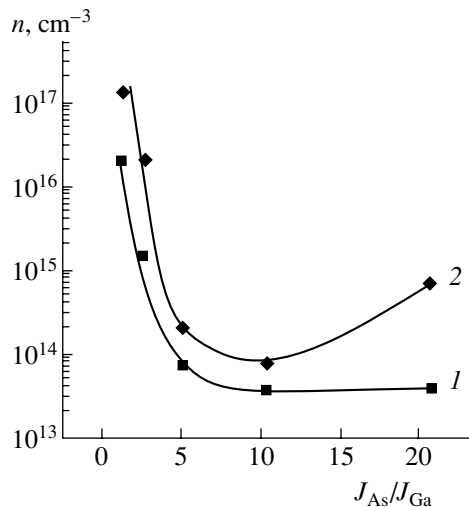


Fig. 2. Influence of flux ratio J_{As}/J_{Ga} on the free-carrier density in Si-doped layers: (1) as-grown and (2) heat-treated at 600°C for 10 min.

layers was monitored using secondary-ion mass spectrometry (SIMS).

3. RESULTS AND DISCUSSION

Two reflection peaks were observed in the X-ray diffraction curves of the LT-GaAs samples. This

permitted us to determine the lattice mismatch between the epilayer and the substrate: $\Delta a/a = (a_l - a)/a$. Here, a_l and a refer to the layer and substrate, respectively.

For all of the as-grown samples, $\Delta a/a > 0$. Thus, as was expected, the lattice parameter of the LT-GaAs layers increases, which is caused by the incorporation of excess As.

The influence of the component flux ratio J_{As}/J_{Ga} on the lattice mismatch $\Delta a/a$ for undoped (1) and Si-doped (2) layers grown at 150°C is shown in Fig. 1a. It can be seen that, with the deviation from stoichiometry conditions, the lattice parameter of the layers increases sharply in the range of $1 < J_{As}/J_{Ga} < 5$. For $J_{As}/J_{Ga} > 5$, the lattice parameter decreases gradually. A similar dependence $\Delta a/a$ on J_{As}/J_{Ga} for undoped GaAs layers was observed previously at the growth temperature of 200°C [10].

The data shown in Fig. 1a demonstrate that doping introduces no variations in the character of the dependence of $\Delta a/a$ on J_{As}/J_{Ga} . However, it does affect the magnitude of $\Delta a/a$. Over the entire range of flux ratios J_{As}/J_{Ga} , the lattice parameter for Si-doped layers is smaller than that for undoped layers. According to the estimation, the relative variation of the lattice parameter due to the substitution of Si atoms for Ga atoms at a concentration of $1 \times 10^{19} \text{ cm}^{-3}$ can be as large as 1.7×10^{-5} . This value is an order of magnitude smaller than the $\Delta a/a$ variation observed experimentally. Consequently, a decrease in the lattice parameter for Si-doped layers is caused by a decrease in the concentration of excess As. This conclusion is confirmed by the results of measuring the concentration of As_{Ga} antisite defects for undoped and Si-doped layers (Fig. 1b). From a comparison of Figs. 1a and 1b, it can be seen that the concentration of antisite defects $[As_{Ga}]$ and the lattice parameter vary similarly as the J_{As}/J_{Ga} ratio increases. In this case, the $[As_{Ga}]$ concentration for a doped layer is always lower compared with undoped layers.

A single reflection peak was observed in the X-ray diffraction curves of the samples annealed at 600°C for 10 min. Thus, heat treatment of the layers causes the lattice parameter to decrease to a value close to that for the GaAs substrate. In this case, the concentration of As_{Ga} defects decreases by more than an order of magnitude.

Measurements of the electrical properties of the layers demonstrated that undoped layers, both as-grown and heat-treated, had high resistivity. The measurement of resistivity is hampered due to the shunting effect of the substrate.

The Si-doped layers have the n -type conduction. The electron density depends on the flux ratio J_{As}/J_{Ga} during layer growth. Even for a slight deviation from the stoichiometry ($J_{As}/J_{Ga} = 1.3$), the electron density in the layers ($2 \times 10^{16} \text{ cm}^{-3}$) is substantially lower compared with the dopant concentration ($N_{Si} \approx 1 \times 10^{19} \text{ cm}^{-3}$). As the flux ratio J_{As}/J_{Ga} increases from 1.3 to 5, the electron density decreases drastically, whereas for $J_{As}/J_{Ga} > 5$ it

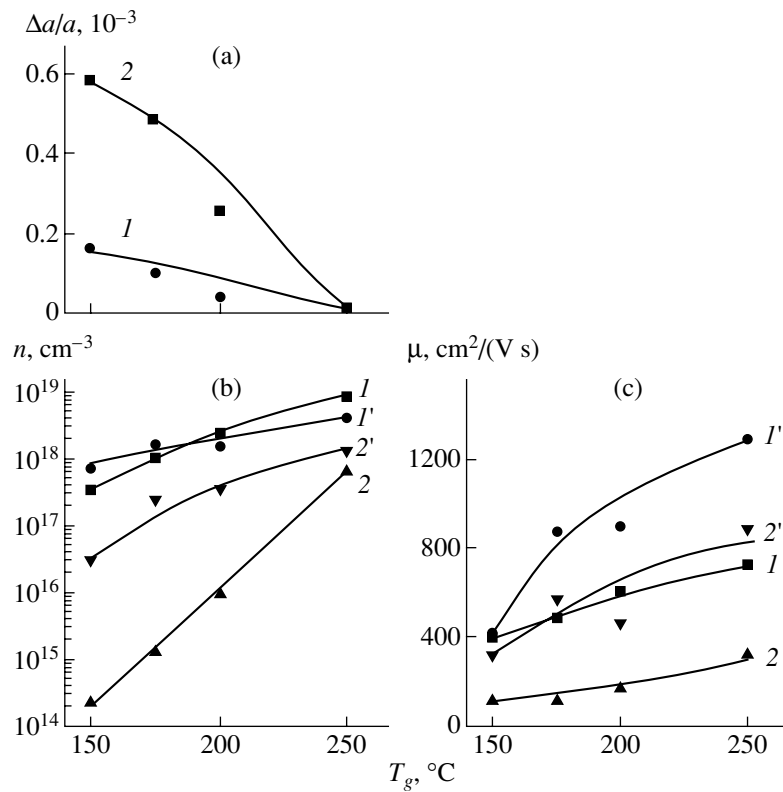


Fig. 3. Influence of the growth temperature on (a) lattice parameter, (b) electron density, and (c) electron mobility for (*I*, *2*) as-grown and (*I'*, *2'*) heat-treated layers. $J_{As}/J_{Ga} = 1.1$ (*I*, *I'*) and $J_{As}/J_{Ga} = 3$ (*2*, *2'*).

varies slightly (Fig. 2, curve *I*). Heat treatment (600°C, 10 min) leads to a decrease in the electron density (Fig. 2, curve *2*). However, for all heat-treated layers, n is substantially lower compared with the total concentration N_{Si} . The Hall carrier mobility for as-grown layers is 100–140 cm² V⁻¹ s⁻¹ and increases to 250–500 cm² V⁻¹ s⁻¹ for heat-treated layers.

Thus, a low electron density ($n \ll N_{Si}$) and low Hall mobility are characteristic of the layers grown at 150°C. It is obvious that a large portion of the Si dopant incorporated into the layers is electrically inactive at this temperature, whereas the hopping conduction over deep levels has great significance for the charge-transport mechanism.

The situation changes radically with increasing growth temperature. The dependences of (Fig. 3a) the lattice parameter, (Fig. 3b) the electron density, and (Fig. 3c) the electron mobility on the growth temperature T_g for two series of samples grown with different flux ratios ($J_{As}/J_{Ga} = 1.1$ and $J_{As}/J_{Ga} = 3$ for the first and second series, respectively) are shown in Fig. 3.

It can be seen from Fig. 3 that with increasing the growth temperature, the lattice distortion $\Delta a/a$ decreases and approaches zero at $T_g = 250^\circ\text{C}$. A simultaneous increase in the electron density for the as-grown layers is observed (Fig. 3b, curves *I*, *2*). This increase is about one order of magnitude for the layers

grown under virtually stoichiometric conditions ($J_{As}/J_{Ga} = 1.1$). However, this increase is as large as three orders of magnitude for a sharper deviation from stoichiometry ($J_{As}/J_{Ga} = 3$). At the same time, the total Si concentration in the layers, according to the SIMS data, varies insignificantly.

At the growth temperature $T_g = 250^\circ\text{C}$ and for the flux ratio $J_{As}/J_{Ga} = 1.1$, the electron density in the layers is equal to 8×10^{18} cm⁻³; i.e., almost all of the Si dopant is electrically inactive. The electron Hall mobilities are rather high. This fact indicates that the conduction is primarily effected by free carriers. Thus, the layers grown even at a relatively low temperature ($T_g = 250^\circ\text{C}$), but with a slight deviation from stoichiometry, have parameters close to those obtained at conventional epitaxy temperatures (500–600°C). If the flux ratio $J_{As}/J_{Ga} = 3$ at the same growth temperature of 250°C, the electron density for the layers is an order of magnitude lower than the Si concentration. Judging from the mobility value, these layers are heavily compensated and the degree of compensation increases with decreasing T_g .

Heat treatment of the layers usually reduces the lattice distortion and increases the electron mobility and density. The layers grown with $J_{As}/J_{Ga} = 1.1$ at a temperature of 200–250°C are exempted from this rule. A slight decrease in the electron density is observed for these heat-treated layers (Fig. 3b, curve *I'*). For heat-

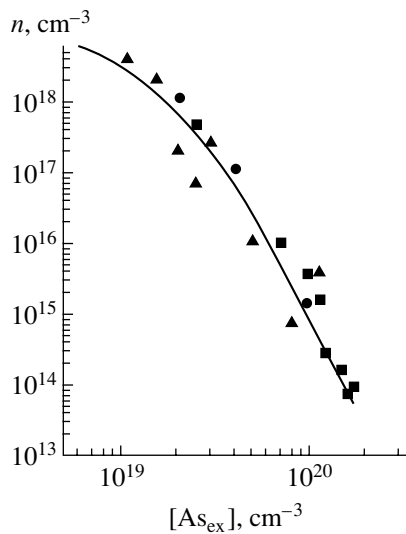


Fig. 4. Influence of excess As concentration on the free-carrier density in Si-doped LT-GaAs layers grown at various temperatures T_g and with flux ratios J_{As}/J_{Ga} .

treated layers that were grown with a higher excess of As ($J_{As}/J_{Ga} = 3$) and at a low temperature (150–175°C), the electron density after heat treatment increases by two orders of magnitude. However, this density remains considerably lower than the impurity concentration. Judging from the electron mobility, which is no higher than $850 \text{ cm}^2 \text{ V}^{-1} \text{ s}^{-1}$, the heat-treated layers remain heavily compensated. It seems that the heat-treatment conditions used in this study (600°C, 10 min) are insufficient for the complete activation of Si in the layers of the second series.

The above results demonstrate that, under conditions of low-temperature MBE, when the flux ratio is close enough to the stoichiometry ($J_{As}/J_{Ga} \approx 1$), it is possible to obtain Si-doped GaAs layers with good electrical parameters. The enrichment of the molecular beam with As leads to the incorporation of excess As into the layer. The As concentration in the layer increases sharply as the flux ratio increases in the range $1 < J_{As}/J_{Ga} < 5$, and the epitaxy temperature decreases below 250°C. In this case, a sharp decrease in the free-carrier density and mobility is observed for the layers. Hence, it follows that an interrelation exists between the concentration of excess As in LT-GaAs layers and their electrical parameters. In order to reveal this interrelation, the correlation dependence of electron density n in the layers on the concentration of excess As $[As_{ex}]$ was plotted (Fig. 4). For this purpose, the results of measurements for all LT-GaAs layers grown under a varying growth temperature and J_{As}/J_{Ga} flux ratio were used. The $[As_{ex}]$ concentration was determined using the previously plotted [3] dependence of the lattice parameter $\Delta a/a$ for LT-GaAs on the concentration of excess As $[As_{ex}]$. This concentration was measured using X-ray spectral microanalysis ($[As_{ex}] = \{[As] - [Ga]\}/\{[As] + [Ga]\}$).

Despite a rather wide scatter of points, Fig. 4 demonstrates a steady regular decrease in the electron density as $[As_{ex}]$ increases in the range $1 \times 10^{19} \dots 2 \times 10^{20} \text{ cm}^{-3}$. It is noteworthy that, as the concentration of excess As increases by one order of magnitude, a decrease in the free carrier density by more than four orders of magnitude is observed.

The effect of a sharp decrease in the free carrier density in Si-doped LT-GaAs layers grown with excess As was reported previously [8, 9, 11]. It seems likely that this effect is caused by the interaction of the impurity with a point-defect ensemble formed due to excess As. The main point defects in LT-GaAs are antisite defects (As_{Ga}), Ga vacancies (V_{Ga}), and interstitial As atoms (As_i). The concentrations of As_{Ga} and V_{Ga} substantially depend on the crystallization conditions [6, 7]. The question of interstitial As in LT-GaAs remains a subject of debate, since there is no trustworthy information either on the concentration or on the electrical activity of this defect [12, 13]. Calculations demonstrated [12] that the lattice distortion observed in LT-GaAs is quite satisfactorily explained by the presence of As_{Ga} defects. Hence, it follows that the concentration of interstitial As is apparently low.

It is known that As_{Ga} antisite defects introduce deep donor levels into the band gap. For this reason, they cannot lead to either the deactivation or compensation of the Si donor impurity. However, they can be responsible for hopping conduction. The major compensating centers in Si-doped GaAs layers are Ga vacancies, which can be singly ionized, doubly ionized, or triply ionized (V_{Ga}^{1-} , V_{Ga}^{2-} , V_{Ga}^{3-}). If we assume that the triply ionized vacancy is the dominant defect, the concentration of vacancies for the compensation of Si donors at a concentration of $1 \times 10^{19} \text{ cm}^{-3}$, which is observed at $T_g = 150^\circ\text{C}$, should be no lower than $3 \times 10^{18} \text{ cm}^{-3}$. Approximately the same concentration of vacancies in LT-GaAs was determined using positron annihilation [13, 14].

Since the defects responsible for the deactivation of the Si dopant are not annealed at 600°C, one may assume that these defects are not simple point defects, but rather stable associations which include native point defects and dopant atoms. Such associations can be complexes of the $[V_{Ga}-Si_{Ga}]$ type detected in LT-GaAs using photoluminescence studies [9, 15]), as well as Si clusters, whose size can reach 1 nm according to [14].

It should be noted that a sharp decrease in the free-carrier density with a deviation from the stoichiometry toward excess As is characteristic not only for Si-doped LT-GaAs layers. A similar dependence was also observed for Be-doped LT-GaAs layers [8, 9, 16]. In this case, the As_{Ga} antisite defects act as compensating centers. The activity of the Be acceptor decreases only after heat treatment at 800°C [16].

It follows from the above results that a shift of the Fermi level to the midgap and an increase in the resis-

tivity of the material occurs for As-enriched LT-GaAs doped with both donor and acceptor impurities. Similar investigations carried out for LT-In_xGa_{1-x}As ($x = 0.53$) solid solutions [17] demonstrated that, under the conditions of low-temperature MBE, the incorporation of excess As into this material also leads to a shift of the Fermi level. However, a shift to the conduction-band edge is observed. A similar pattern of change in the electrical properties and Fermi level shift under the effect of nonequilibrium point defects is observed in GaAs and other III-V compounds irradiated with high-energy particles [18, 19].

It seems likely that the variations in the electrical properties observed in As-rich LT-GaAs reflect a general pattern of variation in the properties of semiconductor materials when the concentration of nonequilibrium point defects increases. The ensemble of point defects that forms in the material leads to a shift and, finally, the pinning of the Fermi level in the limiting position, which is characteristic of this material. This phenomenon is independent of both the method used for introducing the defects and the characteristics of the starting material. According to [20], F_{lim} in GaAs is located close to the midgap, and in In_xGa_{1-x}As this location is close to the conduction band edge.

4. CONCLUSION

The investigations carried out demonstrated that the structure and electrical properties of LT-GaAs layers depend heavily on the growth temperature and As/Ga flux ratio in the molecular beam. A clear correlation between the properties of the layers and the concentration of excess As in them is observed. For growth under nearly stoichiometric conditions, when the incorporation of excess As is reduced, the properties of LT-GaAs layers approach the properties of layers grown at high temperatures.

A sharp decrease in the conduction electron density upon deviation of the composition of LT-GaAs layers from stoichiometry toward excess As is caused by the formation of an ensemble of point defects. This leads to a shift of the Fermi level to the midgap. This phenomenon is a particular case of the general trend, according to which any substantial disordering in the crystal lattice of a semiconductor leads to a shift of the Fermi level to the position F_{lim} .

REFERENCES

1. M. Kaminska, Z. Liliental-Weber, and E. R. Weber, *Appl. Phys. Lett.* **54**, 1881 (1989).
2. Kin Man Yu, M. Kaminska, and Z. Liliental-Weber, *J. Appl. Phys.* **72**, 2850 (1992).
3. N. A. Bert, A. I. Veinger, M. D. Vilisova, *et al.*, *Fiz. Tverd. Tela (St. Petersburg)* **35**, 2609 (1993) [*Phys. Solid State* **35**, 1289 (1993)].
4. I. A. Bobrovnikova, A. I. Veinger, M. D. Vilisova, *et al.*, *Izv. Vyssh. Uchebn. Zaved., Fiz.*, No. 9, 37 (1998).
5. X. Liu, A. Prasad, W. M. Chen, *et al.*, *Appl. Phys. Lett.* **65**, 3002 (1994).
6. X. Liu, A. Prasad, J. Nishio, *et al.*, *Appl. Phys. Lett.* **67**, 279 (1995).
7. M. Luysberg, M. Sohn, A. Prasad, *et al.*, *J. Appl. Phys.* **83**, 561 (1998).
8. M. Missous and S. O'Hagan, *J. Appl. Phys.* **75**, 3396 (1994).
9. S. O'Hagan and M. Missous, *J. Appl. Phys.* **75**, 7835 (1994).
10. A. Suda and N. Otsuka, *Surf. Sci.* **458**, 162 (2000).
11. S. Fukushima, T. Obata, and N. Otsuka, *J. Appl. Phys.* **89**, 380 (2001).
12. T. E. M. Staab, R. M. Nieminen, J. Gebauer, *et al.*, *Phys. Rev. Lett.* **87** (4), 045504 (2001).
13. J. Gebauer, F. Börner, R. Krause-Rehberg, *et al.*, *J. Appl. Phys.* **87**, 8368 (2000).
14. T. Laine, K. Saarinen, P. Hautojarvi, *et al.*, *J. Appl. Phys.* **86**, 1888 (1999).
15. A. E. Kunitsyn, V. V. Chaldyshev, S. P. Vul', *et al.*, *Fiz. Tekh. Poluprovodn. (St. Petersburg)* **33**, 1187 (1999) [*Semiconductors* **33**, 1080 (1999)].
16. D. E. Bliss, W. Walukiewicz, J. W. Ager, *et al.*, *J. Appl. Phys.* **71**, 1699 (1992).
17. M. D. Vilisova, I. V. Ivonin, L. G. Lavrent'eva, *et al.*, *Fiz. Tekh. Poluprovodn. (St. Petersburg)* **33**, 900 (1999) [*Semiconductors* **33**, 824 (1999)].
18. V. N. Brudnyĭ, M. D. Vilisova, and L. P. Porokhovnichenko, *Izv. Vyssh. Uchebn. Zaved., Fiz.*, No. 10, 57 (1992).
19. V. N. Brudnyĭ, S. N. Grinyaev, and V. E. Stepanov, *Physica B (Amsterdam)* **212**, 429 (1995).
20. V. N. Brudnyĭ and S. N. Grinyaev, *Fiz. Tekh. Poluprovodn. (St. Petersburg)* **32**, 315 (1998) [*Semiconductors* **32**, 284 (1998)].

Translated by N. Korovin

ATOMIC STRUCTURE
AND NONELECTRONIC PROPERTIES
OF SEMICONDUCTORS

Mechanism of Copper Diffusion over the Si(110) Surface

A. E. Dolbak, R. A. Zhachuk, and B. Z. Olshanetsky*

*Institute of Semiconductor Physics, Siberian Division, Russian Academy of Sciences,
pr. Akademika Lavrent'eva 13, Novosibirsk, 630090 Russia*

* e-mail: *olshan@isp.nsc.ru*

Submitted January 23, 2002; accepted for publication January 29, 2002

Abstract—The mechanism of Cu diffusion over a clean Si(110) surface was studied by Auger electron spectroscopy and low-energy electron diffraction in the temperature range from 500 to 650°C. It is shown that the Cu transport over the Si(110) surface proceeds by Cu atom diffusion through the Si bulk and Cu atom segregation at the surface during diffusion. The temperature dependence of the effective Cu diffusivities at the clean Si(110) surface was found. The results were compared to those previously found for a Si(111) surface. © 2002 MAIK “Nauka/Interperiodica”.

INTRODUCTION

Surface diffusion plays an important role in many processes at the surface of a solid. However, this process has not been experimentally studied in sufficient detail. Copper diffusion over atomically clean silicon surfaces is of great interest in the context of the active use of copper in the production of microcircuits. Previously, we studied Cu diffusion over the Si(111) surface [1]. In this paper, we present data on Cu transport over the Si(110) surface, which was studied by Auger electron spectroscopy (AES) and low-energy electron diffraction (LEED). Special emphasis is placed on the mechanism of Cu transport over the silicon surface. The Cu/Si system has been studied in sufficient detail for various silicon orientations [2–10]. Copper adsorption at the Si(110) surface was studied by LEED and AES in [10]. It has been established that this process causes the formation of a number of surface structures at the Si(110) surface, depending on the Cu concentration at the surface and annealing temperatures. These are structures 2×1 , 4×5 , 4×3 , and 6×6 .

EXPERIMENTAL

The experiments were carried out with *p*-type Si(100) samples with a resistivity of 5–10 Ω cm and a size of $22 \times 5 \times 0.3$ mm. The surface was cleaned by preliminary annealing at a temperature of 600°C and pressure of $(1-2) \cdot 10^{-10}$ Torr and subsequent annealing at 1200°C for 1–2 min. The samples were heated by alternating current. The sample temperature *T* was measured using an optical pyrometer. The clean surface had the structure (see [11])

$$\begin{pmatrix} 11 & 5 \\ -2 & 2 \end{pmatrix}.$$

A copper strip with an abrupt boundary was deposited onto an atomically clean silicon surface and was used as the Cu source (Fig. 1). The strip thickness was about 40 monolayers (ML). The Cu concentration was measured by AES using the Auger peaks Cu MNN (60 eV) and LMM (920 eV) and the Si Auger peak (92 eV). The coefficients of elemental sensitivity were taken from [12]. To determine the copper coating thickness, we compared our data to those obtained in [10], where the Cu coatings measured using a quartz microbalance were compared to the corresponding Auger signals of Cu and Si. The copper deposition rate was 0.2 ML per minute.

After sample annealing at 500°C and above, LEED patterns corresponding to a Si(110)- 4×3 -Cu surface structure were observed in the silicon surface area where the copper strip was deposited. This is probably caused by the fact that Cu_3Si islands are formed at the surface [2–5]; silicon surface areas with the indicated structure are arranged between these islands. The diameter of the primary electron beam in the Auger spectrometer and in the LEED system was about 30 μm and 0.8 mm, respectively.

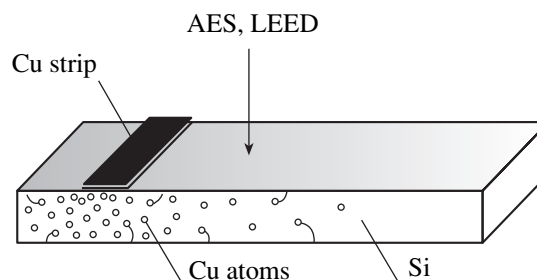


Fig. 1. Experimental scheme.

RESULTS AND DISCUSSION

The experiments with the Si(110) face were carried out in the temperature range of 500–650°C. Studies below 500°C were not carried out, since the measurement of diffusion profiles resolved by the AES method under such conditions would require a long annealing time. At temperatures above 650°C, copper evaporation from the silicon surface becomes significant, which was indicated from the LEED and AES methods through the disappearance of the Si(110)- 4×3 -Cu structure and a decrease of Cu Auger peaks from the strip. To study the Cu transport, we annealed the samples at a certain temperature for time t . After cooling to room temperature, the concentration distribution $C_{\text{Cu}}(x)$ over the silicon surface (x is the distance from the copper strip edge) was measured by AES; the surface structure was studied by LEED.

A typical concentration distribution $C_{\text{Cu}}(x)$ over the Si(110) surface after a 20-h annealing at 600°C is shown in Fig. 2. The structures formed at the surface are indicated. The Si(110)- (6×6) -Cu surface structure caused by copper [10] was not observed.

The Auger peaks from copper at the Si(110) surface could be measured in the course of sample annealing, i.e., during diffusion, as was done in the experiments on Si(111) [1]. The Cu concentration measured in the course of annealing at any surface point at a distance x from the strip edge was equal to the concentration measured at the same surface point after the rapid cooling of the sample to room temperature.

As is known, copper is characterized by high solubility and diffusivity in silicon bulk [13, 14]. Therefore, this study was aimed at determining the contribution of Cu diffusion through the silicon bulk to the Cu transport over the Si(110) surface. To do this, we deposited a 0.2-mm-wide copper strip onto the sample axial line parallel to its long side and heated the sample at 600°C for 1 h. Under such conditions, the boundaries of the found Cu diffusion distribution did not extend to the sample edges. Thereafter, we measured the Cu concentration distribution $C_{\text{Cu}}(y)$ (y is the distance at the normal from the sample midline to the long side). Then, similar measurements were carried out for the sample rear side. The results (see Fig. 3) indicate that the lengths of the concentration distributions $C_{\text{Cu}}(y)$ and the Cu concentration are pretty much the same on both sides of the sample. Since copper could not emerge at the rear side via diffusion over the surface under the chosen experimental conditions, this result means that Cu transport over the Si(110) surface proceeds by diffusion through the bulk. The transport mechanism of adsorbed atoms over the silicon surfaces via their diffusion through the bulk was previously observed in studies of the surface heterodiffusion of Ni on Si [11, 15, 16]. However, the Auger signal from nickel was not measured during Ni diffusion over clean silicon surfaces. The Ni distributions were observed only after sample cooling, owing to nickel segregation at the surface due

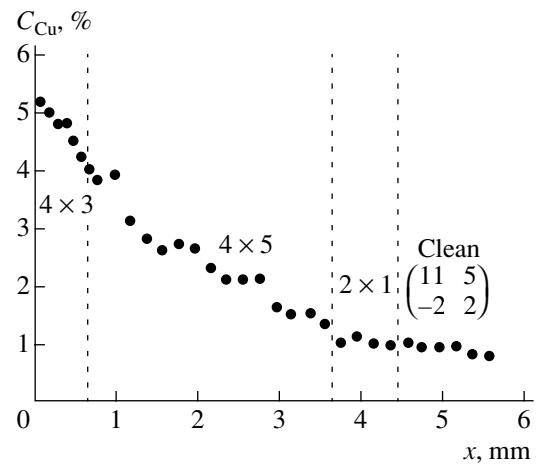


Fig. 2. Typical concentration distribution $C_{\text{Cu}}(x)$ at the Si(110) surface after 20-h annealing at $T = 600^\circ\text{C}$.

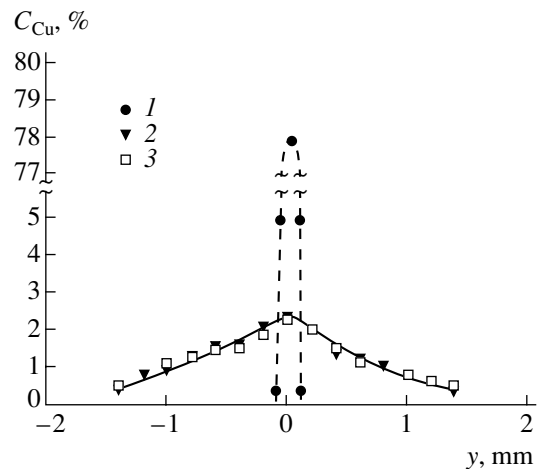


Fig. 3. Concentration distributions $C_{\text{Cu}}(y)$ at the Si(110) surface after copper deposition onto the sample at room temperature (1) and after 1-h annealing at $T = 600^\circ\text{C}$ at the front (2) and rear (3) sides.

to a decrease of its solubility in the silicon bulk as the temperature decreased. The copper presence at the silicon surface in the course of sample annealing means that copper segregation and trapping at the surface takes place even during diffusion. A similar transport mechanism, including diffusion through the silicon bulk and trapping of diffusing atoms at the surface during diffusion, is characteristic of Ni propagation over the silicon surface with submonolayer coatings of adsorbed Co and Fe atoms [17–19].

Thus, taking into account the considered experimental data, the Cu atom transport over the clean Si surface may be conceived as follows. Copper from the deposited strip is dissolved in silicon upon heating. In the temperature range of 500–650°C, the Cu solubility in Si is 1×10^{14} – 3×10^{15} cm^{-3} [13]. Then, copper diffuses in the silicon bulk and is segregated at the surface.

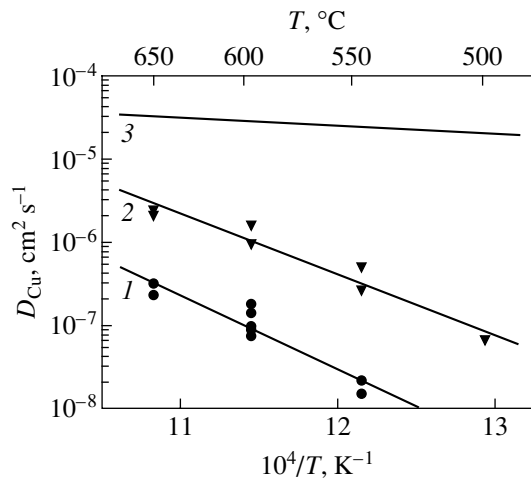


Fig. 4. Temperature dependences of the Cu diffusivities at the Si(111) (1) and Si(110) (2) surfaces, as well as in the Si bulk (3).

A similar experiment was carried out with a Si(111) sample. Identical Cu distributions were found at both sides, although these distributions differed from those characteristic of the Si(110) surface. Hence, the conclusion about the Cu transport at the Si(111) surface via surface diffusion according to the “solid-phase spreading” mechanism we suggested previously, which is based on the shape of the $C_{Cu}(x)$ distribution at the Si(111) surface and the Auger signal from copper at the silicon surface in the course of annealing [1], turns out to be incorrect.

Copper transport over the silicon surface is an intricate process, which includes Cu dissolution in the silicon bulk, diffusion through the bulk, and segregation at the surface. Hence, we can consider only the effective diffusivity of copper over the silicon surface. Furthermore, effective diffusivity can depend on the sample thickness. To estimate the effective diffusivities D of copper atoms over the silicon surface at 500–650°C, the relation $D = x^2/2t$ was used. The measurement data are shown in Fig. 4. The temperature dependence of the effective diffusivity of copper over the Si(110) surface may be given by $D_{Cu/Si(110)} = 1.56 \times 10^2 \exp(-1.42 \text{ eV}/kT) \text{ cm}^2 \text{ s}^{-1}$. For the Si(111) surface, this dependence can be described as $D_{Cu/Si(111)} = 1.52 \times 10^3 \exp(-1.77 \text{ eV}/kT) \text{ cm}^2 \text{ s}^{-1}$.

As is known, the bulk diffusivity of Cu in Si, depending on temperature, is given by $D_{Cu} = 3.0 \times 10^{-4} \exp(-0.18 \text{ eV}/kT) \text{ cm}^2 \text{ s}^{-1}$ [14] and is $3 \times 10^{-5} \text{ cm}^2 \text{ s}^{-1}$ at 600°C. As follows from the data of Fig. 4, the measured coefficients of Cu transport over the Si(111) and (110) surfaces are dissimilar and are smaller than the bulk diffusivity at corresponding temperatures. Since Cu atom transport over the surface proceeds through the Si bulk, the difference between the concentration distributions $C_{Cu}(x)$ and the measured effective diffusivities over the Si(111) and Si(110) surfaces is caused by the features of Cu atom segregation at these surfaces

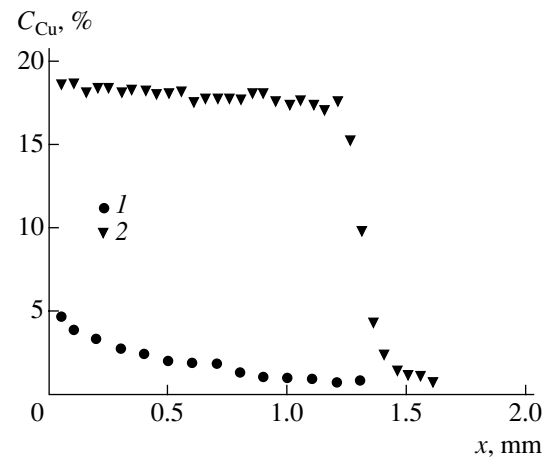


Fig. 5. Distributions $C_{Cu}(x)$ at the Si surface, observed after annealing of Si(110) ($t = 20$ h) (1) and Si(111) ($t = 15$ h) (2) at $T = 600^\circ\text{C}$.

and the properties of the surface phases formed by copper. The dependence of Cu segregation on the Si surface orientation was observed, e.g., in [10]. One can see from the dependences $C_{Cu}(x)$ measured at identical temperatures (Fig. 5) that the Cu concentration at the Si(110) surface gradually decreases as the distance from the source increases. According to the AES data, this concentration amounts to about 5 at. % near the source. At the Si(111) surface, the dependence $C_{Cu}(x)$ has an abrupt boundary and weakly varies with x . The concentration C_{Cu} at this face is as high as about 18 at. %. It is relevant to note that the Auger signal from submonolayer metal coatings adsorbed on silicon is mainly controlled by the concentration of uniformly distributed adsorbed atoms incorporated into the surface phases formed at the Si surface. After completing the surface phase formation with a maximum content of adsorbed atoms, the nucleation of 3D disilicide islands can take place. However, the Auger signal from atoms incorporated in 3D islands is much weaker than that from the same number of uniformly distributed atoms due to a smaller surface-to-volume ratio. The formation of 3D silicide islands at the Si surface was observed, e.g., in the case of Cu, Ni, and Co atom adsorption [10, 11, 20].

The difference between $C_{Cu}(x)$ at the Si(110) and Si(111) surfaces is probably caused by the fact that several surface phases (4×3 , 4×5 , and 2×1) are formed at the Si(110) surface, while only one (5×5) phase is observed at the Si(111) surface.

At the same temperature and for a comparable annealing time, the formation of the Si(111)-(5 × 5) phase has time to come to completion over the entire Cu distribution, while the Si(110)-(4 × 3) phase is formed only in a narrow region of the distribution, although the Cu content in this phase is lower than in Si(111)-(5 × 5). Hence, the Cu segregation coefficient during diffusion to the Si(111) surface is larger than that for Si(110). The

possibility of the Cu segregation coefficient decreasing as Cu concentrations increase at the Si surface must not be ruled out.

CONCLUSION

Auger electron spectroscopy and low-energy electron diffraction methods were applied to study the mechanism of Cu diffusion over the Si(110) surface. It was established that the Cu transport proceeds via Cu diffusion through the Si bulk and the segregation of diffusing Cu atoms at the surface in the course of annealing. The effective diffusivities of Cu over the Si surfaces were found to be lower than those in the Si bulk. The measured effective diffusivities of Cu over the Si(110) surface exceed those for the Si(111) surface. This difference is caused by differences in the segregation processes. Based on the experimental data, it may be concluded that the coefficient of Cu segregation at the Si(111) surface during Cu diffusion is higher than that at the Si(110) surface.

ACKNOWLEDGMENTS

This study was supported by the Russian Foundation for Basic Research (project no. 01-02-16844) and the federal program "Surface Atomic Structures."

REFERENCES

1. A. E. Dolbak, R. A. Zhachuk, and B. Z. Ol'shanetskiĭ, *Fiz. Tekh. Poluprovodn. (St. Petersburg)* **35**, 1063 (2001) [*Semiconductors* **35**, 1018 (2001)].
2. E. Daugy, P. Mathiez, F. Salvan, and J. M. Layet, *Surf. Sci.* **154**, 267 (1985).
3. M. Mundschau, E. Bauer, W. Telieps, and W. Swiech, *J. Appl. Phys.* **65**, 4747 (1989).
4. S. A. Chambers and J. H. Weaver, *J. Vac. Sci. Technol. A* **3**, 1929 (1985).
5. L. Calliari, F. Marchetti, and M. Sancrotti, *Phys. Rev. B* **34**, 521 (1986).
6. H. Dallaporta and A. Cross, *Surf. Sci.* **178**, 64 (1986).
7. R. J. Wilson, S. Chiang, and F. Salvan, *Phys. Rev. B* **38**, 12696 (1988).
8. D. D. Chamblis and T. N. Rhodin, *Phys. Rev. B* **42**, 1674 (1990).
9. J. Nichols, F. Salvan, and B. Reihl, *Phys. Rev. B* **34**, 2945 (1986).
10. T. Ikeda, Y. Kawashima, H. Itoh, and T. Ichinokawa, *Surf. Sci.* **342**, 11 (1995).
11. A. E. Dolbak, B. Z. Olshanetsky, S. I. Stenin, *et al.*, *Surf. Sci.* **218**, 37 (1989).
12. P. W. Palmberg, G. E. Riach, R. E. Weber, and N. C. Mac-Donnald, *Handbook of Auger Electron Spectroscopy* (Physical Electronics Industries, Eden Prairie, 1972).
13. E. R. Weber, *Appl. Phys. A* **30**, 1 (1983).
14. A. A. Istratov, Ch. Flink, H. Hieslmair, and E. R. Weber, *Phys. Rev. Lett.* **81**, 1243 (1998).
15. A. E. Dolbak, B. Z. Olshanetsky, and S. A. Teys, *Phys. Low-Dimens. Struct.* **11/12**, 41 (1999).
16. M. Y. Lee and P. A. Bennett, *Phys. Rev. Lett.* **75**, 4460 (1995).
17. A. E. Dolbak, B. Z. Olshanetsky, and R. A. Zhachuk, *Phys. Low-Dimens. Struct.* **9/10**, 97 (1998).
18. A. E. Dolbak, B. Z. Ol'shanetskiĭ, S. A. Tiĭs, and R. A. Zhachuk, *Pis'ma Zh. Ėksp. Teor. Fiz.* **66**, 611 (1997) [*JETP Lett.* **66**, 643 (1997)].
19. A. E. Dolbak, B. Z. Ol'shanetskiĭ, and S. A. Tiĭs, *Pis'ma Zh. Ėksp. Teor. Fiz.* **69**, 423 (1999) [*JETP Lett.* **69**, 459 (1999)].
20. A. E. Dolbak, B. Z. Olshanetsky, and S. A. Teys, *Surf. Sci.* **373**, 43 (1997).

Translated by A. Kazantsev

ELECTRONIC
AND OPTICAL PROPERTIES
OF SEMICONDUCTORS

Internal Friction and Effective Shear Modulus
of Single-Crystal Silicon in Early Stages of Oxygen Precipitation

V. V. Motskin, A. V. Oleinich-Lysyuck, N. D. Raranskiĭ, and I. M. Fodchuk

Chernovtsy National University, Chernovtsy, 58012 Ukraine

e-mail: Ptkachuk@chnu.cv.ua

Submitted January 28, 2002; accepted for publication February 13, 2002

Abstract—Changes in the temperature spectra of the internal friction and the effective shear modulus in single-crystal silicon were studied in the range of 20–400°C in relation to the annealing duration at 400°C. Stable peaks growing in the course of annealing were observed in the absorption spectra. The peaks were attributed to the migration of point defects and their complexes. A suggestion concerning the probable nature of the detected effects was offered. © 2002 MAIK “Nauka/Interperiodica”.

Oxygen behavior in silicon crystals has been the subject of a number of studies [1, 2]. In particular, it was established that annealing at 350–400°C for a time up to 100 h causes oxygen release and the emergence of the first-type oxygen-containing quenched-in donors (QiD-1) of nine various kinds, whose number and concentration depend on the thermal treatment duration [3]. Nevertheless, their nature has not yet been completely established. There is no common opinion on the mechanism of their formation, on the kinetics of this process, or on the influence of intrinsic silicon defects on QiD-1 defects, etc. [2].

Therefore, we attempt to study the initial stages of oxygen release in silicon by the low-frequency internal friction method, which is characterized, as is known [4], by high structural sensitivity. The internal-friction method allows one to study the release kinetics at the earliest stages and to gain unique information on defect motion and interactions.

Silicon $\langle 111 \rangle$ single crystals grown by the Czochralski method were studied. Samples in the shape of parallelepipeds $1.4 \times 1.4 \times (60\text{--}80)$ mm in size were cut out perpendicularly to the growth direction. To remove layers damaged by cutting, the prepared samples were chemically etched to a depth of 40 to 60 μm and polished.

The temperature spectra of elastic energy absorption were measured with a low-frequency semi-automatic relaxometer of the inverse-torsion-pendulum type at frequencies $f \approx 1$ Hz using the known technique [5] in the temperature and strain ranges of 20–400°C and $\gamma = (1.2\text{--}2.3) \times 10^{-5}$. Simultaneously with internal-friction (Q^{-1}) measurements, the temperature variation of the effective shear modulus (G_{eff}) was measured. The average rates of temperature variation when heating and cooling were about 3 K/min. The relative measuring errors for the internal friction (Q^{-1} proportional to G_{eff})

and the squared frequency (f^2) did not exceed 1% and 0.1%, respectively.

Figure 1 displays the temperature dependences of Q^{-1} and f^2 for the samples in their initial state. One can see that the spectrum of elastic energy absorption in the studied temperature range exhibits a series of insignificant peaks at 125, 180, 210, 240, 275, 300, and 390°C with a height of $(5\text{--}10) \times 10^{-4}$ friction relative units (see Fig. 1, curve 1, and table). A treatment at 400°C for half an hour results in an insignificant growth of peaks in the region of 150–240°C and a temperature hysteresis in the curves $f^2(T)$, which indicates that structural rearrangement occurs in the material in the course of annealing (see Fig. 2, curves 3, 4). The spectra of elastic energy absorption were resolved by the known tech-

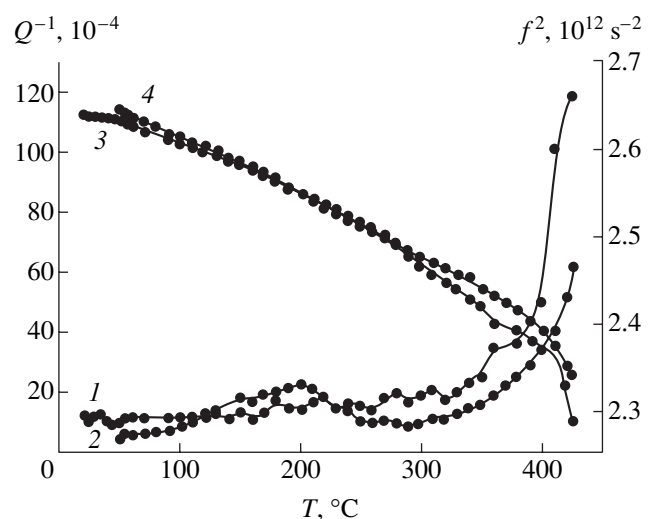


Fig. 1. Temperature dependences of the internal friction Q^{-1} (1, 2) and f^2 (3, 4) for the sample in the initial state. Curves 1, 3 and 2, 4 were measured at heating and cooling, respectively.

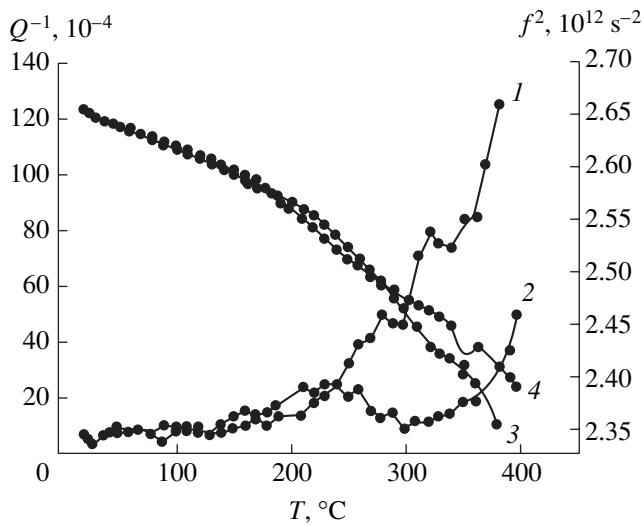


Fig. 2. Same as in Fig. 1, after a 0.5-h annealing of the sample at $T_{\text{ann}} = 400^\circ\text{C}$.

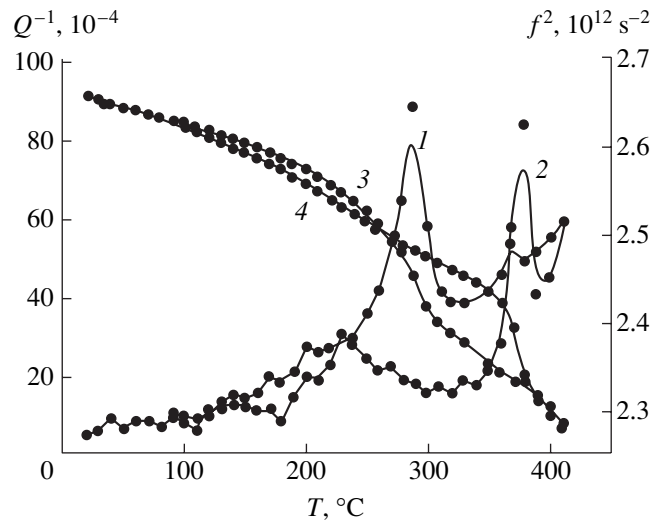


Fig. 3. Same as in Fig. 1, after a 4-h annealing of the sample at $T_{\text{ann}} = 400^\circ\text{C}$.

nique [6]; the activation energies of relaxation processes were calculated by the Wert–Marx formula $H = RT_{\text{max}} \ln \frac{kT_{\text{max}}}{\hbar\omega_{\text{max}}}$, where T_{max} is the temperature of the peak, $\omega_{\text{max}} = 2\pi f_{\text{max}}$, R is the universal gas constant, and k is the Boltzmann constant.

Additional annealing for half an hour at 400°C results in more significant changes in the spectrum of Q^{-1} upon heating (see Fig. 2, curve 1) and to a certain growth of the peaks in the region of $200\text{--}300^\circ\text{C}$ on cooling. The temperature hysteresis in the temperature dependence of f^2 is significantly enhanced.

After a treatment of the samples at 400°C for more than 2 h, the spectra of Q^{-1} exhibit well-reproduced stable peaks above 200°C , which manifest themselves both on heating and cooling (Figs. 3, 4). We emphasize that the intensity of the peak near 280°C on heating is higher than that on cooling by an order of magnitude (76×10^{-4} and 6×10^{-4} Q^{-1} relative units, respectively). An opposite case is the peak at 380°C : the height of the peak on heating (13×10^{-4} Q^{-1} rel. units) is 5.5 times lower than that on cooling (72×10^{-4} Q^{-1} rel. units). In this case, the temperature hysteresis in the temperature dependence of f^2 becomes “two-lobe” (see, e.g., Fig. 3, curves 3, 4).

A detailed analysis of the temperature spectra of elastic energy absorption on heating and cooling in relation to the annealing duration (t_{ann}) at 400°C shows that the average peak intensity grows with t_{ann} in different ways. For example, the peaks near 280°C and 330°C grow on heating by about six and two times, respectively. The peak at 210°C remains almost unchanged (Fig. 5).

A joint analysis of the obtained results and the previous data [7] allows us to suggest the plausible nature of the detected peaks. Indeed, the dependence of the

internal-friction peak height on t_{ann} resembles the dependence of the concentration of quenched-in donors of the first five types on the annealing duration at 400°C [7]. We recall that, according to [7], annealing at 400°C within the first two hours results in formation of the first four QiD-1 types (A, B, C, and D), while (QiD-1)_E appears after annealing for 5 h. The relative concentration of donors of each type varies with time in different ways: the concentrations of (QiD-1)_A and (QiD-1)_B was virtually unchanged and weakly growing, respectively, while the concentrations of (QiD-1)_C and (QiD-1)_D changes by a few times.

An analysis of the relaxation parameters of the found peaks (the activation energy H and the frequency factor ν_m) (see table) indicates that virtually all the detected peaks are caused by migration of point defects

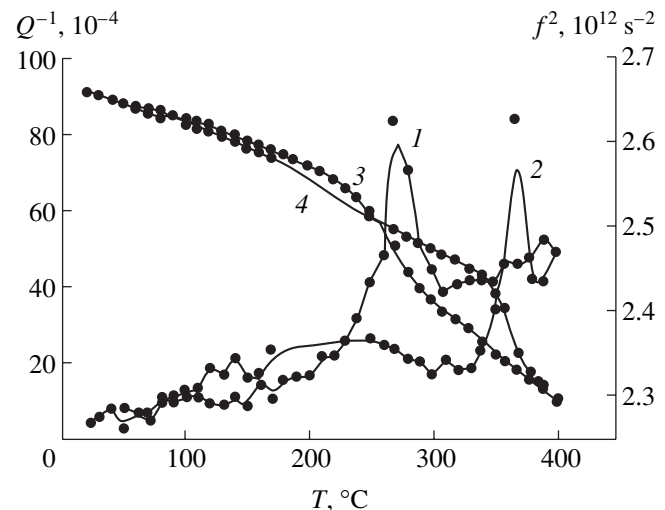


Fig. 4. Same as in Fig. 1, after 5-h annealing of the sample at $T_{\text{ann}} = 400^\circ\text{C}$.

Parameters of the relaxation peaks

Heating				Cooling			
t_{ann}, h	$T_{\text{max}}, \text{°C}$	H, eV	$v_m, 10^{14} \text{s}^{-1}$	t_{ann}, h	$T_{\text{max}}, \text{°C}$	H, eV	$v_m, 10^{14} \text{s}^{-1}$
0.5	125	1.00	–	0.5	120	0.99	–
	180	1.15	–		150	1.07	–
	210	1.23	0.64		180	1.15	–
	240	1.31	0.68		215	1.24	0.64
	275	1.40	0.72		240	1.31	0.68
	300	1.46	0.75		270	1.39	0.71
	390	1.70	0.87		310	1.49	0.76
					380	1.68	0.86
1	110	0.97	–	1	120	0.99	–
	160	1.10	–		160	1.10	–
	210	1.22	0.63		205	1.21	0.63
	280	1.41	0.72		240	1.31	0.67
	330	1.54	0.79		280	1.41	0.73
	390	1.68	0.87		350	1.60	0.82
2	140	1.04	–	2	120	0.99	–
	220	1.25	0.64		160	1.10	–
	290	1.44	0.73		200	1.21	0.63
	370	1.65	0.85		250	1.33	0.68
					305	1.48	0.76
3	120	0.99	–	3	110	0.97	–
	170	1.12	–		150	1.07	–
	215	1.24	0.64		180	1.15	–
	280	1.41	0.72		215	1.24	0.64
	330	1.55	0.79		250	1.33	0.69
	380	1.68	0.86		290	1.44	0.88
					340	1.57	0.78
					380	1.68	0.87
4	140	1.04	–	4	135	1.03	–
	210	1.23	0.63		170	1.12	–
	250	1.33	0.69		200	1.28	0.64
	285	1.43	0.73		240	1.31	0.68
	325	1.53	0.79		270	1.39	0.71
	370	1.65	0.86		305	1.48	0.76
					380	1.68	0.86

or their complexes [6], since the values v_m are within $(0.64\text{--}0.87) \times 10^{14} \text{ s}^{-1}$. This suggests that the relaxation peaks in the high-temperature region of the internal-friction spectra are related to the emergence and migration of QiD-1 defects of various types in the aging silicon lattice (in this case, by migration is meant any elementary diffusion event, e.g., a rotation of an asymmet-

ric quenched-in donor in a field of applied external stresses). Then, the height of these peaks will be controlled by the number of generated donors. Hence, the dependence of Q_{max}^{-1} on the annealing time t_{ann} will be similar to the dependence of the donor concentration on t_{ann} . Therefore, we assume that the peaks near 210, 280, 380, and 330°C are related to the migration of (QiD-1)_A, (QiD-1)_C, (QiD-1)_D, and (QiD-1)_B in the Si structure, respectively. In subsequent experiments, we found a peculiar confirmation of the assumption that the migration of each type of quenched-in donors causes a specific peak: 5-h annealing at 400°C gives rise to an additional peak near 360°C (at cooling) in the internal-friction spectrum, which can be related to donors (QiD-1)_E (Fig. 4).

To reveal the nature of the peak at 240–250°C, we assume (following the authors of [2]) that each subsequent QiD-1 type is formed by the attachment of an oxygen atom to complex SiO_n , which is carried by mobile structural units (MSUs). The study of the nature of MSU carried out, e.g., in [8], has shown that the MSU concentration is directly proportional to the concentration of dissolved oxygen. This allowed the authors of [8] to infer that the MSU contains only one oxygen atom and is not an O_2 quasi-molecule. The MSU is probably an oxygen–vacancy (O–V) or (interstitial silicon atom)–oxygen (Si–O) complex. To check the possible participation of intrinsic defects (vacancies and interstitial atoms) in the formation of quenched-in donors, the authors of [8] have studied silicon irradiated with fast electrons ($E = 4 \text{ MeV}$, $\Phi_e = 2.4 \times 10^{16} \text{ cm}^{-2}$) at 427°C. After such an irradiation, the number of generated quenched-in donors decreased. Based on this fact, the authors of [8] concluded that the MSU is an interstitial metastable oxygen atom O_i that is not bound with the lattice, rather than a V–O or Si–O complex. Such an oxygen atom is characterized by increased diffusivity with the activation energy of 1.8 eV. As for the plausible nature of the MSU, we merely note that the preliminary studies we carried out with silicon irradiated with high-energy electrons (about 18 MeV, various doses) have shown that the rate of QiD-1 formation in irradiated single-crystal silicon grown by the Czochralski method depends nonuniquely on the irradiation dose. Small doses can stimulate this process, while large doses, on the contrary, can suppress it. Apparently, the problem of the nature of the MSU still remains unsolved. Therefore, we carried out further analysis of the high-temperature region of the absorption spectrum of elastic energy in aging silicon on the basis of only the experimental data on internal friction: the characteristics of the peak at 240–250°C (the activation energy $H = 1.3 \text{ eV}$ and the relaxation time $\tau = 1.45 \times 10^{-14} \text{ s}$) count in favor of the assumption that the peak is related to the migration of point defects (single defects or their complexes) to a distance on the order of the interatomic one. In this case, the activation energy of this migration counts in favor of V–O-type complexes [9, 10].

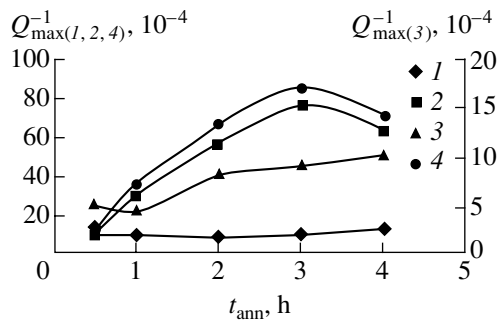


Fig. 5. Kinetic dependences of Q_{max}^{-1} at temperatures $T =$ (1) 210, (2) 280, (3) 330, and (4) 380°C; t_{ann} is the annealing time.

Thus, the intricate process of QiD-1 quenched-in donor formation in Si in the course of aging at 400°C manifests itself in the spectrum of elastic energy absorption as separate peaks caused by the migration of first-type quenched-in donors of five various kinds: (QiD-1)_A, (QiD-1)_B, (QiD-1)_C, (QiD-1)_D, and (QiD-1)_E, as well as mobile structural units (MSUs) in the silicon lattice. However, the problems of the absorption mechanism for each indicated maximum and the nature of the QiD-1 and MSU call for further investigations.

REFERENCES

1. K. V. Ravi, *Defects and Impurities in Semiconducting Silicon* (Wiley, New York, 1981; Mir, Moscow, 1984).
2. V. M. Babich, N. I. Bletskan, and E. F. Venger, *Oxygen in Single-Crystal Silicon* (Interpres, Kiev, 1997).
3. U. Goselle, *Appl. Phys. A* **28** (1), 79 (1982).
4. *Internal Friction Method in Physical Metallurgy: a Handbook*, Ed. by M. S. Blanter and Yu. V. Piguzov (Metallurgiya, Moscow, 1991).
5. I. A. Varus and B. G. Strongin, in *Damping Metallic Materials* (KPI, Kirov, 1988), p. 96.
6. V. S. Postnikov, *Internal Friction in Metals* (Metallurgiya, Moscow, 1974).
7. B. Pajot, H. Compain, J. Lerouille, and B. Clerjoud, *Physica B & C* (Amsterdam) **117–118**, 110 (1983).
8. L. I. Murin and V. P. Markevich, *Fiz. Tekh. Poluprovodn. (Leningrad)* **22** (7), 1324 (1988) [*Sov. Phys. Semicond.* **22**, 840 (1988)].
9. I. D. Konozenko, A. K. Semenyuk, and V. I. Khivrich, *Radiation Effects in Silicon* (Naukova Dumka, Kiev, 1974).
10. L. N. Aleksandrov, M. I. Zotov, and B. P. Surin, in *Physics and Chemistry of Condensed Media* (VPI, Voronezh, 1981), p. 14.

Translated by A. Kazantsev

ELECTRONIC
AND OPTICAL PROPERTIES
OF SEMICONDUCTORS

The Temperature and Concentration Dependences of the Charge Carrier Mobility in PbTe–MnTe Solid Solutions

E. I. Rogacheva* and I. M. Krivul'kin

National Technical University "Kharkov Polytechnical Institute," Kharkov, 61002 Ukraine

* e-mail: rogacheva@kpi.kharkov.ua

Submitted May 8, 2001; accepted for publication February 18, 2002

Abstract—The temperature dependences of conductivity (σ), the Hall coefficient (R_H), and the charge carrier mobility (μ_H) for cast and pressed samples of PbTe–MnTe solid solutions (0–2.5 mol % of MnTe) were studied in the temperature range of 80–300 K. The mobility of cast samples varies only slightly in the temperature range of 80–140 K. At higher temperatures, μ_H decreases according to the power law $\mu_H = aT^{-\nu}$. The mobility μ_H of pressed samples exponentially increases with temperature in the temperature range of 100–160 K, which is related to the energy barriers ΔE_a formed by oxide films at the grain boundaries. The dependences of μ_H , ν , and ΔE_a on the MnTe content have anomalies in the composition range of 0.75–1.25 mol %, which are related to the concentration phase transition of the percolation type. © 2002 MAIK "Nauka/Interperiodica".

1. INTRODUCTION

IV–VI semiconductor compounds and solid solutions on the basis of these belong to a class of materials widely used in optoelectronics (in the infrared region), thermoelectricity, and other fields of science and engineering [1]. Investigations of the concentration dependences of microhardness and transport coefficients [2–4] showed that solid solutions based on IV–VI compounds with a low impurity concentration (~1 mol %) have anomalous characteristics. We associate these anomalies with concentration phase transitions, which are inherent to any solid solution and caused by the transition from the impurity discontinuum to the "impurity condensate" [5]. The effect under consideration requires detailed investigation and should be taken into account in the development of new materials and for the prediction of the properties of a solid solution. The charge-carrier mobility μ_H is among the most important characteristics of semiconductor materials, which, in a number of cases, determines their practicability.

The object of our study is a PbTe–MnTe system of solid solutions, which belong to a class of semimagnetic semiconductors that are currently being intensively studied [6].

In this paper, we report the results of studying the temperature and concentration dependences of the charge-carrier mobility.

2. EXPERIMENT

PbTe–MnTe alloys (0–2.5 mol % of MnTe) were grown in cells, using elements of a high purity, and were subjected to homogenizing annealing for 200 h at

$T = 820$ K. According to the results of microstructural and X-ray analyses of the annealed samples, the content of MnTe in the solid solution based on PbTe was as high as ~3 mol %. Electrical measurements were performed for the samples that were cut out from ingots and had the shape of parallelepipeds $3 \times 3 \times 10$ mm in size. For the preparation of pressed samples, the synthesized alloys were ground in air in an agate mortar (the average size of the particles was ~200 μm). The samples in the shape of parallelepipeds were then prepared by hot pressing at $T = 620$ K and under a pressure of 4 ton/cm². They were annealed for 200 h at $T = 820$ K and cooled in air. Direct-current measurements of the conductivity σ and Hall coefficient R_H were performed in a permanent magnetic field of 1 T. Six ohmic indium contacts were soldered to the sample surface. The Hall mobility was calculated according to the formula $\mu_H = R_H\sigma$. The measurement error for σ and R_H did not exceed 5%. All samples under study were of *p*-type.

3. RESULTS AND DISCUSSION

The temperature dependences of R_H for cast and pressed PbTe–MnTe samples of varied composition are similar: R_H increases with temperature in the entire temperature range, and the ratio R_{300}/R_{100} is about 1.1–1.3 (Fig. 1). An insignificant increase in R_H with temperature in *p*-PbTe is well known and is usually attributed to the complex structure of the valence band that consists of two overlapping subbands with different densities of states [7]. Carriers in the lower subband have lower mobility, and the contribution of the carriers of this subband to the transport properties increases

with temperature. Taking into account heavy and light holes, the relation for R_H takes the form

$$R_H = \frac{r}{e} \frac{p_1 \mu_1^2 + p_2 \mu_2^2}{(p_1 \mu_1 + p_2 \mu_2)^2} = \frac{r}{e p_1} \frac{1 + \eta f^2}{(1 + \eta f)^2}, \quad (1)$$

where p_1 and p_2 are the concentrations of light and heavy holes, respectively; μ_1 and μ_2 are their mobilities; $\eta = p_2/p_1$; $f = \mu_2/\mu_1$; and r is the Hall factor which depends on the degree of degeneracy and the mechanism of scattering. One can see from (1) that R_H increases as the contribution of heavy holes increases with temperature. A similar effect should be also observed in those PbTe–MnTe alloys whose valence band structure is identical to the valence band of p -PbTe [8].

As can be seen in Fig. 2, the temperature dependences of the charge carrier Hall mobility are significantly different for cast and pressed samples. The mobility μ_H for cast samples varies only slightly up to ~ 140 K. At higher temperatures, it decreases according to the power law $\mu_H = AT^{-\nu}$, where the exponent ν depends on the composition of the solid solution and ranges from 1.5 to 2.9 (Fig. 2a). The charge-carrier mobility increases for pressed samples as the temperature increases up to ~ 200 – 220 K. At $\tau > 220$ K, μ_H decreases with increasing temperature according to a power law as in the case of cast samples (Fig. 2b). The dependence $\mu_H(T)$ plotted in $\ln \mu_H = f(1/T)$ coordinates (Fig. 2b) obeys the exponential law up to ~ 160 K: $\mu_H \propto \exp(-\Delta E_a/kT)$, where ΔE_a is the activation energy. ΔE_a was calculated for pressed samples of varied composition in the temperature range of 100–160 K.

The temperature dependences of σ for cast and pressed PbTe–MnTe samples are displayed in Fig. 3. The conductivity of cast samples monotonically decreases with increasing temperature (Fig. 3a), which is characteristic of degenerate semiconductors. A special feature of the $\sigma(T)$ dependences of pressed samples (Fig. 3b) is the distinct section where σ increases in the temperature range of 80–220 K.

The values of the exponent $\nu = 1.5$ – 2.9 , obtained from the dependences of $\mu_H(T)$ for cast and pressed samples, show that the temperature dependence of the mobility for the majority of samples cannot be explained solely by acoustic phonon scattering, because, in this case, $\nu = 3/2$ for nondegenerate and $\nu = 1$ for degenerate semiconductors. Since it is considered established that the basic mechanism of the charge carrier scattering in PbTe is scattering by acoustic phonons at medium and high temperatures, higher values of ν , obtained for PbTe, are now usually related to the temperature dependence of the effective mass [7]. From the data obtained in this study it is clear that there is a tendency towards the reduction of the exponent as the MnTe concentration increases.

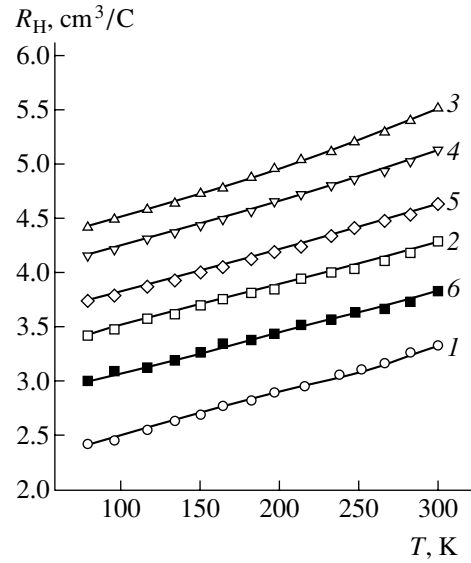


Fig. 1. The temperature dependences of the Hall coefficient R_H for PbTe–MnTe pressed alloys with MnTe contents equal to (1) 0, (2) 0.5, (3) 0.75, (4) 1.25, (5) 1.75, and (6) 2.5 mol %.

The activation character of mobility in the pressed samples in the temperature range of 100–160 K can be related to the energy barriers caused by thin oxide interlayers at the boundary of separate grains. Pressed samples were prepared from powders obtained through the grinding of ingots in air and subsequent hot pressing in air, which could result in oxidation. Apparently, it is oxide films on the grain boundaries that form the energy barriers which cause low mobility μ_H in pressed samples at low temperatures. The sign inversion of the thermoelectric power in the fine-grained pressed PbTe samples of n-type was accounted for in [9] by the formation of acceptor levels in the surface layer of grains due to the adsorption of oxygen. An exponential dependence $\mu_H(1/T)$ in the PbTe films at low temperatures was observed in [10, 11]. This dependence was related to the activation-type conductivity caused by the potential barriers at the grain boundaries. According to [12], in the layer which consists of high-conductivity crystallites surrounded by thin insulating interlayers, R_H is governed by the charge-carrier concentration in the crystallites; simultaneously, μ_H is related to the carrier mobility in the crystallites, μ_{H0} , and the potential-barrier height at the boundaries, ΔE_a , by the expression

$$\mu_H = \mu_{H0} e^{-\Delta E_a/kT}. \quad (2)$$

In the temperature range of 200–240 K, the increased energy of the charge carriers becomes sufficient for overcoming the energy barriers formed by interlayers at the grain boundaries of pressed samples, and due to this fact, μ_H starts to decrease with increasing temperature, as in the case of cast samples.

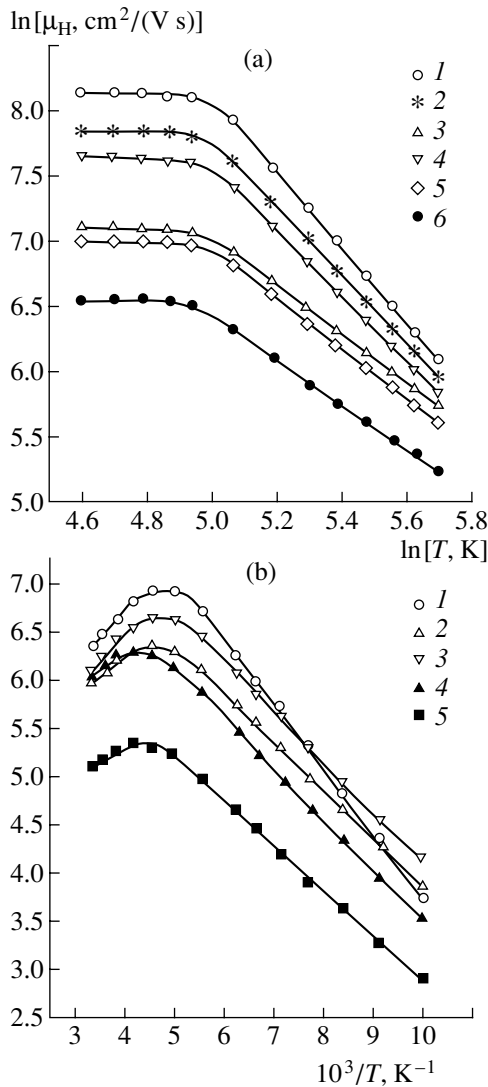


Fig. 2. The temperature dependences of the charge-carrier mobility μ_H in the PbTe–MnTe solid solutions. (a) Cast samples with a MnTe content of (1) 0, (2) 0.25, (3) 0.75, (4) 1.25, (5) 1.75, and (6) 2.25 mol %; (b) pressed samples with a MnTe content of (1) 0, (2) 0.5, (3) 0.75, (4) 1.25, and (5) 1.75 mol %.

Differences between the values and character of the temperature dependences of μ_H for cast and pressed samples shows that it is necessary to use extreme caution when interpreting the results of measurements of the electrical characteristics of pressed samples.

The dependences of the charge-carrier Hall mobility on the MnTe content at different temperatures that were obtained for (a) cast and (b) pressed samples are displayed in Fig. 4. The dependences of the exponent ν (in the temperature region where scattering by acoustic phonons is dominant and ν remains unchanged) and the activation energy ΔE_a (for pressed samples) on the alloy composition are shown in Fig. 5.

As can be seen in Figs. 4 and 5, it is possible to distinguish three sections in the curves. The first and third

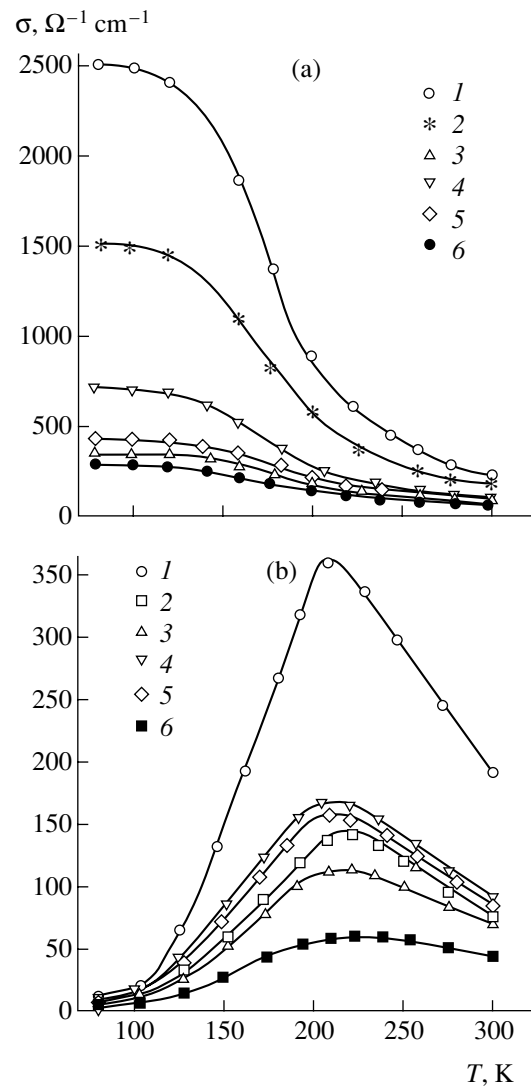


Fig. 3. The temperature dependences of conductivity σ of the PbTe–MnTe solid solutions. (a) Cast samples with a MnTe content of (1) 0, (2) 0.25, (3) 0.75, (4) 1.25, (5) 1.75, and (6) 2.25 mol %; (b) pressed samples with a MnTe content of (1) 0, (2) 0.5, (3) 0.75, (4) 1.25, (5) 1.75, and (6) 2.5 mol %.

sections (0–0.75 and 1.25–2.5 mol % of MnTe, respectively) are characterized by a sharp decrease in μ_H , ν , and ΔE_a , which we associate with an increase in the concentration of the lattice defects and an increase in the electron scattering as the Mn content increases. A significant decrease in the mobility of PbTe was observed as Mn was introduced into the crystal [13]. This fact testifies to a strong disturbance of the periodical lattice potential, and, therefore, in contrast to other isovalent solid solutions, the effect of Mn in a PbTe–MnTe system cannot be considered as a weak perturbation.

In the second section of the curves (0.75–1.25 mol % MnTe), we observed an anomalous increase in μ_H , ΔE_a , and ν , which testifies to radical changes in the solid solution properties as the impurity content varies. We

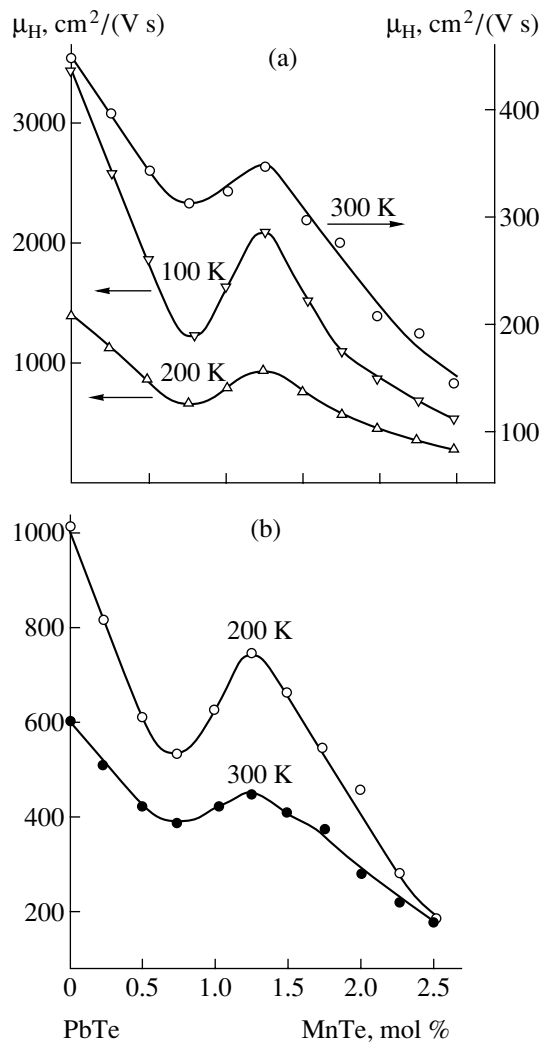


Fig. 4. The composition dependences of the charge carrier mobility for (a) cast and (b) pressed samples in the PbTe–MnTe solid solutions for different temperatures.

observed similar concentration anomalies in the studies of other characteristics of PbTe–MnTe solid solutions (the coefficient of thermal expansion [14], heat capacity [15], and microhardness [16]). We related these anomalies to critical phenomena (see [5]) which accompany the concentration phase transitions of the percolation type. The impurity atoms are the centers of local lattice distortion, the sources of internal stresses, and short-range fields of deformations [17] with a specific radius of the deformation interaction R_0 .

For a low impurity concentration, when the condition $l \gg R_0$ is met (l is the distance between the impurity atoms), the deformation fields formed by individual atoms virtually do not overlap, and they make an additive contribution to the mobility reduction. As the impurity concentration increases, the deformation fields of neighboring atoms start to overlap, which partly compensates the elastic stresses with an opposite sign and reduces total elastic stresses in the sample. As

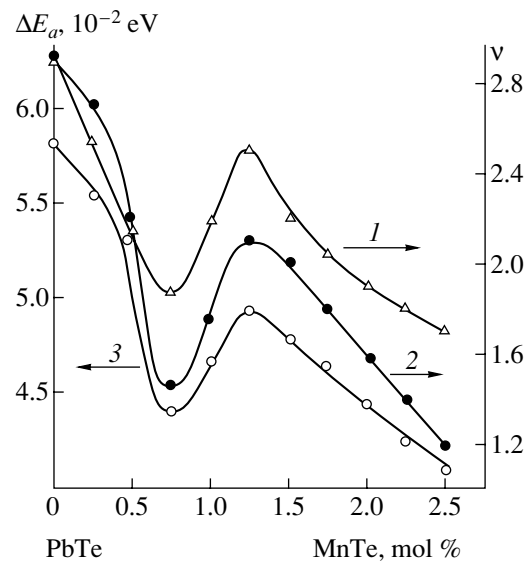


Fig. 5. The composition dependences of the (3) activation energy ΔE_a in the portion, where conductivity obeys activation law (100–160 K), for pressed samples and the exponent ν in the temperature dependence of mobility ($\mu_H \propto T^{-\nu}$) for cast (160–300 K, curve 1) and pressed (240–300 K, curve 2) samples in the PbTe–MnTe solid solution.

this process becomes fairly intense, it can result in an increase in μ_H until the process of stress compensation is completed. The further introduction of impurity atoms will cause additional lattice distortions and, therefore, a further decrease in μ_H . Using percolation theory in the short-range approximation [18], it is possible to relate the onset of the increase in μ_H to the attainment of the percolation threshold and critical concentration x_C , such that a so-called “infinite cluster” is formed at first: a chain consisting of overlapping deformation spheres and threading through the entire crystal. Within the context of this model, the increase in mobility μ_H with the impurity concentration is related to the increase in the infinite-cluster density. This case is similar to the Mott transition when the formation of percolation channels over the electron shells of separate impurity atoms with a fixed concentration gives rise to conduction [19].

The probability of ordering of the impurity atoms increases for optimum compositions. According to a simple calculation, it is possible to order the impurity atom distribution over the sites of a primitive cubic lattice with a period $a = 3a_0$, where a_0 is the unit cell parameter, for ~ 1.0 mol % of MnTe in the PbTe–MnTe solid solution. A significant increase in μ_H , ν , and ΔE_a in the composition range of 0.75–1.25 mol % of MnTe indirectly shows that there are ordering processes which accompany the formation of the impurity continuum.

4. CONCLUSION

We observed an anomalous increase in the charge-carrier mobility μ_H (at $T \approx 100$ – 300 K), as well as in the

exponent ν in the temperature dependence of $\mu_H \propto T^{-\nu}$, in the PbTe–MnTe solid solutions as the MnTe content increased from 0.75 to 1.25 mol %. These results are in disagreement with the usually observed decrease in μ_H and ν with the impurity concentration. We believe that this effect is caused by the interaction between the deformation fields of the impurity atoms when the concentration of these is quite high. In this case, this process has a collective character and leads to the partial relief of elastic stresses that were created by the impurity atoms in the crystal. This effect once again confirms our assumptions [5] that there are concentration phase transitions of the percolation type in any solid solution, and these transitions correspond to the impurity continuum transition. The character of development and the possibility of observing this effect in other semiconductor systems should substantially depend on the character of the host and the impurity.

We found that pressed PbTe–MnTe samples (in contrast to cast samples) have a low-temperature conductivity portion, where the conductivity obeys the activation law, which is related to the formation of energy barriers caused by the oxidation of grain boundaries. The activation energy is also a nonmonotonic function of composition, and it has anomalies in the concentration phase transition region.

ACKNOWLEDGMENTS

This study was supported by the US Foundation for Civil Research and Development (project no. UE2-2069) and the Ukrainian Ministry of Education and Science within the framework of the program "New Materials."

REFERENCES

1. A. V. Lyubchenko, E. A. Sal'kov, and F. F. Sizov, *Physical Foundations of Semiconductor Quantum Photoelectronics* (Naukova Dumka, Kiev, 1984).
2. E. I. Rogacheva, N. K. Zhigareva, and A. B. Ivanova, *Izv. Akad. Nauk SSSR, Neorg. Mater.* **24**, 1629 (1988).
3. E. I. Rogacheva, *Izv. Akad. Nauk SSSR, Neorg. Mater.* **25**, 754 (1989).
4. E. I. Rogacheva, N. A. Sinelnik, and O. N. Nashchekina, *Acta Phys. Pol. A* **84**, 729 (1993).
5. E. I. Rogacheva, *Jpn. J. Appl. Phys., Suppl.* **32** (3), 775 (1993).
6. F. V. Kyrychenko and J. Kossut, *Phys. Rev. B* **61**, 4449 (2000).
7. Yu. I. Ravich, B. A. Efimova, and I. A. Smirnov, *Semiconducting Lead Chalcogenides* (Nauka, Moscow, 1968; Plenum, New York, 1970).
8. I. A. Drabkin, G. F. Zakharyugina, and I. V. Nel'son, *Fiz. Tekh. Poluprovodn. (Leningrad)* **5**, 325 (1971) [*Sov. Phys. Semicond.* **5**, 277 (1971)].
9. B. M. Gol'tsman, V. Sh. Sarkisyan, L. S. Stil'bans, and V. V. Shlykov, *Izv. Akad. Nauk SSSR, Neorg. Mater.* **4**, 2194 (1968).
10. S. V. Plyatsko, *Fiz. Tekh. Poluprovodn. (St. Petersburg)* **32**, 257 (1998) [*Semiconductors* **32**, 231 (1998)].
11. V. D. Okunev and N. N. Pafomov, *Zh. Éksp. Teor. Fiz.* **116** (1), 276 (1999) [*JETP* **89**, 151 (1999)].
12. R. L. Petritz, *Phys. Rev.* **104**, 1508 (1956).
13. B. A. Efimova, O. A. Kazanskaya, É. F. Kosolapova, and L. E. Moskaleva, *Izv. Akad. Nauk SSSR, Neorg. Mater.* **13**, 1403 (1977).
14. E. I. Rogacheva, I. M. Krivulkin, V. P. Popov, and T. A. Lobkovskaya, *Phys. Status Solidi A* **148**, K65 (1995).
15. E. I. Rogacheva and I. M. Krivulkin, *Inst. Phys. Conf. Ser.* **152**, 831 (1998).
16. E. I. Rogacheva, A. S. Sologubenko, and I. M. Krivulkin, *Inorg. Mater.* **34**, 545 (1998).
17. T. Suzuki, H. Yoshinaga, and S. Takeuchi, *Dislocation Dynamics and Plasticity* (Syokabo, Tokyo, 1986; Mir, Moscow, 1989).
18. D. Stauffer and A. Aharony, *Introduction to Percolation Theory* (Taylor and Francis, London, 1992).
19. B. I. Shklovskii and A. L. Efros, *Electronic Properties of Doped Semiconductors* (Nauka, Moscow, 1979; Springer-Verlag, New York, 1984).

Translated by I. Kucherenko

ELECTRONIC
AND OPTICAL PROPERTIES
OF SEMICONDUCTORS

**Electron–Plasmon Interaction
in Acceptor-Doped Bismuth Crystals**

N. P. Stepanov* and V. M. Grabov**

* *Transbaikalian State Pedagogical University, Chita, 672000 Russia*

** *Hertzen State Pedagogical University, St. Petersburg, 191186 Russia*

Submitted February 18, 2002; accepted for publication February 19, 2002

Abstract—By doping the semimetal bismuth, it is possible to equate a plasma-oscillation energy with a band gap at the L point of the Brillouin zone. In this case, modifications in the reflection spectra are observed. The analysis of experimental data shows that the plasmon excitation is an efficient mechanism of electron–hole recombination provided that $\hbar\omega_p = E_G$. © 2002 MAIK “Nauka/Interperiodica”.

In the semimetal bismuth, the plasma-oscillation energy $\hbar\omega_p$ can be made equal to the direct band gap E_{gL} at the L point of the Brillouin zone through acceptor doping of the crystal. In this case, a modification of the spectra shape is observed in plasma-reflection experiments. This fact suggests that there is a mechanism of radiation–crystal interaction in addition to that induced by free carriers and that there are significant distinctions between values of static and optical relaxation times for charge carriers. The analysis of the totality of experimental data available shows that direct band-to-band electron–hole recombination with plasma-wave emission becomes possible in addition to the conventional band-to-band (radiative and collisional) relaxation mechanism of nonequilibrium density of carriers provided that $\hbar\omega_p = E_{gL}$.

In previous investigations of the plasma-reflection spectra [1, 2] for doped bismuth crystals and bismuth–antimony alloys, the authors observed deviations in the behavior of optical functions from that predicted by the Drude model as well as wide discrepancies in the values of the static and optical conductivity. In study [3], similar deviations and special features found for acceptor-doped $\text{Bi}_{0.93}\text{Sb}_{0.07}$ crystals were associated with the fact that the plasma-oscillation energy approaches the energy of the direct band-to-band transition at the L point of the Brillouin zone. In this paper, we report the results of our systematic investigations of the convergence of the indicated energies in bismuth.

We studied the spectra of reflection of polarized infrared (IR) radiation with two orientations ($\mathbf{E} \perp C_3$, $\mathbf{E} \parallel C_3$) of the electric-field strength \mathbf{E} vectors in the electromagnetic wave relative to the optical axis C_3 of the crystal. The spectra were measured using an IFS-113V (BRUKER) infrared Fourier spectrometer in the range of $50\text{--}1000\text{ cm}^{-1}$ with a resolution of 2 cm^{-1} . All the results reported in this paper were obtained at a

temperature of 78 K. The angle of incidence of the radiation to the sample was no larger than 8° .

The optical surfaces were prepared through the spark cutting of the crystal along the corresponding crystallographic direction with subsequent etching of the layer damaged during cutting and further chemical polishing [4]. The distortions introduced by the described procedure of preparing the surface turned out to be minimal. They were controlled by comparing the spectra obtained from the polished surface and from the natural mirror cleavage plane perpendicular to the optical axis C_3 of the crystal.

Single-crystal samples of donor- and acceptor-doped bismuth were grown by zone-melting recrystallization. For all the samples, we measured the resistivity and the Hall coefficient at the liquid-nitrogen temperature. As the galvanomagnetic measurements showed, the free-carrier concentration was the lowest for the $\text{Bi} : \text{Sn}(0.04\text{ at. \%})$ composition, while its resistivity was the highest (see table). In correspondence with the energy diagram shown in Fig. 1a, the lowest number of light carriers should be observed in bismuth when the chemical-potential level is within the band gap between the L extrema of the conductivity band and the valence band. As follows from the expression $\omega_p^2 = e^2 N / \epsilon_\infty m^*$, where N and m^* are the concentration and the effective mass of free charge carriers, and ϵ_∞ is the high-frequency permittivity of the crystal, the lowest plasma frequencies correspond to the lowest concentration of light carriers, which is also corroborated experimentally (Fig. 1b). Determining the plasma frequencies from the experimental reflection spectra of samples with the lowest carrier concentrations, it is easy to verify that their plasma-oscillation energy $E_{p\parallel}$ is virtually equal to the band gap $\hbar\omega_p$ at the L point of the Brillouin zone. At the same time, the energy of the direct band-to-band transition at the L point of the Brillouin zone

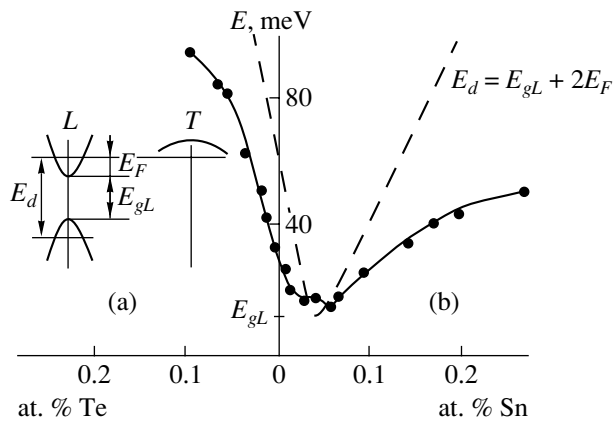


Fig. 1. (a) Band-structure diagram for a bismuth crystal. (b) Plasma-resonance and band-to-band-transition energies $E_{p||}$ and $E_d = E_{gL} + 2E_F$ as functions of the content and type of dopant.

calculated from the expression $E_d = E_{gL} + 2E_F$ in terms of the two-band model with allowance for the Burstein–Moss shift is the lowest and is also equal to E_{gL} , because E_F tends to zero (Fig. 1b) when the chemical-potential level is located in the band gap between the L extrema.

Thus, the samples, which satisfy the condition $\hbar\omega_p = E_{gL}$, were obtained from a single crystal with a tin content (determined from the original material put into the cell) of 0.04 at. %. From the midsection of this single crystal, we prepared samples with a slightly varying ratio of $\hbar\omega_p/E_{gL}$. It is known that the displacement of the crystallization melt zone along the ingot as the crystal grows entrains a fraction of dopants, which are initially distributed uniformly over the entire bulk of material. It is this circumstance that makes it possible to obtain samples with different doping levels and, correspondingly, with different ratios of $\hbar\omega_p/E_{gL}$. The sam-

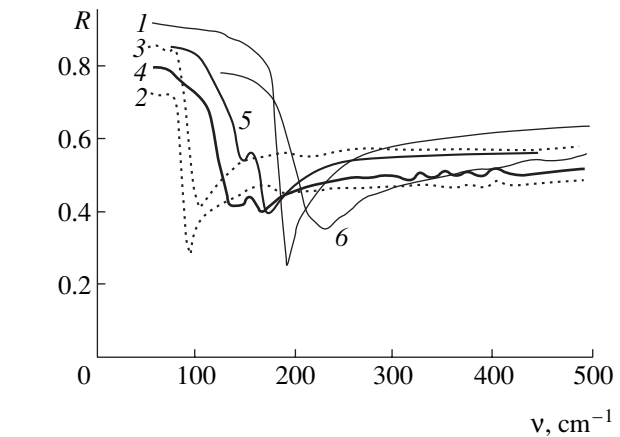


Fig. 2. Reflection spectra of doped bismuth crystals at a temperature of 80 K for the $E \perp C_3$ orientation. The number of a spectrum corresponds to that shown in the table.

ples with a large difference in the quantity $\hbar\omega_p$ and E_{gL} were obtained as a result of the heavy doping of bismuth with impurities of both the acceptor and donor types (Fig. 1b).

Plasma-reflection spectra with almost equal and those with strongly differing energies in the electron and plasma spectra are shown in Fig. 2. All the spectral curves have a shape characteristic of the plasma reflection: the position, depth, and appearance of the reflection-coefficient minimum depend heavily on the impurity content. It can be seen from Fig. 2 that the spectra of crystals with a plasma-oscillation energy almost equal to E_{gL} substantially differ from the spectra of undoped and heavily doped bismuth in which, as follows from Fig. 1b, the plasma-oscillation energy and the band-to-band transition energy differ widely from one another. Such spectra shown in Fig. 2 by curves 1 and 6 are adequately described in terms of the Drude

Table

Sn-dopant content in Bi, at. %	$\rho_{11} \times 10^6, \Omega \text{ m}$	$\rho_{33} \times 10^6, \Omega \text{ m}$	$N \times 10^{-24}, \text{m}^{-3}$	$\omega_{p\perp} \times 10^{-13}, \text{E} \perp C_3, \text{s}^{-1}$	$\omega_{p } \times 10^{-13}, \text{E} C_3, \text{s}^{-1}$	Number of spectrum in Fig. 2
0	—	—	—	3.58	3.35	1
0.02	0.234	2.104	2.38	3.06	1.97	2
0.03	0.675	2.735	2.16	3.75	1.66	
0.04	1.004	3.152	1.74	3.18	2.34	4
0.04	1.134	3.351	—	3.07	2.42	5
0.06	1.116	3.541	4.47	3.72	1.71	
0.07	1.052	2.945	5.15	3.85	1.78	
0.08	0.942	2.673	5.43	3.99	1.89	3
0.1	0.75	2.048	8.73	4.83	2.79	
0.15	0.708	1.592	11.64	5.76	3.87	
0.18	0.676	1.91	13.48	5.86	4.31	6
0.2	0.726	1.464	20.13	7.72	6.59	

classical theory [5]. It is possible to describe spectral curves 2 and 3 in terms of the additive model taking into account the contribution of free carriers and band-to-band transitions according to the procedure described in study [3]. At the same time, the observed splitting in the plasma minimum when $\hbar\omega_p$ approaches E_{gL} (curves 4, 5) points to the fact that, in this case, a strong interaction takes place between the electron-system excitations of the crystal under consideration, which also influences the relaxation processes.

In Fig. 3, we show the optical relaxation time τ_{opt} determined as a result of processing the experimental plasma-reflection spectra by the Kramers-Kronig method from the width of the line of the energy-loss function ($-\text{Im}\epsilon^{-1}$) [6] and the static relaxation time $\tau_{st} = (\rho\epsilon_0\epsilon_\infty\omega_p^2)^{-1}$; the latter was obtained as a result of measuring the dc conductivity $\sigma = 1/\rho$ for donor- and acceptor-doped samples. As follows from Fig. 3, the largest discrepancies in the values of the optical and static relaxation times are observed exactly for crystals with $\hbar\omega_p$ almost equal to E_{gL} , which points to the existence of an additional mechanism of relaxation of carriers.

The possibility of $\hbar\omega_p$ being coincident with E_{gL} was theoretically analyzed in a number of studies [7–9]. In particular, it was shown [7] that direct band-to-band hole-electron recombination with the spontaneous and stimulated emission of plasma waves becomes possible under these conditions in addition to conventional (radiative and collisional) band-to-band mechanisms of relaxation of the nonequilibrium density of carriers. The emission rate in this channel increases as the band gap approaches the plasma-oscillation energy. Under these conditions, the lifetime induced by the band-to-band plasmon recombination was shown [8] to be described by an expression obtained as a result of considering the electron-plasmon interaction [10]:

$$\tau = \left(\frac{1}{n_0} + \frac{1}{p_0}\right)^{-1} \frac{\epsilon_\infty \pi^2 \alpha^2 \hbar (1 + \mu)^{3/2}}{e^2 |I_{c,v}|^2 (\hbar\omega_p)^{3/2} \sqrt{\hbar\omega_p - E_{gL}}} \gamma \times \left[\exp\left(\frac{\hbar\omega_p}{kT}\right) + \exp\left(-\frac{E_{0c} - q}{kT} + \frac{E_{gL} + \mu\hbar\omega_p}{(1 + \mu)kT}\right) \right] \quad (1)$$

$$\gamma = \begin{cases} 1, & \text{if } \frac{\hbar\omega_p}{E_{gL}} \geq 1 + \mu \\ \frac{1}{\sqrt{\left(1 - \frac{E_{gL}}{\hbar\omega}\right)\left(1 + \frac{1}{\mu}\right)}}, & \text{if } \frac{\hbar\omega_p}{E_{gL}} < 1 + \mu \end{cases}$$

where n_0 and p_0 are the electron and hole concentrations, respectively; $\alpha = \hbar^2/2m_c^*$; $\mu = m_c^*/m_v^*$ (m_c^* and m_v^* are the effective masses of electrons and holes); $|I_{c,v}|$ is the matrix element of transition of electrons

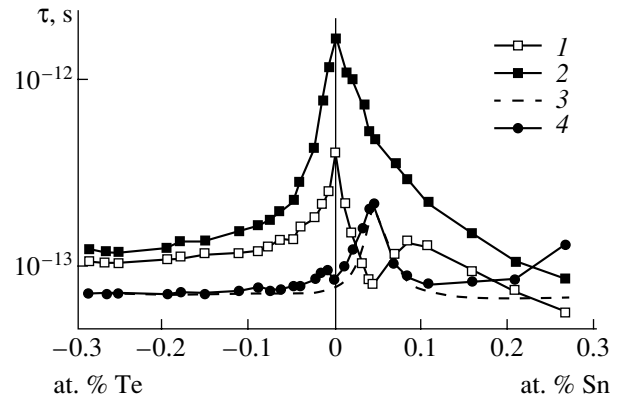


Fig. 3. (1) Optical relaxation time τ_{opt} and (2) static relaxation time τ_{st} as functions of the content and type of dopant. (3) Model calculation according to expression (1), and (4) ratio τ_{st}/τ_{opt} . $T = 80$ K.

from the valence band to the conduction band; $E_{0,c}$ is the energy of the conduction-band bottom; and q is the energy of electrons at the Fermi level.

The authors of [8] used this expression to calculate the relaxation time for the InSb compound. The band gap of $E_g = 180$ meV in this material and, correspondingly, the high free carrier concentrations (about 10^{20} cm $^{-3}$) are necessary for the condition $\hbar\omega_p = E_{gL}$ to be satisfied. In contrast to the case of InSb, the acceptor doping of bismuth with 0–0.04 at. % of tin leads to a decrease instead of an increase in the concentration of free charge carriers and also to $\hbar\omega_p$ approaching E_{gL} (Fig. 1b). No other basic distinctions exist; therefore, expression (1) is also applicable for calculating the relaxation time in bismuth.

In the case of band-to-band recombination, the plasmon-oscillation energy must be higher or equal to the band gap, which is taken into account in expression (1) by the factor γ , which describes the delta function of suppression of the situation where $\hbar\omega_p \ll E_{gL}$. When describing the initiation of plasmon relaxation in doped bismuth, it is necessary to also take into account the Burstein-Moss shift, which is inherent to narrow-gap materials, and to consider the condition for initiating the plasmon relaxation, $\hbar\omega_p \geq E_{gL} + 2E_F$. According to Fig. 1b, the indicated condition is satisfied only in a narrow region of the Sn-dopant content of 0.04 at. %, where the chemical-potential level is located in the vicinity of the energy gap at the L point of the Brillouin zone. As follows from expression (1), it is precisely this case in which the role of plasmon relaxation is the most significant, and this is in good agreement with the experimental results shown in Fig. 3 (curves 1, 2). In Fig. 3, we also show the ratio between static and optical relaxation times (curve 4) and the calculated time of relaxation induced by the plasmon recombination according to expression (1) (curve 3) and normalized to

the relaxation in bismuth crystals heavily doped with tellurium, for which $E_{p\parallel} = \hbar\omega_p \ll E_{gL} + 2E_F$ and the plasmon mechanism of relaxation is impossible. As can be seen from Fig. 3, we succeeded in satisfactorily describing the resonance increase in the ratio between static and optical relaxation times in terms of the assumption that there is a plasmon mechanism of relaxation in crystals for which the condition $\hbar\omega_p \geq E_{gL} + 2E_F$ is met.

Thus, we observed for the first time a modification in the plasma-reflection-spectra shape and a decrease in the optical time of relaxation for charge carriers due to the electron-plasmon interaction arising in acceptor-doped bismuth if the condition $\hbar\omega_p = E_{gL}$ is met, which was previously predicted in [11].

It is necessary to note that the prevalence of plasmon relaxation may become a serious obstacle to the use of single crystals with a narrow band gap for creating infrared detectors operating in the wavelength region on the order of several tens of micrometers. In fact, it was found [12] that there is no photoconductivity in doped semiconductor crystals $\text{Bi}_{1-x}\text{Sb}_x$ with $x = 0.09$ and 0.15 , the cause of which remains unclear. The analysis we carried out shows that an increase in carrier concentration due to doping the semiconductor alloys of the indicated composition leads to the fact that the characteristic energies in the electron and plasmon spectra approach each other; as a result, the relaxation time for the charge carriers decreases, which is the most probable cause for the absence of photoconductivity.

REFERENCES

1. V. D. Kulakovskii and V. D. Egorov, *Fiz. Tverd. Tela (Leningrad)* **15**, 2053 (1973) [*Sov. Phys. Solid State* **15**, 1507 (1973)].
2. M. I. Belovolov, V. S. Vavilov, V. E. Egorov, and V. D. Kulakovskii, *Izv. Vyssh. Uchebn. Zaved., Fiz.*, No. 2, 5 (1976).
3. V. M. Grabov, N. P. Stepanov, B. E. Vol'f, and A. S. Mal'tsev, *Opt. Spektrosk.* **69**, 134 (1990) [*Opt. Spectrosc.* **69**, 82 (1990)].
4. A. S. Mal'tsev, V. M. Grabov, and A. A. Kukharskii, *Opt. Spektrosk.* **58**, 927 (1985) [*Opt. Spectrosc.* **58**, 567 (1985)].
5. P. Grosse, *Freie Elektronen in Festkörpern* (Springer-Verlag, Heidelberg, 1979; Mir, Moscow, 1982).
6. V. V. Sobolev and V. V. Nemoskalenko, *The Methods of Computational Physics in the Theory of Solid State* (Naukova Dumka, Kiev, 1988).
7. N. S. Baryshev, *Fiz. Tekh. Poluprovodn. (Leningrad)* **9**, 2023 (1975) [*Sov. Phys. Semicond.* **9**, 1324 (1975)].
8. P. Tussing, W. Rpsenthal, and A. Haug, *Phys. Status Solidi B* **53**, 451 (1972).
9. R. Dornhaus and G. Nimtz, *Solid State Commun.* **27**, 575 (1978).
10. D. Pines, *Elementary Excitations in Solids* (Benjamin, New York, 1963; Mir, Moscow, 1965).
11. V. L. Bonch-Bruevich and E. G. Landsberg, *Phys. Status Solidi* **29**, 9 (1968).
12. V. I. Trifonov, V. A. Martyakhin, V. A. Stukan, and N. F. Zaets, *Fiz. Tekh. Poluprovodn. (Leningrad)* **12**, 1641 (1978) [*Sov. Phys. Semicond.* **12**, 972 (1978)].

Translated by V. Bukhanov

**ELECTRONIC
AND OPTICAL PROPERTIES
OF SEMICONDUCTORS**

**Study of Zinc Impurity Atoms in GaP, GaAs,
and GaSb $^{67}\text{Ga}(^{67}\text{Zn})$ and $^{67}\text{Cu}(^{67}\text{Zn})$
by Emission Mössbauer Spectroscopy**

N. P. Seregin*, S. A. Nemov*, and S. M. Irkaev**

* *St. Petersburg State Technical University, St. Petersburg, 195251 Russia*

** *Institute for Analytical Instrumentation, Russian Academy of Sciences, St. Petersburg, 198103 Russia*

Submitted March 11, 2002; accepted for publication March 13, 2002

Abstract—The Mössbauer spectra of $^{67}\text{Ga}(^{67}\text{Zn})$ and $^{67}\text{Cu}(^{67}\text{Zn})$ impurity atoms in the bulk of GaP, GaAs, and GaSb samples correspond to isolated zinc centers at Ga sites. The observed shift of the spectral centers of gravity to higher positive velocities at the transition from *p*- to *n*-type samples corresponds to the recharging of a shallow zinc impurity center. Mössbauer spectra of $^{67}\text{Cu}(^{67}\text{Zn})$ impurities at the surface of samples represent a superposition of spectra corresponding to isolated zinc centers at gallium sites with those corresponding to zinc associates with an arsenic vacancy. © 2002 MAIK “Nauka/Interperiodica”.

It is well known that a zinc impurity in III–V compounds forms shallow acceptor levels (0.02–0.04 eV above the valence band edge) [1]. A study of zinc impurity atoms in GaP, GaAs, and GaSb using emission Mössbauer spectroscopy of the $^{67}\text{Ga}(^{67}\text{Zn})$ isotope opens the way to revealing the effect of electrical activity of “daughter” atoms (with the evident inactivity of “parent” atoms) on the Mössbauer spectral parameters of the ^{67}Zn probe, whereas the relevant spectra of the $^{67}\text{Cu}(^{67}\text{Zn})$ isotope make possible the study of a similar effect for both daughter and parent atoms. According to [1], a copper impurity forms shallow donor levels in III–V compounds (in GaAs, they lie at ~0.07 eV below the conduction band edge) and deep two-electron acceptor levels (~0.14 and 0.44 eV above the valence band edge in GaAs).

The samples under study were single-crystal GaP ($n = 2 \times 10^{18} \text{ cm}^{-3}$, $p = 3 \times 10^{18} \text{ cm}^{-3}$), GaAs ($n = 10^{17} \text{ cm}^{-3}$, $p = 5 \times 10^{16} \text{ cm}^{-3}$), and GaSb ($n = 8 \times 10^{18} \text{ cm}^{-3}$, $p = 5 \times 10^{18} \text{ cm}^{-3}$). The samples were doped with the radioactive isotopes ^{67}Ga and ^{67}Cu through diffusion annealing in vacuum for 5 h, at temperatures 100°C lower than the melting temperature of the respective compound. To prevent the evaporation of volatile components, a powder of the corresponding compound was introduced into an ampule. The maximum Zn concentration that formed after the radioactive decay of parent ^{67}Ga and ^{67}Cu atoms did not exceed 10^{15} cm^{-3} (i.e., the Fermi level position in all the samples was determined by the background dopant). The spectra were recorded either without the preliminary treatment of the sample surface (these spectra were associated with the impurity atoms located in the surface region) or an ~50- μm -thick layer was removed from the sample surface prior to the

recording of spectra, and these spectra were assigned to impurity atoms in the sample bulk.

^{67}Zn Mössbauer spectra were recorded using a commercial spectrometer with a modified driving system. A PZT-ceramics piezoelectric converter served as a modulator. The spectra were recorded at 4.2 K using a ^{67}ZnS absorber, which served as a reference for all the experimental spectra. The spectra typical of the bulk and surface regions are shown in Figs. 1 and 2, and the results of data processing for the bulk samples are presented in the table.

$^{67}\text{Ga}(^{67}\text{Zn})$ spectra recorded from the bulk of samples are single lines with a full width at half-maximum (FWHM) close to the instrumental broadening ($2.6 \pm 3 \mu\text{m s}^{-1}$), and their position (center of gravity) shifts steadily to higher velocities at the transition from GaP to GaSb. The line position slightly depends on the type of sample conduction: it shifts to a lower velocity at the

Parameters of $^{67}\text{Ga}(^{67}\text{Zn})$ and $^{67}\text{Cu}(^{67}\text{Zn})$ Mössbauer spectra in GaP, GaAs, and GaSb at 4.2 K

Compound	$^{67}\text{Ga}(^{67}\text{Zn})$ spectra		$^{67}\text{Cu}(^{67}\text{Zn})$ spectra	
	centroid of the spectrum, $\mu\text{m s}^{-1}$	FWHM, $\mu\text{m s}^{-1}$	centroid of the spectrum, $\mu\text{m s}^{-1}$	FWHM, $\mu\text{m s}^{-1}$
<i>n</i> -GaP	+16.0(4)	2.8(3)	+18.0(4)	3.1(3)
<i>p</i> -GaP	+13.5(4)	2.7(3)	+15.6(4)	2.8(3)
<i>n</i> -GaAs	24.9(4)	2.7(3)	26.3(4)	3.0(3)
<i>p</i> -GaAs	22.6(4)	2.6(3)	24.0(4)	3.0(3)
<i>n</i> -GaSb	+31.5(4)	2.8(3)	+33.2(4)	3.0(3)
<i>p</i> -GaSb	+30.8(4)	2.6(3)	+32.5(4)	2.7(3)

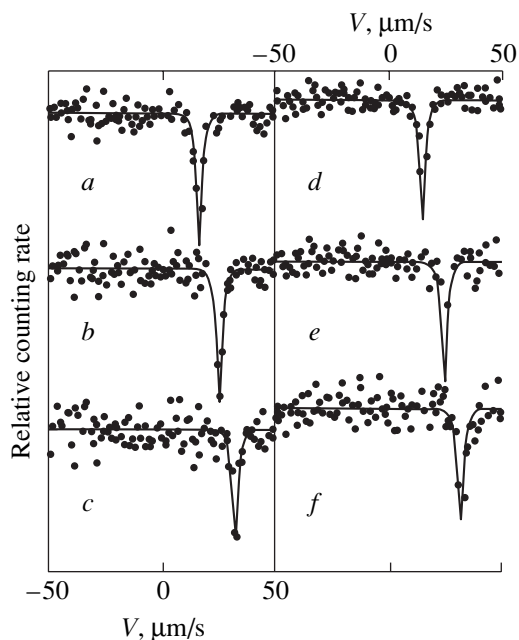


Fig. 1. Emission Mössbauer spectra of $^{67}\text{Ga}(^{67}\text{Zn})$ impurity atoms for (a–c) *n*-type and (d–f) *p*-type samples measured at 4.2 K. (a, d) GaP, (b, e) GaAs, and (c, f) GaSb.

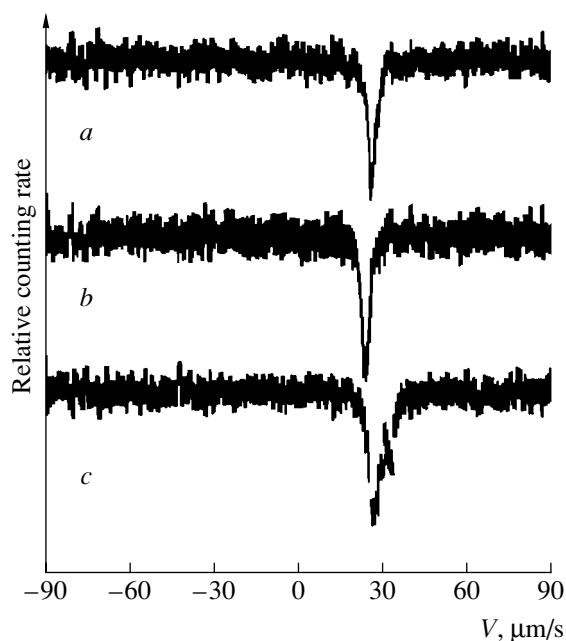


Fig. 2. Emission Mössbauer spectra of $^{67}\text{Cu}(^{67}\text{Zn})$ impurity atoms in (a, b) bulk and (c) surface region of (a) *n*-type and (b, c) *p*-type GaAs measured at 4.2 K.

transition from electron to hole conduction, and this effect is most evident in wide-gap materials.

The center of gravity position in the Mössbauer spectrum depends on two factors: the electron density

at the nucleus of ^{67}Zn under study, and the second-order Doppler shift defined by the Debye temperature of a crystal. Since the Debye temperature is independent of the conduction type, we conclude that the recharging of a shallow impurity level influences the electron density near a ^{67}Zn nucleus: the electron density increases at the transition from *p*- to *n*-type samples, which corresponds to the transition $[\text{Zn}^0] \rightarrow [\text{Zn}^-]$. $^{67}\text{Ga}(^{67}\text{Zn})$ Mössbauer spectra should be related to isolated Zn impurity centers at Ga sites, whereas the positive shift of the spectral centroid along the series GaP–GaAs–GaSb reflects the variation of the chemical bond ionicity of zinc atoms with respect to the atoms in the first coordination sphere of a zinc atom.

The spectra of $^{67}\text{Cu}(^{67}\text{Zn})$ impurity atoms in the bulk of the samples are also single lines corresponding to isolated Zn centers at Ga sites. Similarly to $^{67}\text{Ga}(^{67}\text{Zn})$ spectra, the center of gravity shifts to positive velocities at the transition from *p*- to *n*-type samples (this shift is associated with the transition $[\text{Zn}^0] \rightarrow [\text{Zn}^-]$). The electrical activity of copper impurity atoms does not affect the fine structure of spectra for the bulk of the samples.

In the surface region, the spectra of $^{67}\text{Cu}(^{67}\text{Zn})$ impurity atoms demonstrate a superposition of the above-described single lines related to isolated Zn atoms at Ga sites and a quadrupole triplet [GaAs: spectrum center of gravity $(30 \pm 1) \mu\text{m s}^{-1}$, quadrupole coupling constant $(0.92 \pm 0.03) \text{ MHz}$, line width $(3.0 \pm 0.3) \mu\text{m s}^{-1}$]. The last spectrum is presumably related to the associates of zinc impurity centers with As vacancies (these associates were identified in the study of photoluminescence in GaAs : Cu [1]).

Thus, the Mössbauer spectra of $^{67}\text{Ga}(^{67}\text{Zn})$ and $^{67}\text{Cu}(^{67}\text{Zn})$ impurity atoms in the bulk of GaP, GaAs, and GaSb samples are related to isolated zinc centers at Ga sites, and the recharging of Zn impurity centers is observed. Mössbauer spectra of $^{67}\text{Cu}(^{67}\text{Zn})$ impurities at the surface of samples are related to isolated zinc centers as well as zinc associates with arsenic vacancies.

ACKNOWLEDGMENTS

This study was supported by the Ministry of Education of the Russian Federation (grant no. E 00-3.4-42).

REFERENCES

1. A. G. Milnes, *Deep Impurities in Semiconductors* (Wiley, New York, 1973; Mir, Moscow, 1977).

Translated by D. Mashovets

SEMICONDUCTOR STRUCTURES,
INTERFACES, AND SURFACES

Cathodoluminescence of ZnO/GaN/ α -Al₂O₃ Heteroepitaxial Structures Grown by Chemical Vapor Deposition

M. V. Chukichev*, B. M. Ataev**, V. V. Mamedov**,
Ya. I. Alivov***, and I. I. Khodos***

* Physics Department, Moscow State University, Vorob'evy gory, Moscow, 119899 Russia

** Institute of Physics, Dagestan Scientific Center, Russian Academy of Sciences, ul. 26 Bakinskikh Komissarov,
Makhachkala, Dagestan, 367003 Russia

*** Institute of Problems in Microelectronics Technology, Russian Academy of Sciences,
Chernogolovka, Moscow oblast, 142432 Russia

e-mail: alivov@ipmt-hpm.ac.ru

Submitted February 27, 2002; accepted for publication March 11, 2002

Abstract—The cathodoluminescent properties of ZnO films in ZnO/GaN/ α -Al₂O₃ and ZnO/ α -Al₂O₃ heteroepitaxial structures grown by chemical vapor deposition in a low-pressure flowing-gas reactor were studied and compared. A superlinear dependence of the excitonic-band intensity in the cathodoluminescence spectrum of the ZnO/GaN/ α -Al₂O₃ structures on the electron-beam current is ascertained, which indicates that the emission is stimulated for relatively low thresholds of the excitation intensity. It is shown that the ZnO films grown on the GaN substrates exhibit a much more effective cathodoluminescence compared to the cathodoluminescence in the films grown on α -Al₂O₃. It was observed that the luminescent properties of ZnO layers in the ZnO/GaN/ α -Al₂O₃ structures subjected to long-term heat treatment at 750°C in an oxygen atmosphere exhibit a high thermal stability. © 2002 MAIK “Nauka/Interperiodica”.

1. INTRODUCTION

Zinc oxide (ZnO) is a direct-gap semiconductor, has a band gap of ~3.3 eV at 300 K, and is considered as one of the promising materials for the fabrication of blue and UV light-emitting diodes. This bright outlook for ZnO is based on the fact that it features a high quantum yield of photoluminescence and cathodoluminescence and a comparatively large exciton-binding energy (~60 meV), which makes the excitonic luminescence quite effective at high temperatures [1]; in addition, ZnO is highly radiation-resistant [2]. However, it is worth noting that ZnO bulk crystals and films grown by conventional methods have, as a rule, *n*-type conduction; only recently have *p*-type films been grown and *p*-*n* junctions based on these films fabricated [3–6].

In order to fabricate devices with the above-mentioned characteristics, one should have high-quality ZnO films with a low concentration of defects that act as nonradiative-recombination centers. In most cases, such centers are represented by dislocations. The latter are generated at the film–substrate interface owing to the mismatch between the lattice parameters of the film and the substrate, and they impair the film structure. Thus, if the ZnO film is grown on a (0001) α -Al₂O₃ substrate, this mismatch is as large as 38%. It is also worth noting that the presence of dislocations is one of

the causes of the rapid degradation of semiconductor devices in the course of their operation. Consequently, an important condition for obtaining perfect ZnO films, which possess the required optical properties, is the proper choice of a substrate or buffer layer with insignificant lattice mismatch.

A material with a lattice of the same type as in ZnO and with almost the same lattice parameters is GaN: the lattice mismatch in this case amounts to a mere ~1.8%. These materials not only have almost the same lattice parameters but also possess other nearly identical physical parameters [7, 8], which constitutes an important factor for the development of heterostructure-based highly efficient optoelectronic and other devices. In spite of these circumstances, there have been only a few publications devoted to the growth of ZnO on GaN [8, 9], and the properties of the ZnO/GaN layers have been studied inadequately.

Previously [10], chemical vapor deposition in a gas-flow low-pressure reactor was used to grow ZnO/GaN/ α -Al₂O₃ heteroepitaxial structures. According to the data obtained from X-ray diffraction analysis and photoluminescence measurements, the obtained films had a high structural quality.

In this paper, we report the results of studying the optical properties of such ZnO layers by measuring the

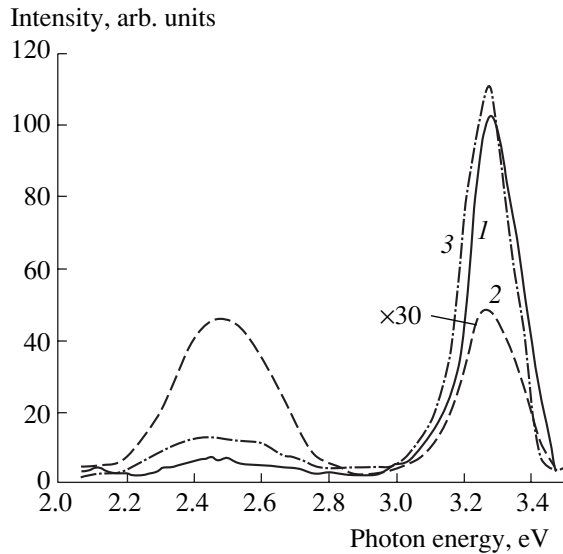


Fig. 1. The cathodoluminescence spectra of the (1) ZnO/GaN/ α -Al₂O₃ and (2) ZnO/ α -Al₂O₃ heteroepitaxial structures and (3) a bulk ZnO crystal at 300 K. The electron-beam current was equal to 1 μ A.

cathodoluminescence spectra. An advantage of cathodoluminescence compared to photoluminescence consists in the fact that the use of an electron beam makes it possible to vary the excitation level in a wide range by varying the current density and to study, layer-by-layer, the cathodoluminescent properties of the film by varying the electron energy. We also studied the effect of heat treatment of the ZnO/GaN/ α -Al₂O₃ and ZnO/ α -Al₂O₃ heteroepitaxial structures on the cathodoluminescence of ZnO in these structures.

2. EXPERIMENTAL

The epitaxial growth of (0001) ZnO films on the (0001)GaN/(0001) α -Al₂O₃ structure was carried out using chemical vapor deposition in a gas-flow low-pressure reactor. This method was described in detail elsewhere [11]. Preliminarily, \sim 0.5- μ m-thick GaN layers were grown on α -Al₂O₃ using gas-phase epitaxy from metal-organic compounds. The ZnO/GaN/ α -Al₂O₃ structures were then grown. For the sake of comparison, ZnO/ α -Al₂O₃ structures were also grown under the same conditions. The thickness of the ZnO films in both types of heteroepitaxial structures was \sim 3 μ m. Cathodoluminescence was studied using an "Elektronnaya pushka" system; the spectra were measured using a DFS-12 spectrometer at temperatures of 78 and 300 K for various electron currents and energies. The current and energy were varied within the ranges of 0.05–2 μ A and 10–50 keV, respectively. The cleaved-surface morphology of a ZnO/GaN/ α -Al₂O₃ structure was studied using a JEOL-2000 electron microscope in the mode of secondary-electron detection. In order to assess the thermal stability of the optical properties of the ZnO

films, we annealed the samples for 5, 20, and 40 h at 750°C in an oxygen atmosphere.

3. RESULTS AND DISCUSSION

In Fig. 1, we show the cathodoluminescence spectra of ZnO layers in the ZnO/GaN/ α -Al₂O₃ and ZnO/ α -Al₂O₃ heteroepitaxial structures (curves 1 and 2, respectively) and of a ZnO bulk crystal (curve 3); the spectra were measured at 300 K using an electron-beam current of 1 μ A. As can be seen from Fig. 1, the spectrum of the ZnO layer on GaN (curve 1) consists of an intense narrow band peaked at 3.29 eV and a very weak broad band peaked at 2.43 eV. The ratio between the peak intensities of the UV and green bands was equal to \sim 50 for the specified electron-current density. The excitonic origin of the UV band was ascertained previously [10]; when measured at 77 K, this band consists of a prevalent free-exciton line A1, a less intense line J_D related to an exciton bound at donors, and LO-phonon satellites.

The cathodoluminescence spectrum (spectrum 2 in Fig. 1) of a ZnO layer grown directly on α -Al₂O₃ differs from spectrum 1 in that the emission intensity in both the edge and impurity-defect spectral regions is much lower (by a factor of about 30) than for the layer grown on the GaN buffer layer (see Fig. 1). The half-width of the excitonic bands in spectra 1 and 2 also differed markedly. At 300 K, the half-width of the band in the spectrum of the ZnO/GaN/ α -Al₂O₃ sample was 112 meV, whereas it amounted to 189 meV for the ZnO/ α -Al₂O₃ sample. For the sake of comparison, we measured the cathodoluminescence spectrum of a bulk ZnO single crystal, which was also grown by chemical-vapor deposition (Fig. 1, curve 3). As can be seen from a comparison of curves 1 and 3 in Fig. 1, the cathodoluminescence intensities of the ZnO/GaN/ α -Al₂O₃ structure and the bulk crystal are close to each other, which indicates that the degree of perfection of the film and crystal are almost the same.

Figure 2 displays the dependences of the cathodoluminescence intensity on the excitation level (electron-current density) for a ZnO/GaN/ α -Al₂O₃ structure. Curves 1 and 2 represent the electron-current (J) dependences of the excitonic- (I_{exc}) and impurity-band intensities, respectively; the curves are plotted on the log-log coordinates. As can be seen, the excitonic-band intensity increases superlinearly with increasing excitation level, $I_{\text{exc}} \propto J^n$. The value of n determined from the slope of the curves was found to be equal to 2.95, which is indicative of a cubic dependence of the excitonic-band intensity on the excitation level. Such a dependence is characteristic of film of a high structural quality at high excitation intensities. In contrast to this, the green-band intensity depends sublinearly on the excitation level ($n = 0.65$) and levels off with increasing electron-beam current. The obtained results show that the ratio between the intensities at the peaks of the excitonic and green bands (I_{exc}/I_g) depends heavily on the

electron-beam current. Thus, for the beam currents of 0.05 and 1 μ A, this ratio was equal to 15 and 50, respectively; for a beam current of 2 μ A, virtually only the UV band was observed. Obviously, we can reliably assess the structural quality of the samples from the ratio $I_{\text{exc}}/I_{\text{g}}$ only if the excitation intensity is relatively low.

Figure 3 displays the electron-energy dependences of the cathodoluminescence UV- and green-band intensities. The electron energy was varied from 10 keV (in which case the depth of electron-beam penetration into ZnO was $\sim 0.1 \mu\text{m}$ [12]) to 50 keV (in which case, the beam penetrated up to the interface with GaN). Dependences of the green- and UV-band intensities on the electron energy for a constant beam power (Fig. 3) indicate that the cathodoluminescence intensity varies little with varying electron energy; only a slight decrease in the UV-band intensity is observed. This indicates that the ZnO film grown on GaN is homogeneous over its entire thickness up to the interface with the GaN surface. This inference is also supported by the electron microscopy data (Fig. 4). It can be seen from Fig. 4 that the ZnO–GaN interface is planar, whereas the GaN– α -Al₂O₃ interface is highly irregular. The planar interface between ZnO and GaN observed in Fig. 4 is indicative of the good heteroepitaxial growth of ZnO on the GaN surface; this phenomenon is caused by the same type of lattices and by a perfect match of the crystal-lattice parameters. Hence, it may be concluded that the film is homogeneous and the dislocation density is low in both the ZnO–GaN transition layer and the film bulk. An insignificant decrease in the intensity of the UV band, which is observed as the electron energy increases (Fig. 3, curve 1), can be explained by the fact that a fraction of radiation is lost in the ZnO layer owing to self-absorption in the excitonic region, where the absorption coefficient can be as large as 10^5 cm^{-1} .

Results of heat treatment indicate that there are considerable differences in the thermal stability of the structures under consideration. The cathodoluminescence intensity of the ZnO/GaN/ α -Al₂O₃ structures increases by a factor of about 1.5 after a 5-h annealing and becomes almost independent of an annealing duration longer than 5 h. Only a slight shift of the UV-band peak to longer wavelengths is observed, which is related (as shown by the cathodoluminescence measurements at 78 K) to a redistribution of energy between the excitonic lines. A completely different pattern was observed for a ZnO film grown directly on the Al₂O₃ substrate. The cathodoluminescence intensity, both in the UV and green spectral regions, decreased with increasing heat-treatment duration: after 20-h annealing, the green-band intensity decreased by a factor of 2 and that of the UV band decreased by a factor of 4; as a result of 40-h annealing, the exciton-band intensity decreased to such an extent that this band was virtually unobserved at room temperature.

Experimental results indicate that the characteristics of the ZnO films grown on GaN are clearly superior to

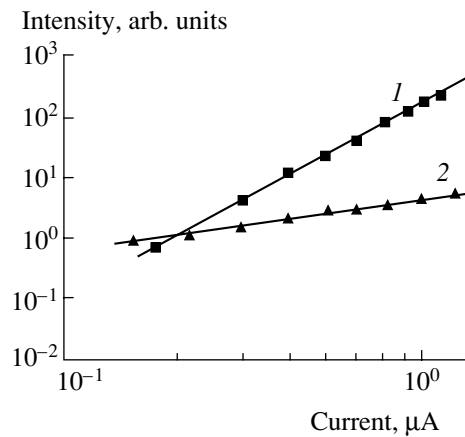


Fig. 2. Dependences of the peak intensities of the (1) UV and (2) green bands in the cathodoluminescence spectrum of the ZnO-based structures at 300 K on the electron-beam current.

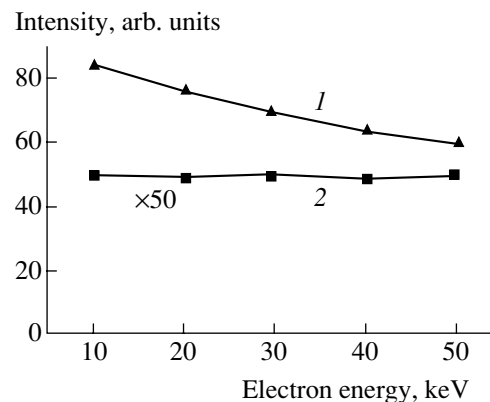


Fig. 3. Dependences of intensities at the peaks of the (1) UV and (2) green bands in the cathodoluminescence spectrum at 300 K on the electron energy.

those of the films grown directly on α -Al₂O₃; in our opinion, this is caused by the good match of the GaN and ZnO lattice parameters. Owing to the matched lattice constants of ZnO and GaN, the ZnO epitaxial layer grown on GaN is characterized by an almost perfect crystal lattice and a low concentration of defects that act as nonradiative-recombination centers. If the ZnO layer is deposited on α -Al₂O₃, the lattice mismatch is large; as a result, the ZnO crystal lattice is found to be highly stressed in the transition region and the layer contains a high concentration of dislocations and other defects. It is not surprising, then, that the radiative-recombination efficiency in ZnO layers grown on α -Al₂O₃ is much lower than in the layers grown on GaN, which is confirmed through the comparative study of cathodoluminescence in these layers. As the comparison of the cathodoluminescence spectra of a ZnO layer and a bulk ZnO crystal under the same excitation conditions (Fig. 1, curves 1, 3) shows, the cathodoluminescence intensity in a ZnO/GaN/ α -Al₂O₃

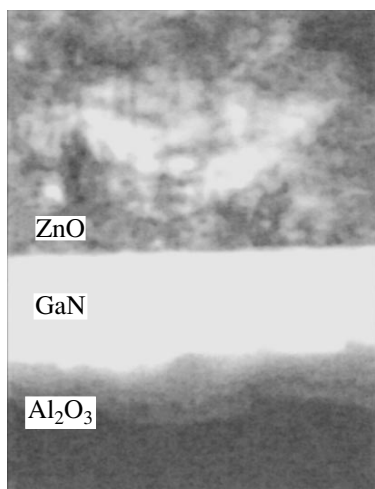


Fig. 4. A cross-sectional electron-microscopy image of a ZnO/GaN/ α -Al₂O₃ structure; the image was obtained under the conditions of the secondary-electron detection.

structure is very nearly equal to that of the bulk ZnO crystal. A slight distinction between the peak positions of the ZnO layer and crystal are caused by different positions of the spectral lines related to the bound excitons, which depend on the type of uncontrolled impurities. The comparison of the cathodoluminescence spectra for the ZnO crystal and the layer grown on the buffer GaN layer shows that the ZnO layer is of high crystalline quality.

The cubic dependence of the UV band intensity in the cathodoluminescence spectrum on the excitation level is also indicative of the high structural quality of ZnO films grown on a GaN buffer layer. This dependence is characteristic of radiative processes with the involvement of three charge carriers in each recombination event; these processes occur if there are high concentrations of nonequilibrium charge carriers. A distinctly superlinear dependence of the cathodoluminescence intensity on the electron-beam current indicates that the emission is of the stimulated type even at relatively low threshold values of the excitation level.

As was mentioned above, dislocations are the main type of defects that reduce the efficiency of radiative recombination in epitaxial layers. This inference is also supported by the results of heat treatments of ZnO layers. In the course of heat treatment of a ZnO film grown on α -Al₂O₃, the crystal-lattice stresses in the transition layer are largely relieved as a result of the generation of dislocations, which then propagate into the film bulk and drastically reduce the radiative-recombination efficiency. In contrast, heat treatment of the ZnO epitaxial

layers that were grown on GaN and contain a low concentration of dislocations does not result in a reduction of the cathodoluminescence intensity.

4. CONCLUSION

We showed that ZnO epitaxial films grown on GaN buffer layers exhibit a more intense cathodoluminescence compared to the films grown on the α -Al₂O₃ substrate and that this is related to the quality of the film's crystal structure.

We ascertained that there is a superlinear dependence of the cathodoluminescence on the electron-beam current, which is indicative of the stimulated character of emission at relatively low excitation-level thresholds.

ACKNOWLEDGMENTS

This study was supported in part by the Russian Foundation for Basic Research, project nos. 01-02-16200 and 00-05-72031.

REFERENCES

1. D. M. Bagnal, Y. F. Chen, Z. Zhu, *et al.*, Appl. Phys. Lett. **73**, 1038 (1998).
2. D. C. Look, D. C. Reynolds, J. W. Hemsky, *et al.*, Appl. Phys. Lett. **75**, 811 (1999).
3. M. Joseph, H. Tabata, and T. Kawai, Jpn. J. Appl. Phys. **38**, L2505 (1999).
4. X.-L. Guo, H. Tabata, and T. Kawai, J. Cryst. Growth **223**, 135 (2001).
5. Y. E. Ryu, S. Zhu, D. C. Look, *et al.*, J. Cryst. Growth **216**, 330 (2000).
6. Y. E. Ryu, W. J. Kim, and H. W. White, J. Cryst. Growth **219**, 419 (2000).
7. Y. Chen, D. M. Bagnal, Hang-jun Koh, *et al.*, J. Appl. Phys. **84**, 3912 (1998).
8. R. D. Vispute, V. Talyansky, S. Choopun, *et al.*, Appl. Phys. Lett. **73**, 348 (1998).
9. S.-K. Hong, H.-J. Ko, Y. Chen, and T. Yao, J. Cryst. Growth **209**, 537 (2001).
10. B. M. Ataev, I. K. Kamilov, V. V. Lundin, *et al.*, Pis'ma Zh. Tekh. Fiz. **27** (2), 30 (2001) [Tech. Phys. Lett. **27**, 55 (2001)].
11. A. Kh. Abduev, B. M. Ataev, and A. M. Bagamadova, Izv. Akad. Nauk SSSR, Neorg. Mater., No. 11, 1928 (1987).
12. B. J. Pierce and R. L. Hengehold, J. Appl. Phys. **47**, 644 (1976).

Translated by A. Spitsyn

**SEMICONDUCTOR STRUCTURES,
INTERFACES, AND SURFACES**

Experimental Observation of Splitting of the Light and Heavy Hole Bands in Elastically Strained GaAsN

A. Yu. Egorov*, E. S. Semenova*, V. M. Ustinov*, Y. G. Hong**, and C. Tu**

* *Ioffe Physicotechnical Institute, Russian Academy of Sciences,
Politekhnicheskaya ul. 26, St. Petersburg, 194021 Russia
e-mail: anton@beam.ioffe.rssi.ru*

** *Department of Electrical and Computer Engineering, University of California,
San Diego, La Jolla, CA 92093-0407, USA*

Submitted January 30, 2002; accepted for publication January 31, 2002

Abstract—Twin peak photoluminescence of a GaAsN solid solution grown on GaAs substrate has been observed at room temperature. The peak splitting increases with an increase in the nitrogen content of the ternary compound. The observed form of the spectra is attributed to the presence of two transitions involving light and heavy holes. The splitting of light- and heavy-hole levels is due to elastic strain in GaAsN layers grown on the GaAs surface. © 2002 MAIK “Nauka/Interperiodica”.

1. INTRODUCTION

Interest in the new materials GaAsN and InGaAsN is due to their potential to increase the wavelength of emission from heterostructures grown on GaAs substrates to 1.3 μm and higher [1]. Lasers with an active region of InGaAsN/GaAs quantum wells (QW) emitting at 1.3 μm have been produced. The parameters of these new lasers are comparable with conventional InGaAsP lasers of the 1.3- μm range, but their temperature characteristics are improved [2]. In spite of the rapid development of devices using the material in question, the fundamental optical properties of GaAsN remain inadequately studied. A substantial nonlinearity in the dependence of the band gap on the composition of a GaAsN ternary solid solution allows the fabrication of materials with a band gap narrower than that in GaAs [3]. In its turn, a large lattice mismatch between the GaAsN layer and GaAs substrate, which arises even when the nitrogen content is low, also results in the changing of the position of the conduction band edges and in the splitting of the energy levels in the valence band. The importance of the latter effect on the properties of GaAsN compounds is the subject of this study. We present experimental data on the photoluminescence (PL) of GaAsN layers, which can be attributed to strain-induced splitting of the heavy- and light-hole energy levels. The obtained data allowed us to calculate the dependence of the band gap in unstrained GaAsN compounds on the content of nitrogen introduced into the layer.

2. EXPERIMENTAL

Strained GaAsN layers were grown by molecular beam epitaxy at 450°C on semi-insulating (001) GaAs

substrate. Elemental beams were produced from solid-state Ga and In sources, thermally decomposed arsine, and an RF-plasma source of nitrogen. The substrate temperature was measured using an IR pyrometer (IRCON). The nitrogen content in the samples under study varied in the range of 1–3.45%; the thickness of the nitrogen-containing layer was 0.1 μm .

In photoluminescence (PL) studies, an Ar⁺ laser (514.5 nm) and a Ge photodiode with thermoelectric cooling were used. A Phillips diffractometer was used for high-resolution X-ray diffractometry (HRXD).

2. RESULTS AND DISCUSSION

Figure 1 presents the room-temperature PL spectra of GaAsN layers with different amounts of nitrogen. As the nitrogen content increases, the PL spectra shift steadily to a longer wavelength. A surprising result of the rise of the nitrogen content in the range of 2–3.5% was an increase of the PL signal intensity. As seen in the figure, each PL spectrum consists of two peaks and the energy distance between these peaks increases with a rise in nitrogen content. At room temperature, the splitting of peaks becomes clearly seen when the nitrogen content is above 1.5%; at lower concentrations, the splitting becomes unobservable owing to homogeneous and inhomogeneous broadening of the PL line. It is well known that the incorporation of nitrogen results in inhomogeneous broadening of the PL line due to fluctuations in the composition. A typical value of the inhomogeneous broadening of the PL line for the GaAsN solid solution is about 30 meV. At lower nitrogen content, the peak related to higher energy is more intense. With a rise in the nitrogen content, the lower-energy peak becomes dominant. We have evaluated the energy positions of both peaks for samples differing in their

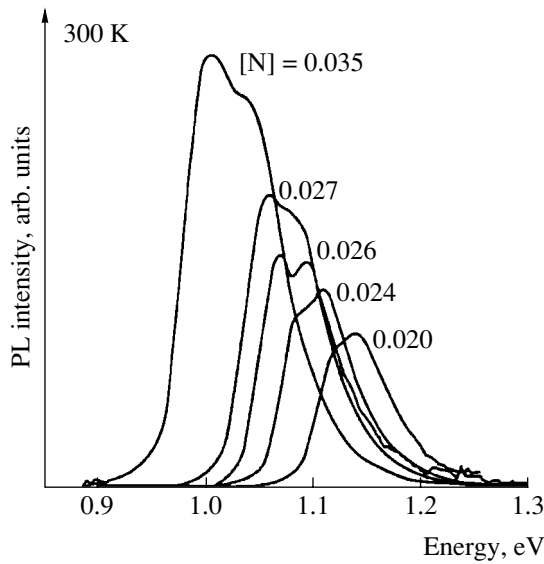


Fig. 1. PL spectra of 0.1 μm thick GaAsN layers with different nitrogen content grown on (100) GaAs substrate. The content of nitrogen [N] is indicated in mo near the curves.

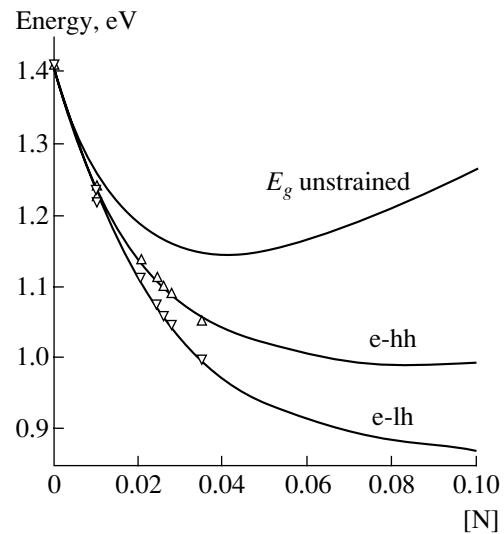


Fig. 2. Energy positions of the PL peaks in elastically strained GaAsN layers and the band gap in unstrained GaAsN vs. the content of incorporated nitrogen [N]. Solid lines e-hh and e-lh were calculated using relations (1a) and (1b), respectively.

nitrogen content. These dependences are shown in Fig. 2. The distance between the PL spectral peaks increases as [N] rises, i.e., with the rising of elastic strain in the nitrogen-containing layer grown on the GaAs substrate. The experimental dependences of the energy positions of the PL peaks presented in Fig. 2 are adequately described by the following relations (shown by solid lines in the figure):

$$E_{e\text{-hh}} = 0.99 + 0.43 \exp(-x/1.87), \quad (1a)$$

$$E_{e\text{-lh}} = 0.86 + 0.56 \exp(-x/2.51), \quad (1b)$$

where x is the nitrogen content (%), and $E_{e\text{-hh}}$ and $E_{e\text{-lh}}$ the energies (eV) of the high- and low-energy transitions, respectively. As is seen, both functions are limited by the minimum energies of 0.99 and 0.86 eV for the high- and low-energy transitions, respectively.

The crystal perfection, pseudomorphic character of growth, i.e., the degree of crystal lattice relaxation, and the composition of the ternary solid solution were determined by HRXD. For illustration, we present the data for the sample with the highest nitrogen content (3.45%). Figure 3 shows typical HRXD rocking curves near symmetric (004) and asymmetric (115) reflections of GaAs. The curves (115)⁺ and (115)⁻ correspond to different incidence configurations of the X-ray beam $\vartheta_{\text{Br}} \pm \alpha$, where ϑ_{Br} is the Bragg angle, and α , the angle between the (004) and (115) directions. HRXD studies have shown that the nitrogen content in the sample is 3.45%, and the degree of strain relaxation in the lattice does not exceed 1%, which is within the limits of experimental accuracy. In the rocking curve recorded for the symmetric reflection, the half-width of the peak from the nitrogen-containing layer is sufficiently small

(close to that calculated for an ideal case), which is confirmation of the good homogeneity of the layer and its high crystal perfection. The presence of interference peaks in the curve indicates planarity of the structure heterointerfaces. Therefore, we can conclude that the samples under study have high crystal perfection; they are elastically strained GaAsN layers grown pseudomorphically on a GaAs substrate, with the nitrogen content in the layer up to 3.45%.

The pseudomorphic growth of elastically strained layers induces a biaxial strain ε_{\parallel} parallel to the plane of growth and a strain ε_{\perp} in the growth direction:

$$\varepsilon_{\parallel, \perp} = \frac{a_{\parallel, \perp}}{a} - 1, \quad (2)$$

where

$$a_{\parallel} = a_0, \quad (3a)$$

$$a_{\perp} = a \left[1 - D \left(\frac{a_{\parallel}}{a} - 1 \right) \right], \quad (3b)$$

$$D^{(001)} = 2 \frac{C_{12}}{C_{11}}. \quad (3c)$$

Here a_0 and a are, respectively, the lattice constants of a substrate and a free (unstrained) layer of the composition studied. The constant D depends on the elastic properties of the material and the substrate orientation (see (3c)). In zinc-blende structure semiconductors, the effect of strain on the energy levels at the Γ point of the Brillouin zone can be resolved into two components: shear and hydrostatic. The hydrostatic component of

strain is responsible for the energy shift of the valence and conduction band edges [4]:

$$\Delta E_v^{\text{hy}} = a_v(\varepsilon_{\perp} + 2\varepsilon_{\parallel}), \quad (4a)$$

$$\Delta E_c^{\text{hy}} = a_c(\varepsilon_{\perp} + 2\varepsilon_{\parallel}), \quad (4b)$$

where a_v and a_c are hydrostatic deformation potentials for the valence and conduction bands.

The shear component induces, via spin-orbit interaction, an additional energy splitting of the light-, heavy-, and spin-orbit-split-hole subbands in the valence band. For (100) oriented substrate, the energy shifts of the light- and heavy-hole subbands with respect to the heavy-hole energy are defined as [4]

$$\Delta E_{\text{hh}}^{\text{sh}} = -\frac{1}{2}\delta E^{\text{sh}}, \quad (5a)$$

$$\Delta E_{\text{lh}}^{\text{sh}} = -\frac{1}{2}\Delta_0 + \frac{1}{4}\delta E^{\text{sh}} \quad (5b)$$

$$+ \frac{1}{2} \left[\Delta_0^2 + \Delta_0 \delta E^{\text{sh}} + \frac{9}{4} (\delta E^{\text{sh}})^2 \right]^{1/2},$$

where Δ_0 is the spin-orbit splitting without strain, and δE^{sh} , the shift defined by strain. In our case of the (001) oriented substrate, this shift is defined as

$$\delta E_{001}^{\text{sh}} = 2b(\varepsilon_{\perp} - \varepsilon_{\parallel}), \quad (6)$$

where b is the shear tetragonal deformation potential. The conduction band at the Γ point is not affected by the shear component of strain.

As follows from (5a) and (5b), the band gap of strained GaAsN is defined by the position of the light-hole energy level. Therefore, the low- and high-energy peaks in the PL spectrum of the GaAsN layer shown in Fig. 1 correspond to the electron-(light hole) and electron-(heavy hole) transitions, respectively.

In terms of the above-stated theory, we have calculated the dependences of the energy level shift and the value of the energy gap between the heavy- and light-hole levels at the Γ point as functions of the nitrogen content in the grown layer. The calculated results are presented in Fig. 4. The distance between the PL spectral peaks for GaAsN layers with differing nitrogen content is also shown in Fig. 4 (points). As seen, the experimental points are consistent with the value of the energy gap between the light- and heavy-hole levels (curve $\Delta E_{\text{lh}}^{\text{sh}} - \Delta E_{\text{hh}}^{\text{sh}}$). The correlation between the calculated and experimental data leads to the conclusion that the above-presented theory and the GaAs constants are applicable in the evaluation of the observed effect. The used values of the GaAs constants a_c (-7.17 eV), a_v (1.16 eV), C_{11} (1.18×10^{12} dyne cm^{-2}), C_{12} (0.54×10^{12} dyne cm^{-2}), Δ_0 (0.34 eV), and b (-1.7 eV) were taken from [4]. The influence of nitrogen incorporated in the GaAs layer on elastic constants and the spin-

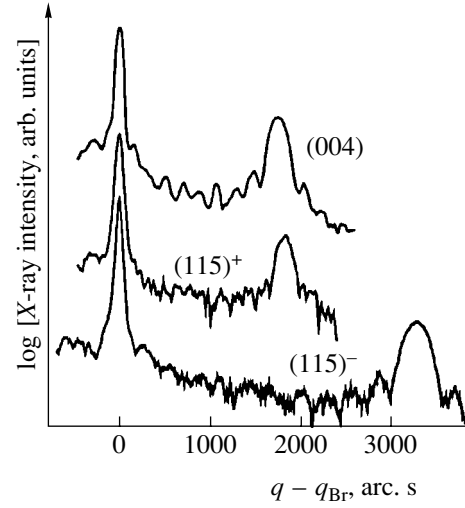


Fig. 3. X-ray diffraction spectra of a 100-nm-thick GaAs_{0.9655}N_{0.0345} layer grown on (100) GaAs substrate, recorded near symmetric (004) and asymmetric (115) reflections of GaAs.

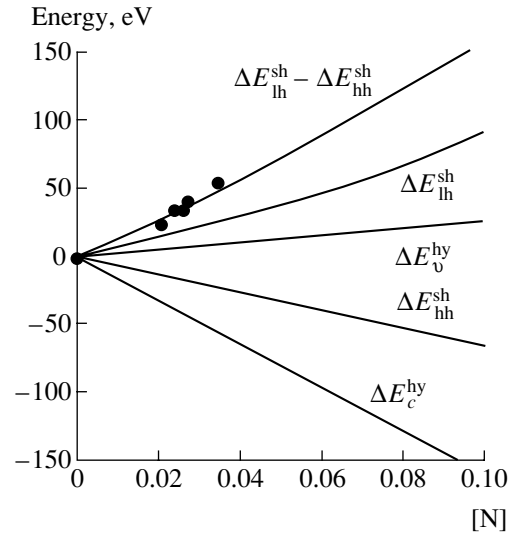


Fig. 4. Changes in the energies of the conduction band bottom (ΔE_c^{hy}), valence band (ΔE_v^{hy}), light- ($\Delta E_{\text{lh}}^{\text{sh}}$), and heavy-hole ($\Delta E_{\text{hh}}^{\text{sh}}$) subbands under the effect of hydrostatic and shear components of elastic strains in GaAsN layers grown on GaAs. The energy splitting between the light- and heavy-hole subbands ($\Delta E_{\text{lh}}^{\text{sh}} - \Delta E_{\text{hh}}^{\text{sh}}$) in a strained GaAsN layer vs. the content of incorporated nitrogen. Solid lines, calculation; points, energy spacing between the peaks in the PL spectra of elastically strained GaAsN layers.

orbit splitting without strain, Δ_0 , was ignored. Thus, we believe that in our experiment we have actually observed the transitions related to light and heavy holes in GaAsN at room temperature.

The dependence of the band gap in strained GaAsN layers grown on GaAs substrate on the concentration of

incorporated nitrogen is shown in Fig. 2; it corresponds to the energy of an electron–hole transition c-lh involving light holes. Using these experimental data and taking into account the effect of elastic strain on the energy position of the valence and conduction bands (Fig. 4), we can obtain the dependence of the band gap for unstrained GaAsN. This dependence is presented in Fig. 2 and is denoted as E_g unstrained. The band gap in the unstrained GaAsN compound decreases in the nitrogen content range of 0–3.99%, and beyond this range it increases steadily. Thus, the dependence is bounded from below by the energy value of 1.145 eV at a nitrogen content of 3.99%. A further decrease of the band gap in ternary GaAsN compounds grown on GaAs substrates is determined only by the effect of elastic strains on the energy position of the bands in a semiconductor. The presented dependence of the band gap in unstrained GaAsN on the nitrogen content differs substantially from the one predicted by the theory [3] assuming that the band gap in GaAsN can be reduced to zero.

4. CONCLUSION

Two electron–hole transitions have been observed in the PL spectra of elastically strained ternary GaAsN solutions grown on GaAs substrate. We attribute the observed spectral peaks to the transitions involving light and heavy holes. The energy spacing between the PL spectral peaks corresponds with the calculated split-

ting of the light- and heavy-hole levels, which are produced by elastic strains in GaAsN layers. Taking into account the effect of elastic strains on the positions of the energy band edges, we obtained the dependence of the band gap in unstrained GaAsN on the nitrogen content, with the minimum possible band gap of 1.145 eV at a nitrogen content of 3.99%.

ACKNOWLEDGMENTS

We are grateful to A.E. Zhukov for valuable discussions.

This study was supported by the National Renewable Energy Laboratory (AAD-9-18668-07), the Russian Ministry of Science program “Physics of Solid-State Nanostructures,” and the Civilian Research and Development Foundation (RE-2221).

REFERENCES

1. V. M. Ustinov and A. E. Zhukov, *Semicond. Sci. Technol.* **15**, R41 (2000).
2. B. Borchert, A. Yu. Egorov, S. Illek, *et al.*, *Electron. Lett.* **35**, 2204 (1999).
3. M. Kondow, T. Kitatani, S. Nakatsuka, *et al.*, *IEEE J. Sel. Top. Quantum Electron.* **3**, 719 (1997).
4. M. P. C. M. Krijn, *Semicond. Sci. Technol.* **6**, 27 (1991).

Translated by D. Mashovets

SEMICONDUCTOR STRUCTURES,
INTERFACES, AND SURFACES

Variations in the Properties of an Implantation-Synthesized Si_xN_y -Si Heterosystem as a Result of Thermal and Ion-Beam Treatments

V. V. Karzanov*, K. A. Markov, V. V. Sdobnyakov, and E. S. Demidov

Nizhni Novgorod State University, pr. Gagarina 23, Nizhni Novgorod, 603600 Russia

e-mail: ett@phys.unn.runnet.ru

Submitted December 18, 2001; accepted for publication February 5, 2002

Abstract—Transmission electron microscopy, infrared spectroscopy, and the measurements of current–voltage characteristics and capacitance were used to study the influence of heat treatment and the long-range effect of irradiation of the rear side of an Si wafer with Ar, Ne, and Si ions on the state of an Si_xN_y layer synthesized at the front side of this wafer. It is ascertained that the argon-ion bombardment of the wafer heated to 500°C is the most effective method for the formation of insulating silicon-nitride layers. The fact that the properties of Si_xN_y layers are scarcely affected by irradiation with neon and silicon ions is consistent with the previously suggested model of a spontaneous-acoustic mechanism of the long-range effect produced by irradiation of silicon with argon ions. © 2002 MAIK “Nauka/Interperiodica”.

1. INTRODUCTION

It has been shown previously [1–4] that argon bombardment of the rear surface of silicon samples heated to $T_i = 500^\circ\text{C}$ and preliminarily irradiated from the front side with nitrogen ions brings about an increase in the fraction of the Si_3N_4 phase in the synthesized Si_xN_y layer. This conclusion was drawn on the basis of an examination of spherical sections [1], studies of infrared (IR) absorption spectra in the range of 700–900 cm^{-1} [1–3], measurements of the energy shift of Auger electrons [2], and determination of electrical characteristics of Si_xN_y layers [3, 4]. It has been shown that an increase in the intensity of IR absorption characteristic of Si_3N_4 as the dose (Φ) of the argon irradiation increases clearly correlates with a corresponding increase in the average resistivity of the nitrated layer of silicon. Significant changes set in in the range from $\Phi = 10^{16}$ to $3 \times 10^{16} \text{ cm}^{-2}$. The process is completed by $\Phi = 3 \times 10^{16}$ – 10^{17} cm^{-2} [5].

An acoustic mechanism of the long-range effect is believed to be most probable [6–8]. For $\Phi \geq 10^{16} \text{ cm}^{-2}$, a network of half-loop dislocations originates under the argon-irradiated layer; at the same time, the coalescence of implanted argon gives rise to large argon bubbles (blisters) in this layer. It is assumed that acoustic pressure pulses are generated with increasing Φ as a result of jumplike processes of origination and evolution of both the dislocation network and blisters and also due to the blisters' burst-out. Notably, the pulsed pressure increases in all stages owing to self-synchronism or spontaneity of the jumplike process.

The objective of this study was to compare the results of the effects of an argon beam on the rear side of a silicon wafer containing a Si_xN_y layer with the results of isochronous postimplantation heat treatments, and also with the effect of ion beams of neon (there is blistering) and silicon (there is no blistering).

2. EXPERIMENTAL

In our experiments, we used wafers of commercial silicon designated as BKÉ-100 (float-zone n -Si, $\rho = 100 \Omega \text{ cm}$), BKD-2000 (float-zone p -Si, $\rho = 1000 \Omega \text{ cm}$), and KÉM-0.005 (n -Si : As, $\rho = 0.005 \Omega \text{ cm}$); all the wafers had the (111) orientation and were 0.3–0.6 mm thick. All the samples were subjected to conventional chemical–mechanical polishing.

In order to form the buried layers, nitrogen ions with an energy $E_N = 150 \text{ keV}$ were implanted into silicon; for the formation of surface Si_xN_y layers, a nitrogen-ion energy of $E_N = 50 \text{ keV}$ was required. The doses were in the range $\Phi_N = (1\text{--}5) \times 10^{17} \text{ cm}^{-2}$, the ion-current density amounted to $j_N = 5 \times 10^{13} \text{ cm}^{-2} \text{ s}^{-1}$, and the wafer temperature during implantation was $T_i = 400^\circ\text{C}$. We then annealed the wafers at temperatures $T_a = 400\text{--}1200^\circ\text{C}$ in an atmosphere of dry nitrogen or irradiated the rear side of the wafers with argon, neon, or silicon ions; the parameters of irradiation were the following: the ion energy $E_{\text{Ar(Ne,Si)}} = 40 \text{ keV}$, the ion dose $\Phi_{\text{Ar(Ne,Si)}} = 10^{17} \text{ cm}^{-2}$, and the ion-flux density $j_{\text{Ar(Ne,Si)}} = 5 \times 10^{13} \text{ cm}^{-2} \text{ s}^{-1}$. The wafer temperature during irradiation was $T_i = 500^\circ\text{C}$, since it was at this temperature

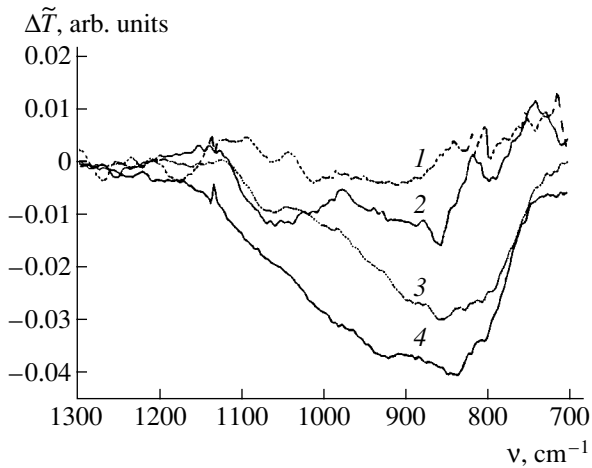


Fig. 1. The difference IR transmission spectra of silicon samples with Si_xN_y layers synthesized using nitrogen-ion implantation ($E_N = 150$ keV, $\Phi_N = 5 \times 10^{17}$ cm^{-2} , $T_i = 400^\circ\text{C}$). The spectra were measured after postimplantation heat treatments and were obtained by subtracting the spectrum of the sample with the same nitride layer without additional treatments. $\Delta\tilde{T}$ represents a variation in the transmittance. Curve 1 corresponds to an annealing for 2 h at $T_a = 500^\circ\text{C}$; curve 2 corresponds to an annealing for 2 h at $T_a = 600^\circ\text{C}$; curve 3 corresponds to an annealing for 2 h at $T_a = 700^\circ\text{C}$; and curve 4 corresponds to the spectrum measured after subsequent irradiation of the rear side with argon ions ($E_{\text{Ar}} = 50$ keV, $j_{\text{Ar}} = 5 \times 10^{13}$ cm^{-2} s^{-1} , $\Phi_{\text{Ar}} = 10^{17}$ cm^{-2} , $T_i = 500^\circ\text{C}$).

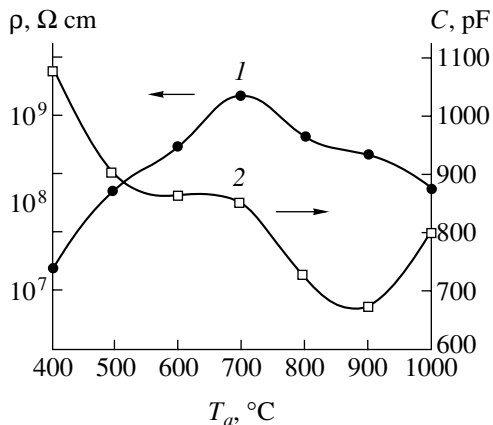


Fig. 2. Dependences of (1) resistivity ρ and (2) capacitance C of the Si_xN_y layer on the annealing temperature T_a .

that the most pronounced effect of an increase in the fraction of Si_3N_4 in the Si_xN_y layers was observed [1, 2].

Since the wafer is heated by an ion beam during implantation, we calculated the equilibrium temperature of the sample using an equation reported elsewhere [9]. The calculation showed that even when the sample is irradiated with 40-keV ions and the ion-flux density is 10^{14} cm^{-2} s^{-1} , the sample can be heated up to 255°C

if the target is not specially heated and the target holder is at room temperature (at 20°C). However, if the heated target holder is used and the sample temperature before irradiation is 500°C , an increase in temperature (with allowance made for the decrease in emissivity to 0.8) amounts to $\sim 20^\circ\text{C}$. These estimates were obtained disregarding the heat removal by the components of the target holder; in fact, the irradiation-induced heating of the samples was even less significant. Thus, the observed variations in the properties of the samples after irradiation with argon ions (see below) do not result from additional heating induced by the ion beam.

We studied the properties of Si_xN_y layers using transmission electron microscopy (TEM) and IR spectroscopy; we also measured the current–voltage (I – V) characteristics and the capacitance of these layers.

In the TEM studies, we used an ÉM-100 electron microscope with an accelerating voltage of 75 kV. The IR spectra were recorded using a Bruker IFS 113V spectrometer; in this case, we employed high-resistivity silicon substrates in order to avoid the effect of screening by free charge carriers. For electrical measurements, we used KÉM-0.005 substrates with a synthesized silicon-nitride surface layer. The I – V characteristics were measured using a two-contact scheme, Me– Si_xN_y –Si–Me (as was done by Demidov *et al.* [3, 4]). The low-resistivity KÉM-0.005 substrate was chosen so as to reduce the contribution of the substrate resistance and the barrier effects on the total structure resistance. The In–Ga eutectic alloy was used as the contact material; the diameter of the contact areas was 5 mm.

3. RESULTS AND DISCUSSION

3.1. The Effect of the Annealing Temperature on the State of the Implantation-Synthesized Si_xN_y Layer

A steady increase in the IR absorption intensity (a decrease in the transmittance \tilde{T}) for the sample in the wave-number range $\nu = 800$ – 900 cm^{-1} (Fig. 1) and a monotonic decrease in the resistivity ρ of the Si_xN_y layer (Fig. 2, curve 1) were observed as the annealing temperature increased in the range $T_a = 400$ – 700°C . At the same time, the capacitance C of the Me– Si_xN_y –Si structure decreased by a factor of about 1.5 (Fig. 2, curve 2). All these data indicate that, as the annealing temperature increases, the composition of the synthesized layer becomes progressively closer to the stoichiometric one; i.e., the insulating properties of this layer improve. However, according to the TEM data, the structure of the Si_xN_y layer remained fine-grained and the interface between this layer and the silicon remained highly imperfect and blurred (Fig. 3).

As the annealing temperature increased to $T_a = 800^\circ\text{C}$, the synthesized layer became less disperse and the interface, more well-defined. However, dendritic precipitates of the Si_3N_4 phase were observed (Fig. 4); simultaneously, the insulating properties of the layer degraded (Fig. 2, curve 1). A similar effect of annealing was mentioned previously [10], in which case the dendritic formations were identified with the $\beta\text{-Si}_3\text{N}_4$ phase. A further increase in the annealing temperature led to the complete crystallization and disintegration of the layers; therefore, it was impossible to examine the layers using an electron microscope (when thinned, the synthesized layers disintegrated).

The crystallization of the Si_xN_y layer is confirmed by the appearance of a fine structure in the IR spectra of the samples subjected to high-temperature annealing; the higher the value of T_a , the more clearly this fine structure manifested itself (in Fig. 5, the spectrum of the sample annealed for 2 h at $T_a = 1200^\circ\text{C}$ is shown). This result is consistent with the data reported in [11]. Crystallization of insulating nitride layers is an undesirable outcome of heat treatment and represents the most serious problem in the formation of these layers by ion-beam synthesis [12].

3.2. Effect of Ion-Beam Treatment of the Wafer's Rear Side on the State of the Si_xN_y Layer

As mentioned above, it has been shown previously [1–4] that argon-ion irradiation of the rear side of a silicon wafer may represent an alternative to heat treatment in the course of the synthesis of nitride layers. As a result of such irradiation, an increase in absorption is observed in the IR spectra, while the fine structure hardly manifests itself (Fig. 1, curve 4). The microdiffraction pattern for the corresponding nitride layers has a form typical of amorphous materials (a diffuse halo can be seen).

In order to confirm that it is the processes of the formation and self-synchronized burst-out of blisters which produce changes in Si_xN_y layers, we studied the effect of additional irradiation of the rear side of silicon wafers with Ne^+ and Si^+ ions under the same conditions as in the case of irradiation with Ar^+ ions. Such a choice of ions is governed by the fact that blistering occurs as a result of irradiation with neon ions as well; however, in the present case, the blisters are located at a greater depth and do not burst out owing to a larger range of neon ions and to a thinner sputtered layer. Irradiation with silicon does not give rise to blisters at all.

Our studies showed that the samples with the Si_xN_y layer are hardly affected by irradiation with Ne^+ and Si^+ ions from the rear side: the interface remains blurred;

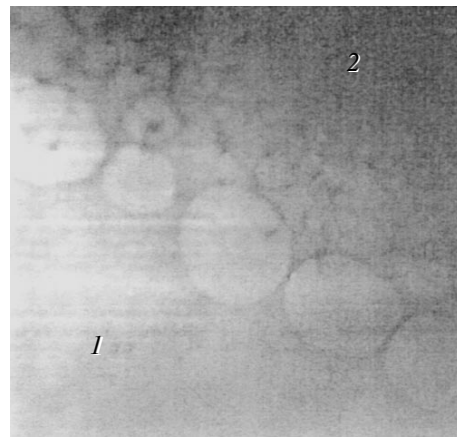


Fig. 3. A TEM image of the $\text{Si-Si}_x\text{N}_y$ interface in the sample implanted with nitrogen ions ($E_N = 50 \text{ keV}$, $\Phi_N = 2.5 \times 10^{17} \text{ cm}^{-2}$, $T_i = 400^\circ\text{C}$) and then annealed at $T_a = 600^\circ\text{C}$. Number 1 indicates the synthesized layer and 2 indicates the substrate. Magnification is equal to 4800.

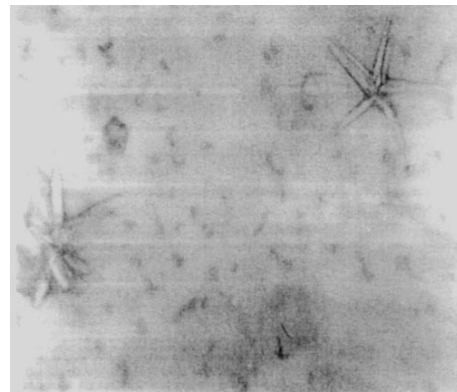


Fig. 4. Dendritic precipitates of the Si_3N_4 phase in the sample irradiated with nitrogen ions ($E_N = 50 \text{ keV}$, $\Phi_N = 5 \times 10^{17} \text{ cm}^{-2}$, $T_i = 400^\circ\text{C}$) and then annealed for 2 h at $T_a = 800^\circ\text{C}$. Magnification is equal to 4800.

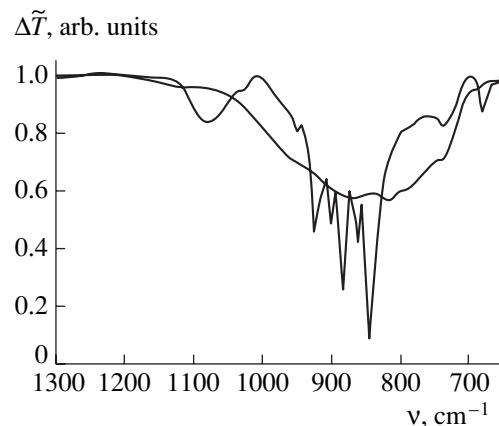


Fig. 5. The IR spectra of transmittance \tilde{T} for the silicon samples after implantation of nitrogen ($E_N = 150 \text{ keV}$, $\Phi_N = 5 \times 10^{17} \text{ cm}^{-2}$, $T_i = 400^\circ\text{C}$): (1) after nitrogen implantation and (2) after an additional annealing for 2 h at $T_a = 1200^\circ\text{C}$.

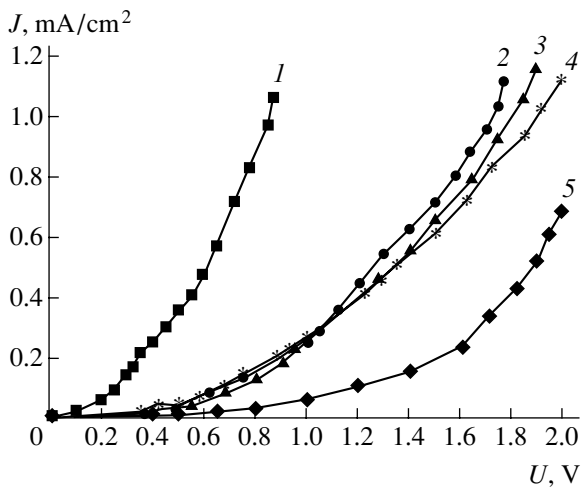


Fig. 6. The current–voltage characteristics $J(U)$ for the silicon samples implanted with nitrogen ($E_N = 50$ keV, $\Phi_N = 5 \times 10^{17}$ cm $^{-2}$, $T_i = 400^\circ\text{C}$) (1) without an additional treatment, (2) after annealing at $T_a = 500^\circ\text{C}$ (the temperature corresponding to that of ion implantation into the rear side of the wafer), (3) after irradiation with Si^+ ions, (4) after irradiation with Ne^+ ions, and (5) after irradiation with Ar^+ ions. Curves 3–5 correspond to the same conditions of ion implantation into the rear surface of the wafer: $E = 40$ keV, $\Phi = 10^{17}$ cm $^{-2}$, $T_i = 500^\circ\text{C}$, and $j \approx 10^{13}$ cm $^{-2}$ s $^{-1}$.

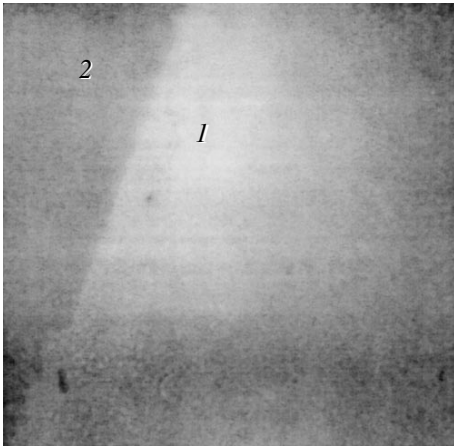


Fig. 7. The TEM images of the Si_xN_y –Si interface in the sample irradiated from the front side with nitrogen ions ($E_N = 50$ keV, $\Phi_N = 2.5 \times 10^{17}$ cm $^{-2}$, $T_i = 400^\circ\text{C}$) and from the rear side with argon ions ($E_{\text{Ar}} = 40$ keV, $\Phi_{\text{Ar}} = 10^{17}$ cm $^{-2}$, $T_i = 500^\circ\text{C}$). Magnification is 4800. (1) Synthesized layer and (2) silicon substrate.

the synthesized nitride layer remains highly imperfect; and a slight decrease in the leakage currents (Fig. 6, curves 4, 3) is apparently caused by the partial annealing of defects and by changes in the state of the surface due to the elevated irradiation temperature ($T_i = 500^\circ\text{C}$).

As a result of irradiation with argon ions, the Si – Si_xN_y interface became the most sharply defined (see Fig. 7), the number of defects in the nitride layer decreased significantly, the synthesized layer became more homogeneous, and leakage currents decreased to the lowest level (Fig. 6, curve 5). We used the linear portions of the I – V characteristics to estimate the resistivity of the Si_xN_y layer; we obtained $\rho \approx 5 \times 10^9$ Ω cm. The dielectric constant for the layers under investigation was found to be equal to $\epsilon \approx 5$.

4. CONCLUSION

It follows from the above-mentioned results that the limiting temperature of the isochronous postimplantation annealing of implantation-synthesized Si_xN_y layers is $T_a = 700^\circ\text{C}$. A further increase in the annealing temperature is not effective because it gives rise to dendritic crystallization and results in the degradation of insulating properties.

Irradiation of the rear side of a silicon wafer with argon ions ($\Phi_{\text{Ar}} \approx 10^{17}$ cm $^{-2}$, $T_i = 500^\circ\text{C}$) stimulates the synthesis of the insulator phase in the Si_xN_y layer that formed at the front side of the wafer, improves the layer's properties as an insulator, and, correspondingly, may represent an alternative to postimplantation annealing performed at temperatures that exceed 500°C .

It is shown that irradiation of the rear side of the single-crystal silicon wafer, which includes a nitride layer at the front surface, with neon and silicon ions under the same conditions as those for the irradiation with argon ions does not affect the characteristics of the nitride layer as an insulator. This observation is consistent with the previously suggested spontaneous-acoustic model of the long-range effect of argon-ion irradiation on the synthesis of a Si_xN_y insulator phase [8].

ACKNOWLEDGMENTS

We thank R.V. Kudryavtseva, E.A. Pitirimova, V.K. Vasil'ev, and V.L. Shargel' for their help with performing the experiments.

REFERENCES

1. P. V. Pavlov, K. A. Markov, V. V. Karzanov, and E. S. Demidov, *Vysokochist. Veshchestva*, No. 2, 56 (1995).
2. V. V. Karzanov, K. A. Markov, and D. V. Masterov, *Neorg. Mater.* **34** (9), 1138 (1998).
3. E. S. Demidov, V. V. Karzanov, K. A. Markov, and D. I. Kuritsyn, *Vestn. Nizhegorodskogo Univ., Ser. Fiz. Tverd. Tela*, No. 2, 105 (1998).
4. E. S. Demidov, V. V. Karzanov, and K. A. Markov, *Fiz. Tekh. Poluprovodn. (St. Petersburg)* **34** (2), 170 (2000) [*Semiconductors* **34**, 163 (2000)].

5. E. S. Demidov, V. V. Karzanov, K. A. Markov, *et al.*, Fiz. Tekh. Poluprovodn. (St. Petersburg) **35** (1), 21 (2001) [Semiconductors **35**, 20 (2001)].
6. V. V. Karzanov, K. A. Markov, S. Yu. Zubkov, *et al.*, in *Proceedings of the All-Russia Conference "Probing Microscopy-99," Nizhni Novgorod, 1999* (IFM Ross. Akad. Nauk, Nizhni Novgorod, 1999), p. 185.
7. E. S. Demidov, V. V. Karzanov, K. A. Markov, and D. A. Lobanov, in *Proceedings of the All-Russia Conference "Probing Microscopy-2000," Nizhni Novgorod, 2000* (IFM Ross. Akad. Nauk, Nizhni Novgorod, 2000), p. 166.
8. E. S. Demidov, V. V. Karzanov, K. A. Markov, and V. V. Sdobnyakov, Zh. Éksp. Teor. Fiz. **120** (3), 637 (2001) [JETP **93**, 558 (2001)].
9. H. Ryssel and I. Ruge, *Ionenimplantation* (Teubner, Stuttgart, 1978; Nauka, Moscow, 1983).
10. P. V. Pavlov, T. A. Kruze, and D. I. Tetelbaum, Phys. Status Solidi A **36** (1), 81 (1976).
11. Yu. N. Volgin and Yu. I. Ukhanov, Opt. Spektrosk. **38** (4), 727 (1975) [Opt. Spectrosc. **38**, 412 (1975)].
12. A. B. Danilin, Élektron. Prom-st., No. 4, 55 (1990).

Translated by A. Spitsyn

SEMICONDUCTOR STRUCTURES,
INTERFACES, AND SURFACES

Optical Storage on the Basis of an n -InSb–SiO₂– p -Si Heterostructure

Yu. A. Nikol'skiĭ

State Pedagogical Institute, Borisoglebsk, 397160 Russia

e-mail: bgpi@mail.ru

Submitted September 18, 2000; accepted for publication February 7, 2002

Abstract—The presence of potential barriers and deep traps in n -InSb/SiO₂/ p -Si heterostructures makes it possible to realize the optical memory function on the basis of this structure. The maximal memory coefficient measured on the forward current voltage characteristic is as large as $\sim 10^4$. This heterostructure can be used as an optoelectronic memory cell, which provides a means not only for the storage of signals but also for their summation. © 2002 MAIK “Nauka/Interperiodica”.

In most cases, the phenomenon of optical memory in semiconductors is due to the presence of inhomogeneities, which give rise to collective potential barriers [1]. The electric field at the barrier causes spatial separation of nonequilibrium charge carriers: in order to enter the region where holes are located, the electrons should overcome a potential barrier, which is referred to as the recombination barrier (E_r). This circumstance is responsible for the anomalously long, up to 10^5 s, experimental lifetimes of nonequilibrium carriers.

In addition to the recombination barriers, another condition necessary for the existence of long-term relaxation and persistent conduction is that the light-induced nonequilibrium carriers be involved in the charge transport; i.e., certain low-resistivity conducting regions should also be present along with the barriers. These regions are connected with each other via the “passes” or the so-called drift barriers (E_d), which are always lower than the recombination ones.

Thus, electrons should overcome the E_r barrier to recombine and should overcome the E_d barrier to be involved in conduction. The potential relief in semiconductors is usually defined by the chaotic inhomogeneities; i.e., it depends on the statistical character of the distribution of impurities. This accounts for the low reproducibility of the results obtained for the samples prepared from the same material and according to the same technology.

It is reasonable, therefore, to investigate structures with an artificially produced potential relief. Among them, heterostructures formed from materials with a considerable lattice mismatch are of special interest. The semiconductor–insulator–semiconductor n -InSb/SiO₂/ p -Si heterostructure is just such an example.

In this study, we consider the n -InSb/SiO₂/ p -Si heterostructure from the viewpoint of its applicability to the production of efficient memory cells.

The n -InSb/SiO₂/ p -Si heterostructures were formed through the discrete evaporation of 0.5- to 1.0- μm -thick n -type indium antimonide film on an oxidized silicon substrate in vacuum under a residual pressure of 10^{-5} Torr at a temperature of $\sim 300^\circ\text{C}$. The resulting n -InSb films were polycrystalline with a crystal size of ~ 0.5 μm and had a carrier concentration $n = (2-5) \times 10^{17}$ cm^{-3} and a mobility $u = (5-8) \times 10^3$ $\text{cm}^2/(\text{V s})$ at room temperature. The carrier concentration in p -Si was about 10^{15} cm^{-3} at room temperature.

Thin copper wires were soldered by an eutectic In–Sn alloy to both the n -InSb film and the p -Si substrate to facilitate measurement of the current–voltage (I – V) characteristics of the samples. The n -InSb film surface was illuminated using an incandescent lamp with the illuminance ranging from 200 to 2000 lx.

We established that, both at room temperature and at 77 K, upon illumination or in darkness, the I – V characteristic of the structures is exponential in the entire range of the bias voltages considered and can be expressed by the empirical function

$$I = I_{s0} \exp(T/T_0) \exp(V/V_0), \quad (1)$$

where I_{s0} , T_0 , and V_0 are constants. This is strongly suggestive of a tunneling mechanism of the current across the heterostructure.

As a result of the investigation of optical memory in polycrystalline n -InSb films grown on insulating substrates from mica and silicon oxide, we demonstrated that the magnitude of the optical memory effect is no larger than 5–7% when the films are held at the liquid-nitrogen temperature. Under the same experimental conditions, the optical memory effect in n -InSb/SiO₂/ p -Si heterostructures is as large as $\sim 40\%$, which points to its relation to the potential barriers and deep traps that are present in heterostructures with a large lattice mismatch, when numerous defects are generated in the

space charge region near the interfaces between the components of the structure. The ellipsometry method yielded an SiO₂ layer thickness of 17–25 Å, which explains its tunnel transparency.

Let us consider the I - V characteristics measured at 77 K upon the illumination of the samples and after the light was switched off (Fig. 1). Under the steady-state effect of integrated radiation, both the forward and the reverse currents increase from their dark values (curve 1) to the values I_l (curve 2). After the light was switched off, neither the forward nor the reverse currents returned to the initial values they had in the dark; instead, we detected a new value of the current, which is denoted as the memory current I_m (curve 3). It turns out to be slightly smaller than I_l and considerably exceeds I_0 . By definition, the coefficient of memory α_m is equal to the ratio of the memory current to the dark current. At the same values of illuminance E , duration of exposure t , and the sign and value of the bias voltage V , the maximal memory coefficient is as large as 10^4 for the forward portion of the I - V characteristics. With an increase in the voltage, α_m increases and then starts to decrease rapidly because of an increase in the dark current. A heterostructure with residual conduction can be returned to the initial state by the application of a reverse bias-voltage pulse of up to 20 V for the duration of a few milliseconds. Such an “erasure” of memory is due to the field-induced suppression of the residual conduction.

The decay of the residual conduction in a system described by a two-barrier model has the following form [2]:

$$I_0/I_{mt} = (1 + \alpha t)^{\nu}, \quad (2)$$

where I_0 is the current across the heterostructure in the absence of the excitation illumination, i.e., at the instant $t = 0$; I_{mt} is the memory current at the instant t ; α is a constant which depends on the temperature and the potential barrier height at $t = 0$; and ν is a constant which depends on the relationship between the drift and the recombination barrier heights ($\nu < 1$).

According to [2], the value of α can be determined from the experimental dependences $\log(I_0, I_{mt}) \propto \nu\alpha t$ and $\log(I_0, I_{mt}) \propto \tan(\alpha t)$ for the limiting cases $\alpha t \ll 1$ and $\alpha t \gg 1$, respectively. Using the relaxation curve (Fig. 2) and excluding from consideration the initial portion, which is governed by conventional processes that are unrelated to the residual conduction, we obtain $\alpha = 1.8 \times 10^{-3} \text{ s}^{-1}$. Substituting this value in (2) and plotting the dependence

$$\log(I_0/I_{mt}) = f[\log(1 + \alpha t)], \quad (3)$$

we find $\nu = 0.25$. This result also satisfies the constraint $E_d/E_r < 0.5$, which was obtained in [3]. The residual conduction current proves to be a function of the illuminance of the sample. Figure 3 shows the forward portions of the I - V characteristics measured for a sample

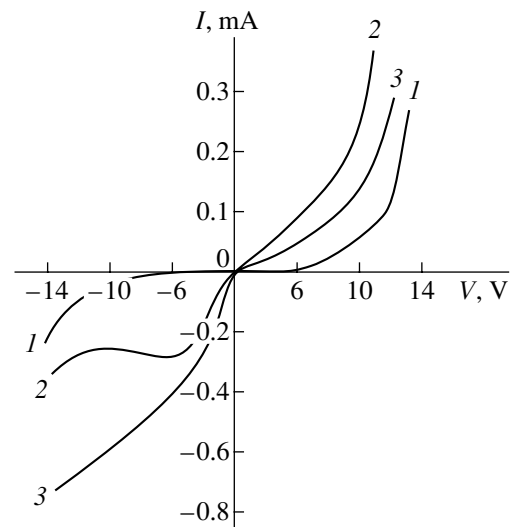


Fig. 1. I - V characteristics of n -InSb/SiO₂/ p -Si heterostructure at 77 K (1) in the dark, (2) under illumination, and (3) the memory current.

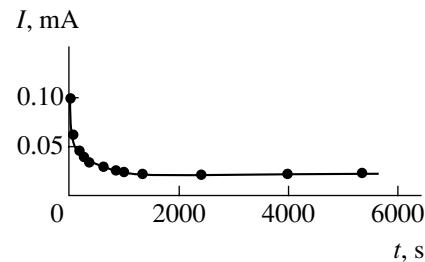


Fig. 2. Relaxation of the residual conduction in an n -InSb/SiO₂/ p -Si heterostructure.

submerged into liquid nitrogen in the dark (curve 1). Then, the sample was illuminated by white light with an illuminance of 200 lx for 10 s. The light was switched off, and after 10 s the residual conduction current was measured as a function of voltage (curve 2). Application of the erasing pulse of voltage restored the initial state of the structure. These measurements were repeated at different intensities of illumination.

It is important to note that any intermediate value of the memory current (Fig. 3, curves 1–4) can be obtained at a constant illumination intensity by varying the time of exposure. In fact, when the first exposure to light is followed by a new exposure rather than by the restoration of the initial state, the memory current in a heterostructure increases from the initial value I_{m1} to I_{m2} , and this process may be continued until the residual conduction current reaches a certain maximal value. Thus, the heterostructure studied is capable of integrating the effect produced by incident radiation.

The phenomena described above are likely to be due to the presence of deep-level surface centers in the space charge region of the heterostructure under study. According to [4], the charge carriers that are released

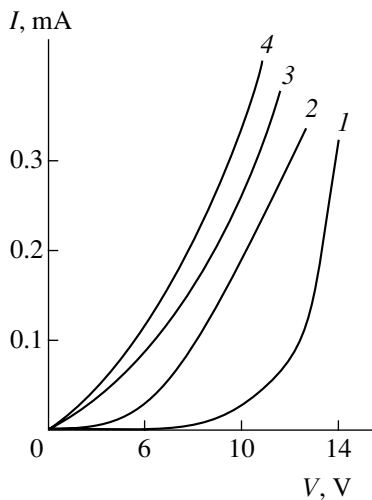


Fig. 3. Forward portions of the I - V characteristics: (1) dark current; (2-4) the residual conduction currents after exposure to light with intensity $E = 200, 1000,$ and 2000 lx, respectively.

from these centers through illumination may be involved in the conduction for a considerable period of time. This is due to a potential barrier that hampers the recombination of carriers and grows with the capture of electrons by the surface states. In contrast to homogeneous semiconductors, where the potential barrier is brought on by only the charge at the surface states, heterostructures feature an additional increase in the barrier height due to a difference between the work function of the materials in contact. Because of this, the phenomenon of optical memory in heterostructures is especially pronounced.

These results indicate that the n -InSb/SiO₂/ p -Si heterostructure can be used as an optical memory cell. In view of the fact that both the source and the detector may be made of the same material, thus ensuring that their spectral characteristics are matched, this heterostructure holds much promise for applications in optoelectronics and, in the future, in integrated optics.

Figure 3 indicates that each subsequent light pulse incident on the heterostructure surface increases the residual conduction current; i.e., the structure sums the incoming information. As was demonstrated above, the residual conduction current is defined by nonequilibrium carriers, whose concentration is controlled by the recombination barrier. Therefore, each subsequent light pulse increases the concentration of nonequilibrium carriers and, thus, the residual conduction current. The concentration of nonequilibrium carriers will evidently increase until the residual conduction current attains a certain ultimate value, since the separation of the carri-

ers gives rise to electric fields that compensate the fields of the inhomogeneities. Consequently, the potential-barrier height and, therefore, the values of E_r and E_d decrease, which promotes the recombination of the separated carriers. This dynamic equilibrium defines the ultimate residual current. In our case, it exceeds the dark current by 3-4 orders of magnitude.

Thus, by varying the intensity of illumination, one can set any current across the sample in the range from the dark current to the ultimate value of the residual current and the n -InSb/SiO₂/ p -Si heterostructure can be used as an optoelectronic memory cell capable not only of storing but also of summing signals. Another specific feature of such a cell is that the signals can be detected without the application of an external voltage, which is only necessary for reading; the cell can detect optical information if it is within the range of the spectral photosensitivity of the materials comprising the heterostructure.

Comparing the operation potentialities offered by the memory cell considered with the known characteristics of the other devices of this type, we should note its high sensitivity in the infrared spectral range, where the magnitude of the optical-memory effect is as large as ~40%.

The following conclusions may be drawn from this study.

(i) A pronounced optical memory effect observed in the n -InSb/SiO₂/ p -Si heterostructure is due to the presence of potential barriers and deep traps, which are introduced owing to a large mismatch between the lattice constants of the components.

(ii) The optical memory cell suggested on the basis of this heterostructure has a high sensitivity in the infrared spectral range, and the magnitude of its optical-memory effect is as large as ~40%.

REFERENCES

1. M. K. Sheĭnkman and A. Ya. Shik, *Fiz. Tekh. Poluprovodn. (Leningrad)* **10**, 209 (1976) [*Sov. Phys. Semicond.* **10**, 128 (1976)].
2. V. B. Sandomirskiĭ, A. G. Zhdan, M. A. Messerer, and I. B. Gulyaev, *Fiz. Tekh. Poluprovodn. (Leningrad)* **7**, 1314 (1973) [*Sov. Phys. Semicond.* **7**, 881 (1973)].
3. A. Ya. Shik, *Zh. Ėksp. Teor. Fiz.* **68**, 1859 (1975) [*Sov. Phys. JETP* **41**, 932 (1975)].
4. M. K. Sheĭnkman, I. V. Markevich, and V. A. Khvostov, *Fiz. Tekh. Poluprovodn. (Leningrad)* **5**, 1904 (1971) [*Sov. Phys. Semicond.* **5**, 1654 (1971)].

Translated by A. Sidorova-Biryukova

SEMICONDUCTOR STRUCTURES,
INTERFACES, AND SURFACES

Field-Dependent Photosensitivity of In–SiO₂–Cd_{0.28}Hg_{0.72}Te Metal–Insulator–Semiconductor Structures with an Opaque Field Electrode

V. V. Vasil'ev, A. F. Kravchenko, and Yu. P. Mashukov

*Institute of Semiconductor Physics, Siberian Division, Russian Academy of Sciences,
pr. Akademika Lavrent'eva 13, Novosibirsk, 630090 Russia*

Submitted January 30, 2002; accepted for publication February 13, 2002

Abstract—The study of the photosensitivity of an In–SiO₂–Cd_{0.28}Hg_{0.72}Te metal–insulator–semiconductor structure with an opaque electrode is continued and the results are reported in this paper. The effect of a drastic decrease in photosensitivity with increasing inversion voltage is considered. This effect manifests itself both under unmodulated illumination (measurements of photocapacitance) and under modulated illumination (measurements of photovoltage), with the onset of a decrease in photovoltage coming ahead of that in photocapacitance. It is believed that this effect is caused by an increase in the longitudinal resistance of the inversion layer and by the anomalous generation of charge carriers at the semiconductor–insulator interface; as a result of the latter, the resistance of the induced *p–n* junction decreases. © 2002 MAIK “Nauka/Interperiodica”.

1. INTRODUCTION

As we have shown previously [1], *p*-Cd_{0.28}Hg_{0.72}Te-based metal–insulator–semiconductor (MIS) structures feature appreciable photosensitivity even if the field electrode is opaque. In this case, photosensitivity is caused by photogenerated charge carriers, which are produced outside the MIS structure and are pulled into this structure by an electric field of the induced *p–n* junction. By measuring experimentally the illumination-intensity dependence of the photocapacitance, we managed to determine the following two parameters of the induced *p–n* junction: (i) the product of resistance under zero bias by the junction area R_0A and (ii) the parameter β , which characterizes the degree of nonideality in the Shockley formula. We also estimated the quantity Δl , i.e., the effective width of the strip surrounding the MIS structure, which “collects” electrons from within this strip.

In this paper, we report the results of further studies of the photoeffect in the aforementioned structures. We consider the effect of a drastic decrease in photosensitivity under high bias voltages; we will also determine the value of Δl directly by scanning the focused laser beam.

It is well known that the photovoltage of a MIS structure is governed by the intensity of the generation–recombination processes. In the case under consideration, where the photogenerated charge carriers arrive at a MIS structure from outside (through its periphery), we should also take into account the resistance which these carriers experience during their distribution over the entire MIS-structure area.

The problem concerning the spread of excess charge in the inversion layers was considered in detail by Ovsyuk [2]. In particular, it was shown that the diffusion length for such a process may be many times larger than the conventional ambipolar-diffusion length in the bulk. This is caused by the separation of electrons and holes, which can recombine only if they cross the *p–n* junction.

In our previous study [1], we assumed that the spreading resistance is fairly low; as a result, all electrical characteristics were considered identical over the entire area. Since, according to [1], we are dealing with eddy electric currents, it is very convenient to use the ratio between the longitudinal resistance of the inversion layer and the resistance of the induced *p–n* junction as a test for the smallness of the spreading resistance. It was found that the photocapacitance does not remain unchanged as the inversion voltage increases; rather, it starts to decrease drastically at voltages higher than 3.5 V. It is the analysis of this effect that this study is concerned with.

2. RESULTS AND DISCUSSION

In our experiments, we used a bulk Cd_{0.28}Hg_{0.72}Te crystal with the following Hall parameters: the hole concentration $p = 8 \times 10^{15} \text{ cm}^{-3}$ and the hole mobility $\mu = 470 \text{ cm}^2 \text{ V}^{-1} \text{ s}^{-1}$. A pyrolytic SiO₂ layer grown at the substrate temperature of 100°C served as the insulator. A system of field electrodes with an area of $0.5 \times 0.5 \text{ mm}^2$ and a thickness of 500 nm was formed by the thermal evaporation of In through a mask. We studied two types of samples differing only in the insulator thickness (70 and 100 nm). The results of studying the samples with

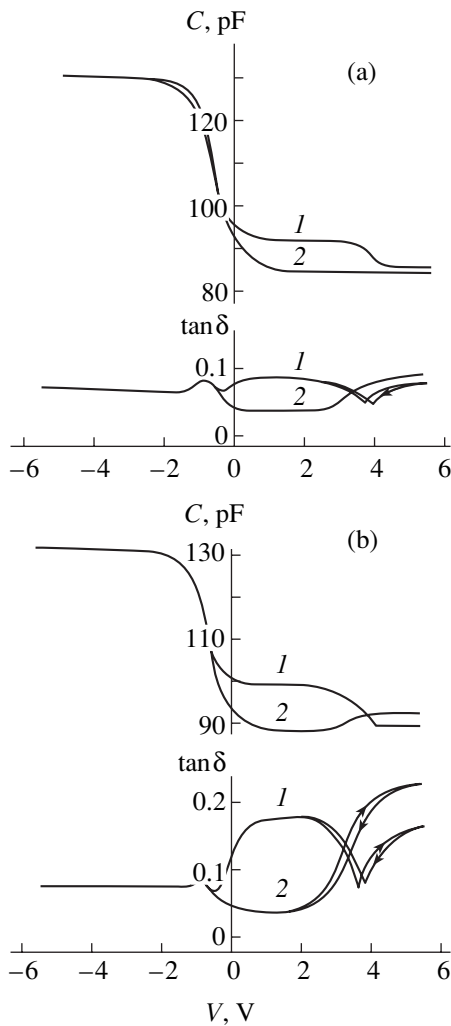


Fig. 1. The capacitance–voltage characteristics and the $\tan \delta(V)$ dependences measured (1) under illumination and (2) without illumination. The structures were illuminated using an incandescent lamp with a light flux of 4×10^{14} photon $\text{cm}^{-2} \text{s}^{-1}$; the voltage-sweep frequency was equal to 5×10^{-3} Hz; and the insulator was a 100-nm-thick pyrolytic SiO_2 . The frequency of the test signal was equal to (a) 500 and (b) 100 kHz.

a 70-nm-thick insulator were reported previously [1]. All measurements were performed at a temperature of 80 K.

In Fig. 1, we show typical capacitance–voltage (C – V) characteristics and also the voltage dependences of the dielectric losses, $\tan \delta = f(V)$, measured in the dark and under illumination. An incandescent lamp was used (as in [1]) for illumination. It can be seen that distinct changes appear in the characteristics measured both in the dark and under illumination at the voltages of ~ 3 – 4 V. A drastic decrease in the photocapacitance and a significant increase in the “dark” capacitance at a frequency of 100 kHz are observed, as well as a drastic increase in $\tan \delta$ in the dark both at 500 and 100 kHz. The effect of

illumination on the dependence $\tan \delta(V)$ is more complicated.

Currently, such effects are typically related to an additional (anomalous) generation of electron–hole pairs at the semiconductor–insulator interface [3–5].

Let us consider the processes occurring in a MIS structure. An increase in the capacitance C of a MIS structure subjected to illumination is caused by the fact that the excess photogenerated electrons, which fill the inversion layer, bring about a decrease in the depletion-layer width. The induced p – n junction is found to be biased in the forward direction; as a result, the junction conductance increases in accordance with the Shockley formula (see [1]). This conductance gives rise to illumination-related $\tan \delta$. Anomalous generation gives rise to an additional flow of holes from the surface into the bulk; as a result, the barrier becomes lower and an equivalent counterflow of holes from the bulk to the surface comes into existence. As a result, the capacitance and conductance of the barrier increase. In addition, the degree of lowering of the barrier is governed by the relation between the electron and hole components of the current through the barrier.

The obtained C – V characteristics and $\tan \delta(V)$ dependences measured without illumination are qualitatively consistent with those reported previously [3] and are attributed to the appearance of additional (anomalous) conductance of the induced p – n junction.

In [1], we determined experimentally the relation between C and $\tan \delta$ of the junction. Applying these data to the curves measured without illumination (Fig. 1), we may conclude that the appreciable increase in $\tan \delta$ is inconsistent with only the slight increase in C . As in [3], this observation can be explained by the fact that anomalous-generation regions occupy only a small fraction of the MIS structure area (in anomalous-generation regions, the capacitance C is varied only moderately, whereas the conductance G may increase by several orders of magnitude).

We now consider the role of illumination of a MIS structure. It can be seen that illumination of a structure biased with a comparatively high voltage brings about a decrease, rather than an increase, in $\tan \delta$. If we assume that (i) illumination-related conductance of the induced p – n junction is added to the conductance produced by anomalous generation and (ii) the simplest equivalent circuit shown in Fig. 2a is valid (in order to simplify the estimations, we ignored the losses in the insulator), the loss tangent $\tan \delta$ will then decrease at the frequencies

$$\omega < \omega_{\max}. \quad (1)$$

Here,

$$\omega_{\max} = G_s / [(C_i + C_s)C_s]^{1/2} \quad (2)$$

is the circular frequency corresponding to a maximum of $\tan \delta$, i.e., $\tan \delta^{(\max)}$; specifically,

$$\tan \delta^{(\max)} = C_i/2[(C_i + C_s)C_s]^{1/2}; \quad (3)$$

C_i is the capacitance of the insulator; and C_s and G_s are the capacitance and conductance, respectively, of the induced p - n junction. Using experimental values of C_i and C_s determined conventionally from the C - V characteristics, we obtain $\tan \delta^{(\max)} = 0.21$, which is in satisfactory agreement with the results of measurements at a frequency of 100 kHz. The frequency 500 kHz is higher than the frequency corresponding to the maximum in $\tan \delta$; in this case, an increase in conductance should bring about an increase in $\tan \delta$, which is in complete contradiction with experimental data. Thus, we have to admit that the equivalent circuit under consideration is inapplicable.

An illumination-induced decrease in $\tan \delta$ measured both at 100 and at 500 kHz can be explained using an equivalent circuit in which an effective series resistance R_l is introduced (Fig. 2b). This resistance appears owing to the fact that inhomogeneities in conductance of certain areas of the induced p - n junction bring about a redistribution of the test current, which crosses the MIS structure, so that this current now flows predominantly through the regions with a high conductance; as a result, the longitudinal component of the test current appears in the inversion layer. When the structure is exposed to light, the resistance R_l may decrease owing to a decrease in the longitudinal component of the test current; it is this circumstance that brings about a decrease in $\tan \delta$ at any of the two frequencies under consideration.

A decrease in the conductance of the inversion layer for the photocurrent may be caused by the capture of free electrons from the inversion layer by the insulator, by an electron-conductivity decrease due to the surface-potential fluctuations, and by partitioning of the inversion layer due to anomalous regions, in which inversion is replaced by depletion.

In order to clarify the question concerning the area from which the MIS structure collects electrons, we measured the photosensitivity under the conditions of scanning the periphery of the MIS structure with a focused laser beam. The beam was modulated with a frequency of 1000 Hz, and the photovoltage signal appearing at the structure was fed to a selective amplifier with an input impedance of $10^6 \Omega$ and 70 pF.

When measuring the photovoltage, we used a "red" laser diode (the wavelengths of $\lambda = 630$ – 680 nm); the laser radiation was directed to a cryostat (described elsewhere [6]) via one of the two optical channels of a binocular microscope, with the second channel being used for the visual examination of the sample.

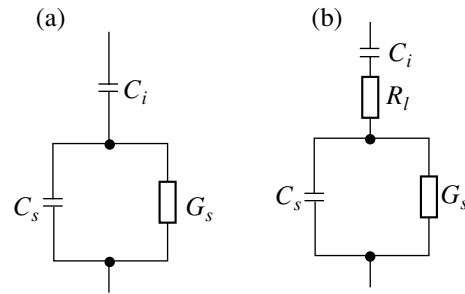


Fig. 2. Two equivalent circuits of a MIS structure. C_i is the insulator capacitance; C_s and G_s are the induced p - n -junction capacitance and conductance, respectively; and R_l is the effective longitudinal resistance of the inversion layer.

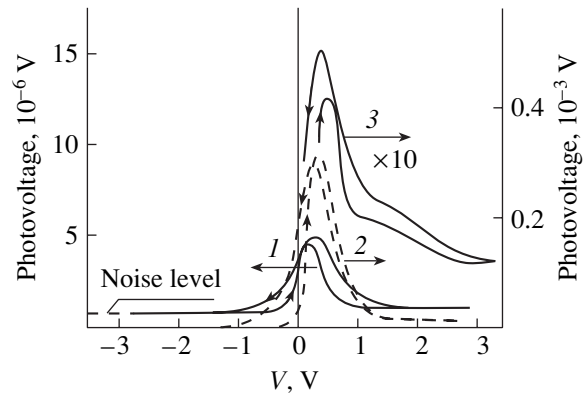


Fig. 3. Photovoltage as a function of bias applied to a MIS structure. The closest periphery of the structure was illuminated with a focused laser beam modulated with a frequency of 1 kHz. The illumination intensity amounted to (1) 5×10^{-8} , (2) 4×10^{-6} , and (3) 1.35×10^{-5} W.

The photocapacitance and photovoltage have the same origin, i.e., a variation in the voltage across the barrier; therefore, it is reasonable to compare these two effects. When a MIS structure is exposed to a modulated (pulsatory) light beam, an increment of the voltage across the barrier has both dc and ac components, with the dc component controlling the photocapacitance and the ac component controlling the photovoltage.

In Fig. 3, we show typical dependences of photovoltage on the voltage across the MIS structure for several intensities of laser radiation focused on a spot in the immediate vicinity of the field-electrode edge.

The capacitance–voltage characteristics of a sample exposed to laser radiation were similar to those obtained under illumination with an incandescent lamp. The effect was the same irrespective of whether the laser beam was focused or defocused (to illuminate the entire area of the MIS structure) and whether the laser radiation was modulated or unmodulated.

In Fig. 4, we show the dependence of one of the photovoltage peaks on the laser-spot position (x) in reference to the field-electrode edge. It can be seen that the

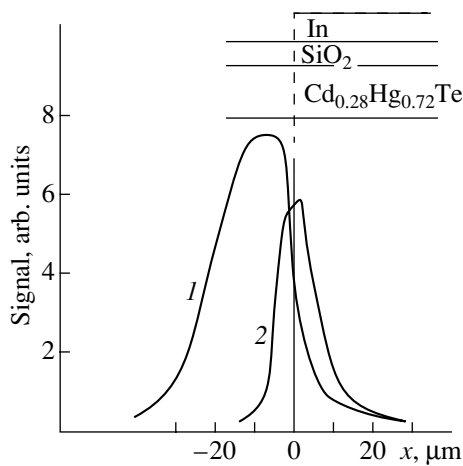


Fig. 4. (1) Dependence of the photovoltage signal on the position of the laser-spot center x in reference to the MIS structure edge and (2) the distribution of the radiation power over the laser spot.

characteristic extension of the region whose illumination governs the photoeffect in the structure amounts to $\sim 15 \mu\text{m}$, which is consistent with the estimate obtained by Ovsiuk *et al.* [1] using a fairly complex indirect method.

In the data represented in Fig. 3, we can also discern the following two features which support the assumption about the profound effect of the longitudinal resistance of the inversion layer. First, the photovoltage begins to decrease at lower voltages than does the photocapacitance; this can be explained by the fact that the conductance of the induced p - n junction not only has an ohmic but also a capacitive component (corresponding to the beam-modulation frequency of 1 kHz), so that the photovoltage will be affected more profoundly by the longitudinal resistance of the inversion layer. Second, a "tail" appears in the dependence of photovoltage on the applied voltage for high voltages and for the highest illumination intensity, which may be attributed to an increase in the inversion-layer conductivity due to the photogenerated electrons themselves.

A parasitic phenomenon which gives rise to a decrease in the photoeffect magnitude at constant current (photocapacitance) may be related to the presence of leakage currents through the insulator, since the direction of a leakage current is opposite to that of photocurrent. However, the leakage currents are fairly low in the case under consideration. If the leakage current is

equal to 5×10^{-9} A at a voltage of 5 V and room temperature, this current becomes lower than 10^{-12} A at 78 K for the same voltage. For comparison, the photocurrent is equal to 5×10^{-10} A for the lowest illumination intensity, which amounts to 10^{13} photon/($\text{cm}^2 \text{ s}$) [1].

3. CONCLUSION

When studying the photovoltage by the conventional method, one uses a semitransparent field electrode. In this case, the effects related to the longitudinal motion of free charges in the inversion layer are obscured by more pronounced effects. In this paper, we described the decrease in the photosensitivity of a MIS structure with an opaque field electrode; we explain this effect by a decrease in the resistance of the induced p - n junction as a result of the anomalous generation of charge carriers at the semiconductor-insulator interface and by an increase in the resistance to the longitudinal motion of free charges within the inversion layer.

In view of the complexity of the studied structures, which are most probably nonuniform over their area, and the complexity of the considered processes, we did not attempt in this paper to explain in detail the obtained experimental data or to process them mathematically.

ACKNOWLEDGMENTS

We thank V.N. Ovsiuk for valuable comments.

REFERENCES

1. V. N. Ovsiuk, V. V. Vasil'ev, and Yu. P. Mashukov, *Fiz. Tekh. Poluprovodn. (St. Petersburg)* **34** (7), 822 (2000) [*Semiconductors* **34**, 794 (2000)].
2. V. N. Ovsiuk, *Electronic Processes in Semiconductors with Space-Charge Regions* (Nauka, Novosibirsk, 1984).
3. R. S. Nakhmanson, P. P. Dobrovolski, and S. S. Amineva, *Phys. Status Solidi A* **9** (2), 699 (1972).
4. Yu. V. Nastaushev, I. G. Neizvestnyĭ, and V. N. Ovsiuk, *Poverkhnost*, No. 11, 1126 (1984).
5. A. A. Guzev, G. L. Kuryshv, V. G. Polovinkin, and V. A. Usova, *Mikroelektronika* **17** (5), 465 (1988).
6. V. V. Vasil'ev, Yu. P. Mashukov, and V. N. Ovsiuk, *Fiz. Tekh. Poluprovodn. (St. Petersburg)* **31** (6), 749 (1997) [*Semiconductors* **31**, 642 (1997)].

Translated by A. Spitsyn

**SEMICONDUCTOR STRUCTURES,
INTERFACES, AND SURFACES**

Effect of Carrier Localization on the Optical Properties of MBE-Grown GaAsN/GaAs Heterostructures

**B. V. Volovik*, N. V. Kryzhanovskaya*, D. S. Sizov*, A. R. Kovsh* **,
A. F. Tsatsul'nikov*, J. Y. Chi**, J. S. Wang**,
L. Wei**, and V. M. Ustinov***

* *Ioffe Physicotechnical Institute, Russian Academy of Sciences,
Politekhnicheskaya ul. 26, St. Petersburg, 194021 Russia*

** *Industrial Technology Research Institute, Hsinchu 310, Taiwan, R.O.C.*

Submitted February 12, 2002; accepted for publication February 13, 2002

Abstract—The optical properties of GaAsN/GaAs heterostructures grown by molecular-beam epitaxy with different nitrogen content in the layers have been studied. The optical properties of GaAsN layers in the growth conditions under study are defined by the carrier recombination via localized states related to a strong composition inhomogeneity in the solid solution. The increasing of the nitrogen content raises the composition inhomogeneity and the carrier localization energy. © 2002 MAIK “Nauka/Interperiodica”.

1. INTRODUCTION

Worldwide interest in the production and study of GaAsN/GaAs heterostructures is due to the fact that, owing to the strongly nonmonotonic dependence of the band gap on the nitrogen content, this system allows the fabrication of devices emitting in the 1.3 to 1.5- μm wavelength range. Lasers based on these heterostructures can find application in optical-fiber communication lines, since they have a better temperature stability than the lasers based on InP substrates which are now being used. Moreover, effective monolithic vertical-cavity surface-emitting lasers (VCSELs) with distributed AlGaAs/GaAs Bragg reflectors (DBR) can be produced. Effective injection lasers of the 1.3- μm range [1, 2], VCSELs included [3, 4], have been fabricated using InGaAsN/GaAs quantum well (QW) heterostructures.

Nowadays, the main problem in the growth of (In)GaAsN/GaAs laser heterostructures is a decrease of the emission intensity as the nitrogen content in a layer rises. This effect is generally attributed to the increased contribution of nonradiative recombination in these solid solutions [5]. Besides this, in the structures produced by molecular-beam epitaxy (MBE), the nitrogen active radicals produced by the plasma source may be responsible for the degradation of the layer quality, owing to the action of high-energy nitrogen ions from the source on the growing surface [6]. A further specific feature in the growing of a GaAsN solid solution, as well as quantum-confined InGaAsN structures, is the composition inhomogeneity of the solid solution, i.e., phase separation, even at low nitrogen content. The layer inhomogeneity may be significantly enhanced in highly strained InGaAsN/GaAs QWs. It was shown

that in such structures the carriers are localized on the fluctuations of potential related to the modulation of the QW layer thickness [6, 7] as well as to the variation of the compound composition (phase decomposition) [8]. The formed nanosize domains can be regarded as an array of quantum dots (QD) [6, 7].

In the present study, we investigated the optical properties of GaAsN/GaAs layers grown using MBE under various conditions of deposition. We found the conditions of the GaAsN layer deposition when a rise in the nitrogen content in the layer is not followed by a significant decrease in the emission intensity. It is shown that even under low (0.6–1.3%) nitrogen content and with the layer-by-layer (two-dimensional) epitaxial growing of layers, the inhomogeneous incorporation of nitrogen and the formation of potential fluctuations can occur, which result in the localization of carriers and, in particular, the related S-shaped temperature dependence of the photoluminescence (PL) peak position.

2. EXPERIMENT

The structures were grown in a Riber Epineat MBE system with solid-state sources of Group III elements and arsenic. Active atomic nitrogen was produced by passing ultrapure nitrogen gas through a UNI Bulb RF plasma source Applied Epi. The studied 0.2- μm -thick GaAsN layers were incorporated into a GaAs matrix that was confined at the substrate and surface sides by AlGaAs/GaAs superlattices (20/20 Å) to eliminate the leakage of nonequilibrium carriers to defective regions in the substrate and at the upper interface. The temperature of growth was 520°C for GaAsN and 600°C for other layers; the growth rate was 1 $\mu\text{m h}^{-1}$. The growth was performed under As enrichment. The crystal perfec-

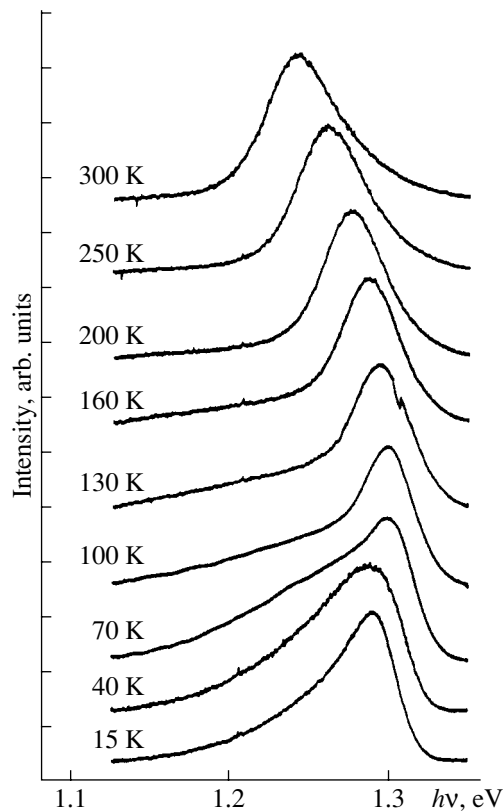


Fig. 1. PL spectra of a $\text{GaAs}_{0.99}\text{N}_{0.01}$ structure recorded at different temperatures at the excitation power density of 100 W cm^{-2} .

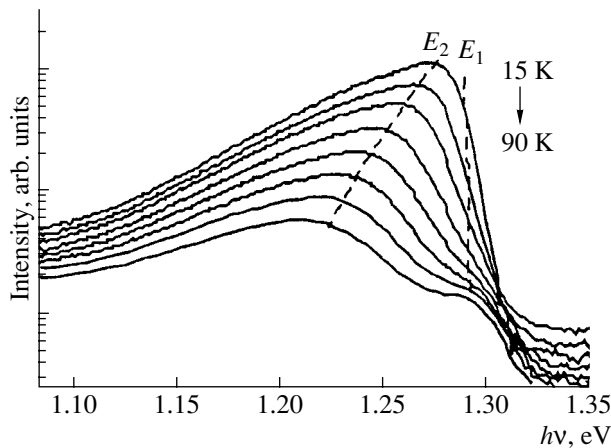


Fig. 2. PL spectra of a $\text{GaAs}_{0.99}\text{N}_{0.01}$ structure recorded at temperatures 15–90 K at the excitation power density of 0.6 W cm^{-2} .

tion of the layers and the content of nitrogen (in mol %) in GaAsN were determined using X-ray diffractometry in [004] azimuth. The PL was excited by an Ar^+ laser (with a power density up to 100 W cm^{-2}) and a pulsed N_2 laser (with a pulse power density up to 100 kW cm^{-2}). The PL emission was detected by a cooled Ge photo-

diode; the excitation spectra were recorded with a cooled photomultiplier.

3. RESULTS AND DISCUSSION

GaAsN/GaAs layers differing in their nitrogen content were studied. The growth conditions were chosen so as to obtain a “striped” pattern of the reflection high-energy electron diffraction, which corresponds to two-dimensional growth. For GaAsN structures produced under the chosen conditions of deposition, the PL intensity appeared to be only insignificantly (3–4 times) lower than that for GaAs layers deposited at the same temperature. The long-wavelength shift of the emission peak is $\sim 300 \text{ meV}$ for GaAsN layers with 2.5 mol % of nitrogen. An additional rise in the intensity was reached using the post-growth annealing of structures in the arsenic media.

To investigate the nature of emission from these layers, we studied the PL spectra at different temperatures. The spectra of a $\text{GaAs}_{0.99}\text{N}_{0.01}$ layer are presented in Fig. 1. As seen, the rise of temperature in the range $T = 15\text{--}70 \text{ K}$ results in a short-wavelength shift of the PL line, while a further increase in temperature up to room temperature shifts the emission peak to lower $h\nu$ energies; i.e., the behavior of the PL peak as the temperature rises is S-shaped. Similar S-shaped characteristics of PL were reported earlier for InGaAsN/GaAs QWs; they were attributed to a strong modulation of the thickness and/or composition of QWs [9]. This behavior of the PL peak is typical of the recombination of electrons localized on potential fluctuations of high density [10]. It is related to the fact that if there the transport of carriers exists between these fluctuations and the temperature is low, then the line shape is defined by the distribution of localization centers over the energy of localization. Only the centers with the highest localization energy are filled with carriers at low temperature. The rise in temperature enables the filling of centers with a lower energy of localization, thus shifting the emission peak to higher photon energies. A further rise in temperature causes a long-wavelength shift of the PL peak due to the decreasing of the band gap E_g .

For a more detailed investigation of the carrier localization in GaAsN layers, we studied the PL spectra at a lower density of the excitation power. Several bands are observed in these spectra; their relative intensity changes as the temperature varies (Fig. 2). At the lowest temperature $T = 15 \text{ K}$, one band is observed, which asymmetrically broadened to lower photon energies. As the temperature rises to $T = 70\text{--}100 \text{ K}$, the PL spectrum is split into two bands denoted as E_1 and E_2 . The E_2 band dominates the spectrum at a low excitation density. This line E_2 is characterized by large broadening ($\sim 100 \text{ meV}$) and a considerable temperature shift, which significantly exceeds the variation of the GaAs band gap. Such behavior with the rise in temperature is typical of PL induced by recombination via localized states with considerable dispersion over the binding

energy; it is associated with the thermal emission of carriers from the regions responsible for the short-wavelength shoulder of the PL line. As shown below, the E_1 band is also related to recombination via localized states. A considerable broadening (~ 30 meV) of the E_1 line, as well as that of E_2 , is due to the fact that, at low temperatures and under hindered transport of carriers, the line shape is defined by the distribution of localization centers over the localization energy. With a further rise in temperature, the intensity of the E_2 line sharply decreases owing to the thermal emission of carriers, and only the E_1 line remains in the spectrum at room temperature. Thus, we believe that the S -shaped shift of the PL peak as the temperature increases, which is observed at sufficiently high intensities of the exciting light, results from the joint contributions of the shifts of the two PL line peaks E_1 and E_2 , which are related to the recombination via different centers of localization.

To determine the band gap of a solid solution and the localization energy of carriers, we studied the transmission and the PL excitation spectra. Figure 3 shows the spectra of PL, PL excitation (PLE), and absorption of a GaAsN structure with a nitrogen content of 1.3%. The absorption spectra were calculated from the experimental transmission spectra of a GaAsN layer on a GaAs substrate and of a free substrate using the relation $\tilde{T}(\text{GaAsN}/\text{GaAs})/\tilde{T}(\text{GaAs}) = C \exp(-\alpha d)$, where \tilde{T} is the transmittance, α is the absorption coefficient, d is the thickness of a GaAsN layer, and C is a constant. The PLE spectra exhibit a peak that is independent of the detection energy and denoted in the figure as E_0 . At excitation energies below E_0 , the luminescence intensity sharply decreases. We assume that the energy E_0 corresponds to the band gap of the GaAsN solid solution, whereas the recombination responsible for the PL occurs via localized states. This interpretation is consistent with the absorption spectra. At $E > E_0$, the obtained absorption spectra are well approximated by the square-root dependence of the absorption coefficient on energy $\alpha \propto (E - E_0)^{1/2}$, which is typical of bulk absorption in a material with the band gap E_0 . A shoulder in the absorption spectrum at lower energies ($E < E_0$) is related to localized states. For moderate densities of excitation energy, the PL peak is significantly shifted from the E_0 line to lower photon energies. When the density of the excitation energy is raised to 100 kW cm^{-2} , the PL peak shifts to higher photon energies; nevertheless, the peak remains appreciably shifted to lower energies with respect to the E_0 energy in the excitation spectrum, which means that the recombination via localized states is still dominant.

To study qualitatively the temperature dependence of the energy of carrier localization in a QD, we measured the temperature dependences of the characteristic energy E_{abs} determined from the experimental absorption spectra. The characteristic energy of the absorption

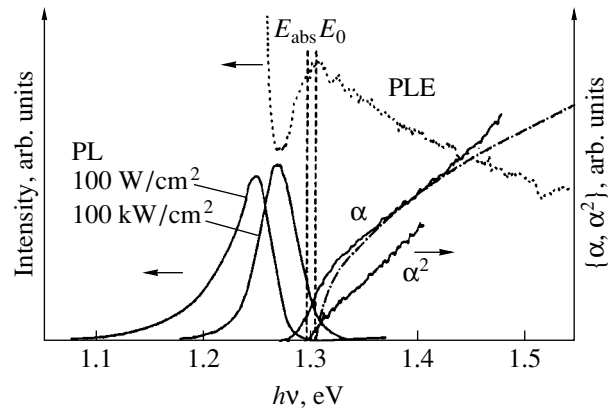


Fig. 3. Photoluminescence (PL), photoluminescence excitation (PLE), and absorption spectra of GaAsN layers with a nitrogen content of 1.3%. Dot-dashed line is calculation of $\alpha \propto E^{1/2}$ for the band gap E_0 .

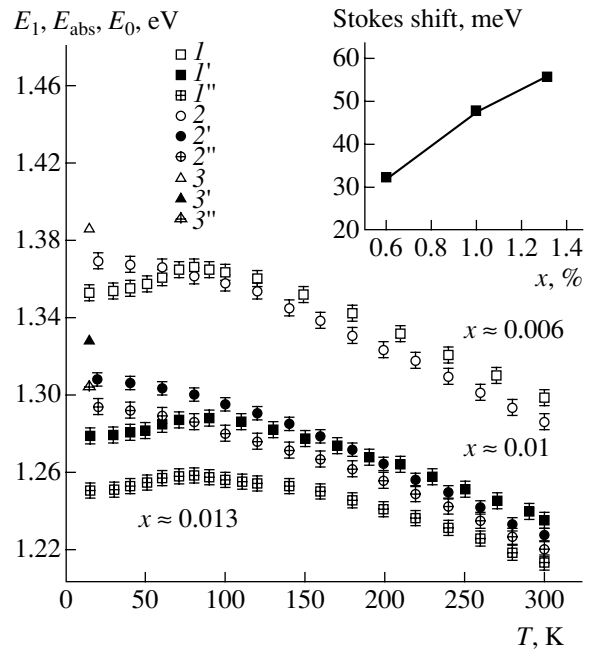


Fig. 4. Temperature dependences of the (I, I', I'') E_1 peak position in the PL spectra, the ($2, 2', 2''$) absorption edge energy E_{abs} , and the ($3, 3', 3''$) E_0 peak position in the excitation spectra for $\text{GaAs}_{1-x}\text{N}_x$ layers with varied nitrogen content in the layer, x : ($I-3$) 0.6%, ($I'-3'$) 1%, and ($I''-3''$) 1.3%. Inset: the Stokes shift vs. the nitrogen content x in GaAsN layers.

edge E_{abs} was determined from a linear approximation of the absorption edge by the dependence $\alpha^2(E)$. The choice of this quantity to estimate the absorption energy is justified by the sharply increasing error in the determination of E_0 at elevated temperatures, which is due to the absorption edge broadening. Figure 4 shows temperature dependences of the E_1 line position in the PL spectra and the characteristic energy E_{abs} in the absorption spectra, and also the position of the E_0 line

at 15 K in the PLE spectra for samples with different nitrogen content in their layers. The presented dependences confirm our assumption that the temperature variation of the PL spectra is governed by the redistribution of carriers between the localized states. The rise in temperature results in the thermal emission of carriers, and the interband recombination becomes dominant (the characteristic temperature of thermalization can be evaluated from the intersection between the temperature dependences of the PL peak and absorption edge E_{abs}). However, for the maximum nitrogen content in the discussed series of samples (1.3%), the PL is defined by the localized states up to room temperature. With the nitrogen content x increasing from 0.6 to 1.3%, the Stokes shift, defined in this case as the energy distance between the peaks in the PL (line E_1) and PLE (peak E_0) spectra at low temperatures, increases from 32 to 55 meV (see the insert in Fig. 4).

4. CONCLUSION

The study of the optical properties of GaAsN/GaAs layers has shown that the growth of a GaAsN solid solution is accompanied by the inhomogeneous incorporation of nitrogen into a layer. In the samples with a comparatively low nitrogen content in their layers, the carrier recombination at low temperatures occurs via the states localized on the fluctuations of the solid solution composition. Raising the nitrogen content results in the deeper localization of carriers, and the recombination via localized states is responsible for the optical properties of structures up to room temperature.

ACKNOWLEDGMENTS

This study was supported by the Russian Foundation for Basic Research, the Joint Program of the Ioffe Institute and the ITRI (Taiwan), and by the CRDF, grant no. RE1-2217.

REFERENCES

1. A. Yu. Egorov, D. Bernklau, D. Livshits, *et al.*, *Electron. Lett.* **35**, 1643 (1999).
2. K. Nakahara, M. Kondow, T. Kitatani, *et al.*, *Electron. Lett.* **32**, 1585 (1996).
3. K. D. Choquette, J. F. Clem, A. J. Fisher, *et al.*, *Electron. Lett.* **36**, 1388 (2000).
4. G. Steinle, H. Riechert, and A. Yu. Egorov, *Electron. Lett.* **37**, 92 (2001).
5. H. P. Xin and C. W. Tu, *Appl. Phys. Lett.* **74**, 2337 (1999).
6. H. P. Xin, K. L. Kavanagh, Z. Q. Zhu, and C. W. Tu, *J. Vac. Sci. Technol. B* **17**, 1649 (1999).
7. B. V. Volovik, A. R. Kovsh, W. Passenberg, *et al.*, *Semicond. Sci. Technol.* **16**, 186 (2001).
8. I. P. Soshnikov, N. N. Ledentsov, B. V. Volovik, *et al.*, in *Proceedings of the 9th International Symposium "Nanostructures: Physics and Technology," St. Petersburg, 2001*, p. 82.
9. A. Kaschner, T. Luttgert, H. Born, *et al.*, *Appl. Phys. Lett.* **78**, 1391 (2001).
10. A. Polimeni, M. Capizzi, M. Geddo, *et al.*, *Appl. Phys. Lett.* **77**, 2870 (2000).

Translated by D. Mashovets